



**MONASH** University

**Quantitative evaluation of fatigue crack using nonlinear  
guided waves in pipelines**

*Ruiqi Guan*

*Bachelor of Engineering (Honours)*

*A thesis submitted for the degree of Doctor of Philosophy at*

*Monash University in 2018*

*Faculty of Engineering*

*August, 2018*

## **Copyright notice**

© The author (2018).

Except as provided in the Copyright Act 1968, this thesis may not be reproduced in any form without the written permission of the author.

## **Abstract**

The interaction between nonlinear guided waves and fatigue crack at its initiation in metallic pipes was investigated. Literature review in terms of Lamb and guided wave propagation and interaction with damage in plate and pipe structures was introduced. Linear and nonlinear methods used to detect the damage in these metallic structures were also presented. Specific investigation as preliminary study have been conducted including the understanding mechanism of different types of nonlinearity, methods and calibration of wave excitation and acquisition, optimisation of numerical modelling, and evaluation and selection of appropriate nonlinear method.

The main content of this study contains three parts. First, theoretical analysis was extended from plate-like to pipe-like scenario and a finite element (FE) simulation model was established to validate the analytical analysis. Through the analysis, it is found that the second harmonic waves contain multiple wave modes and the flexural wave modes occupies a large proportion of the total wave energy induced by contact acoustic nonlinearity (CAN). Therefore, a proper nonlinear index was developed to assess the severity of contact acoustic nonlinearity of a pipe.

Second, the detection of fatigue crack in both plate and pipe structures with second harmonic generation method was then conducted. Both numerical and experimental studies were adopted on these two structures. Third order elastic constant and a seam crack were employed for the numerical model to simulate material nonlinearity and CAN respectively. Piezoelectric transducers accompanied with fatigue test and an advanced signal collecting system were used in the experimental test. Both the numerical and experimental results detect the existence of fatigue crack, and the results from pipe specimens is different from plates, where multiple waves were generated at double

-Quantitative evaluation of fatigue crack using nonlinear guided waves in pipelines-

harmonic as indicated in theoretical analysis. The differences between the results from simulation and experiment were addressed.

The third part of this study is to comprehensively analyse the interaction between fatigue crack propagation and guided waves and to quantify the relation between crack length and nonlinearity induced by a fatigue crack in an aluminium pipe. Through the numerical and experimental analyses, it was found that the nonlinear index increased monotonously with crack length at the early stage but began to decrease at a specific crack length. The increase of nonlinear index indicates the increasing part of crack that contributes to breathing behaviour while the following decrease is mainly because (a) the long crack delayed the wave to travel to the middle part and to generate breathing behaviour in the numerical method; and (b) the crack was changed from micro scale to macro scale in the experimental method. Nevertheless, the results from both studies can quantify the CAN in a pipe structure with nonlinear index and it can detect the initial stage of a fatigue crack within 1 mm in practice, which improved the sensitivity of linear method in terms of microcrack detection.

## Declaration

This thesis contains no material which has been accepted for the award of any other degree or diploma at any university or equivalent institution and that, to the best of my knowledge and belief, this thesis contains no material previously published or written by another person, except where due reference is made in the text of the thesis.

Signature: ...  .....

Print Name: ...Ruiqi Guan.....

Date: .....21/08/2018.....

## **Acknowledgements**

I would like to express my sincere gratitude to my supervisor, Dr. Ye Lu, who provides invaluable guidance, time and patience for my PhD candidature at Monash University. It has been enjoyable to work with him on this project, from the discussions of brainstorming ideas to analysing research outcomes. Throughout the research program, Dr. Ye Lu always helps me patiently and considerably whenever I have problems with my research study. It is my honour to work with Dr. Ye Lu and without his assistance, the research study could not progress smoothly. I would also like to thank my co-supervisor, Prof. Wenhui Duan for his guidance and support on my research progress.

I would like to thank all lab staffs at the Civil Engineering Lab of Monash University for their assistance on my experiment test. Special thanks go to Mr. Long Goh, Mr. Mark Tayler, Mr. Phillip Warnes and Mr. Zoltan Csaki for their professional assistance in operating experiment equipment, and preparing and ordering all materials for the experiment.

I wish to thank all of the staff members in Department of Civil Engineering, Monash University. Especially, thanks for the patient assistance during my candidature from Mrs. Jenny Manson and Ms. Min Major.

I would like to thank Prof. Zhongqing Su at the Hong Kong Polytechnic University for the assistance and support on my research work. He provides assistance and opportunities for my experiment studies in Hong Kong. I am grateful to his postgraduate students Mr. Kai Wang, Mr. Yehai Li and Ms. Feng Duan that I met in Hong Kong who gave me suggestions and assistance on my research work. And thanks to all the friends I met in Hong Kong, we spent a wonderful time in the 6-month study away.

-Quantitative evaluation of fatigue crack using nonlinear guided waves in pipelines-

I am grateful to Monash University and Faculty of Engineering who provided financial support to my project. My scholarships were Monash Graduate Scholarship (MGS) provided by Monash University and Faculty of Engineering International Postgraduate Research Scholarship (FEIPRS) funded by Faculty of Engineering, Monash University.

Finally, I would like to express my huge thank to all my friends for their encouragement and deepest thank to my parents for their support and unconditional love.

Ruiqi Guan

August, 2018

## Table of Contents

Copyright notice .....	I
Abstract.....	II
Declaration.....	IV
Acknowledgements .....	V
Notations.....	XII
List of Figures.....	XIV
List of Tables .....	XXIII
Chapter 1 Introduction.....	1
1.1 Guided waves in pipelines .....	1
1.2 Motivation and objectives.....	2
1.3 Thesis outline .....	4
Chapter 2 Guide waves in metallic structures .....	6
2.1 Guided wave properties .....	6
2.1.1 Dispersion of guided wave modes in pipes .....	6
2.1.2 Mode selection.....	7
2.1.3 Attenuation .....	8
2.2 Lamb wave propagation in plates .....	8
2.3 Guided wave propagation in pipes .....	11
2.4 Wave excitation and acquisition.....	14
2.5 Conclusions .....	17
Chapter 3 Guided wave based damage detection in pipelines.....	18
3.1 Theoretical basis of wave scattering in pipes .....	18

3.2 Damage detection with linear guided waves .....	20
3.2.1 Reflection and transmission of incident waves .....	20
3.2.2 Reflection and transmission from defect-converted wave modes .....	21
3.2.3 Time of flight (ToF) and time reversal.....	22
3.2.4 Synthetically focused imaging.....	23
3.2.5 Tomography .....	24
3.3 Damage detection with nonlinear guided waves .....	26
3.3.1 Background theory .....	27
3.3.2 Damage detection with nonlinear guided waves .....	33
3.4 Special issues in pipe inspection .....	40
3.4.1 Bends in pipes.....	40
3.4.2 Effect of environmental and operational conditions (EOCs) .....	41
3.5 Conclusions .....	44
Chapter 4 Investigation of nonlinear guided wave characteristics in plate and pipe like structures.....	45
4.1 Optimisation, wave excitation and acquisition of simulation model .....	45
4.1.1 Optimisation of simulation model .....	45
4.1.2 Wave excitation and acquisition in simulation model.....	48
4.2 Investigation of wave excitation and nonlinearity acquisition in experiment test	52
4.2.1 Wave excitation and acquisition in experiment.....	52
4.2.2 Voltage calibration for nonlinearity .....	53
4.2.3 PZT type in experiment test of pipe structures.....	55

4.2.4 Low pass filter for experiment system nonlinearity .....	58
4.2.5 Effect of static loading during fatigue .....	60
4.3 Selection of appropriate nonlinear method.....	64
4.3.1 Mixed frequency response.....	64
4.3.2 Higher harmonic generation .....	75
4.4 Conclusion.....	81
Chapter 5 Theoretical analysis of contact acoustic nonlinearity (CAN) in pipe structures .....	82
5.1 Theoretical analysis of nonlinear guided waves caused by CAN in plate structures .....	82
5.2 Theoretical analysis of nonlinear guided waves caused by CAN in pipe structures .....	85
5.2.1 Problem formulation.....	85
5.2.2 Results of analytical analysis.....	90
5.3 Numerical analysis of interaction between guided wave and close crack.....	92
5.3.1 Numerical model .....	93
5.3.2 Results from numerical analysis.....	95
5.4 Nonlinear parameter for nonlinearity measurement in pipes .....	101
5.5 Conclusions .....	103
Chapter 6 Nonlinear guided waves for fatigue crack detection.....	104
6.1 Fatigue crack detection in plates using second harmonic generation.....	104
6.1.1 Mode selection.....	105
6.1.2 Modelling of steel plate .....	106

6.1.3 Experimental studies for crack propagation in steel plates .....	112
6.2 Material nonlinearity in pipes.....	115
6.2.1 Simulation models for material nonlinearity .....	116
6.2.2 Results of simulation methods.....	119
6.3 Fatigue crack detection in pipes with second harmonic generation method .....	121
6.3.1 Excitation selection.....	121
6.3.2 Signal processing method.....	123
6.3.3 Numerical analysis .....	124
6.3.4 Experimental validation.....	130
6.4 Result comparisons between plate and pipe structures .....	138
6.5 Conclusions .....	141
Chapter 7 Quantitative evaluation of fatigue crack in pipe-like structures .....	142
7.1 Numerical analysis for quantitative evaluation of fatigue crack in pipes.....	142
7.1.2 Simulation model.....	142
7.1.3 Simulation results .....	144
7.2 Experimental test for quantitative evaluation of fatigue crack in pipes .....	147
7.2.1 Experiment set up .....	147
7.2.2 Experimental results .....	148
7.3 Nonlinear index with fatigue crack growth .....	151
7.3.1 Nonlinear parameter .....	151
7.3.2 Nonlinear indices from simulation .....	152
7.3.3 Experimental result.....	155

7.4 Conclusions .....	159
Chapter 8 Conclusions.....	160
8.1 Main findings of this thesis .....	160
8.2 Future work .....	163
References .....	166
List of Publications.....	182

## Notations

The abbreviations commonly used in this thesis are listed below with corresponding definitions.

BEM	Boundary element method (BEM)
CAN	Contact acoustic nonlinearity
CISS	Crack-induced second-source-stress loading
CSM	Common source method
DI	Damage index
EMAT	Electromagnetic acoustic transducer
EOCs	Effect of environmental and operational conditions
FBE	Fusion bonded epoxy
FD	Finite difference
FE	Finite element
FFT	Fast Fourier transform
FIR	Finite impulse response
FSE	Finite strip elements
HUT	Helical ultrasound tomography
INELAN	Artificially inhomogeneous and elliptically anisotropic
LISA	Local interaction simulation approach
MI	Modulation index (MI)
MSLM	Mass-spring lattice model
MUT	Meridional ultrasound tomography
NDE	Non-destructive evaluation
NME	Normal mode expansion method

OD	Outer diameter
PCA	Principal component analysis
PE	Polyethylene
PVDF	Polyvinylidene fluoride film
RAPID	Reconstruction algorithm for probabilistic inspection of damage
SH	Shear horizontal wave
SHM	Structural health monitoring
SIRT	Simultaneous iterative reconstruction technique
STFT	Short-time Fourier transform
PDI	Probabilistic-based diagnostic imaging
PZT	Piezoelectric lead zirconate titanate
ToF	Time of flight
VUMAT	Vectorized user-defined material model

## List of Figures

Figure 1.1 (a) Gas pipeline explosion in Qinglong, Guizhou; (b) Aging pipeline blast in Baumgarten, Austria. ....	1
Figure 2.1 Coordinates of a free plate. ....	9
Figure 2.2 Dispersion curve for phase velocity of a 5 mm thick steel plate. ....	10
Figure 2.3 Coordinates of a hollow cylinder. ....	11
Figure 2.4 Dispersion curve for phase velocity of a 73 mm OD schedule 40 steel pipe [25]. ....	13
Figure 2.5 Load applying on outer surface of a hollow cylinder [25]. ....	14
Figure 3.1 Configuration of the scheme: mode $\mu$ of family $N$ is incident in a hollow cylinder with a circumferential crack [60]. ....	19
Figure 3.2 Reflection coefficient vs the circumferential extent of the notch from numerical and experimental analysis for a pipe with a through-thickness notch [53]. ....	21
Figure 3.3 Maximum amplitudes of each received signal after time reversal indicating the location of a notch in a pipe [78]. ....	23
Figure 3.4 The reconstruction geometry of HUT for a pipe treated as unwrapped plate [86]. ....	25
Figure 3.5 Tomogram for a steel pipe elbow [91]. ....	26
Figure 3.6 Stress-strain cure for materials with (a) quadratic nonlinearities and (b) cubic nonlinearities, and relative frequency spectrum [101]. ....	28
Figure 3.7 (a) "Mechanical-diode" effect; (b) modulation of $C(t)$ ; (c) high harmonic spectrum [112]. ....	31

Figure 3.8 Model of a 2D infinite plate with breathing crack [113].	32
Figure 3.9 Stress distribution of CISS and induced wave modes through the thickness of the plate [113].	33
Figure 3.10 Plots of internal resonance points: when (a) fundamental waves are torsional modes, and (b) fundamental waves are longitudinal modes. Colour lines stand for the fundamental modes and the black dashed lines are the possible cumulative secondary modes. The circles represent the potential synchronism points [15].	35
Figure 3.11 The relation between the relative nonlinear parameter ( $A_2/A_1^2$ ) and the propagation distance under different thermal fatigue cycles [17].	36
Figure 3.12 $A_2/A_1^2$ vs circumferential angle $\theta$ at the driving frequency 0.88 MHz [123].	37
Figure 3.13 Modulation of probe signal amplitude, when the probing signal is: (a) vibration, (b) ultrasonic signal [124].	38
Figure 3.14 (a) MI with varying frequency of vibration, (b) MI with changing amplitude of vibration at 50 Hz vibration frequency [131].	40
Figure 3.15 L(0, 2) mode wave propagation at different time for a 30°bent pipe in FE simulation model. The wave is (a) before the bend; (b) at the bend; (c) after the bend [34].	41
Figure 3.16 Attenuation values for T (0, 1) (blue) and L (0, 2) (red) mode over frequency range of 11-34 kHz under different sand conditions [41].	43
Figure 3.17 A plot of range vs sensitivity when the excitation frequency is 16 kHz for different coatings and positions (PE for polyethylene and FBE for fusion bonded epoxy) [144].	43
Figure 4.1 Mesh of plate in simulation model: (a) overview of the mesh; (b) mesh of the hole at the end of plate; (c) mesh of the notch and (d) mesh of the sensor.	47

Figure 4.2 Mesh of the pipe in simulation model: (a) overview mesh of pipe and (b) mesh of the notch. ....	47
Figure 4.3 Circular PZT in simulation model.....	49
Figure 4.4 Lamb wave propagation in the plate model. ....	50
Figure 4.5 PZT in the pipe mode.....	51
Figure 4.6 Sensor ring in the pipe model.....	51
Figure 4.7 Guided wave propagation in the pipe model. ....	51
Figure 4.8 PZTs attached on plate and pipe specimens.....	53
Figure 4.9 Wave amplitude in terms of input voltage for (a) received signal and (b) signal at double frequency. ....	54
Figure 4.10 Transmitted signals from an intact pipe at (a) fundamental frequency and (b) double frequency. ....	55
Figure 4.11 Transmitted signal from different types of PZTs. ....	56
Figure 4.12 Signals after band pass filter at double frequency for different types of PZTs. ....	57
Figure 4.13 Frequency spectrum of received signals from a plate.....	59
Figure 4.14 Frequency spectrum of received signals from a pipe.....	59
Figure 4.15 Relative nonlinear parameter $\beta'$ in terms of crack length/ wavelength (a) transmitted signal; (b) reflected signal.....	61
Figure 4.16 Relative nonlinear parameter in terms of fatigue cycles (a) transmitted signals and (b) reflected signals. ....	62
Figure 4.17 Transmitted signals of plates with 3mm fatigue crack in frequency domain. ....	64

Figure 4.18 Dispersion curve for 194 mm outer diameter, 10 mm wall thickness steel pipe.....	65
Figure 4.19 Location of actuator, shaker and sensor for a pipe model with OD 194 mm. ....	67
Figure 4.20 Load applied on model.....	68
Figure 4.21 A seam crack created in a meshed pipe in simulation (highlighted regions are the two crack surfaces defined as seam crack and contact pair properties). ...	68
Figure 4.22 Snapshots of ultrasonic waves passing through a seam crack with CAN. (a) Transmitted wave cannot pass when the crack is open and (b) stress is transmitting through the closed crack. ....	69
Figure 4.23 Received signal in time domain from the simulation of a pipe with OD194 mm. ....	70
Figure 4.24 Received signal in frequency domain. ....	70
Figure 4.25 Frequency domain results for different locations of vibration and actuator. ....	71
Figure 4.26 Second harmonic enhanced by vibration. ....	71
Figure 4.27 Location of actuators and receiver. ....	72
Figure 4.28 Input signal: (a) 1 ms (10 cycles) 10 kHz tone burst signal (b) 1 ms (100 cycles) 100 kHz tone burst signal. ....	73
Figure 4.29 Received signal in time domain for the 1 ms input signal case. ....	73
Figure 4.30 Received signal in frequency domain (a) 1 ms input (b) 0.5 ms input (c) 0.2 ms input and (d) 0.1 ms input. ....	75
Figure 4.31 Dispersion curve of 101 mm outer diameter, 5.74 mm wall thickness steel pipe for (a) phase velocity and (b) group velocity. ....	76

Figure 4.32 Mode shape for L(0, 4) at 0.71 MHz along the thickness direction.....	77
Figure 4.33 Input signal at the frequency of 0.71 MHz. ....	78
Figure 4.34 Locations of actuators with applied load and receivers in simulation model. .....	79
Figure 4.35 Location of actuators and receivers.....	79
Figure 4.36 Received signal in time domain with 0.71 MHz excitation from simulation. .....	80
Figure 4.37 Received signal in frequency domain with 0.71 MHz excitation. ....	81
Figure 5.1 Configuration of the plate model [153].....	83
Figure 5.2 Configuration of analytical pipe model.....	85
Figure 5.3 Dispersion curve of 80 mm outer diameter, 4 mm wall thickness aluminium pipe for (a) group velocity and (b) phase velocity. ....	87
Figure 5.4 Window function and the crack surface displacement after modulated by the window function. ....	88
Figure 5.5 Frequency spectrum of displacement amplitude.....	89
Figure 5.6 Plot of displacement at double frequency with varying crack length. ....	90
Figure 5.7 Displacement proportion of different wave modes as second harmonic wave. .....	91
Figure 5.8 Configuration of pipe model in simulation. ....	94
Figure 5.9 Signals at double frequency of L(0, 2) and F(1, 2) modes for 1 mm seam crack case. ....	95
Figure 5.10 Signals at double frequency of F(2, 2) and F(3, 2) modes for 1 mm seam crack case .....	96

Figure 5.11 Displacement of different modes at double frequency with crack length in simulation.....	96
Figure 5.12 Proportion of different wave modes as second harmonic wave from simulation.....	97
Figure 5.13 Comparison of numerical and theoretical analysis for (a) L(0, 2) mode; (b) F(1, 2) mode; (c) F(2, 2) mode; (d) F(3, 2) mode; (e) F(4, 2) mode and (f) F(5, 2) mode.....	100
Figure 5.14 Influence of distance between transducer ring and the location of crack.	100
Figure 5.15 Signals from simulation model for 10 mm seam crack case after STFT at (a) fundamental frequency and (b) double frequency. ....	102
Figure 6.1 Dispersion curve of 5 mm steel plate for (a) group velocity and (b) phase velocity.....	105
Figure 6.2 (a) Configuration of steel plate and (b) simulation model in Abaqus.....	107
Figure 6.3 Modelling of “seam” crack. ....	108
Figure 6.4 (a) Transmitted signal in the time domain and (b) frequency domain. ....	109
Figure 6.5 Relative nonlinear parameter $\beta'$ in terms of crack length/wavelength (a) transmitted signal; (b) reflected signal.....	110
Figure 6.6 Nonlinear index verses the crack length in reference [153].....	111
Figure 6.7 (a) Amplitude profiles at the fundamental frequency and (b) amplitude profiles at the double frequency.....	111
Figure 6.8 5 mm steel plate specimen. ....	113
Figure 6.9 Data acquisition procedure in experiment.....	113
Figure 6.10 Fatigue machine (a) test procedure and (b) set up. ....	114

Figure 6.11 Signal after FFT in the frequency domain of (a) reflection and (b) transmission. ....	115
Figure 6.12 Transmitted signal after band pass filter at (a) fundamental frequency and (b) at double frequency. ....	115
Figure 6.13 Dispersion curve of a 80 mm outer diameter aluminium pipe for (a) group velocity and (b) phase velocity. ....	117
Figure 6.14 Relative nonlinear parameter with propagation distance for (a) 907 kHz and (b) 200 kHz. ....	120
Figure 6.15 Dispersion curve of 30 mm OD and 4 mm wall thickness aluminium pipe. (a) Phase velocity; (b) Group velocity. ....	122
Figure 6.16 Signal processing procedure. ....	124
Figure 6.17 Loads applied in simulation model. ....	125
Figure 6.18 Configuration of the specimen. ....	126
Figure 6.19 Seam crack in pipe model. ....	127
Figure 6.20 Transmitted signal from simulation model. ....	128
Figure 6.21 Transmitted signal from model with material nonlinearity after STFT (a) at fundamental frequency; (b) at double frequency. ....	128
Figure 6.22 Transmitted signal from model with CAN after STFT (a) at fundamental frequency; (b) at double frequency. ....	129
Figure 6.23 Reflected signal from model with material nonlinearity after STFT (a) at fundamental frequency; (b) at double frequency. ....	130
Figure 6.24 Reflected signal from model with CAN after STFT at double frequency. ....	130
Figure 6.25 Pipe specimen preparation. ....	131

Figure 6.26 Design of steel frame for three-point bending fatigue test.....	132
Figure 6.27 Three-point bending fatigue test. ....	132
Figure 6.28 Signal generation and collection system. ....	133
Figure 6.29 Transmitted signal from experiment. ....	135
Figure 6.30 Transmitted signal from experiment before fatigue test after STFT (a) at fundamental frequency; (b) at double frequency. ....	135
Figure 6.31 Transmitted signal from experiment before fatigue test (blue line) and after 22000 fatigue cycles (red line) at double frequency (a) specimen 1; (b) specimen 2.....	136
Figure 6.32 Reflected signal from experiment after 22000 fatigue cycles after STFT (a) at fundamental frequency; (b) at double frequency. ....	137
Figure 6.33 Signals after 42000 fatigue cycles and with static load. ....	138
Figure 6.34 Calculation of nonlinear index. ....	140
Figure 6.35 Nonlinear indices under different loading conditions.....	141
Figure 7.1 (a) Seam crack in simulation model; (b) waves pass through the seam crack when it closes; (c) waves are blocked by the seam crack. ....	144
Figure 7.2 Transmitted signal from model with CAN after STFT compared with benchmark signals (a) at fundamental frequency; (b) signals at fundamental frequency after zoomed in; (c) signals at double frequency and (d) benchmark signal at double frequency. ....	145
Figure 7.3 Reflected signal from model with CAN after STFT compared with benchmark signals (a) at fundamental frequency; (b) at double frequency and (c) benchmark signal at double frequency.....	147
Figure 7.4 Transmitted signal from experiment at different fatigue cycles compared with benchmark signal (a) at fundamental frequency; (b) at double frequency.....	149

Figure 7.5 Reflected signal from experiment at different fatigue cycles compared with benchmark signal (a) at fundamental frequency; (b) at double frequency.....	151
Figure 7.6 Nonlinear index vs crack length at each tip of notch in pipe model. ....	153
Figure 7.7 (a) Original model; (b) Modified model with notch extended in the middle. .....	154
Figure 7.8 Nonlinear index vs fatigue cycle from experimental testing for (a) transmitted signals; (b) reflected signals. ....	156
Figure 7.9 Reflected signals under different fatigue cycles at fundamental frequency.	157
Figure 7.10 Nonlinear index vs the propagation distance. ....	158
Figure 7.11 Integral of amplitude profile of second harmonic wave vs propagation distance.....	158

## List of Tables

Table 2.1 Advantages and disadvantages of different sorts of sensors .....	16
Table 3.1 Potential cumulative secondary wave field when the fundamental wave mode is self-interaction or mutual interaction of torsional (T) and longitudinal (L) waves in cylinders. Y: the secondary mode is cumulative; N: the secondary mode is not cumulative [15]. .....	30
Table 4.1 Dimensions of different shapes of transducers in experiment test. ....	56
Table 4.2 Material properties for steel pipe OD 194 mm. ....	66
Table 4.3 Material properties for steel pipe OD 101 mm. ....	76
Table 5.1 Material properties for 5 mm aluminium pipe. ....	93
Table 6.1 Material properties for 5 mm steel plate. ....	106
Table 6.2 Material properties for simulation model. ....	118
Table 6.3 Material properties of aluminium pipe. ....	125

## Chapter 1 Introduction

### 1.1 Guided waves in pipelines

Pipelines are crucial infrastructure which transport oil, gas, chemical and water supplying the industries around the world. In-service pipelines are suffering from a variety of damage caused by aging, impact or corrosion, which may cause catastrophic consequence if there is no timely inspection and maintenance. An explosion of a gas pipeline on Varanus Island, Western Australia occurred on June 3<sup>rd</sup>, 2008 [1]. Due to the wall thinning caused by corrosion, the pipeline blast cost about \$2.4 to \$3 billion, as well as long time for the fire extinguishing and restart of the gas supply. On July 2<sup>nd</sup>, 2017, another gas pipeline explosion was seen in Qinglong, Guizhou Province, Southwest China with 8 dead and 35 injured [2]. Because of heavy rain, the landslide crushed the pipeline, which caused the gas leakage and explosion. At the end of same year, without proper maintenance, an aging gas pipeline in Baumgarten, Austria exploded which killed one worker and injured at least 24 people [3].



Figure 1.1 (a) Gas pipeline explosion in Qinglong, Guizhou; (b) Aging pipeline blast in Baumgarten, Austria.

These disasters can be avoid if appropriate inspection is carried out before the defects deteriorate. There are many types of non-destructive testing methods for pipeline

-Quantitative evaluation of fatigue crack using nonlinear guided waves in pipelines-

inspection, such as X-rays, magnetic particles and ultrasonic waves, among which the ultrasonic guided wave testing is very attractive nowadays. Ultrasonic guided wave testing has the advantages of high sensitivity, long propagation distance and ease of installation.

In conventional guided waves testing, an array of transducers will be attached on the circumference of the pipe, which generate guided waves and propagate along the pipe. When the waves come to any position with discontinuities, it will be recorded in reflection or transmission, revealing the information from damage in the pipe. However, the conventional guided wave testing is limited by the wavelength of the excitation, which can only detect gross damage, such as open crack in the pipes. In some circumstances, it is necessary to detect damage at its early stage which is in micro-scale, such as corrosion at early stage, initial fatigue crack, and the material degradation. For these cases, guided waves with nonlinear characteristics have been proved well-performed and studied by many researchers recent years in plate structures but limited studies have been carried out in pipe structures. Therefore, this study will focus on the detection of fatigue cracks in pipes using nonlinear guided waves.

## **1.2 Motivation and objectives**

Many studies have been carried out for the pipeline inspection with guided wave technique successfully [4-8]. However, it is difficult to detect microcrack at its early age with conventional linear guided wave technique. Nonlinear ultrasonic guided waves have shown great capability in these cases using nonlinear ultrasonic behaviour including higher-harmonic generation, sub-harmonic generation, nonlinear resonance or mixed frequency response. These approaches have been studied in plate-like structures by many researchers [9-12]. However, due to the curvature of the surface of pipelines, as well as

-Quantitative evaluation of fatigue crack using nonlinear guided waves in pipelines-

the inherent properties of guided waves such as dispersion, attenuation and boundary reflection, guided wave modes in pipe structures are generally more complex than those in plate-like structures. Thus, interpretation of the received signal for pipe inspection is always difficult. So far, studies conducted in pipes have been most focused on material nonlinearity. Theoretical and numerical analyses of higher harmonic generation have been conducted in nonlinear waveguides with arbitrary cross-sections [13], in weakly nonlinear cylinders [14, 15], and from plates to large radius pipes [16]. Moreover, the simulation method of material nonlinearity in plate structures can also be applied to pipe counterparts. Experiments concerning material nonlinearities in pipes [17, 18] have confirmed the phenomenon of cumulative second harmonic generation with longitudinal or circumferential wave excitation.

However, limited studies on local damage evaluation using nonlinear guided waves have been undertaken for pipe-like structures, such as initial fatigue crack inducing nonlinearity in pipe structures. The objectives of this study are therefore as follows:

- To extend a theoretical model of contact acoustic nonlinearity (CAN) from plate structures to pipe structures.
- To compare different nonlinearity methodologies, i.e. mixed frequency response method and higher harmonic generation method for the detection of the existence of fatigue crack in metallic pipes;
- To identify the existence of fatigue crack in metallic pipes using higher harmonic generation method with the comparison of the results from plate structures;
- To quantitatively analyse the propagation of fatigue crack in metallic pipes with higher harmonic generation method.

### **1.3 Thesis outline**

The first chapter introduces the background, motivation and objectives of the study and the contents of following chapters, which indicates the research gap and aims of this study.

Chapter 2 provides the fundamental of guided wave properties. The propagation of Lamb waves in plate structures is simply presented, followed by the propagation of guided waves in pipe structures and comparison with the plate structures. With the understanding of fundamental properties of guided waves, the excitation and acquisition methods of different wave modes in simulation model and experiment test are reviewed. These reviews provide a comprehensive understanding of basic information of the guided waves in plates and pipes.

Chapter 3 presents the theoretical basis and research studies on interaction between the guided waves and damage in both plate and pipe structures. Different damage detection methods in previous studies with linear and nonlinear guided waves are reviewed. Typical simulation models and experiment test methods are introduced for damage detection in plate and pipe structures, as well as in some special conditions for pipe detection.

Chapter 4 provides investigation of wave excitation and acquisition method used in this study, including calibration and figuring out factors that may influence the wave excitation and signal received. The specimen and sensor configuration is designed for both simulation and experiment. Optimised simulation models utilised in this projected are presented. Different approaches including mixed frequency response method and second harmonic generation method for the detection of CAN are analysed and compared with simulation models to select an appropriate method for the following studies.

Chapter 5 introduces the theoretical analysis from plate to pipe structures about the interaction between breathing crack and the nonlinear guided waves. Simulation model with longitudinal mode excitation is carried out to confirm the results from theoretical analysis. From the analysis, a nonlinear index are developed for the quantitatively assessment of fatigue crack growth in a pipe structure.

Chapter 6 presents the effectiveness of nonlinear guided waves with second harmonic generation method fatigue crack detection in aluminium pipes. The numerical model and experimental test are conducted and the results are discussed. The results from similar models and tests of plate and pipe structures are also compared.

Chapter 7 presents the application of nonlinear guided waves with second harmonic generation method with the nonlinear index for quantitative assessment of fatigue crack propagation in aluminium pipes. The numerical model and experimental test are elaborated and the results are discussed.

Chapter 8 provides the conclusions of this thesis and recommendations for future work.

## **Chapter 2 Guide waves in metallic structures**

Basis properties and propagation of guided waves in plate and pipes are illustrated in this chapter summarised from previous studies for comprehending the characteristics of guided waves. The theoretical analysis of wave excitation in a pipe structure and features of different transducers used in pipe detection are also introduced as the preparation for latter wave excitation and acquisition in simulation and experiment work.

### **2.1 Guided wave properties**

#### ***2.1.1 Dispersion of guided wave modes in pipes***

Guided waves in free solid bar were first investigated by Pochhammer [19] in 1876 and Chree [20] in 1889. Later in 1959, the analytical fundamental of a three-dimension hollow cylinder of infinite extent is established by Gazis [21, 22], who presented a general solution for the displacement field components of wave particles in long hollow cylinders. Due to the curved structure in pipes and the dispersion characteristics, wave propagation and interaction in this sort of structure are complicated, and therefore, there are infinite number of wave modes in cylinders. Meitzler and Zemanek [23, 24] developed a typical notation for the wave modes, in which guided wave modes in circular-section pipes can be generally labelled  $L(0, n)$ ,  $T(0, n)$  and  $F(m, n)$ , respectively, referring to longitudinal, torsional and flexural modes, where  $n$  is the harmonic number of circumference variation and  $m$  represents the order of wave modes. A different notation from Rose [25] was also presented, in which  $L(n, m)$  was defined as a longitudinal mode group, including axisymmetric modes  $L(0, m)$  and non-axisymmetric modes  $F(n, m)$ . This notation is used in this thesis. The equivalent mode notation for plate waves is also discussed by Silk and Bainton [26]. The longitudinal and torsional modes are axis-symmetrical modes whereas the flexural modes are non-symmetrical [27]. In general, there are longitudinal, torsional

-Quantitative evaluation of fatigue crack using nonlinear guided waves in pipelines-  
or flexural modes separately propagating in a pipe at low frequencies, while at higher frequencies guided waves behave to a greater extent like those in a curved plate or shell, i.e. Lamb wave modes. In particular,  $L(0, 1)$  can be regarded as the fundamental anti-symmetrical Lamb wave mode ( $A_0$ ), while  $L(0, 2)$  shows similar properties to the fundamental symmetrical Lamb wave mode ( $S_0$ ) [26].

### **2.1.2 Mode selection**

Due to the multiple wave modes in pipe structures, it is necessary to select a proper mode for different detection purposes. The mode selection is based on many factors such as dispersion, sensitivity, proper cycles and frequency range [28].

In practice, symmetric modes including longitudinal and torsional modes are more attractive for testing. In particular,  $L(0, 2)$  is found travelling faster than the other modes and it is non-dispersive over a wide range of frequency [21]. Some researchers prefer  $L(0, 2)$  since it is sensitive to depth variation and to the defect circumference variation [29-33]. It also has a simple acoustic field and can be excited easily [34]. Although  $L(0, 2)$  generally co-exists with  $L(0, 1)$ , the latter can be suppressed by adding further rings or by adjusting the length of transducer elements [30]. Moreover, in a simple pipe system, the velocity of  $L(0, 1)$  is much slower than that of  $L(0, 2)$ , so it is easy to be removed in the time domain.

Torsional mode  $T(0, 1)$  is an alternative mode to  $L(0, 2)$  and is widely analysed and applied by many researchers [4, 7, 8, 35-39].  $T(0,1)$  has the advantage of being non-dispersive over the whole frequency range and no other axially symmetric torsional modes will be excited along the  $T(0, 1)$  mode when keeping the frequency of the excitation signal less than the cut-off frequency of  $T(0, 2)$ . Furthermore, compared with  $L(0, 2)$  mode, it is more sensitive to cracks along the axis of pipes. The reflection coefficient changes periodically with axial extent when there is an axisymmetric defect

-Quantitative evaluation of fatigue crack using nonlinear guided waves in pipelines-  
with 20% thickness depth in pipe and the excitation mode is T(0,1) [4]. In addition, non-symmetrical modes have also been used for damage detection in pipes after appropriate mode tuning [40].

### **2.1.3 Attenuation**

In addition to the dispersion phenomena, guided waves in pipes are also influenced by attenuation. Attenuation in pipes generally exists in different cases, including leakage into surrounding material [41], material attenuation such as bitumen coatings [42], reflection from features like welds and scattering at rough surfaces.

The attenuation caused by coating loss and rough surfaces can be minimised by choosing a lower excitation frequency [43]. Also, mode T(0,1) is suitable for pipelines with coating and carrying or buried in liquid since it is insensitive to the presence of liquid and insulation materials [4, 5, 39, 43, 44].

## **2.2 Lamb wave propagation in plates**

Lamb wave propagation in plate structures is introduced in this section for comparison with the pipe structures and for better understanding of the nonlinear theoretical derivation in later chapter. The exact solution of wave propagation in free plate problem has different approaches. Two typical approaches are displacement potentials [45] and the partial wave technique [46]. The method of displacement potentials will be briefly introduced here. For an infinite domain, the equation of motion based on theory of elasticity can be expressed in a Cartesian coordinate system as

$$\mu u_{i,jj} + (\lambda + \mu) u_{j,ji} + \rho f_i = \rho \ddot{u}_i, \quad (2.1)$$

where  $\mu$ , and  $\lambda$  are Lamé constants,  $\rho$  is density,  $\ddot{u}$  is the acceleration,  $u$  is displacement field and  $\rho f_i$  is inertia force.



Figure 2.1 Coordinates of a free plate.

Using the coordinates of the free plate in Figure 2.1, with displacement potential methods and considering infinite plane harmonic wave, the displacements and stresses can be described in terms of the potentials as

$$u_1 = \left[ ik\Phi + \frac{d\Psi}{dx_3} \right], \quad (2.2)$$

$$u_3 = \left[ \frac{d\Phi}{dx_3} + ik\Psi \right]; \quad (2.3)$$

$$\sigma_{31} = \mu \left( 2ik \frac{d\Phi}{dx_3} + k^2\Psi + \frac{d^2\Psi}{dx_3^2} \right), \quad (2.4)$$

$$\sigma_{33} = \left[ \lambda \left( -k^2\Phi + \frac{d^2\Phi}{dx_3^2} \right) + 2\mu \left( \frac{d^2\Phi}{dx_3^2} - ik \frac{d\Psi}{dx_3} \right) \right], \quad (2.5)$$

where,  $\Phi = \Phi(x_3)\exp[i(kx_1 - \omega t)]$ ,  $\Psi = \Psi(x_3)\exp[i(kx_1 - \omega t)]$  and  $k$  is wavenumber. The solution is split into two sets of modes: symmetric and antisymmetric modes. For displacement in the  $x_1$  direction, with middle plane of the plate as axis, if  $u_1$  contains cosines, the motion will be symmetric while it will be antisymmetric if  $u_1$  contains sines. The reverse is true for displacements in the  $x_3$  direction.

When considering the boundary conditions which is traction free at top and bottom surface of the plate, and the definition of  $c_L$  and  $c_T$ , the dispersion equation can be written as

$$\frac{\tan(qh)}{\tan(ph)} = -\frac{4k^2pq}{(q^2-k^2)^2} \quad \text{for symmetric modes,} \quad (2.6)$$

$$\frac{\tan(qh)}{\tan(ph)} = -\frac{(q^2-k^2)^2}{4k^2pq} \quad \text{for antisymmetric modes,} \quad (2.7)$$

where,  $p^2 = \frac{\omega^2}{c_L^2} - k^2$  and  $q^2 = \frac{\omega^2}{c_T^2} - k^2$ . These equations are known as Rayleigh–Lamb frequency relations, and can be used to calculate the velocity of specific wave mode at a fixed frequency. The plot of solutions of these equations are known as dispersion curves. Figure 2.2 shows Lamb wave dispersion curves for a steel plate plotted with DISPERSE [61].

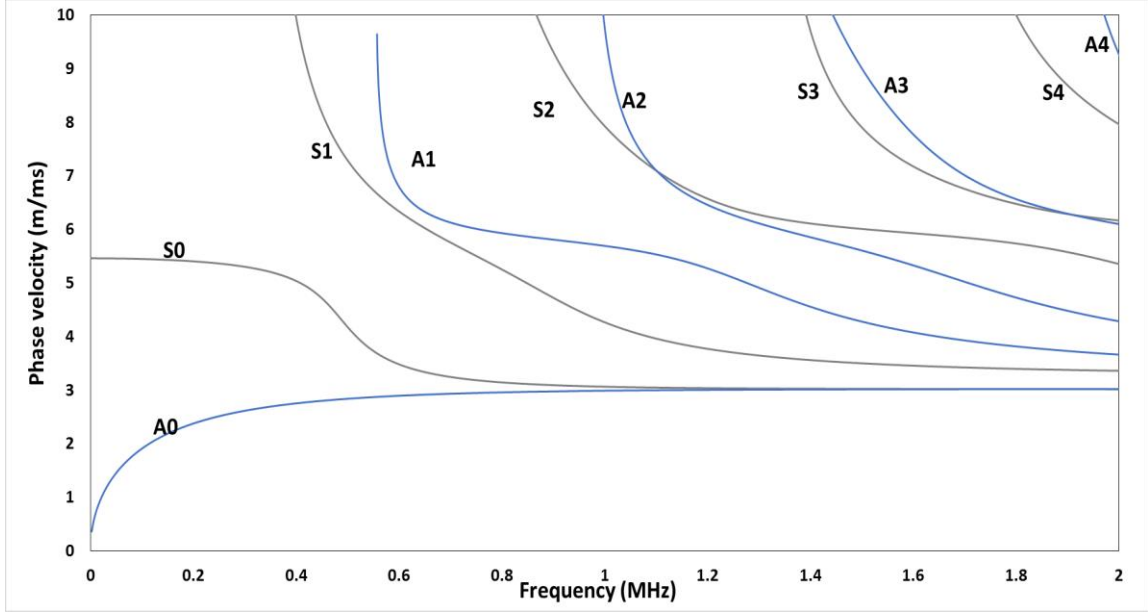


Figure 2.2 Dispersion curve for phase velocity of a 5 mm thick steel plate.

Another wave mode called shear horizontal wave also exists in the plate structures. Considering Navier displacement equations of motion

$$\mu \nabla^2 u(x, t) + (\lambda + \mu) \nabla \nabla \cdot u(x, t) = \rho \frac{\partial^2 u(x, t)}{\partial t^2}, \quad (2.8)$$

if only the  $u_3$  component of the particle displacement field is nonzero and if  $u_3$  is independent of  $x_3$ , then Equation 2.8 reduces to

$$\frac{\partial^2 u_3}{\partial x_1^2} + \frac{\partial^2 u_3}{\partial x_2^2} = \frac{1}{c_T^2} \frac{\partial^2 u_3}{\partial t^2}, \quad (2.9)$$

With the general displacement field and similar boundary conditions as in symmetric and antisymmetric modes,

$$u_3(x_1, x_2, t) = [A \sin(qx_2) + B \cos(qx_2)] e^{i(kx_1 - \omega t)}, \quad (2.10)$$

$$\sigma_{22}(x_1, x_2, t)|_{x_2=\pm h} = \tau_{12}(x_1, x_2, t)|_{x_2=\pm h} = \tau_{23}(x_1, x_2, t)|_{x_2=\pm h} = 0, \quad (2.11)$$

the displacement fields of the symmetric and antisymmetric SH modes can be expressed as

$$u_3^s(x_1, x_2, t) = B \cos(n\pi x_2/d) \cos(kx_1 - \omega t), \quad (2.12)$$

$$u_3^a(x_1, x_2, t) = A \sin(n\pi x_2/d) \cos(kx_1 - \omega t), \quad (2.13)$$

where  $n \in (0, 2, 4, \dots)$  for symmetric SH modes and  $n \in (1, 3, 5, \dots)$  for antisymmetric modes and  $d$  is the plate thickness:  $d=2h$ .

And the dispersion equation is

$$c_p(fd) = \pm 2c_T \left\{ \frac{fd}{\sqrt{4(fd)^2 - n^2 c_T^2}} \right\}. \quad (2.14)$$

### 2.3 Guided wave propagation in pipes

Guided wave propagation in the axial direction of a pipe will be described in this section and the notation  $L(m, n)$  and  $T(m, n)$  stand for longitudinal mode group and torsional mode group is used [25]. For a hollow cylinder with surface traction free and coordinates in Figure 2.3, the wave propagation follows the Navier equation in cylinder coordinates as

$$\mu \nabla^2 \vec{U} + (\lambda + \mu) \nabla \nabla \cdot \vec{U} = \rho \left( \frac{\partial^2 \vec{U}}{\partial t^2} \right), \quad (2.15)$$

where  $t$  is the time and  $U$  represents the displacement field. The density  $\rho$  and Lamé constants  $\mu$  and  $\lambda$  determine the bulk wave velocities in the material.

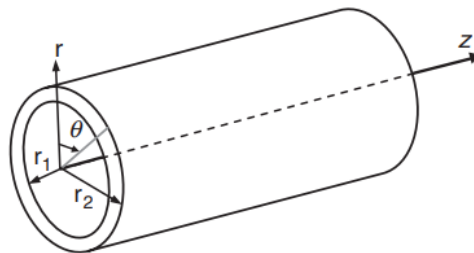


Figure 2.3 Coordinates of a hollow cylinder.

Using Helmholtz decomposition and the gauge invariance conditions, the followings can be obtained

$$\nabla^2 \Phi = \frac{1}{c_1} \frac{\partial^2 \Phi}{\partial t^2}, \quad (2.16)$$

$$\nabla^2 \vec{H} = \frac{1}{c_2} \frac{\partial^2 \vec{H}}{\partial t^2}, \quad (2.17)$$

where  $c_1$  stands for the longitudinal bulk wave velocity and  $c_2$  is the shear bulk wave velocity. The displacement field is described by dilatational scalar potential  $\Phi$  and the equivoluminal vector potential  $\vec{H}$ .

Gazies [21] provided the equations for the potentials

$$\begin{aligned} \Phi &= f(r)\Theta(m\theta)e^{i(kz-\omega t)} \\ H_r &= h_r(r)\Theta_r(m\theta)e^{i(kz-\omega t)} \quad (m=0, 1, 2, \dots) \quad (2.18) \\ H_\theta &= h_\theta(r)\Theta_\theta(m\theta)e^{i(kz-\omega t)} \\ H_z &= h_z(r)\Theta_z(m\theta)e^{i(kz-\omega t)} \end{aligned}$$

The part  $\Theta_r(m\theta)$  can be changed to  $e^{im\theta}$  for the complete solution of both longitudinal and torsional wave modes.

Let

$$2h_1 = (ih_r - h_\theta), 2h_2 = (ih_r + h_\theta), h_3 = h_z \quad (2.19)$$

These values can be expressed with Bessel functions

$$f = AZ_m(\alpha_1 r) + BW_m(\alpha_1 r)$$

$$h_3 = h_z = A_3 Z_m(\beta_1 r) + B_3 W_m(\beta_1 r)$$

$$h_1 = \frac{ih_r - h_\theta}{2} = A_1 Z_{m+1}(\beta_1 r) + B_1 W_{m+1}(\beta_1 r) \quad (2.20)$$

$$h_2 = \frac{ih_r + h_\theta}{2} = A_2 Z_{m-1}(\beta_1 r) + B_2 W_{m-1}(\beta_1 r)$$

Where A, B, A<sub>1</sub>, B<sub>1</sub>, A<sub>2</sub> and B<sub>2</sub> can be solved by the boundary conditions, which are traction free at inner and outer surfaces and two gauge invariance condition equations.

With the known solutions of f, h<sub>1</sub>, h<sub>2</sub> and h<sub>3</sub>, the displacement fields can be derived as

$$U_r = [f' + (im/r)h_3 + kh_1 - kh_2]e^{im\theta} e^{i(kz-\omega t)}$$

$$U_\theta = [(im/r)f + kh_1 + kh_2 - h_3']e^{im\theta} e^{i(kz-\omega t)} \quad (2.21)$$

$$U_z = \left[ ikf + h_2' - h_1' - (m+1)\left(\frac{h_1}{r}\right) - (m-1)\left(\frac{h_2}{r}\right) \right] e^{im\theta} e^{i(kz-\omega t)}$$

The solving of eigenvalue values lead to the dispersion curve of the hollow cylinder. A typical dispersion curve example for a 73 mm outer diameter schedule 40 steel pipe is shown in Figure 2.4 [10], where different wave modes can be observed.

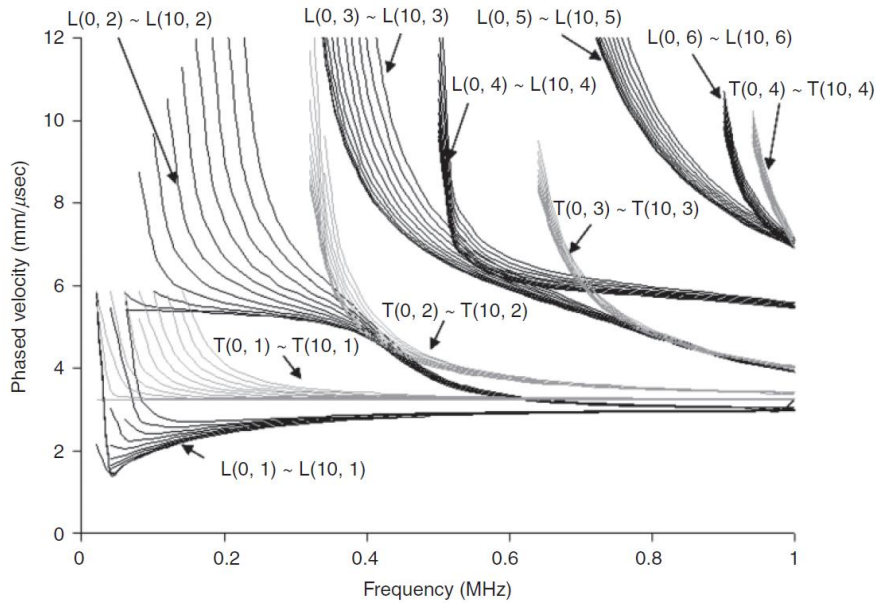


Figure 2.4 Dispersion curve for phase velocity of a 73 mm OD schedule 40 steel pipe [25].

## 2.4 Wave excitation and acquisition

The analytical analysis of wave generation induced by surface load is described firstly in this section for understanding of the wave excitation in simulation model and experiment.

When load is applied on the outer surface of a hollow cylinder as in Figure 2.5,

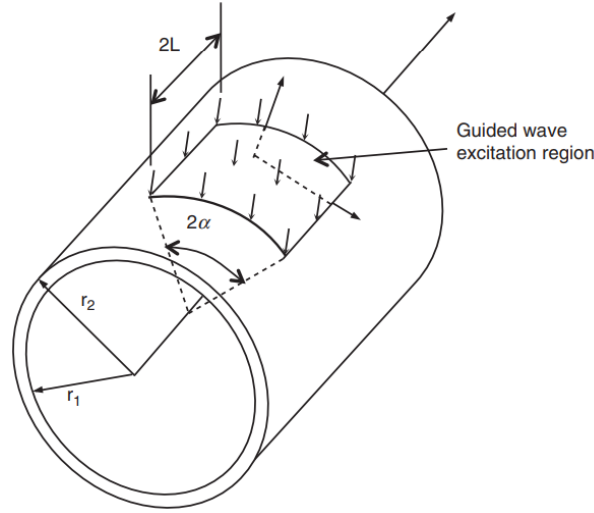


Figure 2.5 Load applying on outer surface of a hollow cylinder [25].

the load conditions can be described as

$$\hat{\mathbf{T}} \cdot \vec{\mathbf{n}} = \begin{cases} -p_1(\theta)p_2(z)\vec{\mathbf{e}}_{\xi}, & |z| \leq L, |\theta| \leq \alpha, r = b \\ 0, & |\theta| > \alpha, \text{ or } r \neq b \end{cases}. \quad (2.22)$$

Based on displacement field described in Section 2.2 and the orthogonality relation between two modes  $M(m, n)$  and  $M(l, s)$

$$P_{mlns} = -\frac{1}{4} \iint_D (\vec{\mathbf{v}}_{mn}^* \cdot \hat{\mathbf{T}}_{ls} + \vec{\mathbf{v}}_{ls}^* \cdot \hat{\mathbf{T}}_{mn}) \cdot \vec{\mathbf{e}}_z dV = 0, \quad m \neq l \text{ or } k^{mn} \neq k^{ls}. \quad (2.23)$$

The stress amplitude of each mode  $M(m, n)$  generated by the load condition on the hollow cylinder can be calculated by

$$A_+^{mn} = -\frac{R_{\xi}^{mn}(r)e^{-ik^{mn}z}r_{n+1}}{4P_{mnnn}} \int_{-\alpha}^{\alpha} e^{im\theta} p_1(\theta) d\theta \int_{-\infty}^{\infty} p_2(z) e^{ik^{mn}z} dz, \quad (2.24)$$

$$z \geq L, \xi = 1, 2, 3$$

From the equation it can be seen that the amplitude of wave modes highly depends on the conditions of source, such as the length and the width of the actuator.

A single transducer element attached on a pipe always excites both  $L(0, m)$  and  $F(n, m)$  modes. Therefore, a series of elements arranged asymmetrically around the circumferential direction of the pipe to form a ring are popularly used, so as to suppress the non-axisymmetric modes. A dry coupled piezoelectric transducer system for the excitation of the axially symmetric  $L(0, m)$  in pipes had been developed, which consists of a ring of piezoelectric elements to apply a force to the pipe wall in the axial direction [47].

Besides, the transducer ring system developed by Guided Ultrasonic Ltd. [48] can generate the torsional mode by applying forces in the circumferential direction on the pipe [7]. Furthermore, a necked pipe waveguide unit was developed to effectively transmit the lowest torsional mode only at a high frequency range [49].

In addition, the excitation and propagation of non-axisymmetric guided waves were studied by the normal mode expansion method (NME) [50]. With numerical calculation, the excitation of  $L(M, 2)$  modes was achieved by angle beam partially loading and rotating the transducer around the pipe or sweeping the frequency to cover the whole surface regions of the pipe. For the number of elements in the ring, it must be greater than  $n$  where  $F(n, 1)$  is the highest order flexural mode whose cut-off frequency is within the bandwidth of the excitation signal [30]. Furthermore, excitation method of  $F(1, 2)$  and  $F(1, 3)$  was achieved with using two transducer arrays and appropriate selection of the array position, and phase of each element in the transducer array [51]. Meanwhile, sometimes more than one ring is used to control the direction of wave propagation and

-Quantitative evaluation of fatigue crack using nonlinear guided waves in pipelines-

typically transducer rings spacing a quarter of a wave length apart and separated by  $\pi/2$  in phase are applied [52]. To acquire different flexural modes, a phase delay of  $N\theta/2\pi$  is needed to add to signal of each node around the circumference before summing them together where N is the circumferential order and  $\theta$  is the distance from the node to the centre of the damage [53].

A variety of ultrasonic transducers can be used to generate and receive guided waves, e.g. piezoelectric lead zirconate titanate (PZT) [32], angle beam transducer with wedge, polyvinylidene Fluoride Film (PVDF) [54] and electromagnetic acoustic transducer (EMAT) [55]. The comparison between these different sorts of sensors when applied for guided wave generation and acquisition are listed in Table 2.1 [55-59].

Table 2.1 Advantages and disadvantages of different sorts of sensors

<b>Transducer type</b>	<b>Advantages</b>	<b>Disadvantages</b>
<b>Piezoelectric transducers</b>	<p>Ability to provide mode control through element spacing (comb and interdigitated transducers);</p> <p>Flexibility for wrapping around pipe (e.g. PVDF);</p> <p>Easy to manufacture with low cost.</p>	<p>Require coupling medium and smooth contact surface.</p>
<b>Electromagnetic acoustic transducer (EMAT)</b>	<p>No gel couplant and non-contact with pipe;</p> <p>Ability to control wavelength of excited wave through changing spacing between the coil's limbs;</p> <p>Flexibility for mode generation and collection;</p>	<p>Low transduction efficiency; Limited to metallic or magnetic products;</p> <p>Lack of circumferential resolution for buried pipe.</p>

---

	Applicable on surfaces with curvatures;	
	Good signal-to-noise ratio for buried pipe.	
	Light weight;	
	Flexibility for complex surface;	High dissipation factor;
<b>Polyvinylidene Fluoride Film (PVDF)</b>	High piezoelectricity;	High requirement on the clean of processing machinery.
	Stability for chemical resistance and high temperature	
	Low acoustic impedances.	

---

## 2.5 Summary

In this chapter, fundamental properties of guided waves are introduced such as dispersion and attenuation. Based on these properties, the selection of proper mode from previous studies is introduced. Also, the propagation of guided waves in both plate and pipe structures are reviewed for better understanding on the characteristics of guided waves. These theoretical studies will be used on the derivation of analytical model of nonlinear guided waves in pipes in chapter 5. The excitation and acquisition methods of different types of wave modes are also introduced and commonly used transducers on the pipe inspection were presented. In this thesis, piezoelectric transducers are mainly adopted and the excitation and acquisition of both longitudinal and flexural wave modes are achieved.

## Chapter 3 Guided wave based damage detection in pipelines

With the understanding of the properties of guided waves in waveguides, the interaction between guided waves and discontinuities is introduced in this chapter. From theoretical interpretation to damage detection in terms of linear and nonlinear methods through simulation and experiment analyses in pipes, the principles of guided wave-based pipe detection are explained comprehensively.

### 3.1 Theoretical basis of wave scattering in pipes

The expression of guided wave scattering in pipes is usually a complex three-dimensional problem which needs the assistance of numerical solutions. A simplified method using the S-parameter formalism to investigate elastic wave scattering in hollow cylinders with circumferential cracks which are through the wall thickness is introduced in this section [60], as schematically defined in Figure 3.1. The scattered field can be generally written as

$$\mathbf{u}^{\text{sc}}(r, \theta, z) = \begin{cases} \sum_{v,N} C_{v+}^N(z) \mathbf{u}_{+v}^N(r, \theta) & z > z_c, \\ \sum_{v,N} C_{v-}^N(z) \mathbf{u}_{-v}^N(r, \theta) & z < z_c, \end{cases} \quad (3.1)$$

where  $z_c$  is the “z” coordinate of the crack;  $\mathbf{u}_{+v}^N(r, \theta)$  and  $\mathbf{u}_{-v}^N(r, \theta)$  are the modal particle displacement distribution of mode “v” of family “N” propagating in two directions  $z > z_c$  and  $z < z_c$ ;  $C_{v+}^N(z)$  and  $C_{v-}^N(z)$  are the amplitudes of scattered mode “v” of family “N” in the regions  $z > z_c$  and  $z < z_c$  respectively, which can be related to the amplitude of incident modes through S parameters.

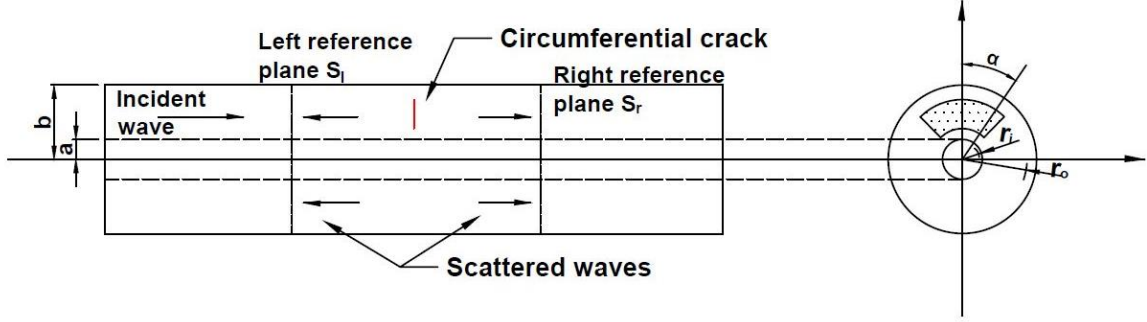


Figure 3.1 Configuration of the scheme: mode  $\bar{\mu}$  of family  $\bar{N}$  is incident in a hollow cylinder with a circumferential crack [60].

After determining S parameter using the angular orthogonality relation detailed in [61], the general scattering formula for the guided waves by a crack in cylinders was expressed as

$$\tilde{S}_{\bar{\mu}l;\bar{\nu}l}^{\bar{N},\bar{M}} = \frac{i\omega}{4} \iint_{S_c} \{ [\mathbf{u}_2] \cdot \mathbf{T}_{\bar{\mu}}^{\bar{N}} \} \cdot \hat{\mathbf{e}}_z d\sigma, \quad (3.2)$$

where  $[\mathbf{u}_2]$  is crack opening displacement,  $\mathbf{T}_{\bar{\mu}}^{\bar{N}}$  is the modal stress field and  $\hat{\mathbf{e}}_z$  is a unit vector in “z” direction.

When considering the incidence of longitudinal axisymmetric modes which satisfies the requirements that the mode has a large wavelength and an entirely axial stress field, and the crack was a sufficiently long through crack ( $r_i=a$ ,  $r_o=b$  in Figure 3.1) of angular extent  $\alpha$  under a uniform tension, Equation 3.2 can be approximated as

$$\tilde{S}_{\bar{\mu}l;\bar{\nu}l}^{0,0} = \frac{i\omega_{zz} T_v^0 \bar{R} \alpha^3}{3\sqrt{2} E \epsilon} \int_a^b r R_{\bar{\mu}zz}(r) dr, \quad (3.3)$$

where  $\bar{R} = (a + b)/2$ ; E is the Young’s modulus;  $\epsilon^2 = \frac{1}{[12(1-\nu^2)]^{1/2}} \left(\frac{H}{\bar{R}}\right)$ ;  $\nu$  is Poisson’s ratio;  $H = b - a$ ;  $R_{\bar{\mu}zz}(r)$  consists of modified Bessel function. From this equation, it is noticed that the amplitude of scattered axisymmetric mode is related to the angular extent of the crack  $\alpha$ .

For pipes with a diameter much larger than wall thickness, they can be approximately considered as unwrapped plates. In this case, pipe mode amplitudes could be obtained through the forced 3D solution in plates. In particular, the circumferential modal amplitudes scattered from defects in pipes can be related to the wave scattering in plates [62].

## 3.2 Damage detection with linear guided waves

### 3.2.1 Reflection and transmission of incident waves

When guided waves approach a discontinuity in a pipe, the reflected signal from the defect usually contains useful information related to characteristics of the defect. The acoustic pressure and velocity relations among waves propagating in a pipe can be presented as [63]:

$$p_i + p_r = p_t \quad (3.4)$$

$$S_1 (v_i + v_r) = S_2 v_t \quad (3.5)$$

where  $p_i$ ,  $p_r$  and  $p_t$  are acoustic pressures of incident, reflected and transmitted waves at the defect, respectively,  $v_i$ ,  $v_r$  and  $v_t$  are velocities of the corresponding wave components, and  $S_1$  and  $S_2$  are the areas of cross-sections of two sides at the defect edge. Many experimental studies [29-31, 64-67] have established the relation between reflection and transmission amplitude and crack characteristics in terms of the orientations of crack for simple cases, showing good consistency with the results from numerical simulations. Moreover, studies focusing on circumferential guided wave based detection have provided screening of the corrosion surface of the pipes with transmission and reflection [68, 69]. For complex features in pipes, such as circumferential defects in pipe bends, a study shows the detectability of using reflection of the torsional mode  $T(0, 1)$  and some factors that influence the reflection [70].

### 3.2.2 Reflection and transmission from defect-converted wave modes

When the incident guided wave is oblique to a defect, one form of wave energy can be converted to another form, known as mode conversion. Some studies have been carried out on the mode conversion of guided waves in pipes [34, 53]. The utilisation of mode conversion improves pipe inspection, especially for bent pipes [34, 71] and for some specific defect types. For example, in a study of detecting a circumferential notch in a weld, the axisymmetric  $L(0, 2)$  mode was excited and the  $L(0, 2)$  mode with converted  $F(1, 3)$  and  $F(2, 3)$  modes were reflected [53]. The reflection coefficient of the received signals with different extents of the circumferential notch is shown in Figure 3.2, where the converted non-axisymmetric wave mode could be used to identify the presence of the notch because the reflection of axisymmetric mode  $L(0, 2)$  could be superimposed by the reflection from the weld. Similarly, mode conversion also occurs in torsional mode excitation from  $T(0, 1)$  to flexural modes [72] and from  $T(0, 2)$  to  $T(0, 1)$  [73], indicating the discontinuities in pipes.

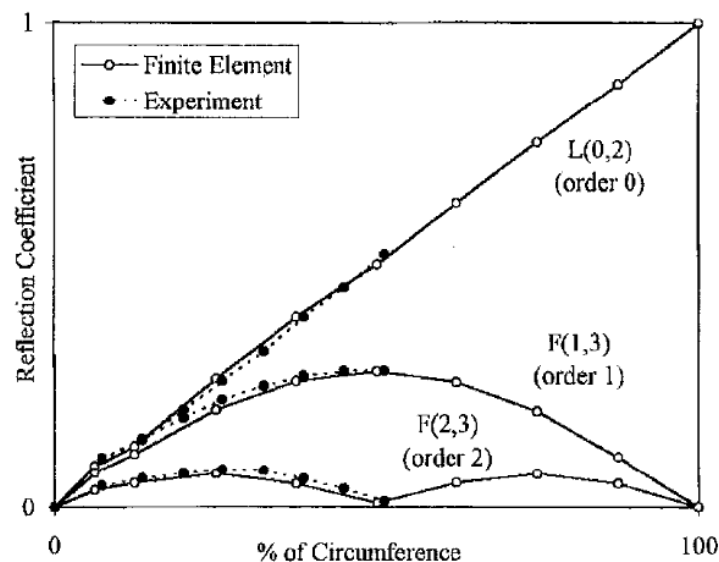


Figure 3.2 Reflection coefficient vs the circumferential extent of the notch from numerical and experimental analysis for a pipe with a through-thickness notch [53].

### **3.2.3 Time of flight (ToF) and time reversal**

The ToF of propagating waves can provide direct information about the location of damage in pipes. For example, in combination with features related to amplitude or energy, ToF has been used to determine the size of a small notch and its location in a pipe [74]. Moreover, with the assistance of a cross-correlation technique, a small change in ToF has been used to detect the lamination on the surface of a steel pipe [75] and hole-type defects in it [76].

The concept of time reversal has also been used to compensate for wave dispersion, so as to improve spatial and temporal wave focusing [77]. When a wave propagates in a pipe, it is understood that a defect serves as a passive guided wave source and generates scattered waves which are received by different transducers. After time reversal, the signal is sent back into the same pipe without defect and will focus at the defect with the maximum amplitude, as indicated in Figure 3.3 [78]. Usually, a window is used on the received signal to extract the defect-induced echoes, and the detection results are highly dependent on the selection of the width and starting time of the window. A baseline subtraction method combined with time reversal without using the window has shown a better imaging effect [79]. Furthermore, for a thick-walled pipe with a large diameter, use of circumferential guided waves has been suggested to detect different types of cracks with a multichannel time reversal focusing method [80].

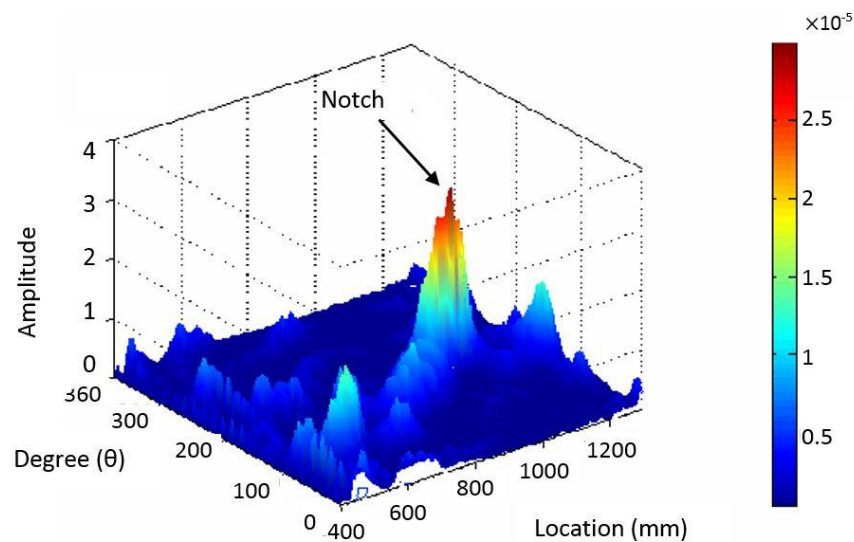


Figure 3.3 Maximum amplitudes of each received signal after time reversal indicating the location of a notch in a pipe [78].

### **3.2.4 Synthetically focused imaging**

The synthetically focused imaging technique has been widely used in NDE with bulk waves. Recently it has also been applied in guided wave inspection in pipes. There are three main imaging algorithms: the synthetic aperture focusing technique, the common source method (CSM), and the total focusing method. These algorithms are distinguished by their actuator-receiver arrangement for data acquisition [81]. Due to the utilisation of transducer rings in pipe inspection, the CSM has been applied and analysed for guided wave imaging in pipes to detect defects, where all transducer elements are triggered simultaneously and the reflected signal is received at each transducer element. After interacting with cracks, the wave signals are decomposed into relevant mode clusters and then focused synthetically to points on the pipe with a series of time-space transforms for imaging construction.

For example, T(0, 1) was selected as the excitation mode to obtain the dimension of the cracks from the image of the pipe and it was found that compared with a linear array used in plate imaging, the defect image was not influenced by the size of pipe and axial defect location [82]. A similar CSM analysis was applied using L(0, 2) mode which was decomposed into a L(m, 2) mode cluster after interacting with cracks in a steel pipe, to determine the axial and circumferential location of damage [83]. A comprehensive study using different wave modes excitation with CSM to realise the imaging of the oblique defect and detail analysis considering axial resolution, reflection amplitude, and oblique angle were also carried out [84].

### **3.2.5 Tomography**

Different from early tomography schemes with parallel projection, cross-hole geometry scheme is now used for pipe inspection. Cross-hole tomographic geometries can be divided into helical ultrasound tomography (HUT) and meridional ultrasound tomography (MUT), with different arrangements of the transducer system. With HUT, two circumferential rings of transducers are placed on the pipe separately to obtain a set of helical pitch-catch measurements [85]. In contrast, a row of transducers is arranged along the middle of the pipe surface for MUT, which is more suitable when the entire circumference of the structure is inaccessible. In particular, a technique known as the simultaneous iterative reconstruction technique (SIRT) has been proved more robust and applicable to a variety of geometries [86, 87]. To utilise the SIRT algorithm, tomographic reconstruction geometry can be demonstrated on an unwrapped pipe, as in Figure 3.4 [86].

In each cell of the image, the wave velocity  $v[m, n]$  can be solved as:

$$T[i, j] = \sum_{m, n \in ray[i, j]} t[i, j, m, n] = \sum_{m, n \in ray[i, j]} \frac{d[i, j, m, n]}{v[m, n]}, \quad (3.6)$$

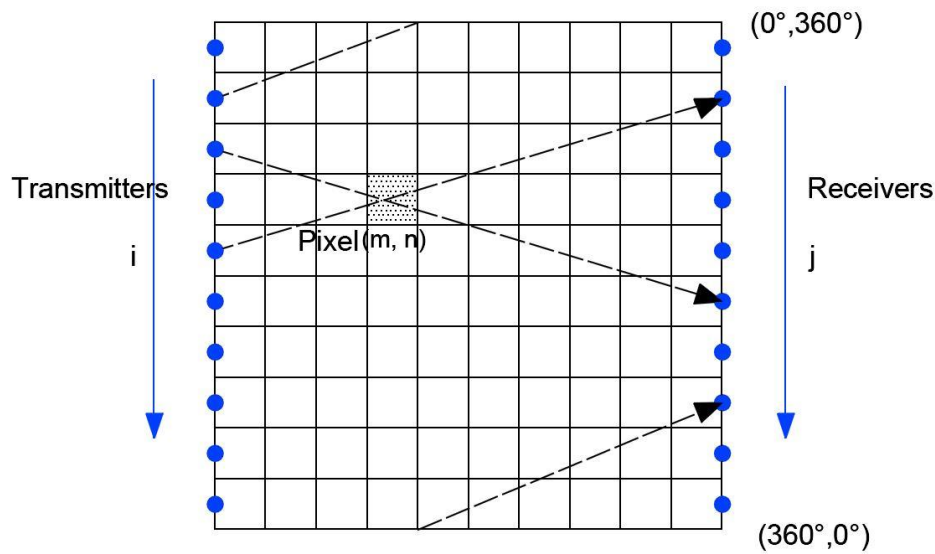


Figure 3.4 The reconstruction geometry of HUT for a pipe treated as unwrapped plate [86].

Where,  $d[i, j, m, n]$  is the segment length, which can be calculated and the total time  $T[i, j]$  can be obtained from the experiment. A velocity map for the whole analysed region can then be formed through a series of iterations with SIRT. It is noticed that both MUT and HUT scanning schemes only consider a single mode of interest under a predetermined frequency, such that incomplete datasets sometimes reduce the accuracy of the image reconstruction. Certain methods have thus been developed to improve these techniques, such as frequency compounding [87] and helical path separation [88].

Another algorithm with the concept of tomography is a reconstruction algorithm for probabilistic inspection of damage (RAPID). Fundamentally, this algorithm extracts a signal difference coefficient from the current signal and the baseline signal of the structure, accounting for changes in signal amplitude, wave velocity and mode conversion [89], and then forms ray ellipses around several pairs of source-receivers which will superpose and generate the final tomogram. RAPID has been applied in measuring the wall thickness of pipes and some critical zones in pipelines, e.g. socket welds [90] and pipe elbows [91].

An example of pipe elbow tomography is shown in Figure 3.5 for a 7 mm wall thickness steel pipe elbow with a 16-sensor array, where the red region indicates the damage in the form of 0.23 mm wall thinning [91].

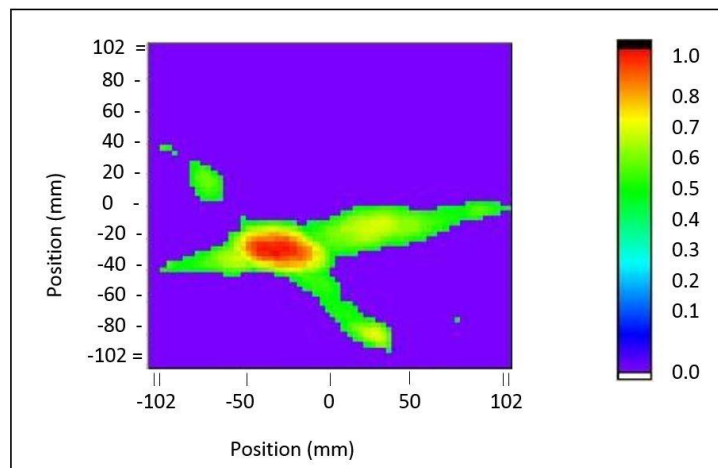


Figure 3.5 Tomogram for a steel pipe elbow [91].

Furthermore, guided wave tomography on pipe bends was simulated in a model where a new curved ray tomography algorithm based on inverse and forward 2-D rectangular domain was used and the model was made artificially inhomogeneous and elliptically anisotropic (INELAN) [92, 93].

### 3.3 Damage detection with nonlinear guided waves

This section reviews main findings up to date in nonlinear guided waves applied on pipes for damage detection including theoretical, numerical and experimental analyses for a deep understanding of the properties and capability of different nonlinear methods in pipe structures.

Techniques using linear ultrasonic guided waves generally perform well when detecting gross defects rather than micro-damage. However, sometimes it is necessary to detect small-scale damage in its early stage. In this respect, techniques using nonlinear ultrasonic guided waves have shown great capability using nonlinear ultrasonic behaviour including higher-harmonic generation, mixed frequency response, sub-harmonic generation and

nonlinear resonance. In the literature, nonlinear guided waves in plate-like structures have been widely studied [9, 94-100] but the information is relatively limited for pipe structures, where higher harmonic generation and mixed frequency response methods have been mainly studied numerically and experimentally.

### **3.3.1 Background theory**

Nonlinear ultrasonic can be simply grouped into four sorts: classical nonlinear elasticity, contact acoustic nonlinearity, hysteresis and non-classical dissipation [101]. It should be noticed that the mechanisms of nonlinearity are complicated and sometimes similar nonlinear effects can be manifested by different physical mechanisms and vice versa [101]. Based on the current studies of nonlinear guided waves in pipes, two commonly involved mechanisms in pipes are introduced in this chapter, i.e. classical nonlinear elasticity and contact acoustic nonlinearity.

#### **3.3.1.1 Classical nonlinear elasticity**

There are two types of classical nonlinearity, i.e. geometrical and physical nonlinearity. However, in solids, the former can be ignored since it is generally much weaker than the latter [102, 103]. Physical nonlinearity describes a nonlinear relationship between the stress and strain of material, such as dislocations in the structure or material degradation. Nonlinear Hooke's law usually accounts for higher order elastic terms, together with higher order terms in elastic energy. The nonlinear wave equation with second and third order terms can be presented as [102]

$$\frac{\partial^2 u}{\partial t^2} - c_0^2 \left\{ 1 - \epsilon \frac{\partial u}{\partial x} + \beta \left( \frac{\partial u}{\partial x} \right)^2 \right\} \frac{\partial^2 u}{\partial x^2} = 0, \quad (3.7)$$

where  $c_0$  is the linear wave velocity,  $x$  is the coordinate in propagation direction,  $u$  is the displacement,  $\epsilon$  and  $\beta$  are the quadratic and cubic nonlinearity coefficients. The quadratic nonlinear system generates both odd and even harmonics in the frequency spectrum while

-Quantitative evaluation of fatigue crack using nonlinear guided waves in pipelines-

the cubic nonlinear system generates only odd harmonics [101], as shown in Figure 3.6

Stress-strain curve for materials with (a) quadratic nonlinearities and (b) cubic nonlinearities, and relative frequency spectrum [101].

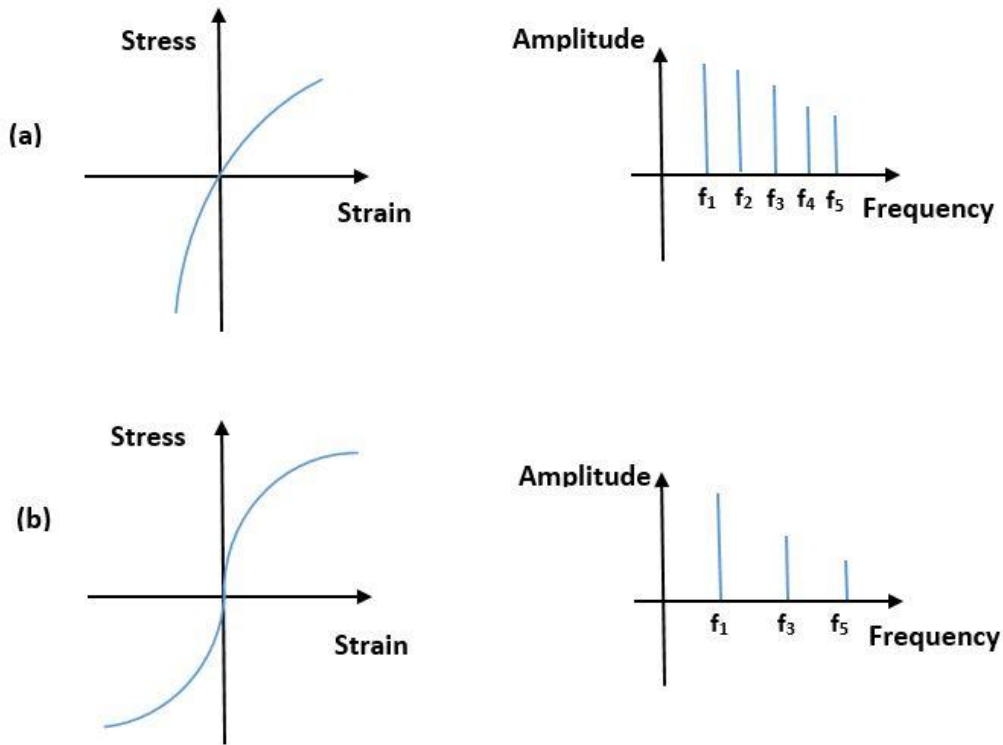


Figure 3.6 Stress-strain curve for materials with (a) quadratic nonlinearities and (b) cubic nonlinearities, and relative frequency spectrum [101].

Theory of higher harmonic generation in nonlinear elastic isotropic waveguides with arbitrary cross-section was firstly studied, and then cylindrical rods and shells were presented as examples [13]. In this study, firstly, a nonlinear Navier equation presenting wave motion in Lagrangian coordinates was expressed as

$$(\lambda + 2\mu)\nabla(\nabla u) - \mu\nabla \times (\nabla \times u) + f = \rho_0 \frac{\partial^2 u}{\partial t^2}, \quad (3.8)$$

and on the surface of the waveguide, the stress-free boundary condition was

$$[S^L(u) - \bar{S}(u)]n = 0 \quad \text{on } S, \quad (3.9)$$

where  $\lambda$  and  $\mu$  are the Lamé's elastic constants,  $u$  is particle displacement,  $\rho_0$  is the initial density of the body,  $\bar{S}$  and  $f$  are the surface traction and body force which include all nonlinear terms,  $S^L$  is the linear component of the first Piola-Kirchhoff stress tensor,  $n$  stands for unit vector perpendicular to the surface  $S$  [104].

Then a perturbation method was applied to solve the nonlinear boundary value problem and  $u$  is expressed as

$$u = u^{(1)} + u^{(2)}, \quad (3.10)$$

where  $u^{(1)}$  stands for the primary wave and  $u^{(2)}$  represents the second harmonic, which is solved by using modal expansion and a reciprocity relation. It should be noticed that  $|u^{(1)}| \gg |u^{(2)}|$ . The solution of  $S^{(2)} \cdot n_z$  and particle velocity  $v^{(2)}$  can be found in [105]. Both of them are related to parameter  $A_m(z)$ , which is the modal amplitude and can be determined from [106]

$$4p_{mn} \left( \frac{d}{dz} - ik_n^* \right) A_m(z) = (f_n^{surf} + f_n^{vol}) e^{i(k_a \pm k_b)z}, \quad (3.11)$$

where

$$A_m(z) = \begin{cases} \frac{i(f_n^{surf} + f_n^{vol})(e^{i(k_a \pm k_b)z} - e^{ik_n^*z})}{4p_{mn}[k_n^* - (k_a \pm k_b)]}, & k_n^* \neq (k_a \pm k_b) \\ \left( \frac{f_n^{surf} + f_n^{vol}}{4p_{mn}} \right) z e^{i(k_a \pm k_b)z}, & k_n^* = (k_a \pm k_b) \end{cases}, \quad (3.12)$$

and  $f_n^{surf}$  and  $f_n^{vol}$  are the complex external powers of the surface traction and the volume force respectively,  $p_{mn}$  is the complex power flux and  $k$  is the wavenumber. From the above equations, it can be seen that the amplitude of second harmonic increases with the propagation distance under the conditions that  $k_n^* = (k_a \pm k_b)$  and  $f_n^{surf} + f_n^{vol} \neq 0$ . These are conditions known as (1) phase matching and (2) nonzero power flux for the generation of second harmonic with accumulative effect along the propagation direction. This phenomenon can be used to distinguish the material nonlinearity and the nonlinearity from the instrument.

Another research formulated the nonlinear forcing term in general curvilinear coordinates and analysed the longitudinal and torsional fundamental modes in weakly nonlinear cylinders [15]. In a weakly nonlinear system, while nonlinear effects do play an essential role, linearised equations can be used to provide a first approximation for those slight disturbances [107]. Both the fundamental mode self-interaction (one fundamental mode) and mutual interactions (two mutually interacting fundamental modes) which generate higher harmonic were studied. The possible cumulative secondary wave fields due to interaction of longitudinal and torsional waves in cylinders are summarised in Table 3.1. A further study illustrated an analysis of higher order guided wave interaction in weakly nonlinear tubes [14, 108]. Moreover, the second harmonic generation in pipes was also studied via applying a large-radius asymptotic approximation, which extended the conclusions obtained from the second harmonic generation in plates to large radius pipes [16].

Table 3.1 Potential cumulative secondary wave field when the fundamental wave mode is self-interaction or mutual interaction of torsional (T) and longitudinal (L) waves in cylinders. Y: the secondary mode is cumulative; N: the secondary mode is not cumulative [15].

<b>Fundamental wave field</b>		<b>Secondary wave mode</b>	
		<b>T</b>	<b>L</b>
<b>Self-interaction</b>	L	N	Y
	T	N	Y
<b>Mutual interaction</b>	T-T	N	Y
	L-L	N	Y
	L-T	Y	Y

### 3.3.1.2 Contact acoustic nonlinearity (CAN)

CAN occurs when ultrasonic waves pass through the interface between two surfaces of a microcrack. As the incident wave approaches a contact interface, the compressional and tensile parts will cause the closing and opening of the crack, which induces the localised nonlinearity. The first model of this nonlinearity was provided by Richardson [109]. This model contains two semi-infinite elastic materials with intimate contact separated by a planar interface, across which no traction forces exist. Another model considered the contact between two rough surfaces with changeable contact area under applied stress, which induced nonlinearity of the interface [110]. It acts as a nonlinear spring with varying stiffness when stress was applied. A more popular model for CAN was called bi-linear stiffness model [111]. It had different stiffness under compression and tensile phases of a wave and the crack became similar to a “mechanical diode” (Figure 3.7(a)).

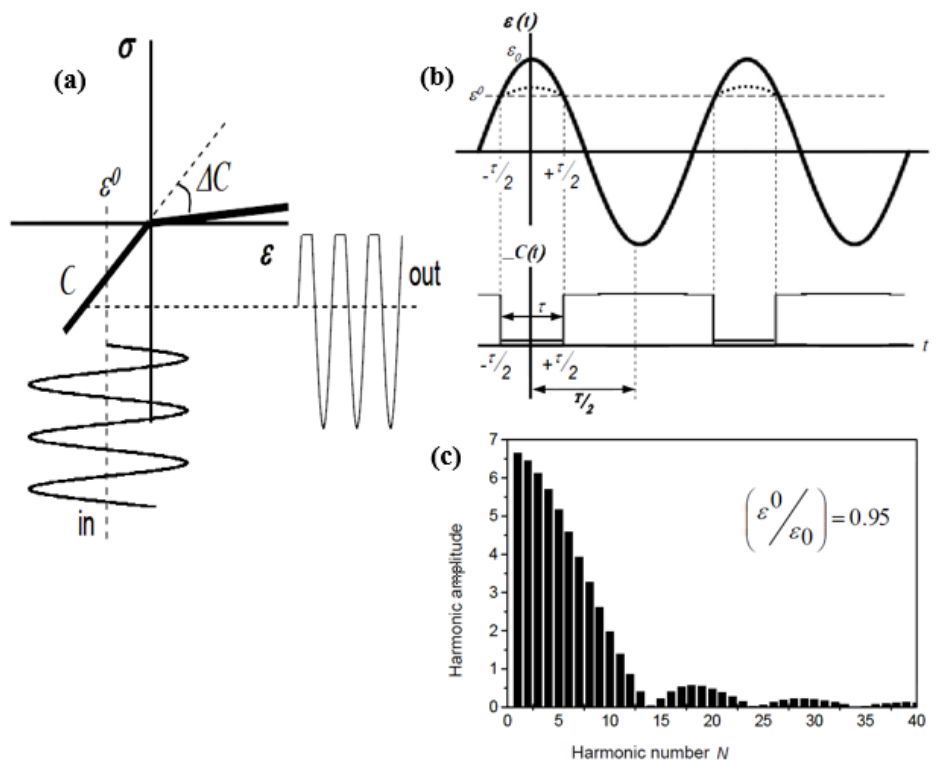


Figure 3.7 (a) “Mechanical-diode” effect; (b) modulation of  $C(t)$ ; (c) high harmonic spectrum

[112].

The stress-strain relation can be expressed as

$$\sigma = C^{II} \left[ 1 - H(\varepsilon - \varepsilon^0) \left( \frac{\Delta C}{C^{II}} \right) \right] \varepsilon, \quad (3.13)$$

where  $H(\varepsilon)$  stands for the Heaviside unit step function,  $\varepsilon^0$  represents the initial contact strain,  $C^{II}$  is the intact second-order linear elasticity of material and

$$\Delta C = \left[ C^{II} - \left( \frac{d\sigma}{d\varepsilon} \right)_{\varepsilon > 0} \right]. \quad (3.14)$$

If the input strain was

$$\varepsilon(t) = \varepsilon_0 \cos \omega_0 t, \quad (3.15)$$

it would lead to a modulation of the stiffness  $C(t)$  (Figure 3.7(b)) and the nonlinear part in the spectrum contained a number of higher harmonics whose amplitudes were modulated by sinc-envelope function [112], as shown in Figure 3.7(c).

The disadvantage of the above model is that the strain field was calculated with incident wave only without considering the waves scattered by the crack. Therefore, an analytical model as illustrated in Figure 3.8 was developed to involve the scattered wave with the variational principle and modal decomposition method in a 2D scenario [113]. It introduced the crack-induced second-source-stress loading (CISS) and treated it as a source of the scattered wave.

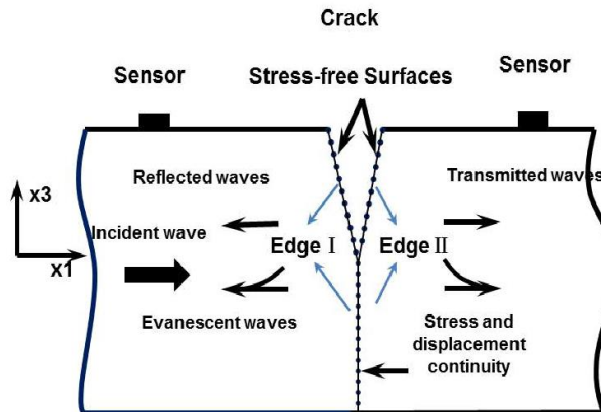


Figure 3.8 Model of a 2D infinite plate with breathing crack [113].

The CISS at double frequency were

$$\sigma_{11}^{\text{CISS}-2f_0} = A_{2f_0} [\sigma_{11}^{\text{Crack}}(x_3) - \sigma_{11}^{\text{Inc}}(x_3)] e^{i2\omega t}, \quad (3.16)$$

$$\sigma_{13}^{\text{CISS}-2f_0} = A_{2f_0} [\sigma_{13}^{\text{Crack}}(x_3) - \sigma_{13}^{\text{Inc}}(x_3)] e^{i2\omega t}, \quad (3.17)$$

where  $A_{2f_0}$  is the amplitude of second harmonic,  $\sigma^{\text{Inc}}$  and  $\sigma^{\text{Crack}}$  are the stress field induced by incident wave and crack, respectively. The stress distribution through the thickness of the plate of both CISS and induced wave modes is in Figure 3.9.

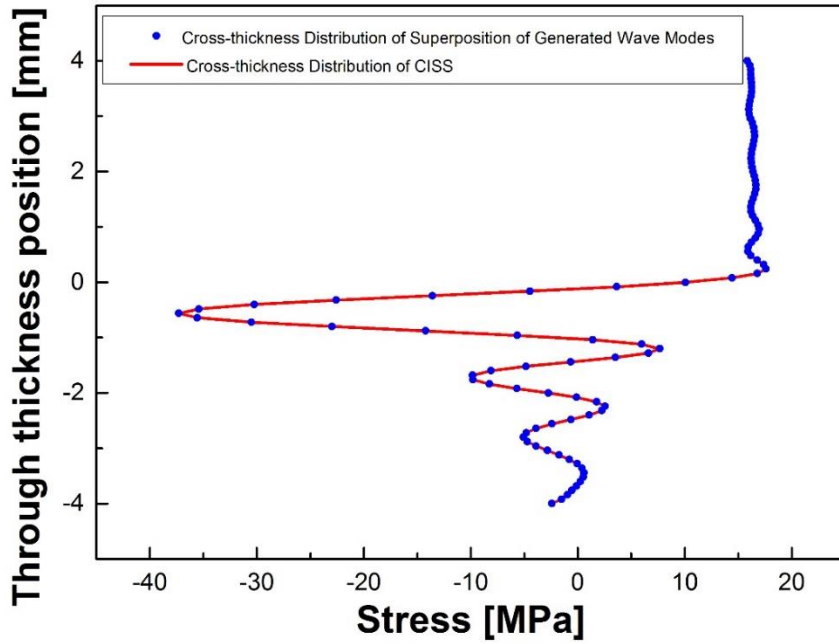


Figure 3.9 Stress distribution of CISS and induced wave modes through the thickness of the plate [113].

### 3.3.2 Damage detection with nonlinear guided waves

#### 3.3.2.1 Higher-harmonic generation

The physical mechanisms of higher-harmonic generation are two-fold, encompassing classical nonlinear elasticity and CAN [114], where the nonlinear parameter  $\hat{\beta}$  is used to describe the classical nonlinear elasticity [115, 116]:

$$\hat{\beta} = \frac{8}{k^2 x} \frac{A_2}{A_1^2}, \quad (3.18)$$

where  $A_1$  is the amplitude of the fundamental frequency;  $A_2$  is the amplitude of the second harmonic;  $x$  represents the propagation distance and  $k$  is the wavenumber of the wave at the fundamental frequency. The magnitude of the nonlinear parameter indicates the degree of nonlinearity in the material.

To simulate the generation of second harmonic due to material nonlinearity in a pipe with longitudinal and torsional mode excitation, a FE model was set up with Landau and Lifshitz third order elastic constants [15]. The internal resonance plots indicate the mode pair which can generate cumulative second harmonic (Figure 3.10). A similar simulation study compared the mode pair in a steel pipe with that in a plate [96]. It is found that both longitudinal and torsional mode excitation can generate higher harmonics in frequency spectrum after a fast Fourier transform (FFT) and the relative nonlinear parameter  $\frac{A_2}{A_1^2}$  was cumulative along the propagation distance. A more general numerical study including flexural modes in weakly nonlinear hollow cylinders was also performed [14]. Additionally, a numerical simulation of nonlinear guided waves for microcrack detection in pipelines found that the addition of a low-frequency vibration could enhance the higher harmonics [117].

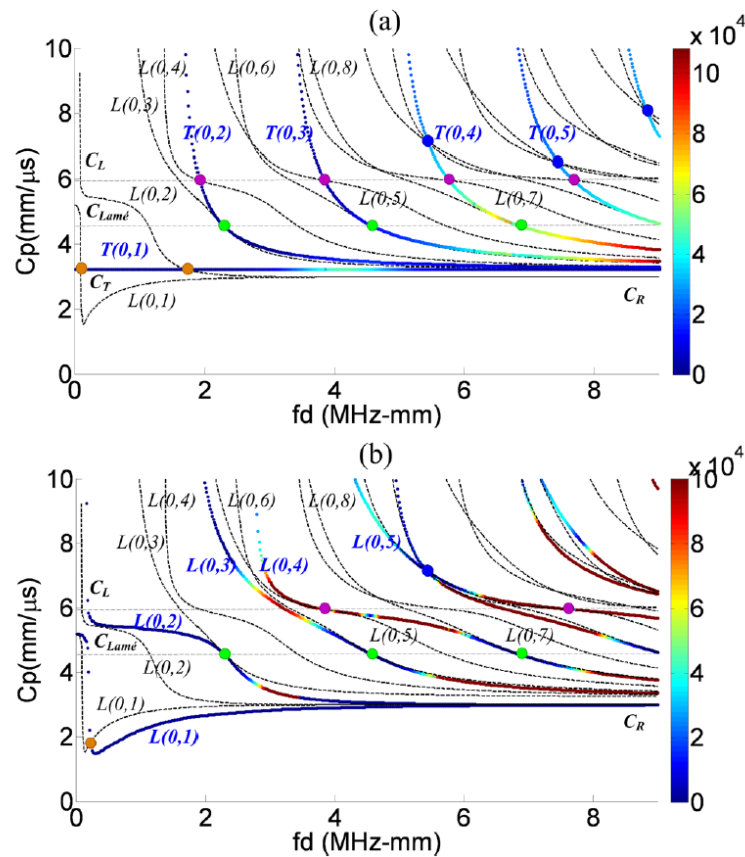


Figure 3.10 Plots of internal resonance points: when (a) fundamental waves are torsional modes, and (b) fundamental waves are longitudinal modes. Colour lines stand for the fundamental modes and the black dashed lines are the possible cumulative secondary modes. The circles represent the potential synchronism points [15].

Besides nonlinear elasticity and CAN, other nonlinear material behaviours can also generate higher harmonics, e.g. stress-strain hysteresis, which is related to factors such as plasticity, viscosity and the presence of cracks. Such nonlinearity exhibits odd harmonics only [118], and a model considering the Preisach-Mayergoyz space [119] was used to simulate this nonlinearity due to microcracks in materials. A 3D model was developed accordingly to detect micro scale fatigue cracks in a steel pipe and time reversal imaging method was applied to obtain the location and dimension of the crack [120]. Some other simulation methods, such as finite difference (FD) method [121], and local interaction simulation approach (LISA) [95, 122], have been developed to simulate fatigue cracks in

plate structures to generate nonlinearities. These fatigue crack simulation methods can be referred for the studies in pipes.

Using the nonlinear parameter, micro-structure changes caused by different cycles of thermal fatigue in an aluminium pipe were evaluated experimentally with longitudinal fundamental wave excitation [17] and it is shown that the magnitude of the nonlinear parameter grew with thermal fatigue cycles, as shown in Figure 3.11. Another experimental study observed the accumulation of second harmonic as the circumferential angle  $\theta$  increased with the excited circumferential wave in a tube [123], as shown in Figure 3.12  $A_2/A_{12}$  vs circumferential angle  $\theta$  at the driving frequency 0.88 MHz [123].

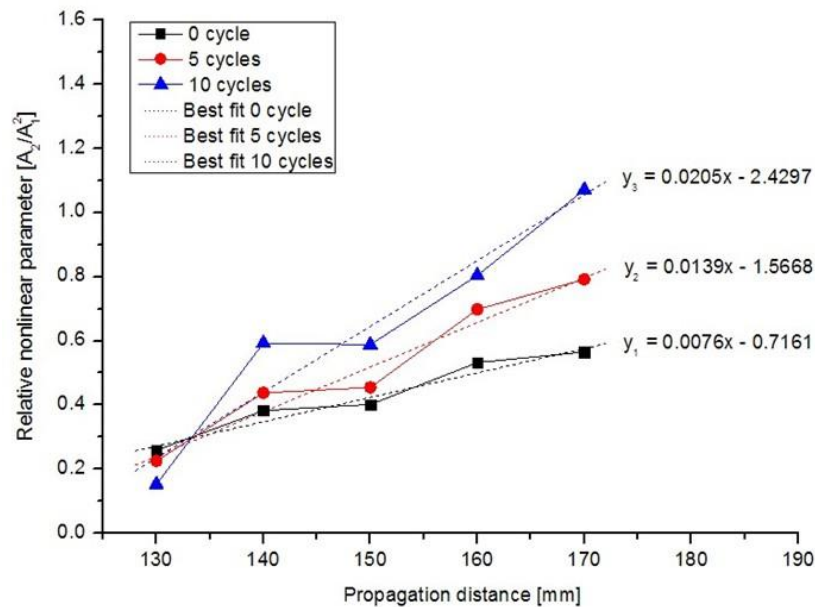


Figure 3.11 The relation between the relative nonlinear parameter ( $A_2/A_{12}$ ) and the propagation distance under different thermal fatigue cycles [17].

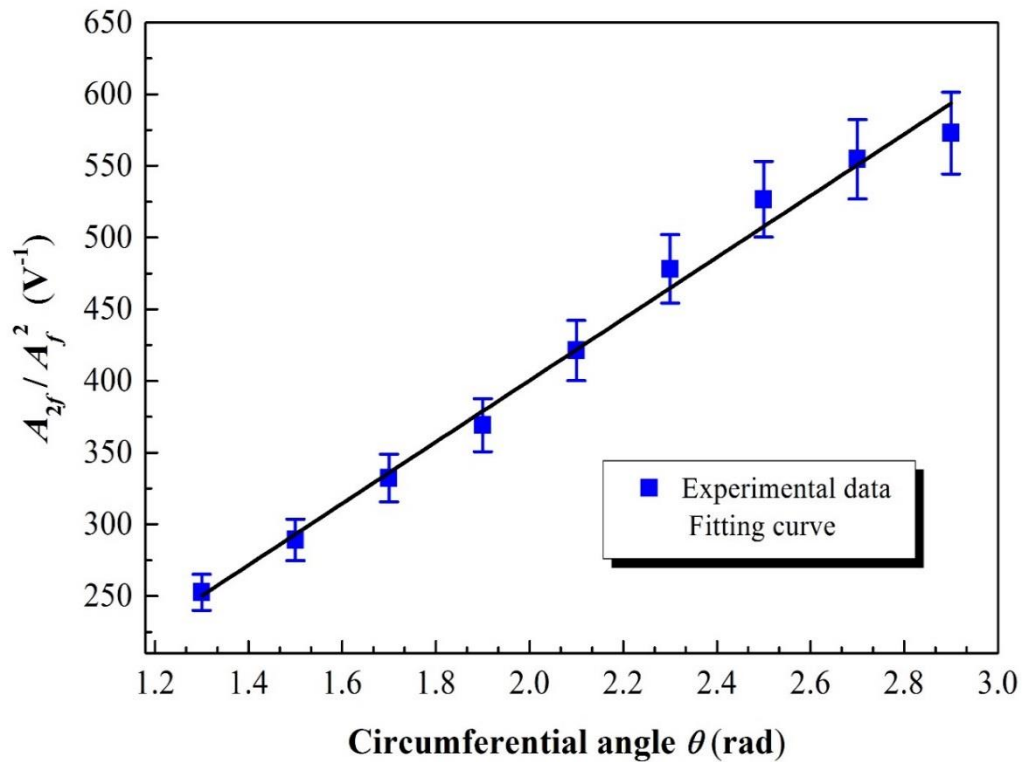


Figure 3.12  $A_{2f}/A_f^2$  vs circumferential angle  $\theta$  at the driving frequency 0.88 MHz [123].

### 3.3.2.2 Frequency modulation

Although there is still debate as to the physical mechanism, frequency modulation is another way of evaluating nonlinearity, where a low-frequency hammer impact or vibration or wave (pumping signal) with frequency  $f_1$  and a high-frequency wave (probing signal) with frequency  $f_2$  are excited simultaneously in the investigated structure. One explanation for the mechanism of nonlinearity is CAN, which results in changing in the amplitude and modulation of signals (as shown in Figure 3.13) [124].

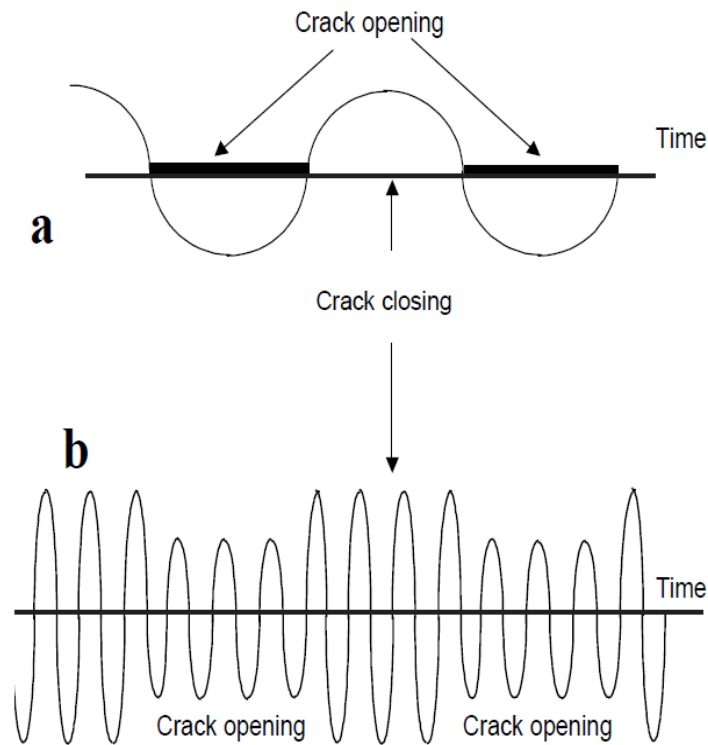


Figure 3.13 Modulation of probe signal amplitude, when the probing signal is: (a) vibration, (b) ultrasonic signal [124].

However, some other studies point out that the major mechanism for modulation is energy dissipation instead of crack breathing behaviour [9, 125]. Nevertheless, both explanations perceive modulated sidebands with frequency  $(f_2 \pm f_1)$  around the input high frequency from the received signal if there is nonlinearity caused by fatigue cracks in the structure. Usually, the severity of the damage can be evaluated by a modulation index (MI) in comparison with the baseline data. One of the most commonly used damage indices is [126]

$$MI = \frac{\sum_{i=1}^n (A_{LSB}^i + A_{RSB}^i)}{A_{HF}}, \quad (3.19)$$

where  $A_{LSB}^i$  and  $A_{RSB}^i$  are the amplitudes of  $i^{\text{th}}$  pair of left and right modulation sidebands and  $A_{HF}$  is the amplitude of high-frequency component of the probing signal.

For the cases using multiple ultrasonic frequency steps, the index is modified as [127]

$$MI = 20 \log_{10} \left( \frac{1}{q} \sum_{m=1}^q \frac{A_{m-n} + A_{m+n}}{2A_m} \right), \quad (3.20)$$

where  $A_{m+n}$  and  $A_{m-n}$  represent the amplitudes of sidebands with frequency  $f_m \pm f_n$ ,  $A_m$  is the amplitude of the probing signal at frequency  $f_m$  and  $q$  is the number of the frequency increments of interest.

To generate the modulation, when two waves are excited for the modulation, the two signals must arrive at the crack simultaneously [128]. It should be noticed that numerical work for modulation method in pipes with a single breathing crack is limited. Also, for the simulation work, some studies investigated the modulation method in pipes with classical nonlinear elasticity [14, 96, 129]. For example, the wave mixing of a T(0, 3) mode and a L(0, 2) mode at 2.5 MHz and 1 MHz respectively was simulated on a steel pipe with material nonlinearity [96]. In the frequency spectrum, modulations can be seen at the sum and difference frequencies which indicate the existing of nonlinearity. Furthermore, to locate the position of localised degradation in a pipe, tomographic scanning method combined with mixing wave excitation was applied in another numerical study [129].

Experimental studies using impact-modulation method and a new vibro-modulation system to detect stress corrosion cracks [130] and fatigue cracks of a welded joint [127] in steel pipes were reported respectively. These two studies have demonstrated the ability of modulation methods to detect nonlinearities and the severity of nonlinearities with the MI in pipes. A further experiment study analysed factors that influence the MI [131], where 50 kHz pure sine ultrasonic signal and flexural vibration at different frequencies are applied. MI in terms of vibration frequency and vibration amplitude are shown in Figure 3.14(a) and (b), respectively, indicating that both the amplitude of the vibration and the frequency would influence the MI.

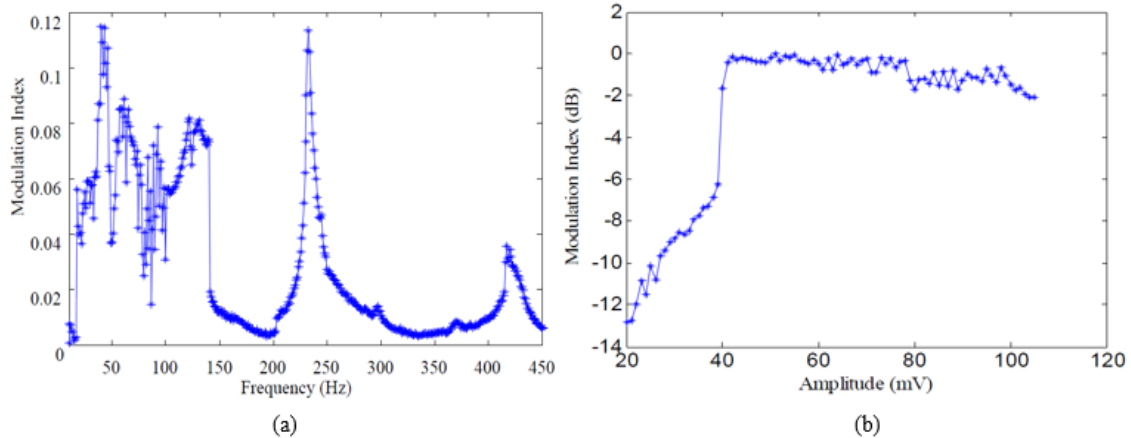


Figure 3.14 (a) MI with varying frequency of vibration, (b) MI with changing amplitude of vibration at 50 Hz vibration frequency [131].

## 3.4 Special issues in pipe inspection

### 3.4.1 Bends in pipes

Practical testing in pipelines always encounters problems on bends, which can distort wave propagation. Some studies [132, 133] based on both FE method and experimental study have been conducted to obtain dispersion curves for cylinder structures, seeking better comprehension of the reflection and transmission properties of waves when traveling through a bend. An analytical model has also been set up to estimate the effects of pipe bends on a range of signals and to diminish the distortion caused by pipe bends [133]. A study of more general bend angles and the mean bend radius in terms of mode wavelength and pipe thickness has been performed. Wave propagation at different times illustrated by total displacement value in a 30° pipe bend captured from simulation models is shown in Figure 3.15 [34]. It was also noticed that as the bend angle decreased, the mode conversion effect was enhanced and the velocity of excitation wave increased. However, even for the worst case, the energy loss caused by the bend was only 20%. In terms of the effects of multiple bends in a pipe on guided wave properties, an

-Quantitative evaluation of fatigue crack using nonlinear guided waves in pipelines-

experimental study was conducted to identify propagation velocity, mode conversion and energy attenuation [71]. All these efforts provide useful references for guided wave applications in bent pipes.

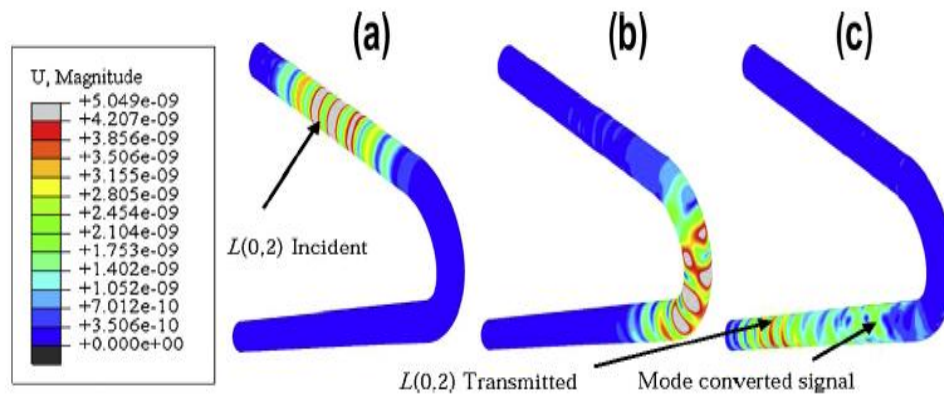


Figure 3.15 L(0, 2) mode wave propagation at different time for a 30 ° bent pipe in FE simulation model. The wave is (a) before the bend; (b) at the bend; (c) after the bend [34].

### 3.4.2 Effect of environmental and operational conditions (EOCs)

EOCs always affect the propagation of guided waves, where the changes in temperature, humidity or flow rate, etc., generally mask the changes caused by structural anomalies [134, 135]. In this thesis, the influence of both temperature change and surrounding materials of pipelines are reviewed, in recognition of the fact that many pipelines are exposed to these two conditions.

Two case studies have focused on the time shift and amplitude change in the received signal from a piping system with changing flow rate and temperature, indicating that the influence on guided wave properties becomes more obvious when both of the EOCs occur [136]. Temperature change can also cause shape distortion and nonlinear relations of guided waves. These effects were studied and removed by a nonlinear principal component analysis (PCA) of a multimode scattering signal in an aluminium pipe [137]. To minimise this challenge, proper method such an energy-based sparse representation

-Quantitative evaluation of fatigue crack using nonlinear guided waves in pipelines-

was proposed for online damage detection in pipes under varying EOCs, which showed less dependence on the EOCs [138].

On the other hand, the surrounding material of pipelines can be classified into two categories: weakly loaded waveguides, e.g. pipe surrounded by water, and strongly loaded waveguides, e.g. pipe embedded in concrete or rock [139]. For the former, it leads to attenuation of guided waves, but wave properties will not change significantly. For the latter, significant changes in the properties of guided waves occur. Studies of weakly loaded waveguides such as water-filled pipes or pipes immersed in water are common. Analytical and experimental studies of fluid-filled cylindrical pipes have shown that the cut-off frequencies and group velocities of all wave modes were affected by the water [140]. Other studies [141, 142] have shown that water inside or outside a pipe caused slight wave attenuation, but this is not a remarkable influence on the ability of defect inspection in pipe.

For pipelines buried in sand, different soil conditions have different influences on the guided wave properties. To find the attenuation of different sand conditions, a schedule-40 9 mm wall thickness pipe was tested in a variety of sand conditions [41, 143], where transducer rings were used to generate both  $T(0, 1)$  mode and  $L(0, 2)$  mode within 11-34 kHz. As shown in Figure 3.16 [41], compared with  $T(0, 1)$ , the  $L(0, 2)$  mode exhibited lower attenuation while the shear velocity in the sand played a dominant role for the attenuation of these two modes. The attenuation of guided waves increased in sand when overburden pressure was applied, such as compacted and mechanically compacted sand.

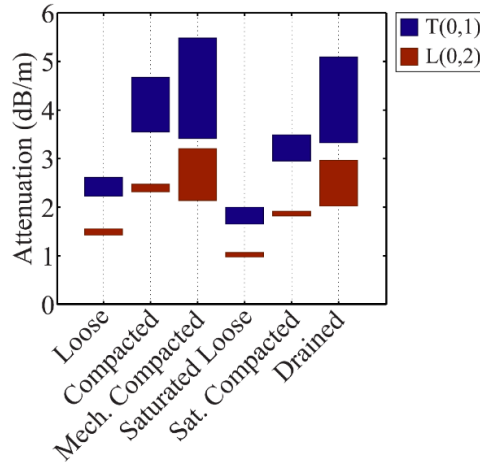


Figure 3.16 Attenuation values for T (0, 1) (blue) and L (0, 2) (red) mode over frequency range of 11-34 kHz under different sand conditions [41].

In addition, the attenuation of guided waves and the corresponding propagation distance for insulation pipe with different coating materials were also studied, as shown in Figure 3.17. It was demonstrated that for detection sensitivity, which was the sensitivity to detect damage with a size greater than 5 percent of the pipe wall cross-section area, a bitumen coated pipe above ground achieved a relatively low inspection range, whereas the distance between transducer and receiver could be more than 20 m for a polyethylene (PE) coated pipe above ground [144].

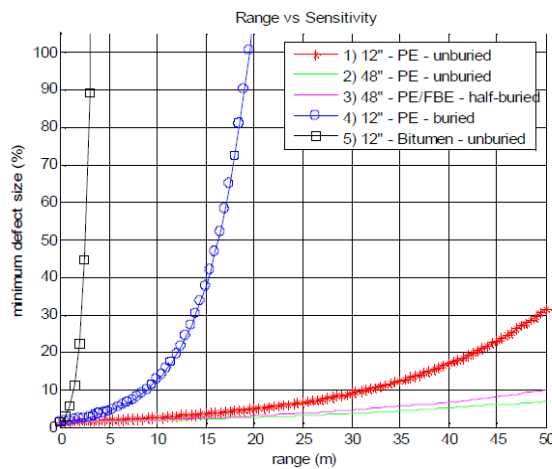


Figure 3.17 A plot of range vs sensitivity when the excitation frequency is 16 kHz for different coatings and positions (PE for polyethylene and FBE for fusion bonded epoxy) [144].

### **3.5 Summary**

This chapter reviews the theoretical model of guided wave scattering by the damage in pipes in terms of linear and nonlinear characteristics. With linear method, the interactions of guided waves with defects in pipes cause reflection, transmission, mode conversion, which have been widely used to identify different types of gross damage. Studies based on simulation models and experimental tests are introduced for abovementioned methods revealing the detectability of guided wave based methods in pipes. Apart from linear methods, nonlinear methods have higher sensitivity and are more suitable for micro-scale damage. The theory of different nonlinearity analyses, and some typical numerical and experiment examples that studied the relation between the nonlinear parameter and the material dislocation or microcrack have also been reviewed as a basis for the following simulation and experiment analyses.

In practice, more challenges are seen including the EOCs and the complex features of pipes, causing the attenuation of guided waves or the changes in received signals. It is concluded that ultrasonic guided wave-based inspection improves the conventional ultrasonic based techniques and is suitable for long-range inspection in pipelines, although many challenges still remain for future study.

## **Chapter 4 Investigation of nonlinear guided wave characteristics in plate and pipe like structures**

This chapter carried out some preliminary investigation work as the basis for the main part of this study. Optimisation and wave excitation method in simulation modelling are introduced. Followed by wave excitation in experiment test and some calibration of different factors that influence the generated signals or received signals. Two widely used nonlinear methods in pipe structures are analysed and compared so as to select a suitable one for the following study.

### **4.1 Optimisation, wave excitation and acquisition of simulation model**

#### ***4.1.1 Optimisation of simulation model***

Different numerical methods have been used to simulate nonlinear wave interaction with damage, such as finite difference (FD) method [31], and local interaction simulation approach (LISA) [3, 32], finite element (FE) analysis, boundary element method (BEM), finite strip elements (FSE), and mass-spring lattice model (MSLM) [71]. Among these numerical methods, FEM is the most commonly used technique with the advantage of cost-effectiveness. A commercial FEM software Abaqus Dynamic/Explicit® was chosen to simulate the interaction between nonlinear Lamb waves or guided waves and close crack in this study. This section elaborates the mesh optimisation for an accurate and time-saving simulation model and illustrates the selection of appropriate method for material nonlinearity and CAN modelling.

#### **4.1.1.1 Mesh convergence**

In the plate model in this study, through-thickness hole with notches and circular piezoelectric lead zirconate titanate (PZT) are simulated in these models. Uniform square mesh throughout the model cannot be applied in this occasion, and therefore mesh convergence on the models was conducted, aiming for creating appropriate mesh strategy for the FE modelling efficiently and accurately.

In the plate model, the minimum element size was calculated based on [30, 145], where at least 7 to 8 elements per smallest wavelength in this model should be applied. For a conservative calculation, at least 8 elements per wavelength of second harmonic wave was selected for the element size determination. Except the specific partitions for PZT part and the notch in model, the mesh size is uniform and the adjacent element size is similar to avoid calculation errors.

The plate model is meshed using eight-node brick elements (C3D8R). The model consists of three special parts, i.e. the PZTs, the hole in the middle with two notches and two holes at two end of the plate to be consistent with experiment sample. Two seed sizes have been used in this model. A finer seed size 0.5 mm was used for the PZT, hole and notch in the middle and the wave propagation region of interests. A seed size of 1 mm is used for the large hole at two ends and remaining regions. To be continuous with the sensing region with 0.5 mm seed size, part of the seed size around the holes at two ends of the plate was 0.5 mm as well. In the thickness direction the seed size was also 0.5 mm. 1036100 elements were therefore modelled in total and detail mesh is in Figure 4.1.

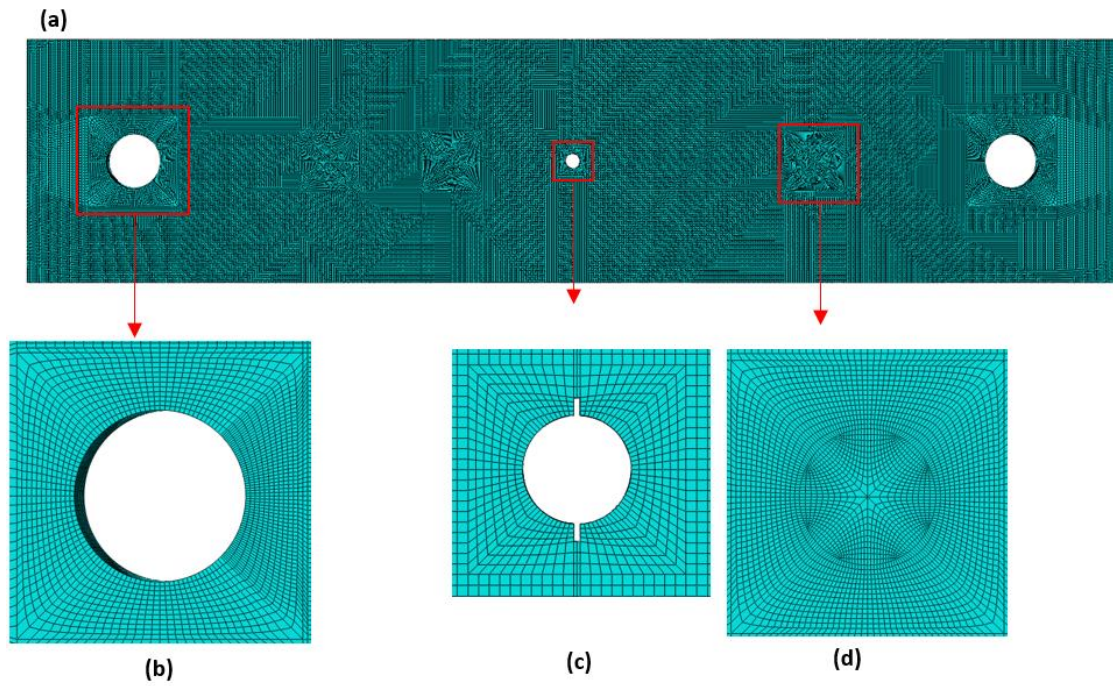


Figure 4.1 Mesh of plate in simulation model: (a) overview of the mesh; (b) mesh of the hole at the end of plate; (c) mesh of the notch and (d) mesh of the sensor.

For the pipe model in this study, at least 8 elements per wavelength of second harmonic wave was also selected. Since the PZT part is rectangular or square one, it can be meshed with the same size as the other parts while only one through thickness notch was simulated in the middle of the pipe. Thus, the element size is kept uniformly for accurate calculation in the model of pipe with element size 1 mm and the total element number is 340972.

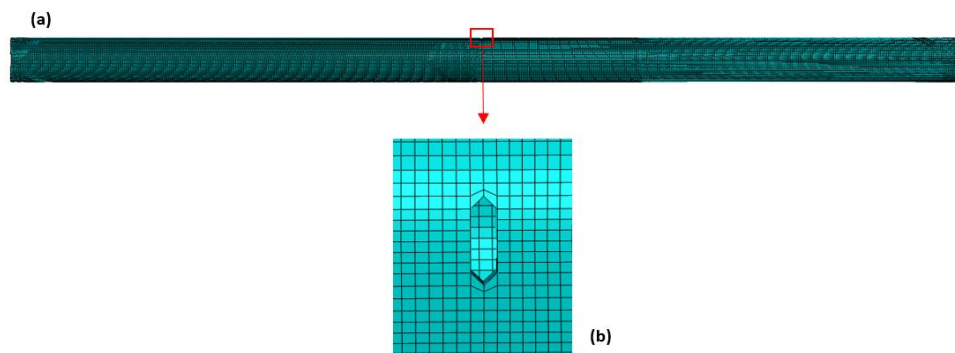


Figure 4.2 Mesh of the pipe in simulation model: (a) overview mesh of pipe and (b) mesh of the notch.

#### **4.1.1.2 Simulation of material nonlinearity and CAN**

To introduce the material nonlinearity which exists homogeneously in the simulation pipe model, third order elastic constants [13] were considered for material properties and then imported into the model with a user subroutine VUMAT file [97]. The material nonlinearity is much smaller compared to the CAN in pipe model. The input load in simulation is usually selected as 0.1 N to generate equivalent stress level as in experiment. However, for the model with material nonlinearity, to enhance this sort of nonlinearity, a higher input load was applied at 100 N.

There are many numerical models for the breathing crack to introduce nonlinearity, such as bilinear stiffness model [146], breathing crack with gap element [147] and rough surface contact model [148]. In this study Abaqus function “seam crack” was used on the location of breathing crack and a surface-to-surface contact with small sliding and associated properties were applied on the crack interfaces. The close crack will interact with the passing wave to open or close under tensional and compressional phase of the wave and introduce CAN in this model.

#### **4.1.2 Wave excitation and acquisition in simulation model**

To simulate the PZT actuator/sensor attached on a pipe in Implicit/Dynamic or Explicit/Dynamic Abaqus FE simulation model, different simulation methods have been reviewed including effective PZT (assign the displacement induced by PZT on the location of it) [149] and full PZT ( PZT model and specimen model assembled together) [150] and full PZT with an adhesive layer [151] in plate and pipe models. Although both Abaqus Implicit/Dynamic and Explicit/Dynamic can be used to analyse the wave propagation problem, the explicit solver performs computation more efficiently and is less time-consuming, achieving the wave propagation problem more technically

appropriate. However, the explicit dynamic method in Abaqus cannot employed piezoelectric elements. Therefore, effective PZT modelling were adopted in all simulation models in this study.

For the wave excitation in plate models, the PZT has been modelled as a disc partitioned in the relative location of the steel plate model. Time varying forces at a maximum amplitude of 0.1 N were excited by applying in-plane concentrated loads on the nodes along the periphery of the actuator to simulate the Lamb wave excitation from the circular PZT as shown in Figure 4.3. The Lamb waves therefore propagate radially from the actuator as shown in Figure 4.4. The simulation of sensor is similar as actuator. Stress along the direction of wave propagation was recorded at all the elements in the partition of PZT and the average value is calculated as the final received signal of each PZT.

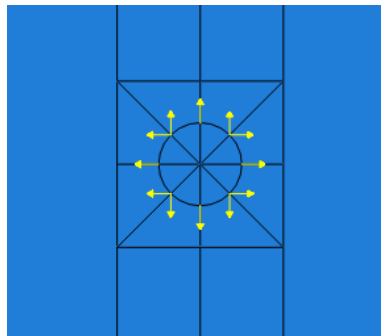


Figure 4.3 Circular PZT in simulation model.

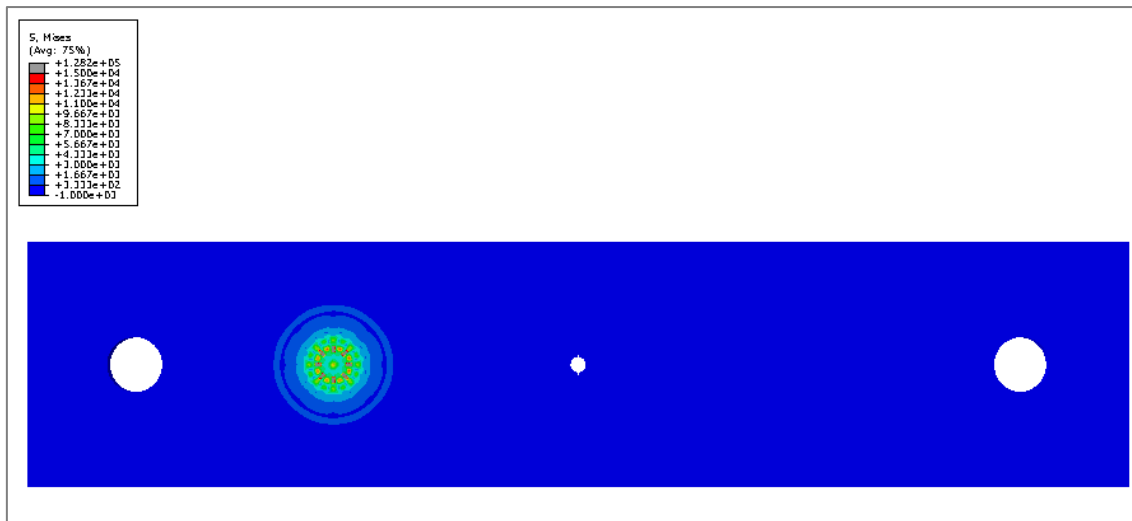


Figure 4.4 Lamb wave propagation in the plate model.

As for the wave excitation in pipe models, with one actuator excitation, the PZT has been modelled as a rectangular area partitioned in the assigned location of the model. Time varying forces at a maximum amplitude of 0.1 N or 100N were excited by applying as the load at four corners of the actuator at one end of the pipe along the longitudinal axis of pipe as shown in Figure 4.5. And the signal was received at the other end in terms of S33 stress along the pipe axis and displacement in the propagation direction.

For an actuator ring in pipe model, multiple elements around the circumference of the pipe were modelled, each of the element was simplified as a point and point load with varying amplitude at maximum of 0.1 N applied to the node along the pipe axis, as in Figure 4.6. The guided waves then propagate from the transducer ring as in Figure 4.7. The signals were collected at another end of pipe by a sensor array as well with same simulation method, and displacement in propagation direction at all the elements were recorded. The sum of these signals are considered as the final received longitudinal wave signal.

-Quantitative evaluation of fatigue crack using nonlinear guided waves in pipelines-

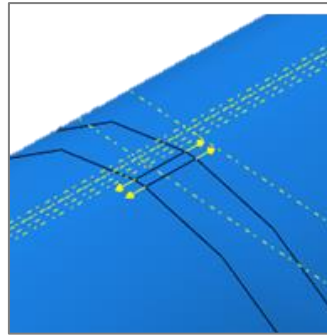


Figure 4.5 PZT in the pipe mode.

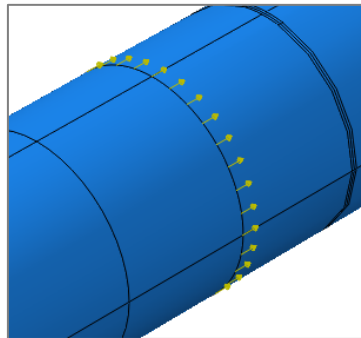


Figure 4.6 Sensor ring in the pipe model.

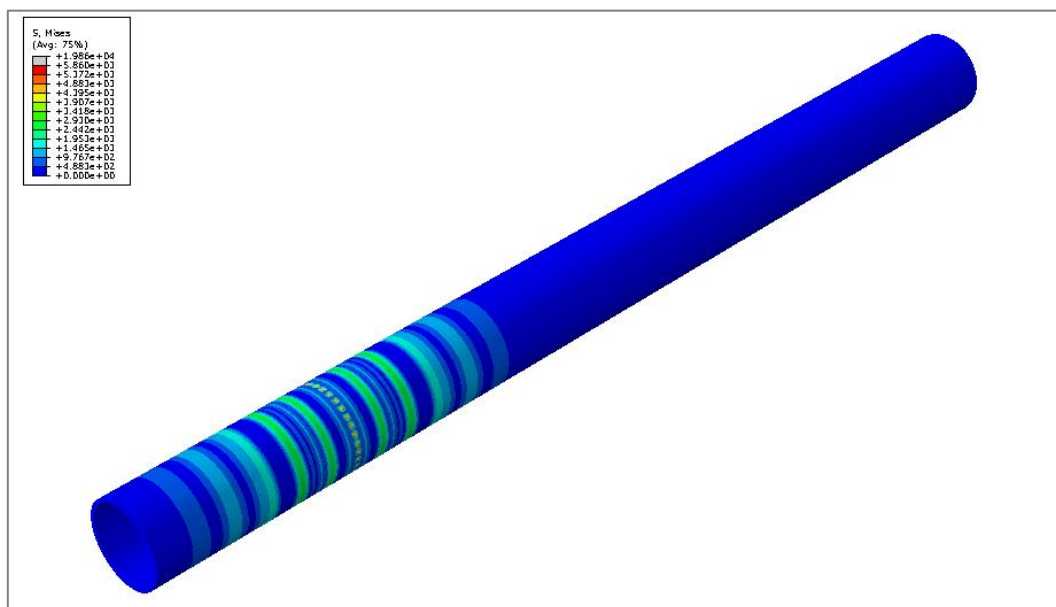


Figure 4.7 Guided wave propagation in the pipe model.

## **4.2 Investigation of wave excitation and nonlinearity acquisition in experiment test**

### ***4.2.1 Wave excitation and acquisition in experiment***

For both pipe and plate specimens, circular or rectangular PZT transducers with the same dimension in simulation model were attached on the specimen. Before the mounting of transducers, the surfaces of the PZTs were cleaned with acetone. Both the surface of the pipe and the plate where PZTs were attached was polished to make sure a flat surface and therefore to provide a well contact between PZT and specimen. Then PZT transducers were bonded to the surface of the specimen with superglue at the designed location. Before soldering wire to the PZT, all of them are covered by tape and stay for at least 24 hours to dry the glue. Wires are connected to the PZT pitches with soldering machine and the connecting condition is checked with the multimeter. All the wires are labelled for the convenience of signal collection. The specimens are supported by hard foam block to reduce the influence of boundary conditions.

Before the experiment, all PZT transducers are tested on the intact pipe to check if they can generate desired wave modes. The signal was excited at the actuator and received by the sensors as the reflected and transmitted configurations with a sampling frequency of 50 MHz after 512 samples were averaged for the plate specimen, while for pipe, the sampling frequency was 200 MHz and the signals were averaged 1024 times. The arrangement of sensors of plate and pipe specimens is in Figure 4.8.

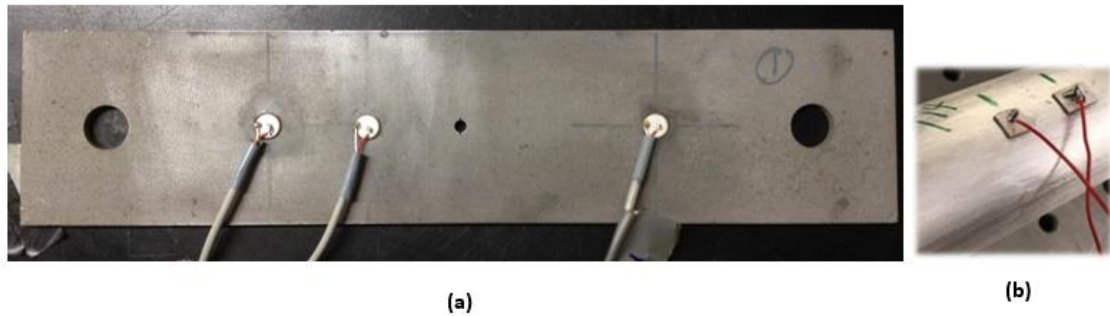
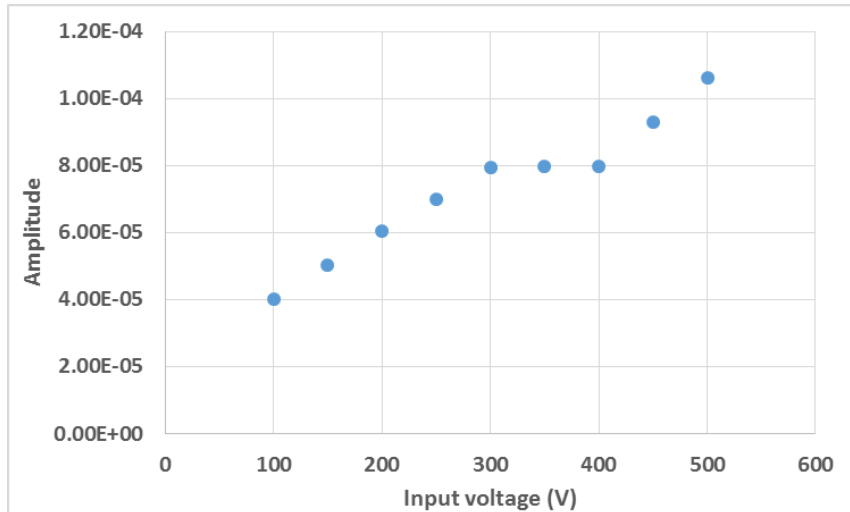


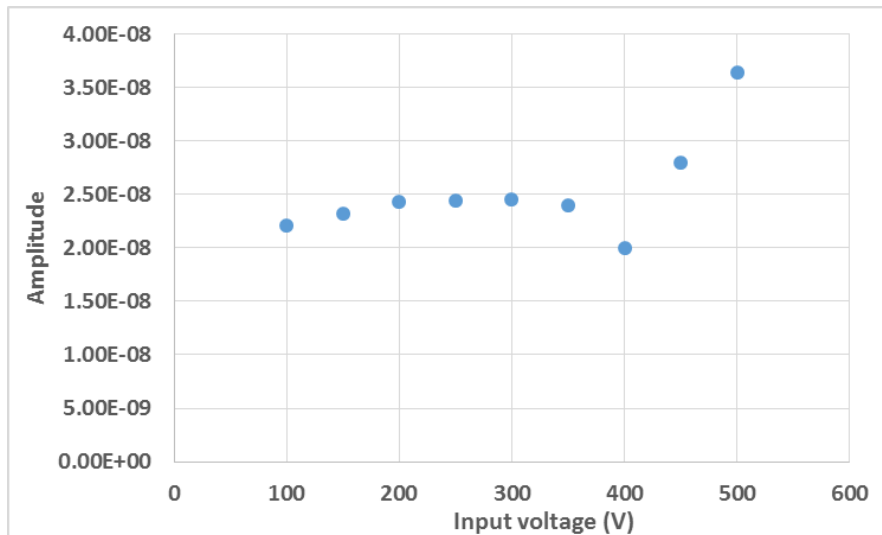
Figure 4.8 PZTs attached on plate and pipe specimens.

#### **4.2.2 Voltage calibration for nonlinearity**

A voltage calibration in the experiment test of the plate was carried out. Before introducing the fatigue crack in the plate, the excitation signal was calibrated to obtain a proper input voltage where the nonlinearities from other sources, e.g. hardware and environmental conditions, should be minimal. The excitation was a 15.5-cycles tone burst signal at a central frequency of 763 kHz with a voltage from 50  $V_{p-p}$  to 500  $V_{p-p}$  with an increment of 50  $V_{p-p}$ . Transmitted signals were received and processed by a band pass filter in MATLAB around the double frequency of 1526 kHz. The amplitudes of the first arrived wave packet and that at double frequency were compared in terms of input voltage, illustrated in Figure 4.9. As can be seen, the amplitude increases with the input voltage for the received signal while the nonlinearities at double frequency shows an evident drop when the input voltage is 400  $V_{p-p}$ . Thus, 400  $V_{p-p}$  was selected as input voltage which has high amplitude in the input signal but low nonlinearities at the double frequency.



(a)



(b)

Figure 4.9 Wave amplitude in terms of input voltage for (a) received signal and (b) signal at double frequency.

For the experiment test in pipe structures, a different advanced signal generation and collection system was used with minimal nonlinearity from the system. A benchmark signal at fixed location and same voltage was collected at different days. The signal was processed with bandpass filter at fundamental and double frequencies separately. As in

the Figure 4.10, there is no obvious difference between these signals at both fundamental and double frequencies. Therefore, the signal was stable sufficiently and would not be easily affected by the environment change. As above, a relatively large input voltage 400  $V_{p-p}$  was selected to provide sufficient power for the CAN generation in the experiment tests of pipes.

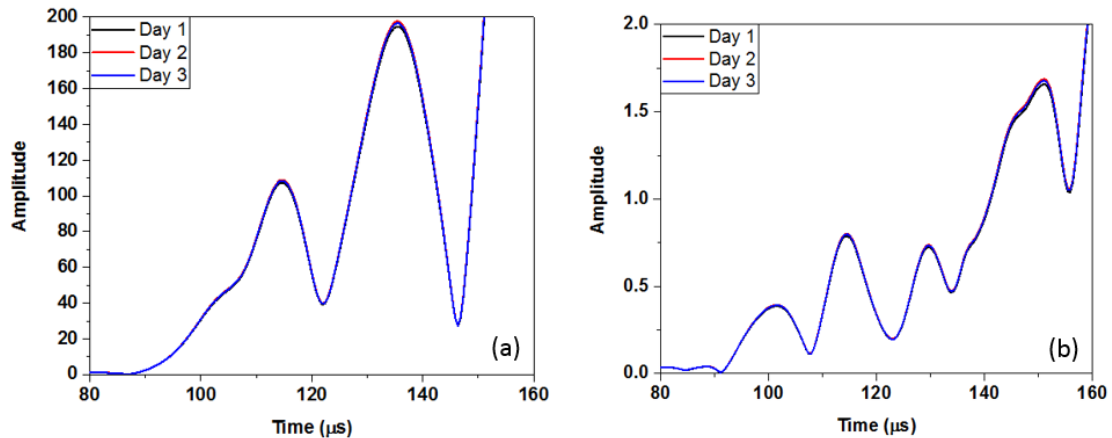


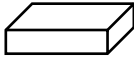
Figure 4.10 Transmitted signals from an intact pipe at (a) fundamental frequency and (b) double frequency.

#### **4.2.3 PZT type in experiment test of pipe structures**

The curvature of the pipe surface, not only complicates the wave mode propagation in pipes, but also makes it a tough operation when attaching the transducer to the surface of the pipe. Different shapes of transducers affect the contact condition with the pipe and also determine the efficiency of wave excitation. In the pipe experiment test, three different shapes of PZT transducers were applied to excite a 6-cycle tone burst at 300 kHz. Signals from different shapes of actuators and sensors were evaluated to figure out the optimised PZTs for the wave excitation in pipe specimen.

Dimensions of three different shapes of transducers are summarised in Table 4.1.

Table 4.1 Dimensions of different shapes of transducers in experiment test.

Circular PZT	Square PZT	Rectangular PZT
		
Diameter: 5 mm Thickness: 1 mm	Length/Width: 5 mm Thickness: 1 mm	Length: 10 mm Width: 5 mm Thickness: 1 mm

To determine the actuator used in pipe experiment test, signals from the same sensor but different actuators at the same location were collected. The distance between actuator and sensor is 400 mm and the theoretical group velocity of first arrived longitudinal wave is 4950 m/s.

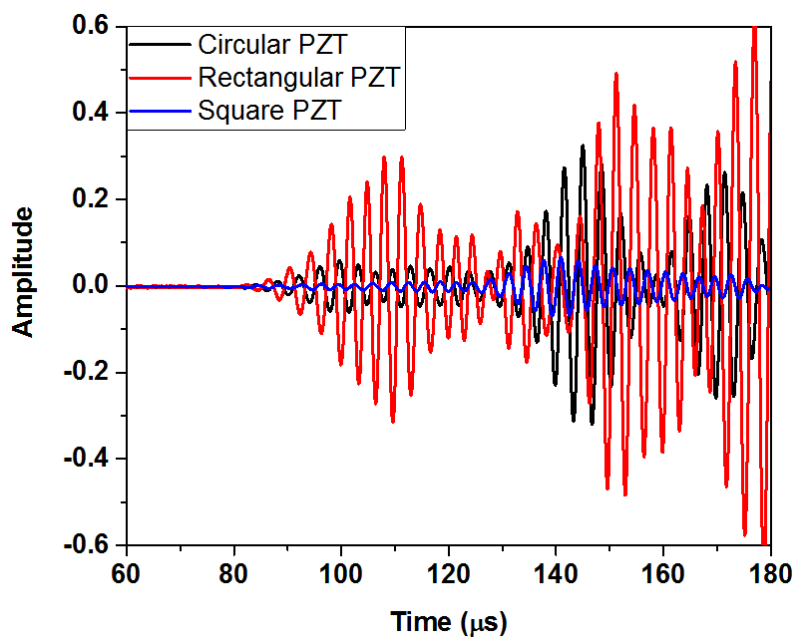


Figure 4.11 Transmitted signal from different types of PZTs.

As shown in Figure 0.17 for direct transmitted signals, all three PZTs recorded signals arrived at about 82  $\mu\text{s}$ , which is consistent with the theoretical velocity. Due to one actuator excitation, multiple flexural wave modes following the first wave were excited. However, for the signal before 130  $\mu\text{s}$  which is the segment of interests in this study, the

rectangular PZT generates the highest amplitude signals and more wave modes than the other two transducers.

To find out the proper sensor applied in the pipe experiment test, signals from the same actuator but different sensors at the same location were collected. Since for the sensors nonlinearity at double frequency is the most concerned, signals after bandpass filter at double frequency are plotted to assess the ability of measuring nonlinearity from the system. The distance between actuator and sensor and the theoretical group velocity of the first arrived longitudinal wave are the same as before. The signals at double after processing is shown in Figure 4.12

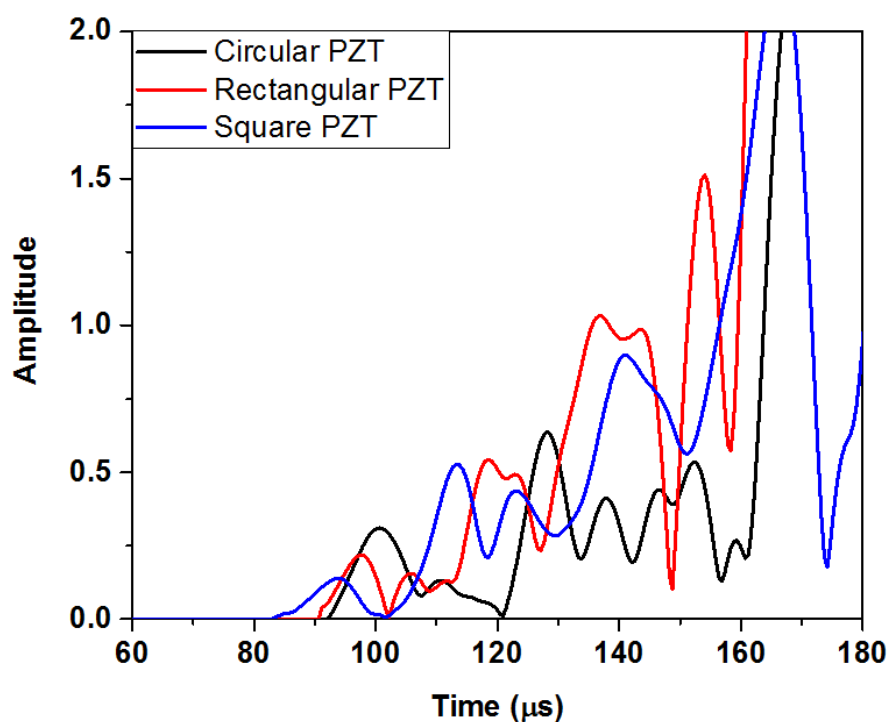


Figure 4.12 Signals after band pass filter at double frequency for different types of PZTs.

From the figure, it can be seen that only the square PZT receives the signal with similar arrival time at fundamental frequency, which is reasonable for an intact pipe with only material nonlinearity in it. Also, since the pipe is intact, it is more acceptable if the

nonlinearity of first arrival wave packet is relatively small, avoiding covering the nonlinearity from CAN after fatigue test. The length of the square and diameter of circular PZT is 5 mm, which is close to the half wavelength (12 mm) of the second harmonic mode. From a previous study [152], the received signal has the maximum amplitude when the wavelength is half of the PZT size. However, the circular PZT has worse contact with the pipe surface than the square one and therefore exhibit higher nonlinearity in the receiving. Thus, the square PZT is chosen as the sensor and the rectangular PZT is selected as actuator in the later experiment.

#### ***4.2.4 Low pass filter for experiment system nonlinearity***

The nonlinearity from signal generating and collecting system highly affects the observation of the nonlinearity from the damage in the structure, especially the nonlinearity from the amplifier. In this study, Ritec low-pass filters were used with cut-off frequency at 350 kHz and 1 MHz according to different fundamental frequency excitation to filter the higher harmonics from the sources. The effect of applying filter in both intact plate and pipe structures are illustrated in this section.

Transmitted signals from a  $360 \times 80 \times 5$  mm thick steel plate with one actuator and one sensor attached on it were received. Two different cases carried on the same plate were considered including with and without the low-pass filter after the amplifier. The excitation signal is a 15.5 cycle Hanning-windowed tone burst at a central frequency of 763 kHz and the filter has cut-off frequency 1 MHz. A similar procedure was also performed on a steel pipe with outer diameter 101.6 mm and thickness 5.74 mm. A 15.5 cycle Hanning-windowed tone burst at a central frequency of 711 kHz and the filter is the same with that in plate. The received signals from two cases in both plate and pipe

-Quantitative evaluation of fatigue crack using nonlinear guided waves in pipelines-

specimens were processed with a fast Fourier transform (FFT) and the results are in

Figure 4.13 and Figure 4.14.

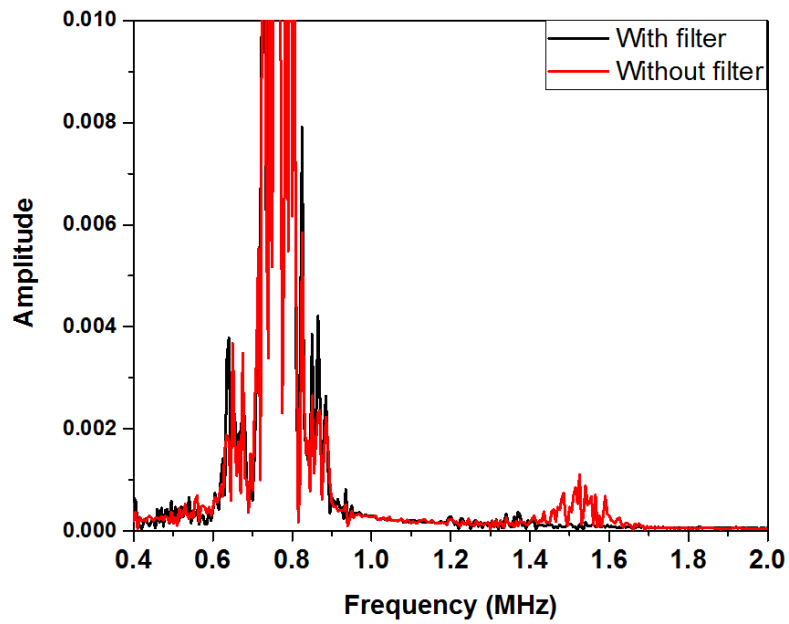


Figure 4.13 Frequency spectrum of received signals from a plate.

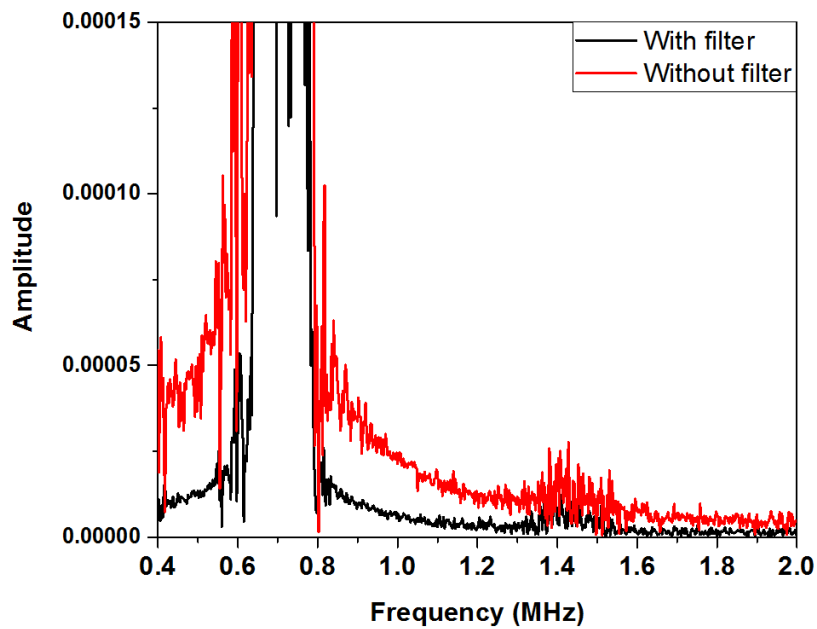


Figure 4.14 Frequency spectrum of received signals from a pipe.

It can be observed that signals that passed through the filter generate lower second harmonic than the case without filter, where the drop of second harmonic from source is more obvious for the plate structure. Although some nonlinearities still exist after using the filter, which were mainly induced by the material itself and the nonlinearities from the bonding of sensors, the low-pass filter successfully minimises the nonlinearity from the system and therefore it is adopted in following experiment test in this study.

#### **4.2.5 Effect of static loading during fatigue**

When introducing the fatigue crack in the specimen for the CAN evaluation through fatigue test, it is noticed that the static load from the fatigue machine during signal collection will influence the nonlinearity from the microcrack. Simulation and experiment studies were carried out to compare with each other and find out the influence of load during signal collection in the plate fatigue test.

A 3D model with solid elements (C3D8R) was developed using FEM software Abaqus Dynamic/Explicit<sup>®</sup> to study the nonlinearity caused by a fatigue crack in a 360×80×5 mm steel plate. The actuator was simulated with the same dimension as the one used in the experiments. Two sensors labelled TR and RE were used to receive the transmitted and reflected signals respectively. In the middle of the plate, a hole with two notches was simulated for the initiation of the fatigue crack, following the same geometry in the experiment test. Seam crack definition was used on each surface of the crack at the tips of notch and the same simulation method as Section 4.1.1.2 was used to achieve the modelling of CAN. The crack was changed from 1 mm to 7 mm on each side of the hole with an increment of 0.5 mm for the analysis of relation between seam crack length and the nonlinear parameter.

Relative nonlinear parameter  $\beta' = \frac{A_2}{A_1^2}$  [115, 116] was then calculated for all cases with different crack lengths. After calculation, the relationship between  $\beta'$  and the crack length to wavelength ratio is plotted in Figure 4.16, where the wavelength of the fundamental wave mode is 7.52 mm. The results show that nonlinear parameter increases monotonously with the crack length for both reflection and transmission signals, which is consistent with the results in [153]. The nonlinear relation is mainly because of the influence of diffraction.

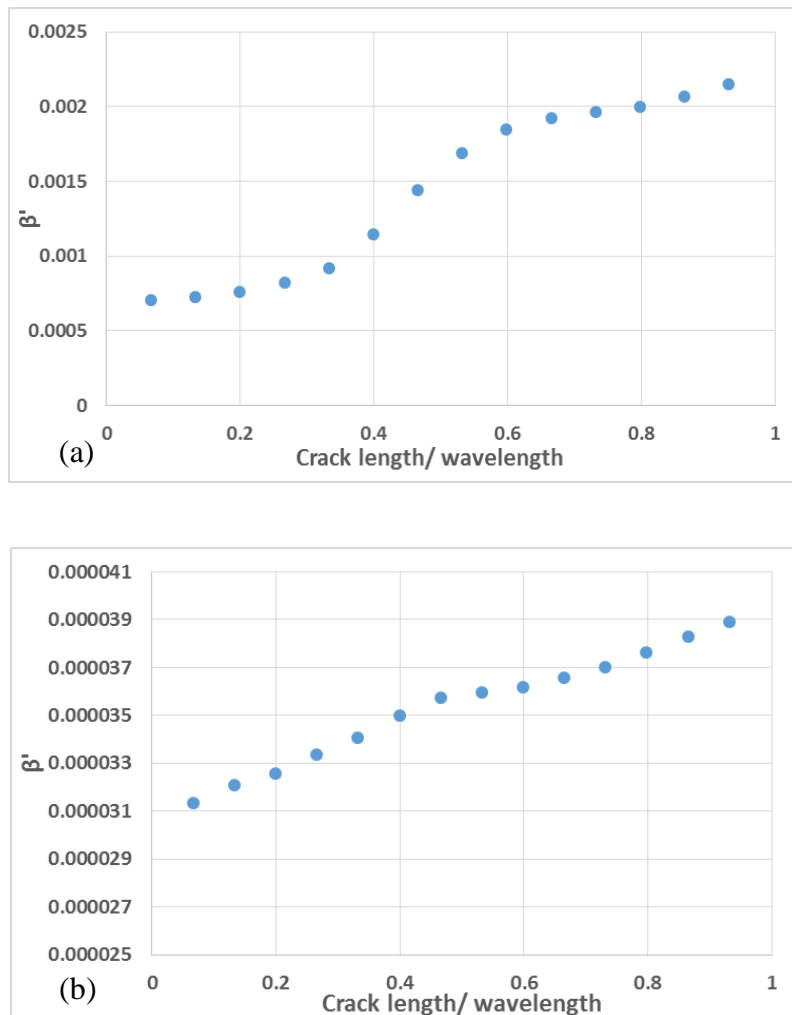


Figure 4.15 Relative nonlinear parameter  $\beta'$  in terms of crack length/ wavelength (a) transmitted signal; (b) reflected signal.

In experiment test, the fatigue crack in the steel plate was generated using a testing machine. Cyclic tensile loads ranging from 6 kN to 60 kN were applied, with a frequency of 20 Hz and a stress ratio of 0.1. To monitor the crack growth, the test was stopped each 10,000 cycles for signal collection and a digital microscope was used to observe the crack. Relative nonlinear parameter  $A_2/A_1^2$  was also calculated for all the received signals in experiment. The relation between it and the crack length was plotted in Figure 4.16.

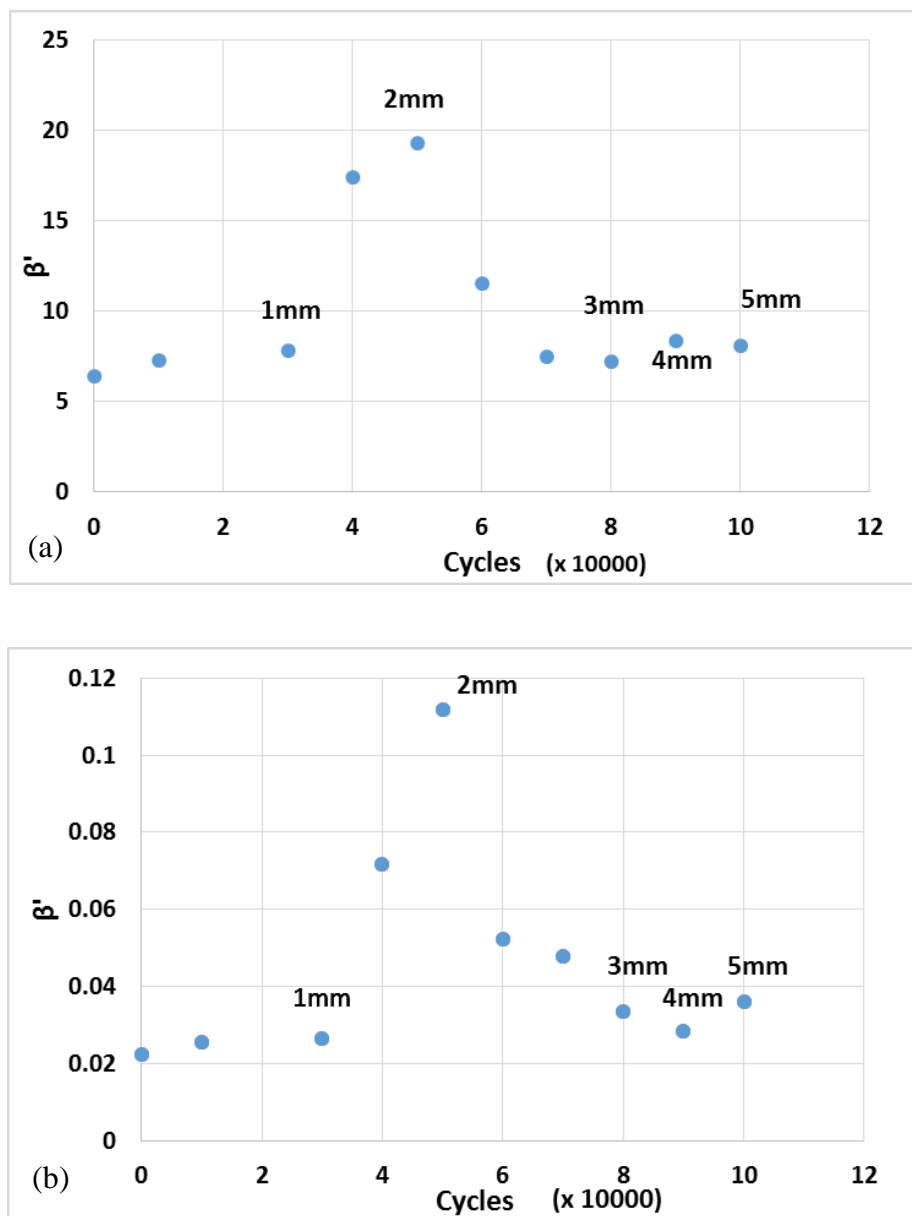


Figure 4.16 Relative nonlinear parameter in terms of fatigue cycles (a) transmitted signals and (b) reflected signals.

It is noticed that the nonlinearities increase with crack length till about 2 mm and then start to drop, which is not consistent with the simulation results. During the fatigue test, the cyclic load was stopped during signal collection but there was a holding tensile load from the machine at two ends of the plate. The holding load was 25 kN which could open the fatigue crack and diminish the nonlinearities when collecting the signals during the fatigue test. To verify this assumption, a simulation work was carried out for the same plate model with a tensile load at 25 kN at two ends of the plate. Abaqus Static/General was used to generate the deformed model under tensile load and then the deformed model was imported into Abaqus and analysed with dynamic/explicit procedure where Lamb wave propagation was simulated in the plate. The transmitted signals in the frequency domain with a 3 mm fatigue crack are shown in Figure 4.17. Compared with the benchmark and the unloaded case, it is obvious that the nonlinearities for the loaded case almost disappeared to the level as in the benchmark. In addition, the signals with a 5 mm fatigue crack was collected after the plate was unloaded at the end of the fatigue test. Following the same procedure for the calculation of relative nonlinear parameter, the value was about four times higher than that for the case of 2 mm fatigue crack. It is therefore approved that the tensile load during the tests significantly affected the acquisition of wave nonlinearities.

Therefore, the holding load in all the fatigue test was removed in this study during signal collection.

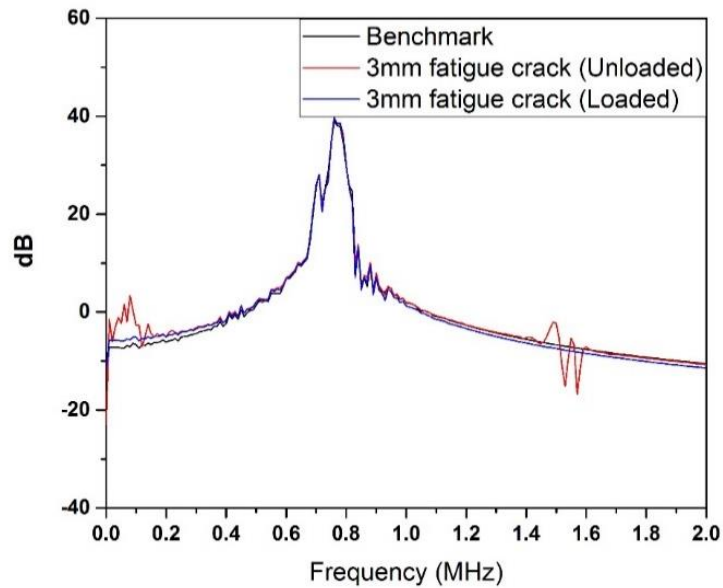


Figure 4.17 Transmitted signals of plates with 3mm fatigue crack in frequency domain.

### 4.3 Selection of appropriate nonlinear method

The past studies have done a lot of experiments and simulations to investigate the second harmonic generation and mixed frequency response method in steel or composite plates. In this and next section, these two methods were conducted in pipe structures to figure out the feasibility of these methods on detection, evaluation and location of close crack in a pipe. The more proper method would then be selected for further studies in pipe structures.

#### 4.3.1 Mixed frequency response

The scheme of this method is to use one actuator to act as high frequency input and another actuator or shaker to act as low frequency input. When they come to the breathing crack, the high frequency input will be modulated by the low frequency signal and in the frequency spectrum of the received signal, small sidebands will appear beside the main frequency whereas there is only main frequency in the frequency domain when the

-Quantitative evaluation of fatigue crack using nonlinear guided waves in pipelines-  
specimen is undamaged. In this research, different types of signals are studied and the effect of the location of the actuator or shaker on modulation result is also investigated.

#### 4.3.1.1 Vibro-acoustic modulation

Before the simulation model is set up, the frequency input is determined based on the criterion mentioned in Section 3.3.2.2 Dispersion curves are drawn by DISPERS software for a steel pipe with 194 mm outer diameter and 10 mm wall thickness as shown in Figure 4.18.

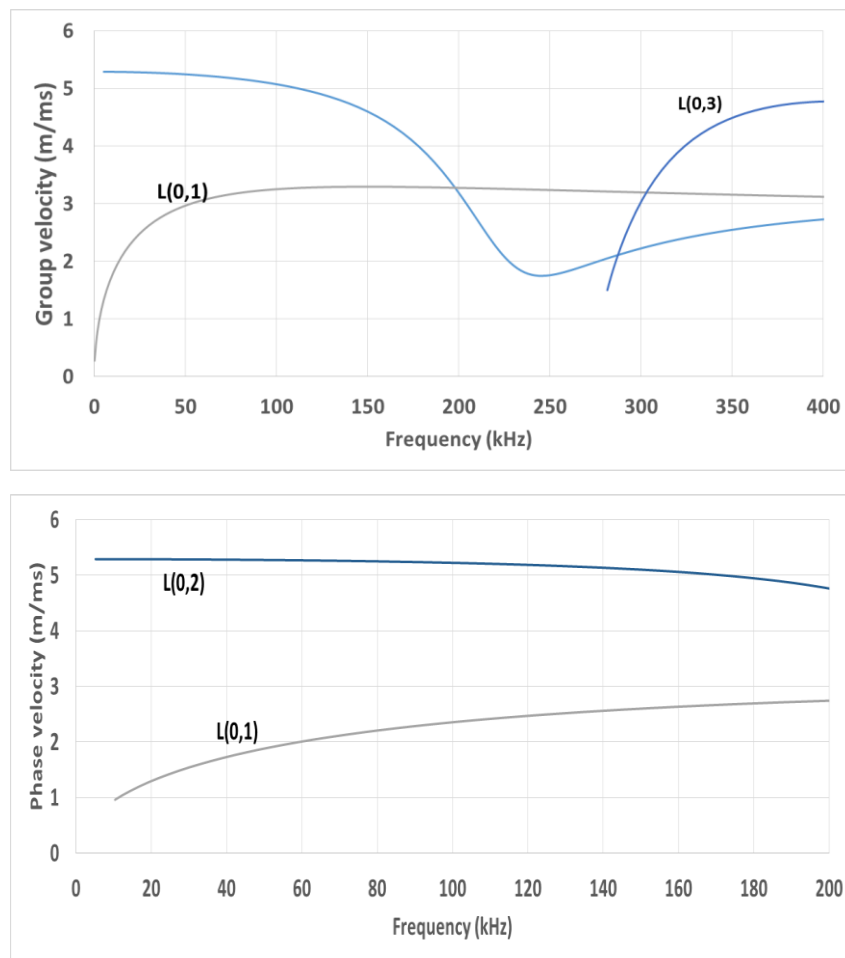


Figure 4.18 Dispersion curve for 194 mm outer diameter, 10 mm wall thickness steel pipe.

The wave mode is selected as L(0, 2) since it is non-dispersive over a wide frequency range. And according to the criterion to generate sidebands, 100 kHz is selected as the

-Quantitative evaluation of fatigue crack using nonlinear guided waves in pipelines-

probing wave frequency, so that the modulation phase velocity is identical to that of the probing wave frequency.

A cylinder with outer diameter 194 mm, wall thickness 10 mm and 2 m length is simulated with Abaqus/Explicit 6.14 and the material properties are in Table 4.2.

Table 4.2 Material properties for steel pipe OD 194 mm.

<b>Material properties</b>	<b>Density (kg/m<sup>3</sup>)</b>	<b>Young's Modulus (GPa)</b>	<b>Poisson's Ratio</b>
	7800	206	0.28

The maximal element size should be small enough to allow the smallest wavelength of the wave can exist in the computation domain. Also, the time step should be short enough to meet the convergence criterion. The maximum element size and minimum time step are calculated by equations [154]

$$L_{max} \leq \frac{\lambda_{min}}{8} = \frac{50.77}{8} = 6.34 \text{ mm}, \quad (4.1)$$

$$\Delta t \leq \frac{L_{max}}{c_g} = \frac{0.002}{5.077} = 3.925 \times 10^{-7} \text{ s}, \quad (4.2)$$

where  $\lambda_{min}$  is the shortest wavelength of any waves which may travel in the structure, and  $L_{max}$  is the largest element size in the model;  $c_g$  is the fastest group velocity of the wave. Finally, the maximum element size is taken as 2 mm and the minimum time step is  $1 \times 10^{-7}$  s.

One actuator and one shaker are arranged at one end of the pipe with distance of 0.3 m. Another receiver is allocated at the other end of the pipe. The distance between actuator and receiver is 1 m. The locations of them are shown in Figure 4.19.

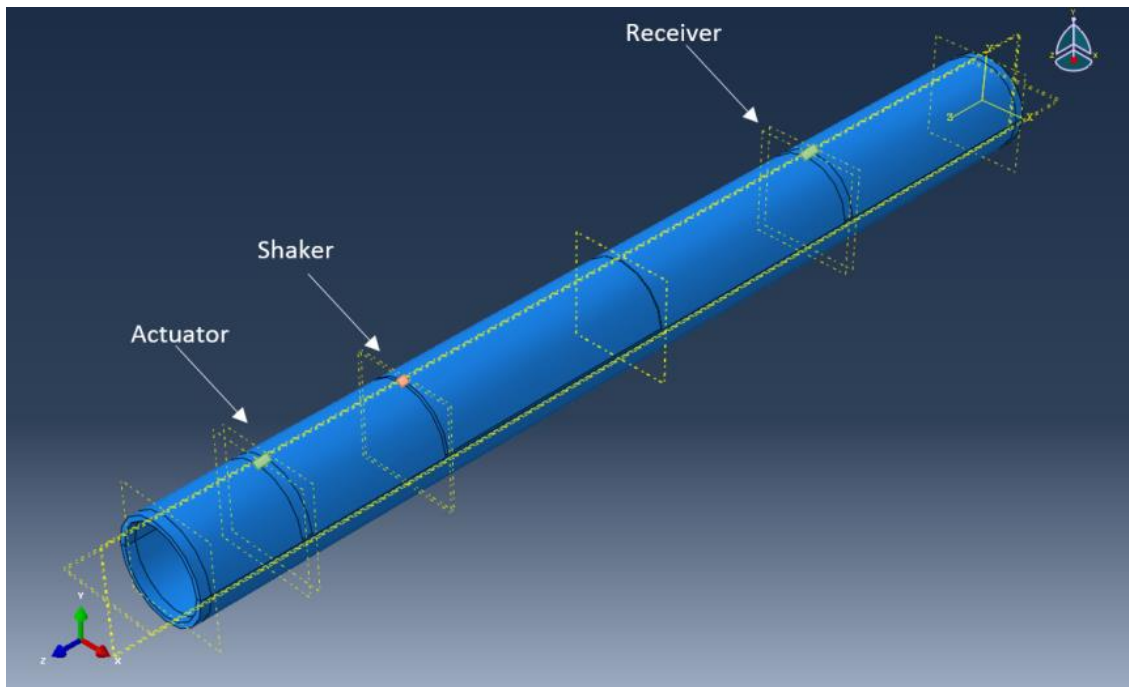


Figure 4.19 Location of actuator, shaker and sensor for a pipe model with OD 194 mm.

The actuator is simulated with the same dimension of the real piezoelectric lead zirconate titanate (PZT) used in lab testing. The sources is 100 kHz, 10 cycles Hanning-windowed tone burst signal, generated as point load applied at the short edge of the actuator along the axial direction of the pipe to simulate the longitudinal wave. For the vibration, a continuous pure sine signal is applied downward with the first order natural frequency of the pipe, which is 272 Hz obtained from modal analysis. The pipe is fixed at both ends. The applied load are shown in Figure 4.20.

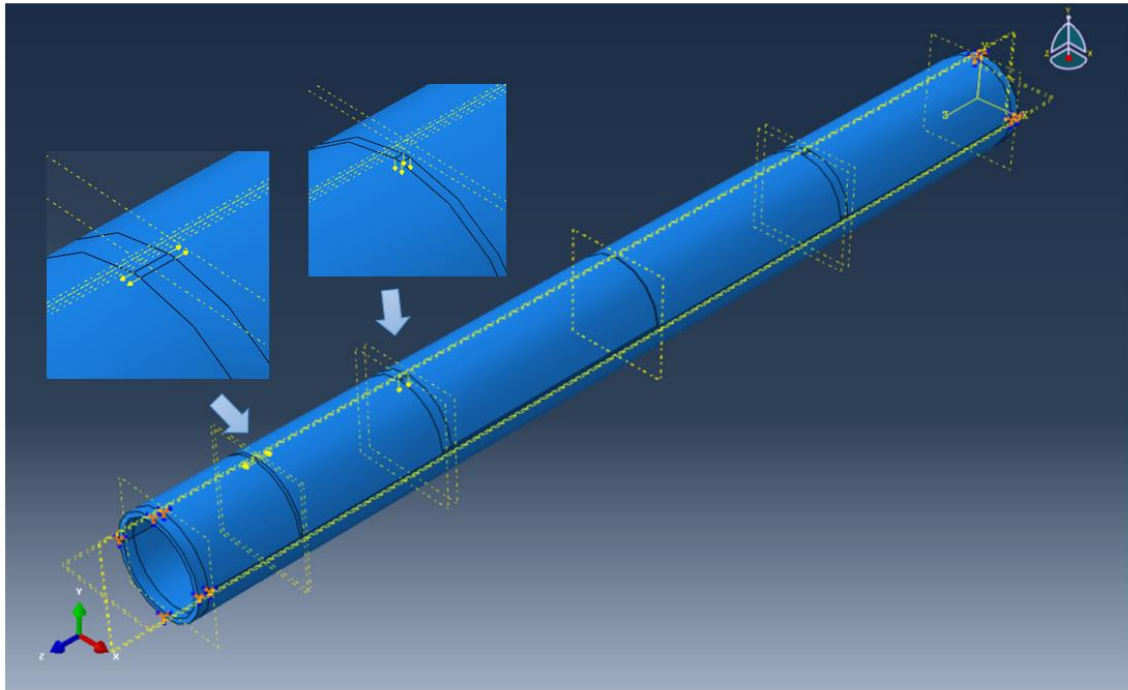


Figure 4.20 Load applied on model.

To model a close crack in the pipe, the simulation method is used as in Section 4.1.1.2, as illustrated in Figure 4.21, to enable the breathing behaviour when waves interact with the crack. The crack is through thickness and 5mm length in circumferential direction, located at the middle of the pipe. Figure 4.22 shows the process of ultrasonic guided waves interacting with the breathing crack. It can be seen that the stress induced by wave transmitted through the crack when it is closed while it cannot pass through when the crack is open.

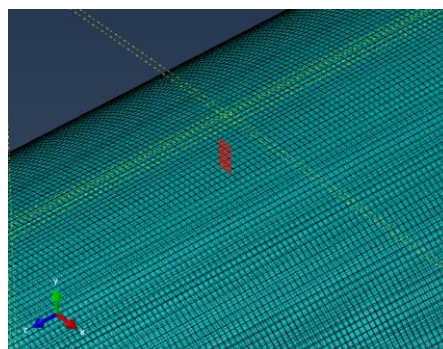


Figure 4.21 A seam crack created in a meshed pipe in simulation (highlighted regions are the two crack surfaces defined as seam crack and contact pair properties).

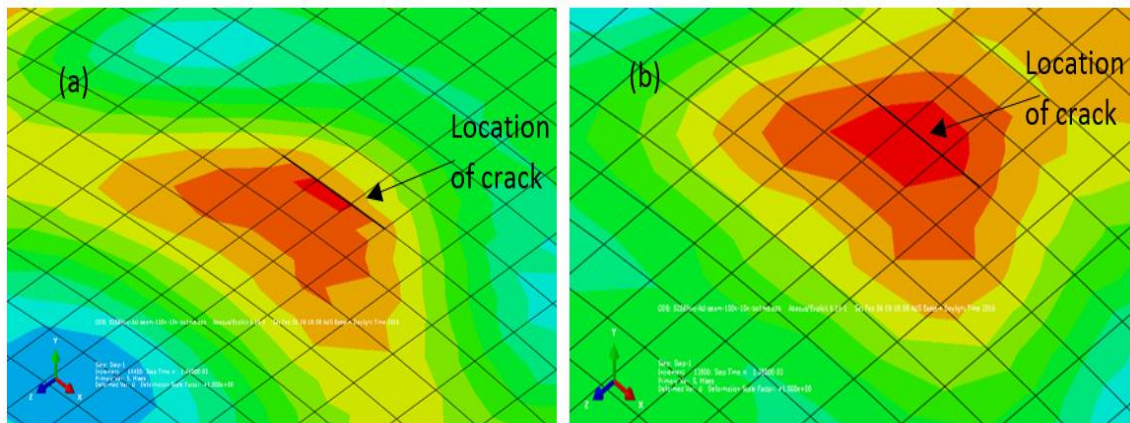


Figure 4.22 Snapshots of ultrasonic waves passing through a seam crack with CAN. (a) Transmitted wave cannot pass when the crack is open and (b) stress is transmitting through the closed crack.

One of the received signals is shown in Figure 4.23 presented by the stress in axial direction in terms of time compared with the benchmark in which no seam crack is induced. There is no big difference between the current and benchmark signal in time domain.

After a fast Fourier transform (FFT), it can be seen that the result is not as expected (Figure 4.24). There is no obvious sidebands beside the main frequency but only second harmonic for the damaged pipe compared with the benchmark. It is mainly because the bandwidth of main frequency is large and the modulation frequency is close to the main frequency.

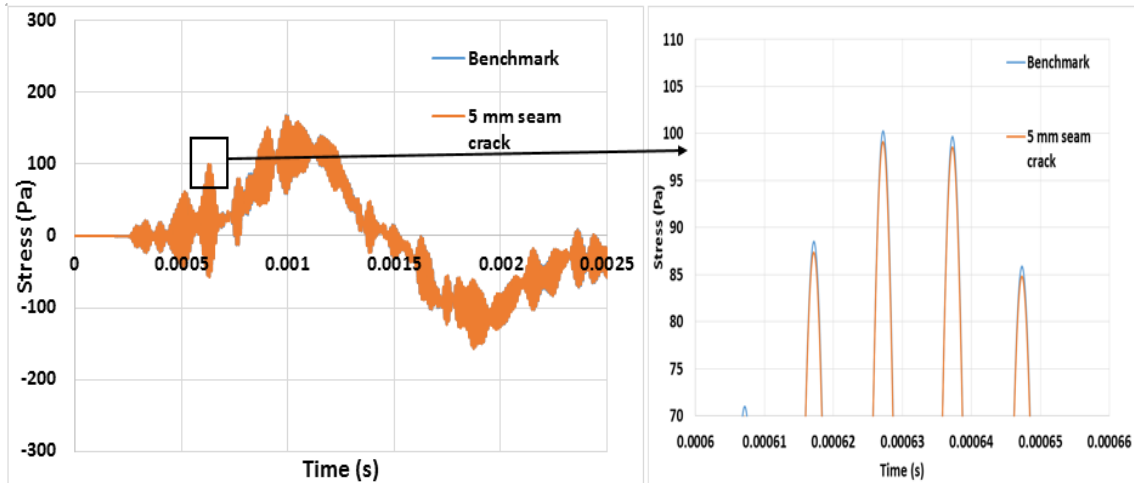


Figure 4.23 Received signal in time domain from the simulation of a pipe with OD194 mm.

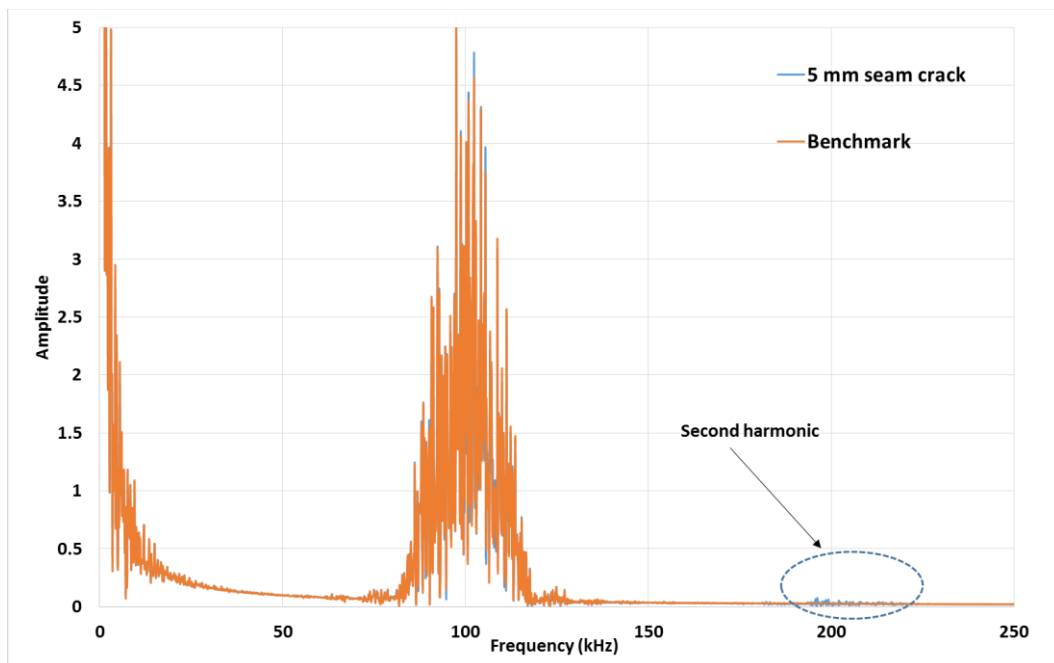


Figure 4.24 Received signal in frequency domain.

However, it is found that if the location of vibration is changed, its influence on the second harmonic will change as shown in Figure 4.25 when the actuator is close to crack, shaker is close to crack, and both of the actuator and shaker are at the same circumference of the pipe, respectively. When the actuator and shaker are at the same circle, since the vibration is closer to the actuator compared with another two cases, the wave is disturbed and

-Quantitative evaluation of fatigue crack using nonlinear guided waves in pipelines-

bandwidth in frequency increases. Therefore, to generate concentrate second harmonic, the shaker should not be put too close to the actuator. Also, addition of vibration can increase the second harmonic in the frequency domain compared with the case when only ultrasonic wave was excited, as indicated in Figure 4.26. This conclusion may be useful when applying second harmonic method since the amplitude of the second harmonic is quite small compared with the signal at fundamental frequency.

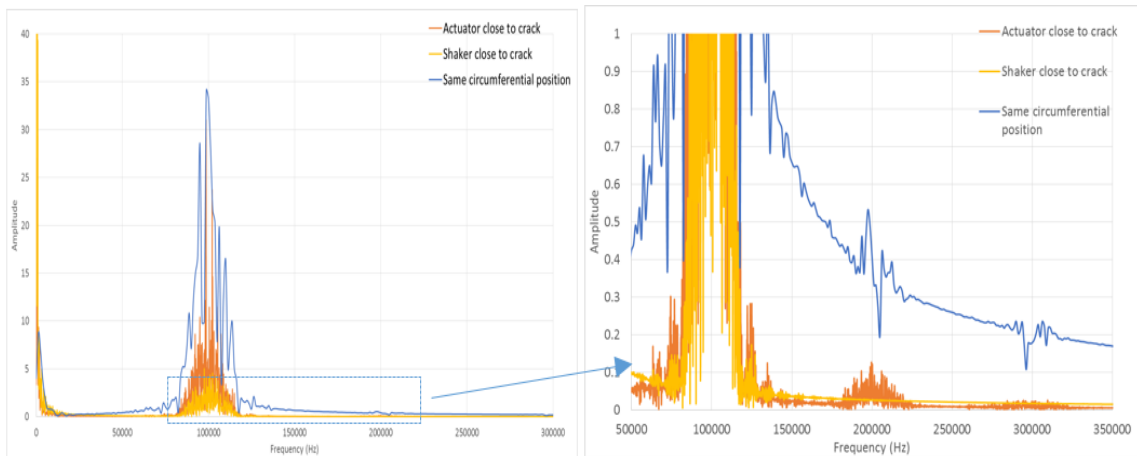


Figure 4.25 Frequency domain results for different locations of vibration and actuator.

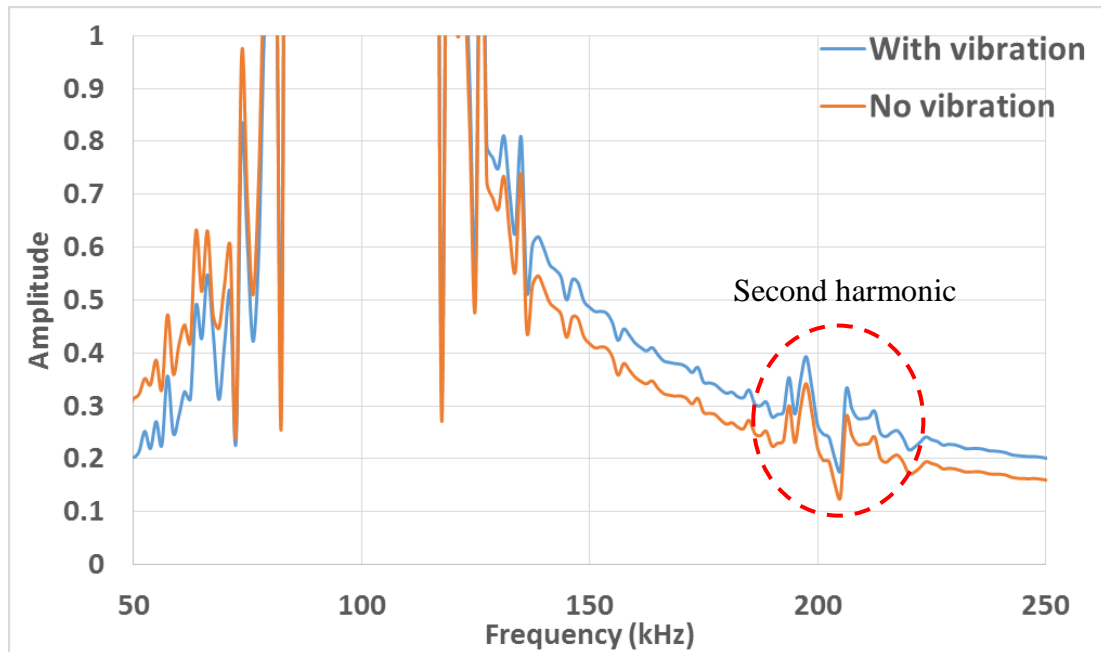


Figure 4.26 Second harmonic enhanced by vibration.

#### 4.3.1.2 Acoustic and ultrasonic modulation

In this case, vibration was changed into a low frequency wave which has the same excited direction with the high frequency wave.

The frequency input is determined based on the criterion mentioned in Section 3.3.2.2 and selected from dispersion curves in Figure 4.18. The high frequency input is still 100 kHz, while the low frequency input is 10 kHz. Both of them are L(0, 2) wave mode.

Same simulation model with in Section 4.3.1.1 is used. The locations of two actuators are shown in Figure 4.27. They are allocated at the same location since two input waves have similar group velocity. Different duration of the input signal is applied to investigate the effect on modulations, including 1 ms, 0.5 ms, 0.2 ms and 0.1 ms. All the input signals are tone burst signals and the input signal for 1 ms as an example is shown in Figure 4.28.

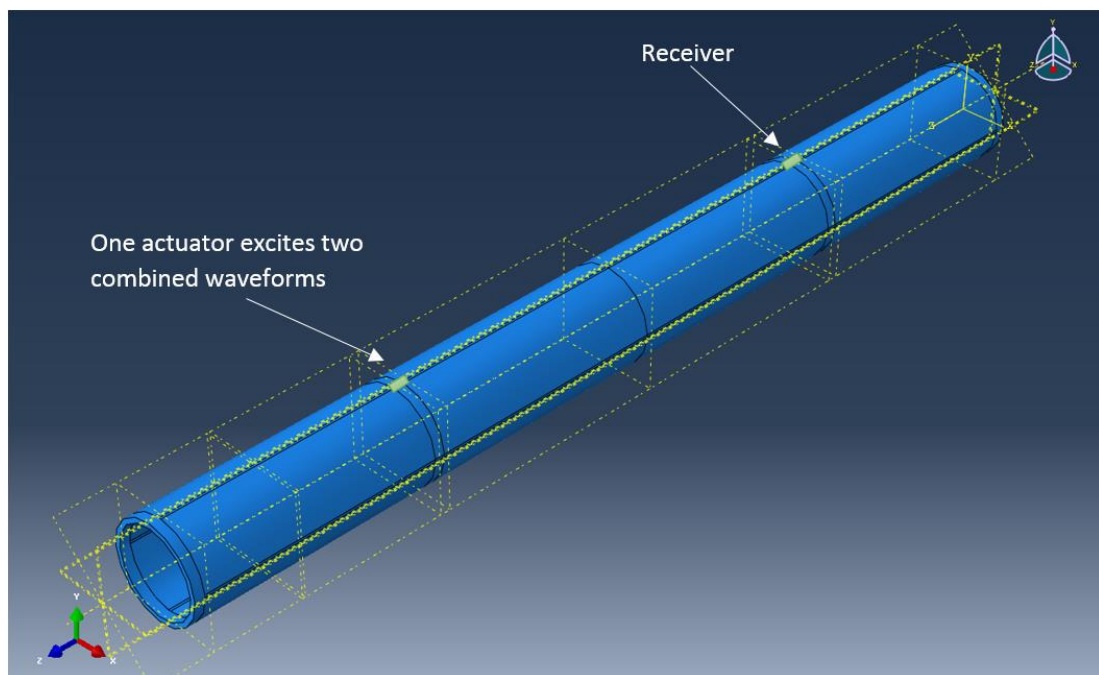


Figure 4.27 Location of actuators and receiver.

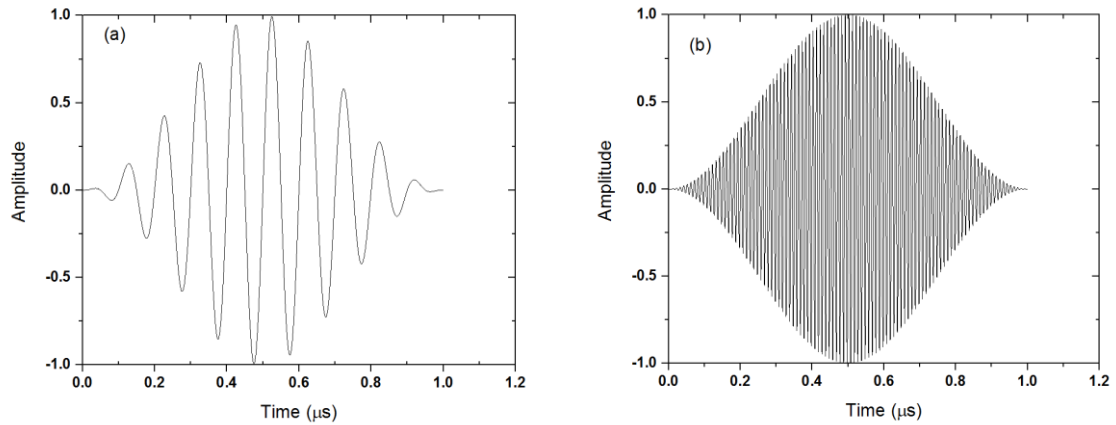


Figure 4.28 Input signal: (a) 1 ms (10 cycles) 10 kHz tone burst signal (b) 1 ms (100 cycles) 100 kHz tone burst signal.

For the received signal in the time domain, there is no big difference between the damaged specimen and the benchmark whatever the duration of input signals, as shown in Figure 4.29 for the case of 1 ms cycles. However, in the frequency domain, when the input signal is shorter 0.2 ms, the sidebands will disappear beside the main frequency component (Figure 4.30). This may be because the longer interaction time between the input signals, the higher the energy of modulation. And also, the longer duration of the input signal, the narrower bandwidth of it.

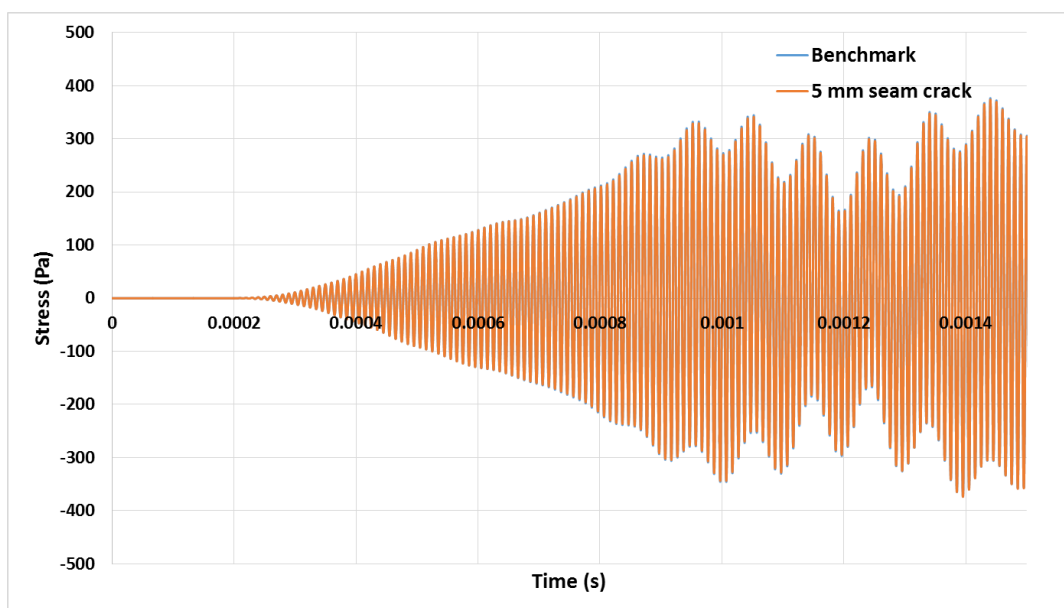
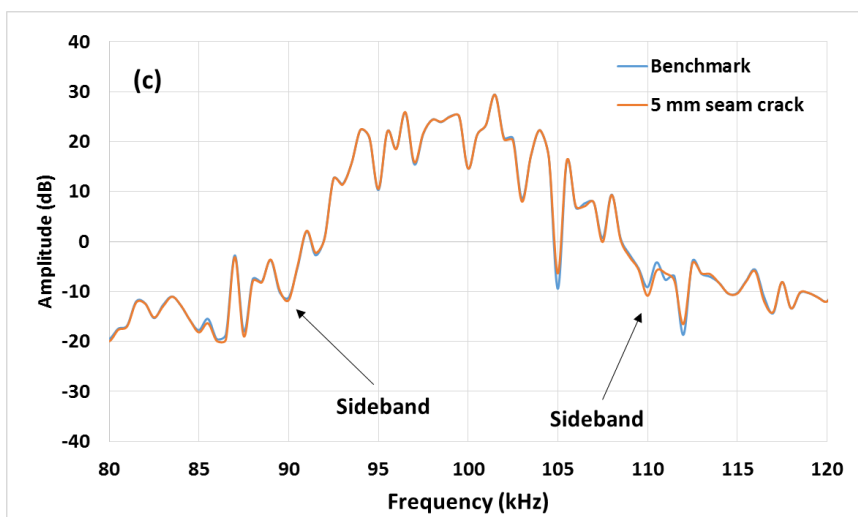
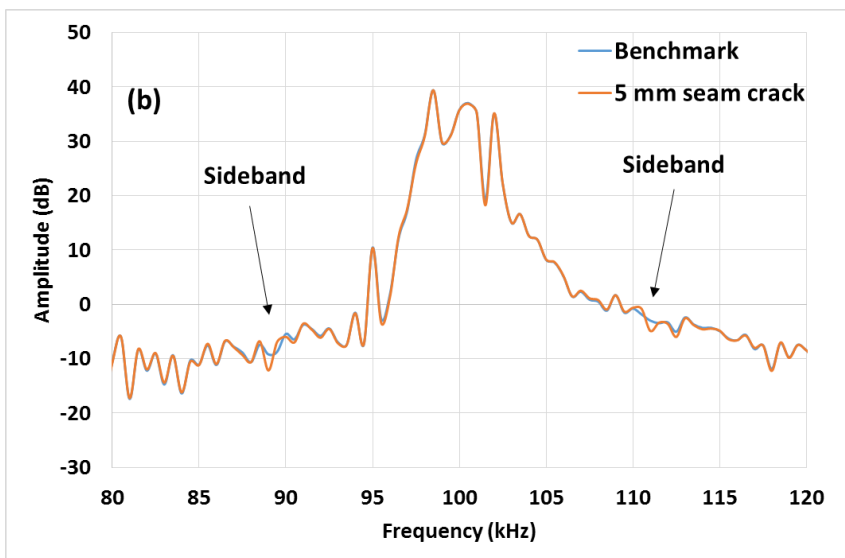
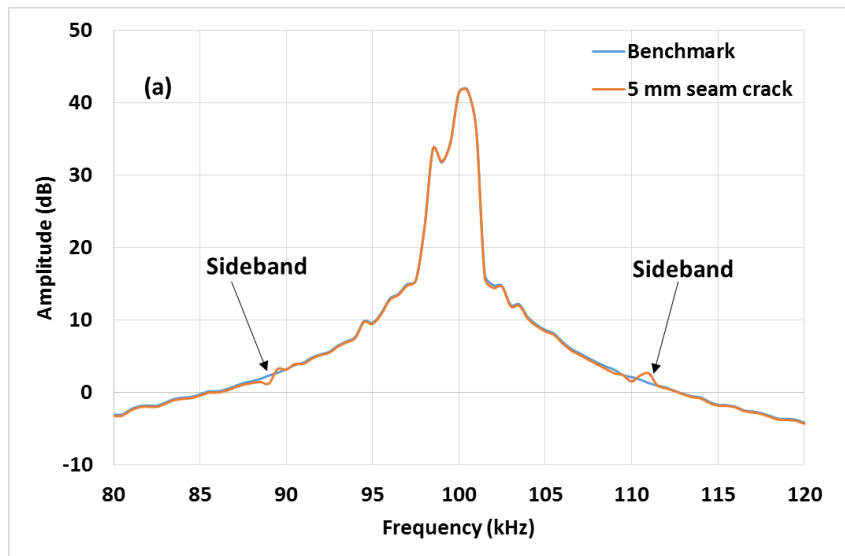


Figure 4.29 Received signal in time domain for the 1 ms input signal case.



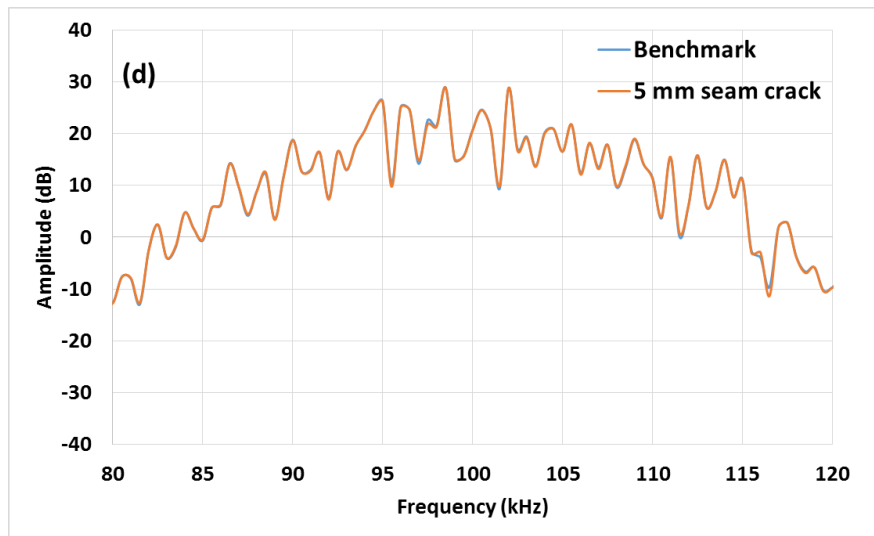


Figure 4.30 Received signal in frequency domain (a) 1 ms input (b) 0.5 ms input (c) 0.2 ms input and (d) 0.1 ms input.

Thus, to use mix frequency response method, the input signal should be long and stable enough to generate the sidebands, which however is not suitable to extract the time information and to locate the damage position.

### **4.3.2 Higher harmonic generation**

Another method to measure the nonlinearity is known as the second harmonic generation. When there is nonlinearity existing in the specimen, apart from the input fundamental frequency, a double frequency component will appear in frequency spectrum. As a preliminary research, a simulation model is set up to verify this method in a steel pipe.

#### **4.3.2.1 Wave mode selection**

Since the amplitude of second harmonics is usually much smaller than the fundamental ones, to generate the strong second harmonic, proper wave mode needs to be determined based on the criterion in Section 3.3.1 before the numerical modelling. The wave mode is selected from the dispersion curve, as in Figure 4.31 generated by software DISPERSE for a steel pipe with diameter 101.6 mm and 5.74 mm wall thickness and with the material properties listed in Table 4.3, which would be the same as the pipe to be modelled.

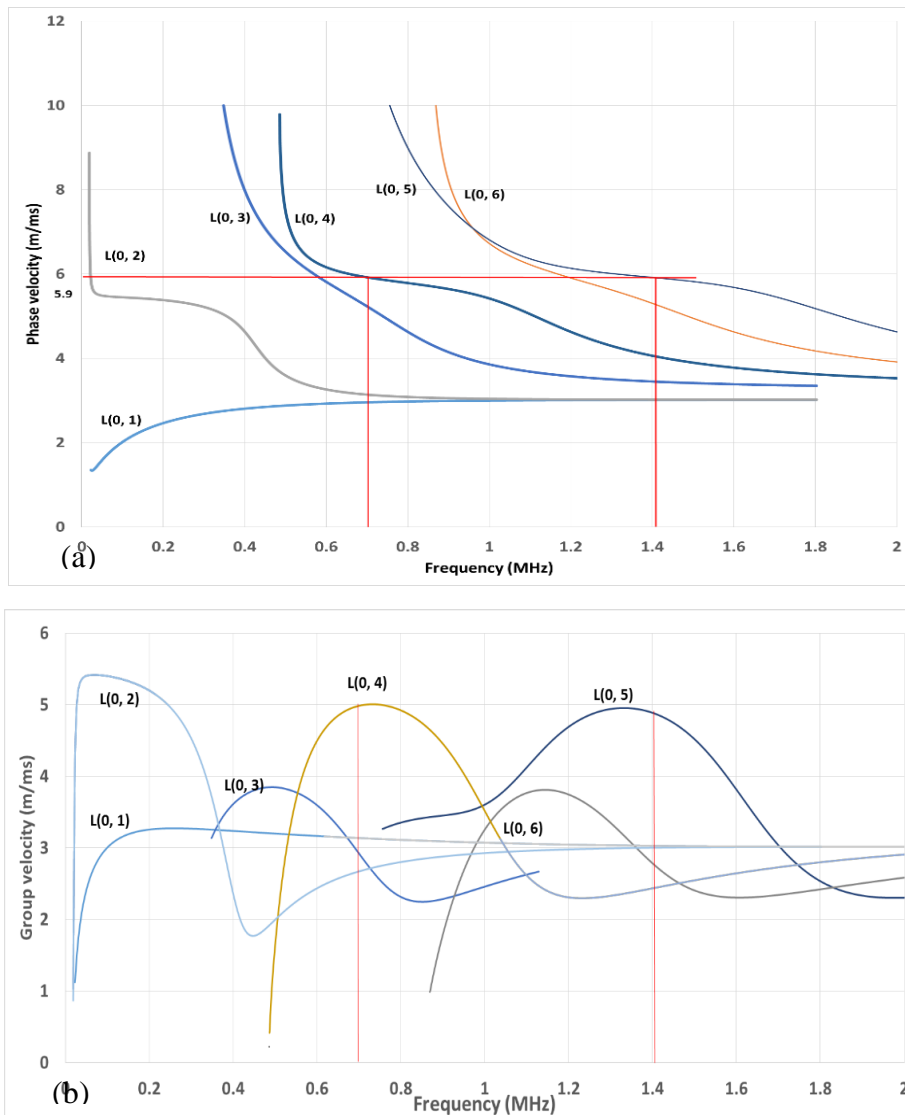


Figure 4.31 Dispersion curve of 101 mm outer diameter, 5.74 mm wall thickness steel pipe for (a) phase velocity and (b) group velocity.

Table 4.3 Material properties for steel pipe OD 101 mm.

Material properties	Density (kg/m <sup>3</sup> )	Young's Modulus (GPa)	Poisson's Ratio
	7850	210	0.28

L(0, 4) and L(0, 5) modes are selected as the fundamental and secondary wave mode, and 0.71 MHz is the fundamental frequency which has the same phase velocity and group velocity with the wave at 1.42 MHz. Also, since L(0, 4) mode is a longitudinal mode, it

-Quantitative evaluation of fatigue crack using nonlinear guided waves in pipelines-

is easy to excite in both simulation and experiment and it has great axial displacement at the outer surface of the specimen as shown in the mode shape (Figure 4.32). It is noticed that L(0, 4) travels fastest at the fundamental frequency, which makes it easy to be separated from the other modes at this frequency.

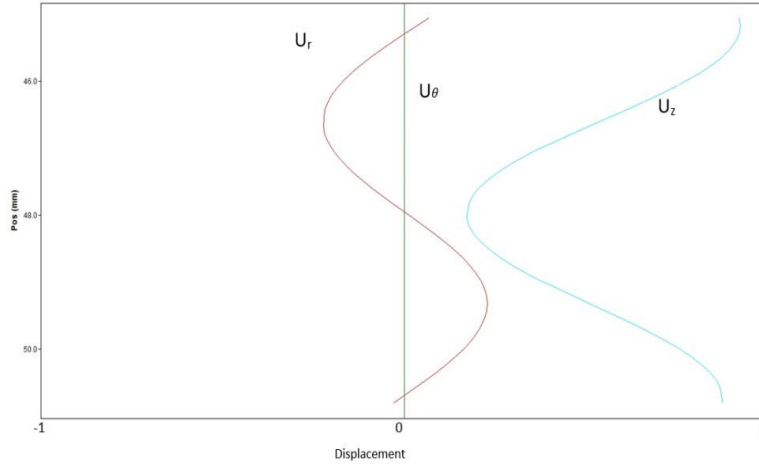


Figure 4.32 Mode shape for L(0, 4) at 0.71 MHz along the thickness direction.

#### 4.3.2.2 Simulation model

A cylinder with outer diameter 101.6 mm, wall thickness 5.74 mm and length 1 m is simulated with Abaqus/Explicit 6.14 and the material properties are in Table 4.3. The maximum element size and minimum time step is calculated by equations

$$L_{max} \leq \frac{\lambda_{2f}}{8} = \frac{4.21}{8} = 0.53 \text{ mm}, \quad (4.3)$$

$$\Delta t \leq \frac{0.8L_{max}}{c_g} = \frac{0.8 \times 0.0005}{4.99} = 8 \times 10^{-8} \text{ s}, \quad (4.4)$$

where  $\lambda_{2f}$  is wavelength of secondary wave, and  $L_{max}$  is the largest element size in the model;  $c_g$  is the fastest group velocity of the wave. Finally, the maximum element size is taken as 0.5 mm and the minimum time step is  $5 \times 10^{-8} \text{ s}$ .

Eight actuators and eight receivers are arranged at the circumferential direction and at two ends of the pipe. Eight partitions with same dimension of the real PZT are simplified as actuators. The sources, a series of 0.71 MHz, 15.5 cycles Hanning-windowed tone burst signal, generated as point load along the axial direction of the pipe are applied at the short edge of each actuator to simulate the longitudinal wave. The actuators are excited one by one and all the receivers will receive the transmitted signals at the same time. The input signal is shown in Figure 4.33.

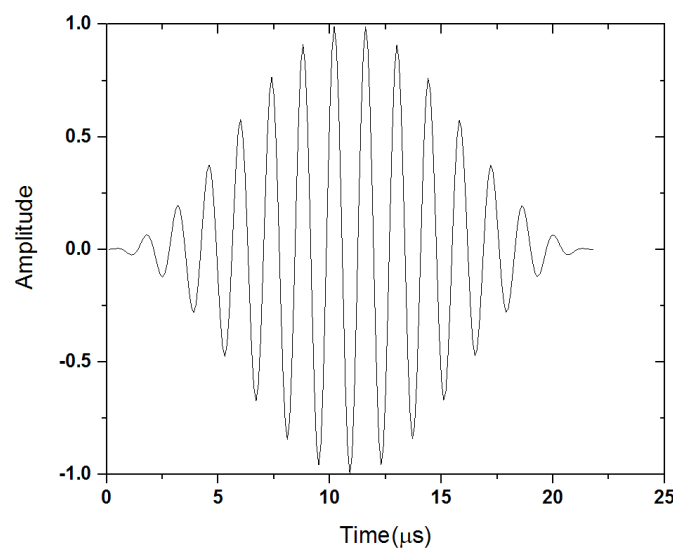


Figure 4.33 Input signal at the frequency of 0.71 MHz.

To check the excited wave is  $L(0, 4)$  mode and the generated second harmonic is  $L(0, 5)$ , another two monitoring points are placed after receiver and between actuator and crack, respectively. The locations of these actuators with applied load and receivers are shown in Figure 4.34 and Figure 4.35 respectively. Receiver AC0 is used to collect the reflected secondary wave. And the RS1 and RS0 are used to calculate the group velocity of the fundamental wave.

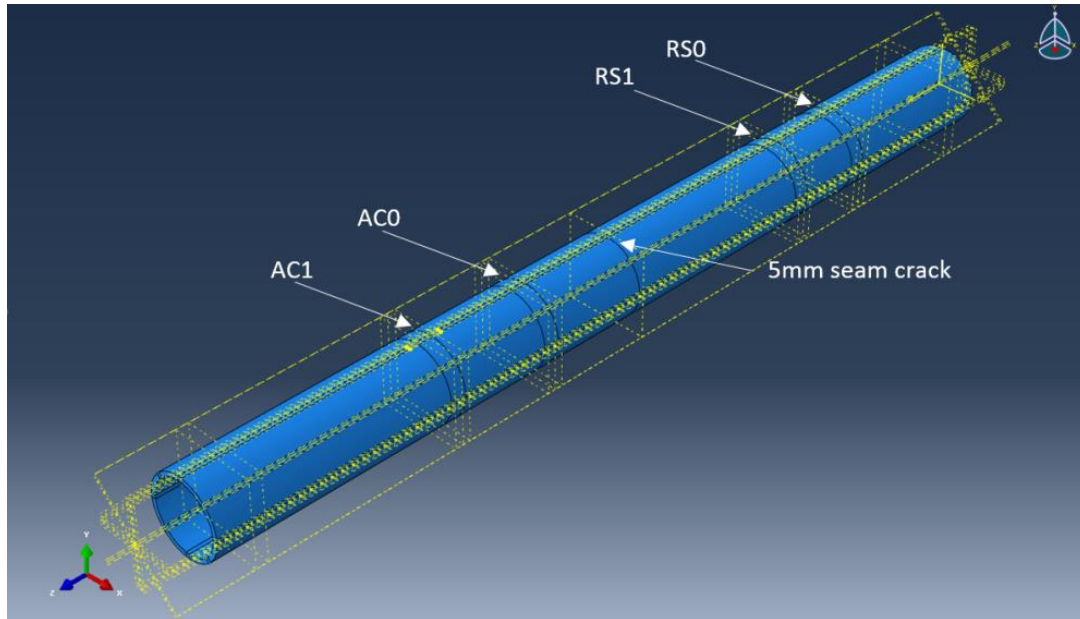


Figure 4.34 Locations of actuators with applied load and receivers in simulation model.

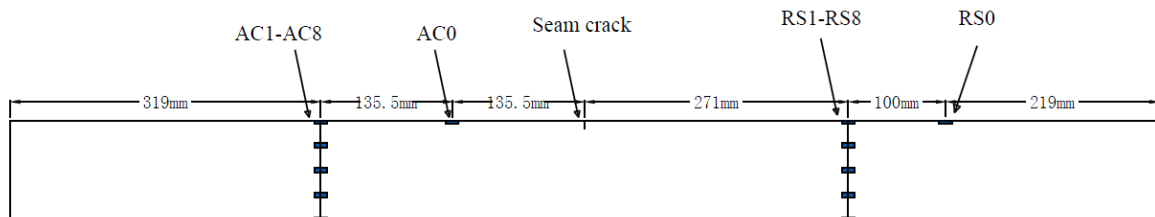


Figure 4.35 Location of actuators and receivers.

To model a fatigue crack in the pipe, a seam crack definition is used on each surface of the crack, similar with crack in mixed frequency response method simulation, to enable the breathing behavior when waves interact with the crack. The crack is through thickness and 5 mm length in circumferential direction, located at the middle of the pipe.

#### 4.3.2.3 Results from simulation model

One of the received signals is shown in Figure 4.36 presented by the stress in axial direction compared with the benchmark in which no seam crack is induced. There is no big difference between the current and benchmark signal in the time domain. After a fast Fourier transform (FFT), it is clearly seen that for the damaged pipe in the frequency

domain (Figure 4.37) there are both fundamental and second frequency components at 0.71 MHz and 1.42 MHz respectively. While for the undamaged one, only fundamental frequency exists. To confirm the wave mode, after calculating the time difference between RS1 and RS0, the first arrived wave has a group velocity of 4983 m/s, which is close to the theoretical value 4990 m/s from the dispersion curve. The reflected signal is filtered with a bandpass filter around the second harmonic frequency 1.42 MHz. Then group velocity of secondary wave is calculated 4830 m/s, which is consistent with the dispersion curve at 4840 m/s. Since the crack is at the same line with the actuator and receiver, the location of crack can be simply calculated by the reflected signal, the location is 271.8 mm to the position of the actuator, which is close to the actual value of 271 mm.

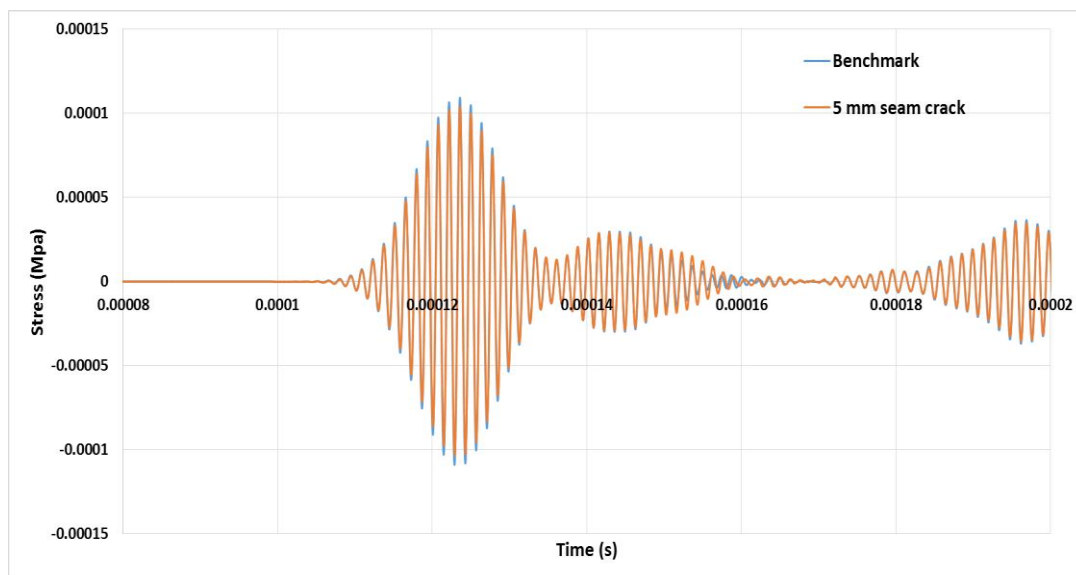


Figure 4.36 Received signal in time domain with 0.71 MHz excitation from simulation.

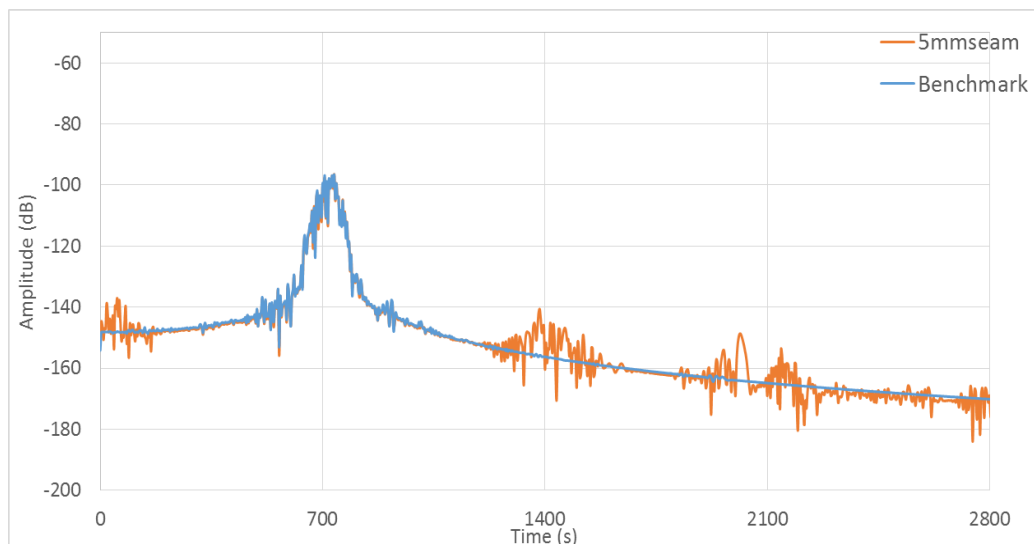


Figure 4.37 Received signal in frequency domain with 0.71 MHz excitation.

The results have shown that second harmonic method is more suitable for locating the position of the crack since it works well with a tone burst signal which indicated the time of arriving at the crack. Also, a short signal is convenient for signal processing and interpretation, especially for the pipe structures which has complex wave modes. Therefore, the second harmonic method will be used to detect the fatigue crack in the pipe.

#### 4.4 Summary

This chapter illustrates the optimisation and modelling of material nonlinearity and CAN in simulation which would be utilised in this study. Specific wave generation and collection method in simulation and experiment test are elaborated, along with some calibration and assessment of certain factors which influence the quality of signals. The last section analyses two commonly used nonlinear methods as a preliminary investigation for the detection of breathing crack in a pipe model. Higher harmonic generation method are selected for the following analysis and detection of fatigue crack.

## **Chapter 5 Theoretical analysis of contact acoustic nonlinearity (CAN) in pipe structures**

From previous chapters, it has been concluded that the theoretical analysis of CAN in plate structures was carried out by many researchers whereas the basic theoretical analysis on nonlinear guided waves in pipe structures was quite limited, where most of them were about material nonlinearity. A simplified theoretical analysis developed from plate to pipe structures will be addressed in this chapter and numerical studies will also be carried out to validate the results from theoretical analysis.

### **5.1 Theoretical analysis of nonlinear guided waves caused by CAN in plate structures**

Apart from the analytical 1D and 2D models in Section 3.3.1, a 3D model interpreting the mechanism of a breathing crack in a plate [153] is introduced in this section as a reference for the development of the analytical model of a pipe in later sections.

A plate with a through-thickness crack was investigated in [153] and a point load as input was applied at one end in the middle of the plate normal to the crack direction, as in Figure 5.1. One sensor was set in a line with the input to receive the reflected signal and both the sensor and crack are in plane.

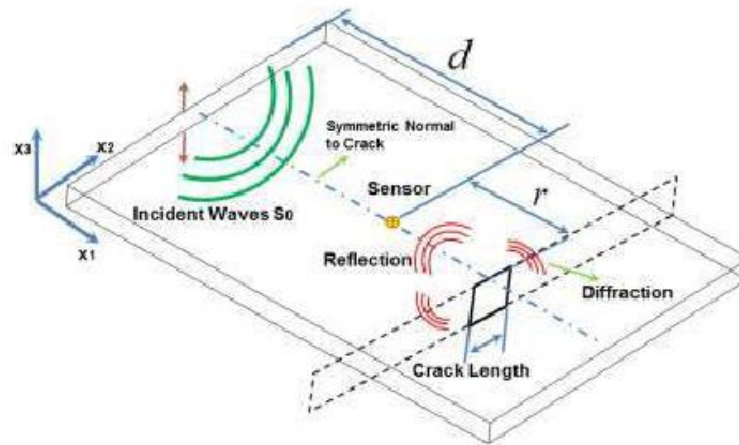


Figure 5.1 Configuration of the plate model [153].

The basic idea of this model is, when wave travels through the crack, the crack is treated as the second source which could generate crack-induced second source stress (CISS). When the crack is close, compressive stress of Lamb waves are transmitted and no CISS occurs, when the crack is open, the CISS is generated and the wave is blocked. The CISS was regarded as a point force which is the stress of incident wave integration over the crack surface. And the amplitude of wave received by the sensor was calculated based on elasto-dynamic method [155].

In a 3D scenario, the wave propagation is complex and the duration of crack open and close was influenced by many factors, such as shear horizontal waves (SH) induced during the breathing behaviour. This diffraction radiated from the tips of crack and distorted the stress field [111]. An approximation about the duration of the crack opening and closing was proposed considering the diffractions and CISS. The total duration of the crack opening induced by the CISS in the crack surfaces was assumed as half period of the incident waves plus the duration caused by diffraction as

$$t = \frac{T_{inc}}{2} + \frac{LT_{inc}}{2\lambda_{SH}}, \quad (5.1)$$

-Quantitative evaluation of fatigue crack using nonlinear guided waves in pipelines-

where  $L$  is the crack length,  $T_{inc}$  is the period of incident wave and  $\lambda_{SH}$  stands for the wavelength of the diffracted SH waves.

The integration of the stress on the crack surface is the total force which will be modified by function  $f(t)$

$$T = \int_{crack\ surface} \sigma_{crack} ds \cdot e^{i\omega t} f(t), \quad (5.2)$$

$$f(t) = \begin{cases} 1, & t_{open} < t < t_{close} \\ 0, & t_{close} < t < t_{open} + \frac{T_{inc}}{2} + \frac{LT_{inc}}{2\lambda_{SH}} \end{cases} \quad (5.3)$$

The modulation function and the spectrum of CISS can be refer to [153].

With the modulation function and the spectrum of crack induced stress, the amplitude  $A_{2f}$  at double frequency in the frequency spectrum can be obtained. As a result, the stress field on the crack at double frequency is

$$T_{2f} = A_{2f} \int_{crack\ surface} \sigma_{crack} ds, \quad (5.4)$$

An index was then used to describe the nonlinearity caused by the crack

$$NI = \frac{u_{x_1}^{2f_0}}{u_{x_1}^{f_0}}, \quad (5.5)$$

where  $u_{x_1}^{2f_0}$  is the CISS-induced displacement at double frequency and  $u_{x_1}^{f_0}$  is displacement of incident waves at fundamental frequency.

This method developed an analytical model on the interaction between nonlinear Lamb waves and the breathing crack, providing a nonlinear index for quantitative assessment of the CAN in a plate structure. This method will be referred for the following study to establish the analytical model for a pipe structure.

## 5.2 Theoretical analysis of nonlinear guided waves caused by CAN in pipe structures

Due to the curvature of the pipe structure, theoretical analysis in a 3D pipe was usually semi-analytical which combines with numerical simulation. In this section, a simplified condition was assumed where only longitudinal wave mode was excited and the theory of scattering of waves in elastic hollow cylinder with S-parameter in linear method was used. This theoretical analysis developed a model for the generation of second harmonic waves after the excited longitudinal mode interacts with breathing crack.

### 5.2.1 Problem formulation

The pipe configuration in this analytical study was set as in Figure 5.2 where pure longitudinal wave was excited and it will interact with a crack in the middle of the pipe. The transmission was received by monitoring points at the other end with proper signal processing method.

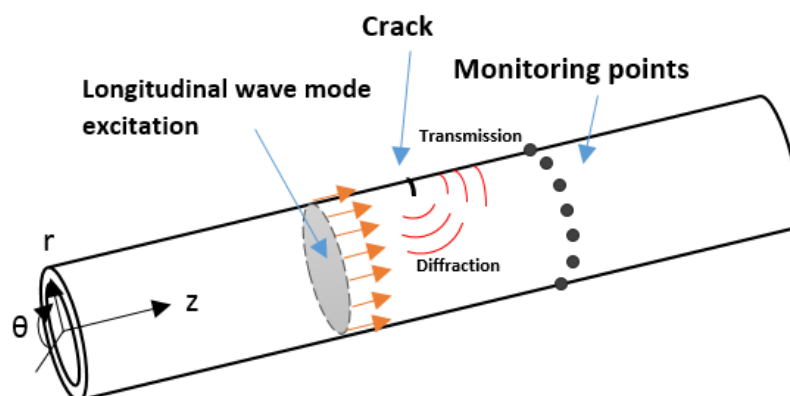


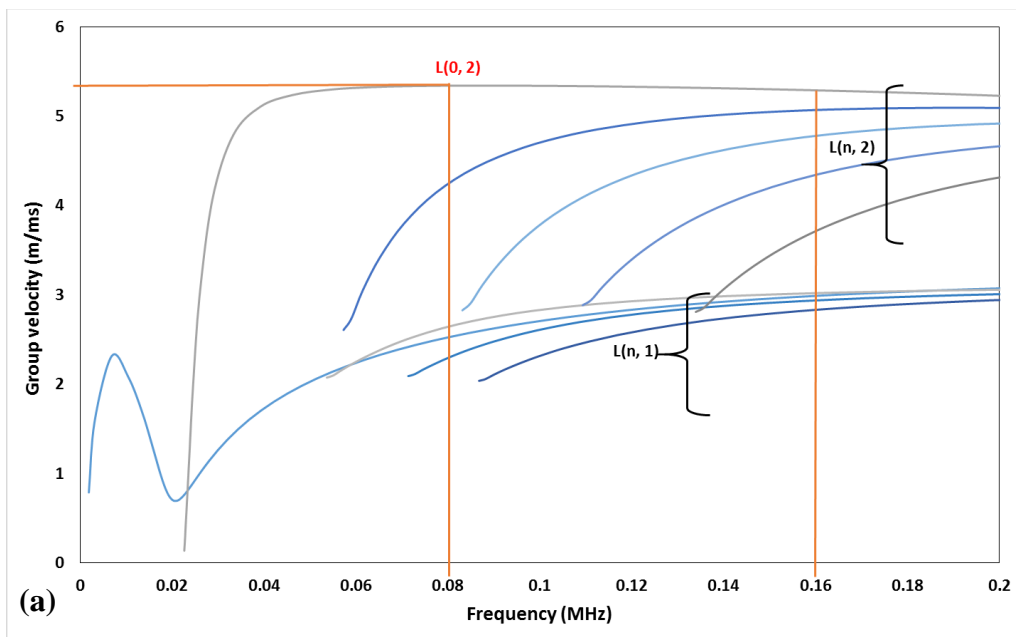
Figure 5.2 Configuration of analytical pipe model.

It is assumed that the incident longitudinal wave stress which caused crack opening displacement was simply equivalent to the stress on the crack surface.

$$T_{inc} = T_{crack} \quad (5.6)$$

To select a proper wave mode and frequency for the generation of CAN, the dispersion curve of an 80 mm outer diameter, 4 mm wall thickness is plotted as in Figure 5.3. It should be noticed that a notation from Rose [37] was adopted in the subsequent study, in which  $L(n, m)$  was defined as a longitudinal mode group, including axisymmetric modes  $L(0, m)$  and non-axisymmetric modes  $F(n, m)$ . The integer  $n$  is the circumferential order of a mode and the integer  $m$  denotes the group order of a mode.

The fundamental wave as the excitation was selected as 80 kHz and the wave mode is  $L(0, 2)$ , the fastest wave mode of  $L(n, 2)$  group, which also included flexural waves with close velocities to  $L(0, 2)$  and it is non-dispersive over a wide range of frequency. From the dispersion curve, it can be seen that at the double frequency, multiple wave modes exist.



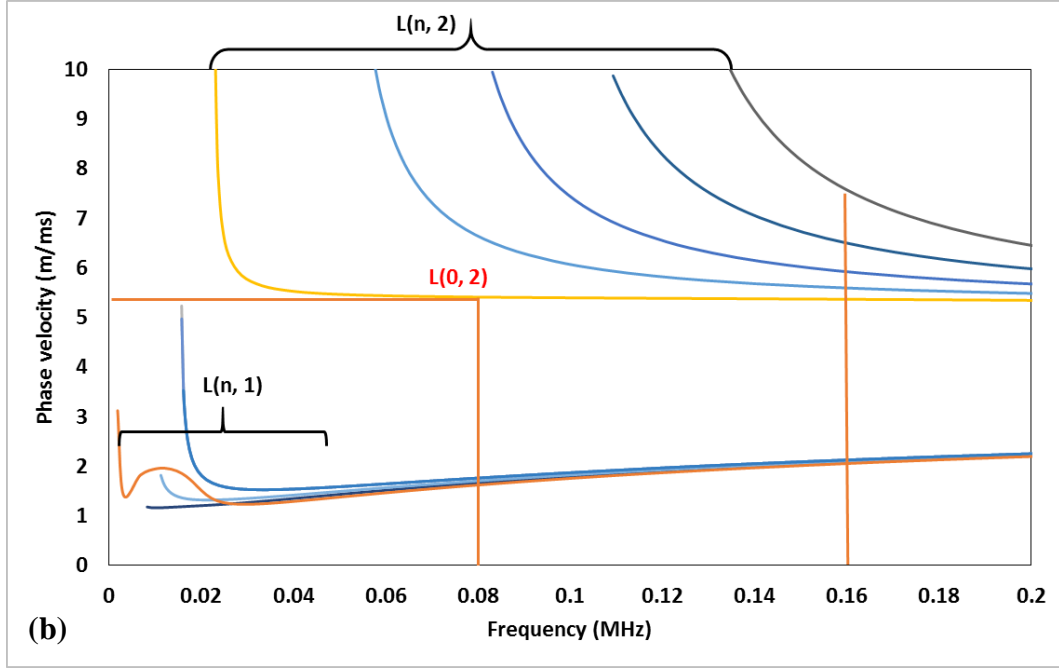


Figure 5.3 Dispersion curve of 80 mm outer diameter, 4 mm wall thickness aluminium pipe for (a) group velocity and (b) phase velocity.

Since the crack opening and close behaviour caused diffraction at the tip of the crack, which is circumferential shear horizontal wave propagating in the circumferential direction, it disturbed the duration of crack open and close. The duration of diffraction was estimated as the time of wave travels from the middle of the crack to the tip, which is  $\frac{LT_{inc}}{2\lambda_{SH}}$ . And the duration of crack opening due to the stress on the crack is  $\frac{T_{inc}}{2}$ . With the duration of crack close and opening the stress on the crack was modulated by function [153]

$$f(t) = \begin{cases} 1, & t_{open} < t < t_{close} \\ 0, & t_{close} < t < t_{open} + \frac{T_{inc}}{2} + \frac{LT_{inc}}{2\lambda_{SH}} \end{cases} \quad (5.7)$$

The relation between this wave function and the displacement of crack surface is plotted in Figure 5.4.

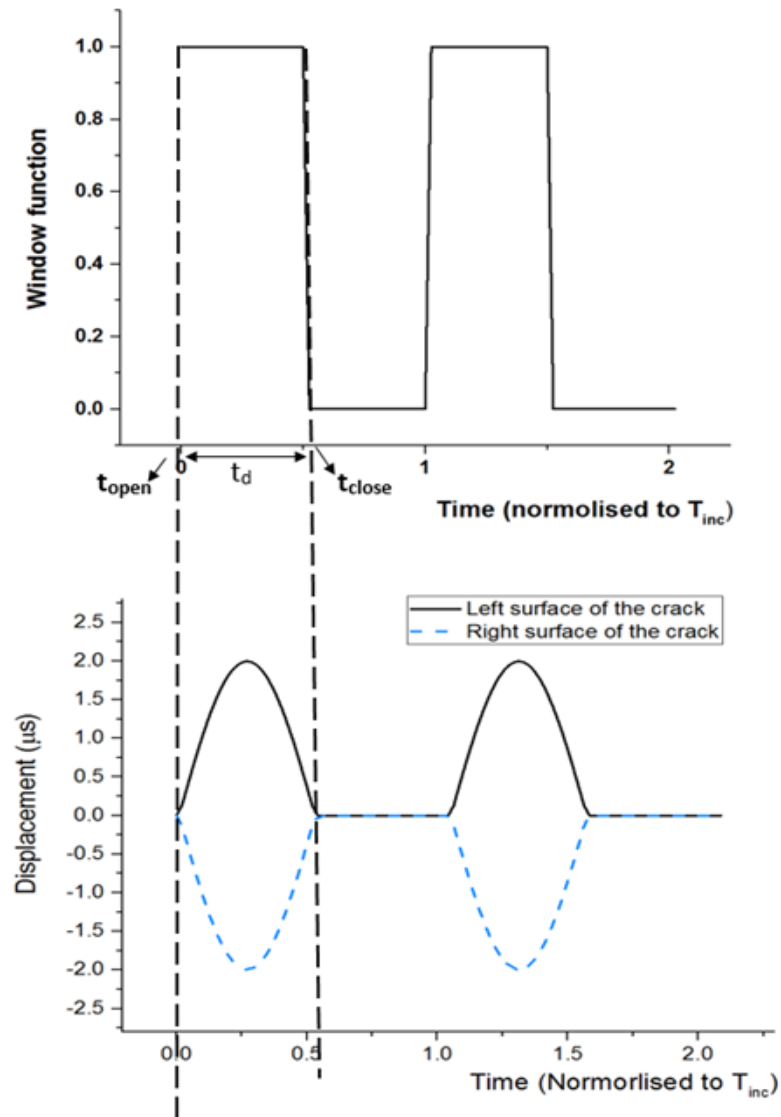


Figure 5.4 Window function and the crack surface displacement after modulated by the window function.

With the modulation function and the spectrum of crack induced stress, the amplitude  $A_{2f}$  at double frequency in the frequency spectrum can be obtained through Figure 5.5.

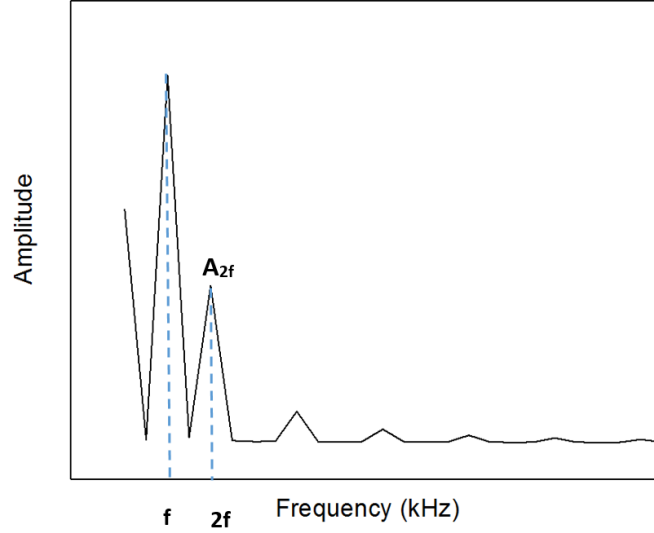


Figure 5.5 Frequency spectrum of displacement amplitude.

As a result, the stress field on the crack at double frequency is

$$T_{2f} = A_{2f}T_{inc} \quad (5.8)$$

So the stress on the crack was modulated and it was treated as a second source with stress  $T_{2f}$  which would generate second harmonic waves at double frequency. Recall from the introduction in Chapter 3.1, when the incident mode satisfies the condition that it has a large wavelength and the stress field of it is entirely axial so that the cylinder was under uniform tension, the crack opening displacement in Equation 3.2 can be approximated by elastostatic solutions [60]. And the general wave scattering formula with a longitudinal mode excitation can be expressed with S parameter as [156, 157]

$$\tilde{S}_{\bar{u}l;\bar{v}l}^{\bar{N},0} = \frac{-i\omega_{zz}T_v^0\bar{R}}{\sqrt{2E\epsilon}} \left\{ \frac{\alpha\cos(\bar{N}\alpha)}{\bar{N}^2} - \frac{\sin(\bar{N}\alpha)}{\bar{N}^3} \right\} \int_a^b rR_{\bar{u}zz}(r) dr, \quad (5.9)$$

where  $\tilde{S}_{\bar{u}l;\bar{v}l}^{\bar{N},0}$  stands for the S parameter when the incident mode is a longitudinal wave and the circumferential order  $M=0$ ,  $\bar{R} = (a + b)/2$ ;  $T_v^0$  represents the stress magnitude of the crack after modulated;  $\alpha$  is half of the crack angle;  $E$  denotes the Young's modulus;  $\epsilon^2 =$

$\frac{1}{[12(1-\nu^2)]^{\frac{1}{2}}} \left(\frac{H}{R}\right)$ ;  $\nu$  is Poisson's ratio;  $H = b - a$ ;  $R_{\bar{\mu}zz}(r)$  consists of modified Bessel function, which was calculated by equations in [25];  $r$  is the coordinate along radius direction.

From equation, it can be seen that the S parameter changes with crack length and the trend is different for different wave modes. After calculating the S parameter for multiple wave modes at double frequency, their amplitudes can be defined by

$$b_{\mu l}^N = \tilde{S}_{\bar{\mu}l, \nu l}^{\bar{N}, 0} a_{\nu l}^M, \quad (5.10)$$

where,  $b_{\nu l}^N$  is the amplitude with circumferential order  $N$  and group number  $\nu$ ;  $l$  and  $\lambda$  are the reference plane and in this case is at the location of monitoring plane;  $a_{\nu l}^M$  is the amplitude of incident wave.

### 5.2.2 Results of analytical analysis

The results of all converted modes at double frequency calculated with above equations are plotted in Figure 5.6.

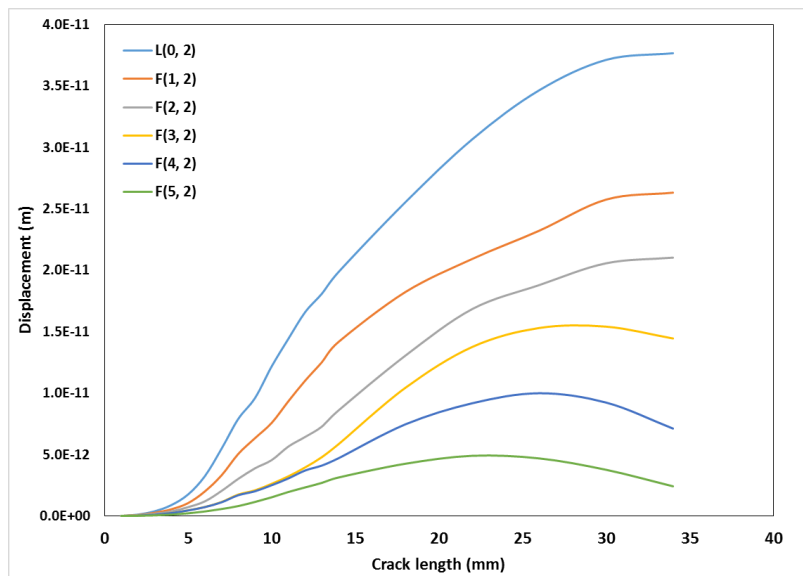


Figure 5.6 Plot of displacement at double frequency with varying crack length.

It is noticed that the trend of the first three modes L(0, 1), F(1, 2) and F(2, 2) keep increasing monotonously but for F(3, 1), F(4, 2) and F(5, 2), they start to drop at around 26 mm crack length. It is therefore within the crack length shown in the figure, the first three modes perform better than higher order modes for the quantification of crack length. It is similar to the study with linear method, where the guided wave was scattered by a circumferential crack and in these waves, the axisymmetric mode ( $n=0$ ) was most efficiently scattered by the crack but the other modes were not changing monotonically with the crack length [60].

Since more than one wave mode was generated as second harmonic waves, the proportion of different modes was calculated to investigate the contribution of each mode for the second harmonics. The percentage of each mode is calculated as the ratio of amplitude each mode and the sum of amplitudes of all modes, as shown in Figure 5.7 with crack length.

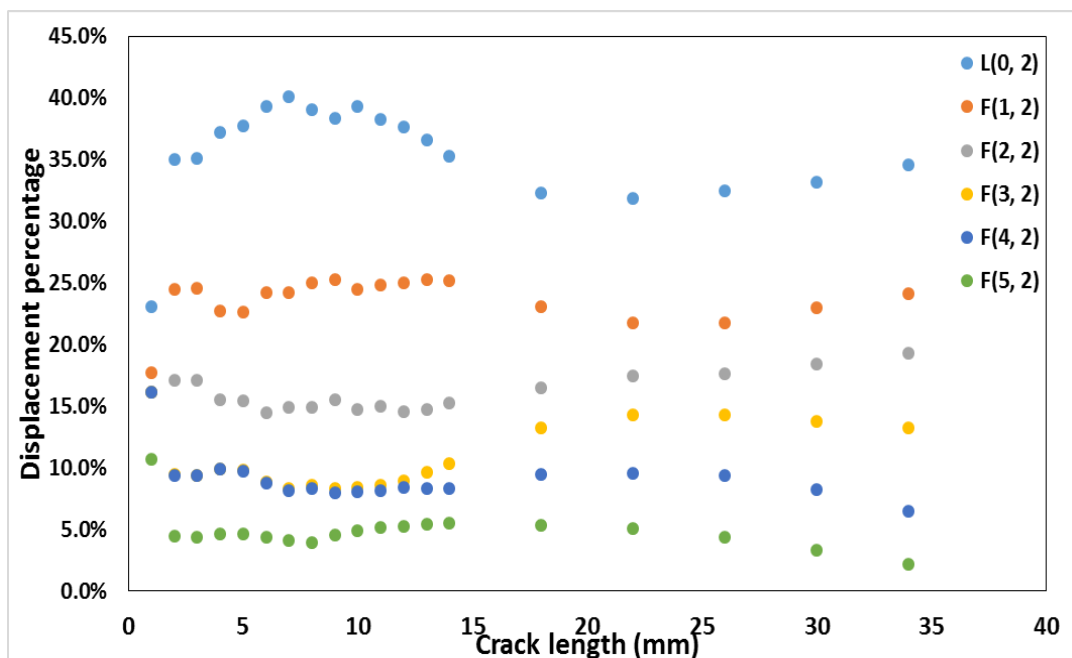


Figure 5.7 Displacement proportion of different wave modes as second harmonic wave.

From the figure, it is obvious that L(0, 2) occupies the largest displacement proportion, revealing the highest percentage of the total energy, and the percentage is higher when the crack length is smaller than 18 mm. However, flexural modes at lower order (n=1, 2) also take 15% to 25% of the total energy, which cannot be ignored when measuring the nonlinearity caused by the crack. Furthermore, as the crack length increases, the proportion of flexural modes F(3, 2) increases, which should also be considered for nonlinearity evaluation.

The results from analytical study show that multiple wave modes will generate after longitudinal wave interacts with breathing crack and the flexural waves play a vital role which should be considered when measuring the second harmonics caused by CAN.

It should be noticed that in order to use the Equation 5.9 with the elastostatic solutions, the length of the crack should satisfy  $\alpha \sim O(\epsilon^2)$ . For the pipe used here with  $\nu=0.33$  and thickness to mean radius ratio of 0.1, after calculate  $\epsilon$  through equation  $\epsilon^2 = \frac{1}{[12(1-\nu^2)]^{\frac{1}{2}}} \left(\frac{H}{R}\right)$ , the minimum crack length is about 2.4 mm. It can be seen that in

Figure 5.7, first point of each wave mode has obvious error because the crack length is only 1 mm and the equation cannot perform well for this case.

### **5.3 Numerical analysis of interaction between guided wave and close crack**

To validate the theoretical analysis results, FE simulation was applied to model the interaction between longitudinal wave and a close crack in the pipe and all second harmonic wave modes were extracted from the simulation.

### 5.3.1 Numerical model

A 3D model in Abaqus/Explicit was utilised to simulate the nonlinearity caused by the breathing crack. The pipe model had the same dimension as in the analytical model. The excitation signal is a 5-cycle Hanning-windowed tone burst signal at central frequency 80 kHz. To achieve the convergence and accuracy of the computation, the minimum element length and time increment were selected as 1 mm and  $5 \times 10^{-8}$  s respectively. The material properties of the aluminium are listed in Table 5.1.

Table 5.1 Material properties for 5 mm aluminium pipe.

<b>Material properties</b>	<b>Density (kg/m<sup>3</sup>)</b>	<b>Young's Modulus (GPa)</b>	<b>Poisson's Ratio</b>
	2700	70	0.33

To generate pure longitudinal wave, the number of element in the sensor ring should be greater than  $n$ , where  $n$  is the highest circumferential order flexural mode which has cut-off frequency within the bandwidth of the excitation [30]. Therefore, at least 16 elements need to be assigned in the sensor ring. In this study, 32 elements with 11.25 degree spacing was adopted and the excited signal was applied as point load at the node of the centre of each element along the direction of pipe axis.

The crack modelling followed the same procedure as abovementioned in Section 4.1.1.2 to enable the closing and opening behaviour. The length of the through-thickness crack was changed from 1 mm to 14 mm with an increment of 1 mm and from 14 mm to 34 mm with an increment of 4 mm. The configuration of this model is in Figure 5.8.

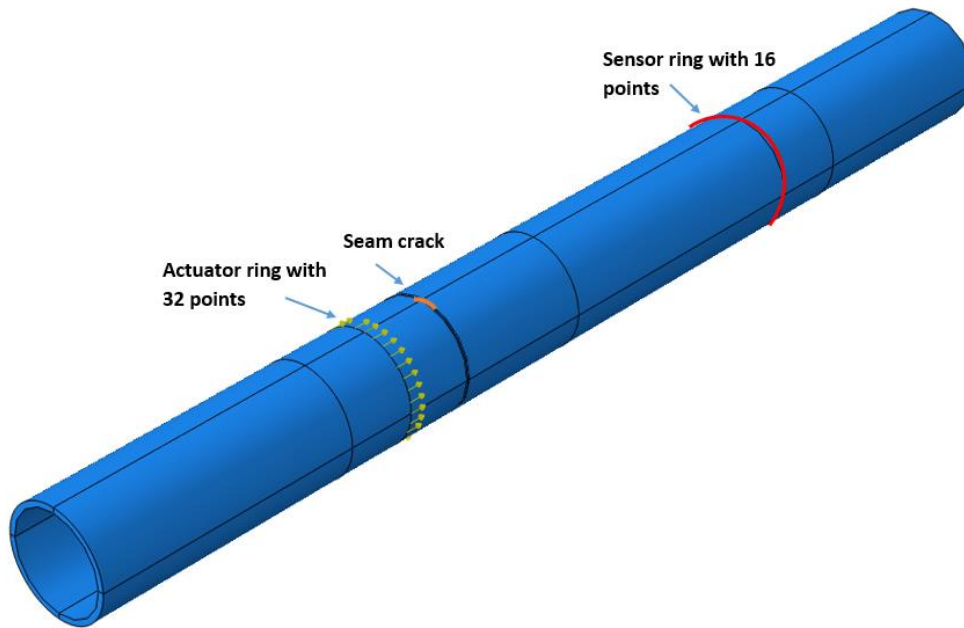


Figure 5.8 Configuration of pipe model in simulation.

From the dispersion curve of this pipe and the analytical analysis, the second harmonic waves should be multiple wave modes including  $L(0, 2)$  and  $F(n, 2)$  at double frequency. Thus, it is necessary to extract each mode at the monitoring points so that they can be analysed separately. 16 monitoring points at 350 mm away from the crack was assigned in the circumference direction. All the points would receive signals at the same time and after that an appropriate signal separating method was applied on these received signals to obtain different modes at double frequency. First, to enhance the second harmonic wave and remove the influence from fundamental wave, after all excited signals were received, a  $180^\circ$  out-of-phase inversed signal was sent into the pipe again at the same location. The combination of these two signals would turn to signals that contain nonlinearity at higher harmonics only. Secondly, for the longitudinal mode, each signal from monitoring points was processed with a band pass filter in MATLAB at double frequency with bandwidth  $\pm 15$  kHz and then added together to get the final signal. For the flexural mode, same band pass filter was also used on each of the received signals and

then a phase delay of  $N\theta/2\pi$  was applied to each signal, where  $N$  is the circumferential order and  $\theta$  is the angular distance to the centre of the notch. Finally, sum of these delayed signals generate final flexural modes [30].

### 5.3.2 Results from numerical analysis

Some of the typical signals from the case with 1 mm seam crack of different wave modes at double frequency after signal processing are shown in Figure 5.9 and Figure 5.10. It is seen from the figures that the flexural waves arrive almost at the same time as  $L(0, 2)$ , consistent with the dispersion curve that flexural wave modes have close group velocity to the longitudinal one. The separation of flexural mode from longitudinal one is not ideally accurate for higher order modes which are highly dispersive as in Figure 5.3.

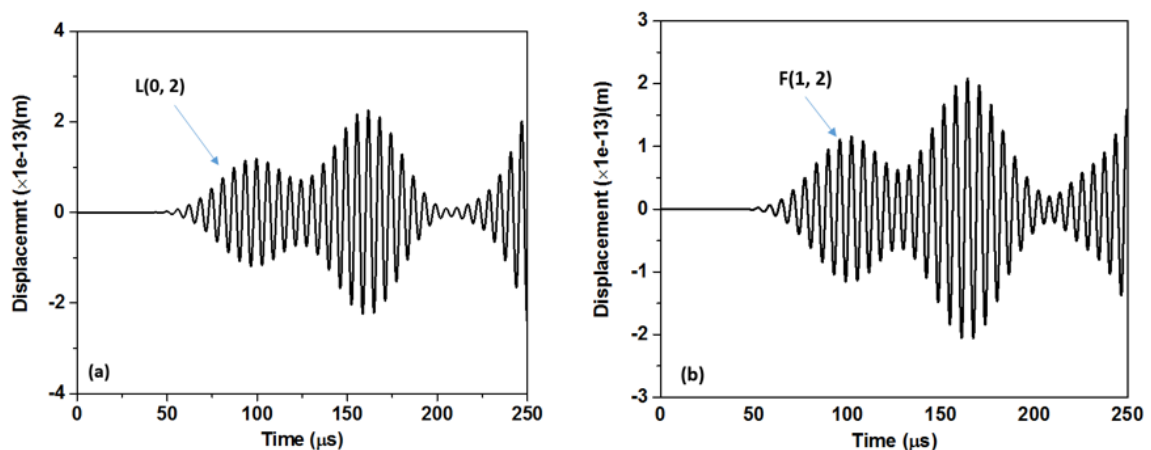


Figure 5.9 Signals at double frequency of  $L(0, 2)$  and  $F(1, 2)$  modes for 1 mm seam crack case.

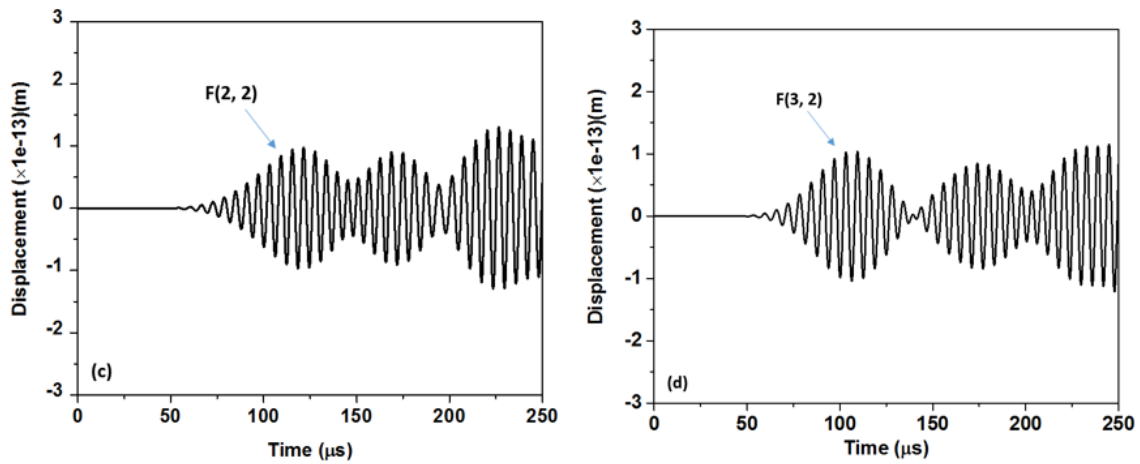


Figure 5.10 Signals at double frequency of F(2, 2) and F(3, 2) modes for 1 mm seam crack case

To observe the change of different second harmonic modes generated by different crack lengths, the displacement amplitude of each mode was also plotted in terms of crack length as in Figure 5.11.

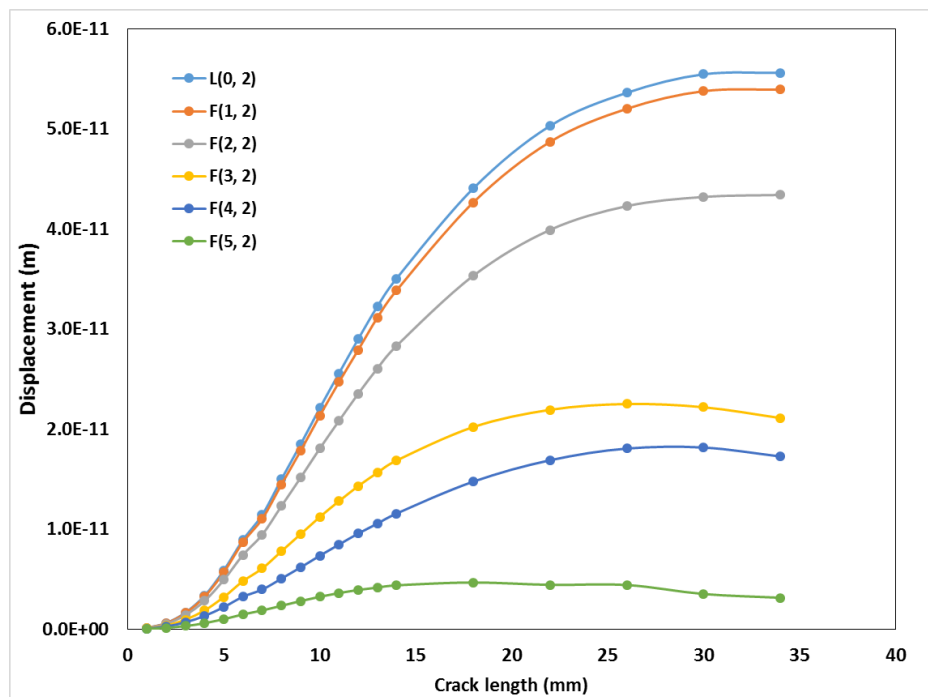


Figure 5.11 Displacement of different modes at double frequency with crack length in simulation.

Similar to the analytical results, the increasing of first three modes are monotonously while  $F(3, 2)$ ,  $F(4, 2)$  and  $F(5, 2)$  start to decrease at around 26 mm, 30 mm and 18 mm, respectively. the amplitude of flexural wave mode  $F(1, 2)$  is close to  $L(0, 2)$ , which is different from the analytical results.

The proportion of different modes were also calculated in the simulation study as shown in Figure 5.12, where both  $L(0, 2)$  mode and  $F(1, 2)$  mode take main proportion of the total amplitude around 50%. The first three modes slightly increase with the crack length while  $F(3, 2)$  and  $F(5, 2)$  show the opposite trend. The proportion of flexural wave modes are similar with analytical results, while it is 10% lower for the longitudinal mode. However, the first three modes still dominate the induced nonlinearity and none of them can be ignored when evaluating the severity of close crack.

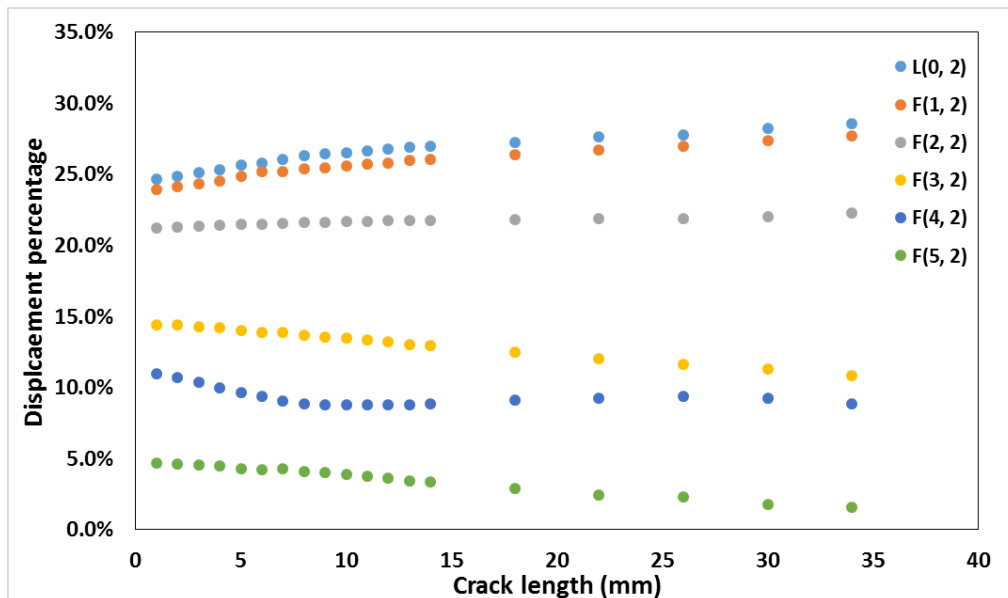
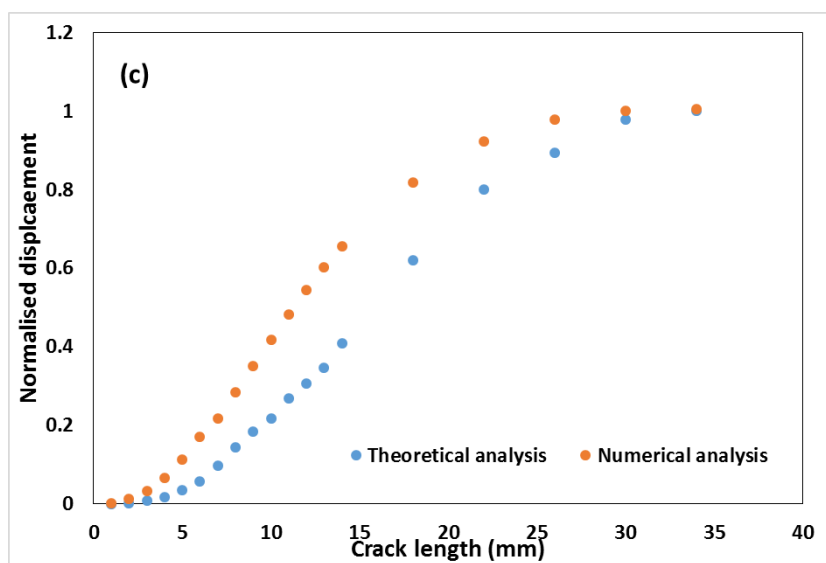
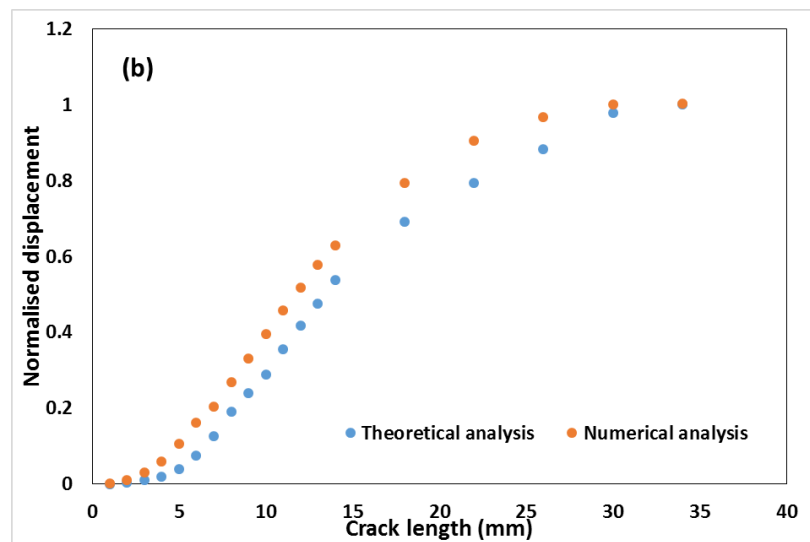
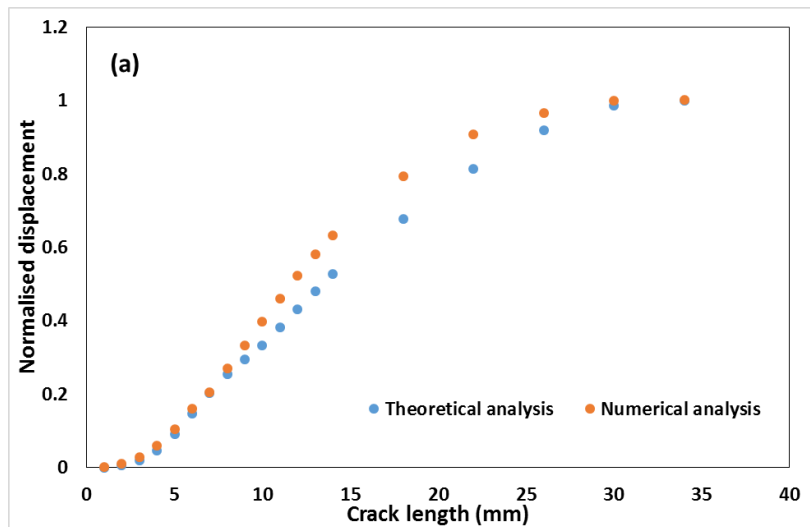


Figure 5.12 Proportion of different wave modes as second harmonic wave from simulation.

To further analyse the difference between analytical and simulation results, the displacement change of each mode with crack length was illustrated in Figure 5.13.



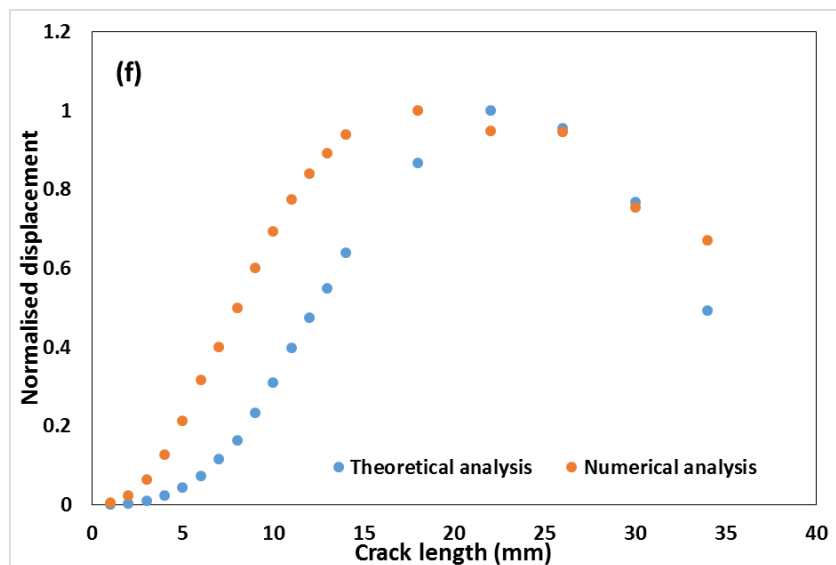
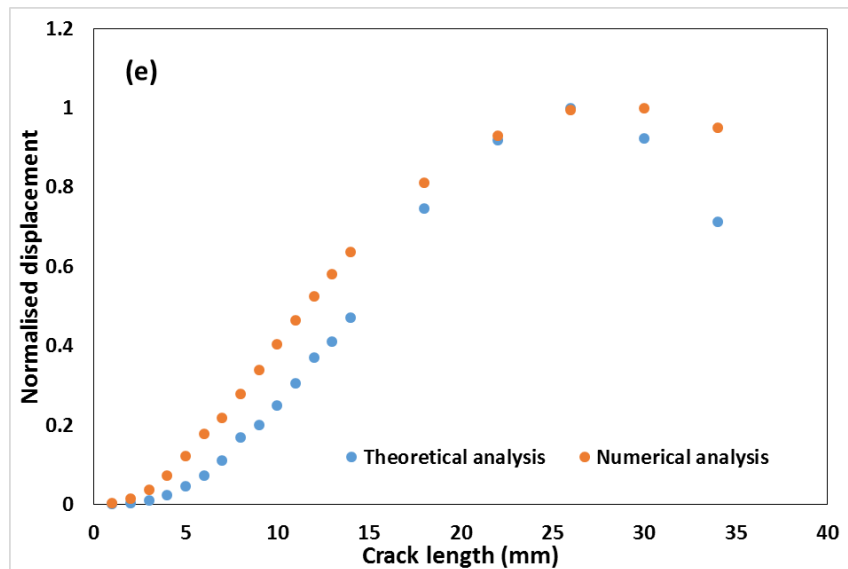
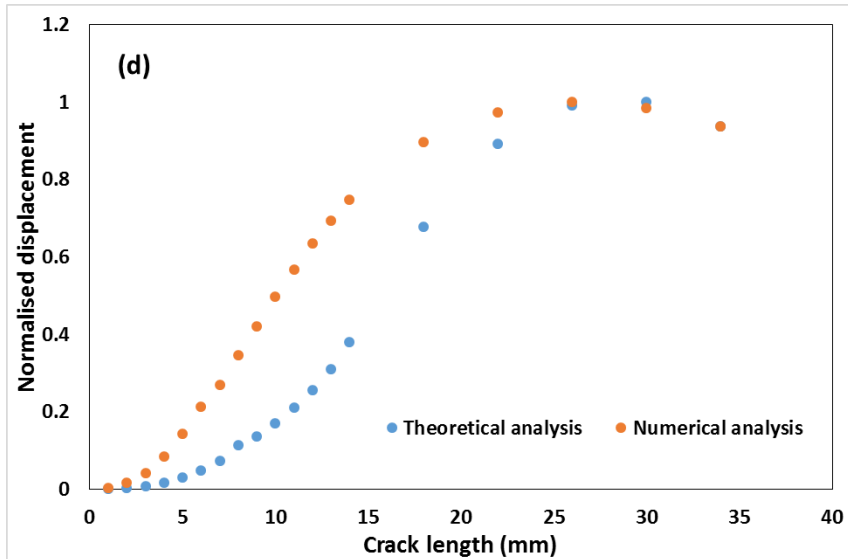


Figure 5.13 Comparison of numerical and theoretical analysis for (a) L(0, 2) mode; (b) F(1, 2) mode; (c) F(2, 2) mode; (d) F(3, 2) mode; (e) F(4, 2) mode and (f) F(5, 2) mode.

As seen in the figure, the first three modes have similar trend for simulation and theoretical results. However, for the higher order flexural waves ( $n > 2$ ), the differences are more obvious than the first three modes. The theoretical values are lower than its simulation counterparts, which is mainly because the stress on the crack was assumed as uniformly distributed for the theoretical analysis whereas the stress cannot be ideally uniform due to the beam spreading of wave excited by point load and the blind zone between each element for the simulation model. The distance between the transducer ring and the crack would also influence the stress distribution on the crack. Another transducer ring was added on the same model with a farther distance 0.3 m to the crack. The displacement of second harmonic wave L(0, 2) of this case compared with the original distance is shown in Figure 5.14. As can be seen in the figure, the closer the actuator to the crack, the lower values of the numerical analysis, revealing the location of actuator ring will influence the stress distribution on the crack and the CAN generated by the crack.

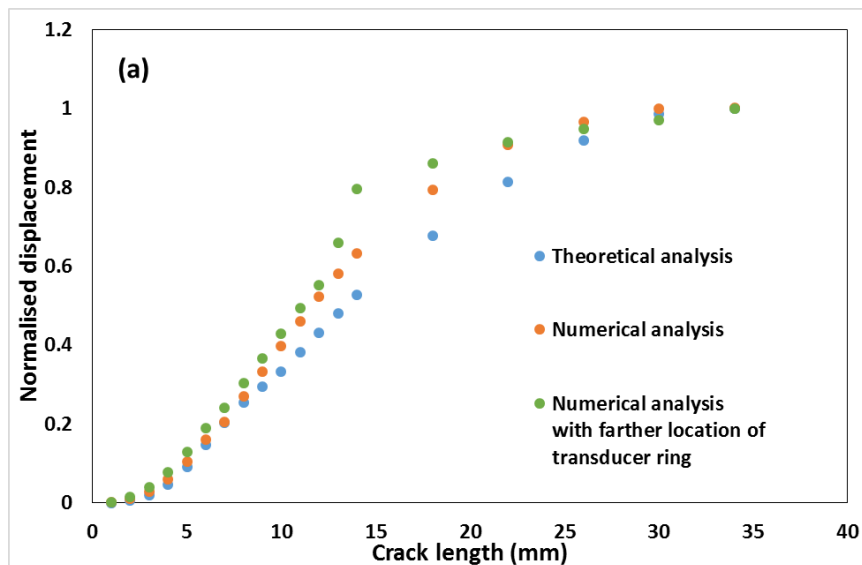


Figure 5.14 Influence of distance between transducer ring and the location of crack.

Another possible reason is that the simulation results for higher order flexural wave modes may be unstable due to the heavily dispersive properties and therefore when comparing with the analytical model, the higher order flexural modes show lower confidence than longitudinal and other flexural modes ( $n \leq 2$ ). However, from the proportion evaluation of each mode that contributes to the nonlinearity,  $L(0, 2)$ ,  $F(1, 2)$  and  $F(2, 2)$  modes take the major role and show monotonous increase in contrast to the higher flexural modes.

Moreover, since analytical analysis established a simplified model and therefore ignored the influence from flexural wave modes which may cause bending of the pipe on the closing and opening behaviour of the crack.

In conclusion, the trend of different modes generated at double frequency from theoretical model are observed to be consistent with simulation model, especially for longitudinal and lower order flexural modes ( $n \leq 2$ ). The differences between theoretical and simulation results were acceptable since the analytical model is a simplified model without considering bending caused by the flexural modes and the uniform stress on the crack. From both the simulation and theoretical results, it reveals the multiple mode generation at double frequency with longitudinal mode excitation and it is noticed that the magnitudes of lower order flexural modes are comparable with the longitudinal mode at double frequency.

#### **5.4 Nonlinear parameter for nonlinearity measurement in pipes**

In the literature, the severity of nonlinearity in a system was measured with a nonlinear parameter, such as the nonlinear parameter  $\beta$  in isotropic plate [115, 116] and composites [158], which is the ratio of the peak value of the amplitude of the second harmonic wave to the square of the peak value of the amplitude of the fundamental wave. In this chapter,

the received wave modes can be separated in theoretical analyses due to pure longitudinal excitation and the number of second harmonic modes can be predicted through dispersion curve. However, when one actuator and one sensor in a line is used for damage detection in pipe structures, which is usually adopted in experiments with PZT transducers, the second harmonic wave modes will be more complex where more than one wave packet may present because group velocity of each modes is too close to separate. As a result, it is difficult to calculate nonlinear parameter based on a single peak value of the amplitude and a new parameter is required to measure the nonlinearity. In this circumstance, a parameter considering all generated wave packets was proposed, which was the integral of amplitude profile of the second harmonic wave of concern within a time period divided by the integral of amplitude profile of the fundamental wave. An example is shown in Figure 5.15 for the model in simulation study from last section. Signal from one of the monitoring point was processed through STFT and signal at fundamental and double frequency were extracted, details of this signal processing method will be introduced in Section 6.3.2. The pure longitudinal wave  $L(0, 2)$  generated multiple wave modes  $L(n, 2)$  at double frequency, including  $L(0, 2)$  and Flexural modes  $F(n, 2)$  ( $n=1, 2, 3, 4, 5$ ) from the same group.

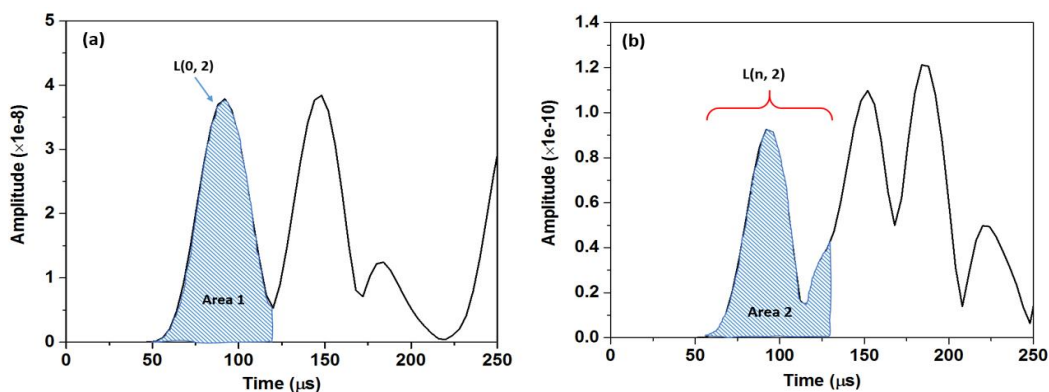


Figure 5.15 Signals from simulation model for 10 mm seam crack case after STFT at (a) fundamental frequency and (b) double frequency.

Therefore, the new nonlinear index was calculated by

$$\text{Nonlinear index} = \frac{\text{Area 2}}{\text{Area 1}} \quad (5.11)$$

Following Equation 5.11, the nonlinear indices can be calculated. In the following studies where multiple modes are generated at double frequency caused by CAN, this index will also be used with certain time windows of interest. Also, the length and end point of time windows were adjusted to make sure a stable results of the calculation whenever it was applied for the evaluation of CAN. Instead of using amplitude of one wave mode as nonlinear parameter  $\beta$ , this parameter considers all the possible second harmonic wave modes, which is commonly observed in a pipe structure with circumferential close crack so as to avoid underestimate the contribution of flexural modes to the nonlinearity.

## 5.5 Summary

This chapter develops a theoretical model for the longitudinal wave interaction with circumferential breathing crack in a pipe for the understanding of the mechanism of CAN in the pipe structures. The idea is based on an analytical model in a plate with CAN and wave scattered in a pipe by circumferential crack with linear method. S parameter is used to calculate the amplitude of each second harmonic mode induced by the breathing crack, followed by a simulation study with the same model as in the analytical analysis. The results from both methods are compared and the analytical model is useful to describe the interaction between longitudinal wave and the breathing crack. It also shows the second harmonic waves contain different modes and the flexural wave modes occupies a large proportion of the total energy induced by CAN. Based on this analysis, a nonlinear index suitable for the measurement of CAN in pipe structure is proposed, which will be used in the following studies.

## **Chapter 6 Nonlinear guided waves for fatigue crack detection**

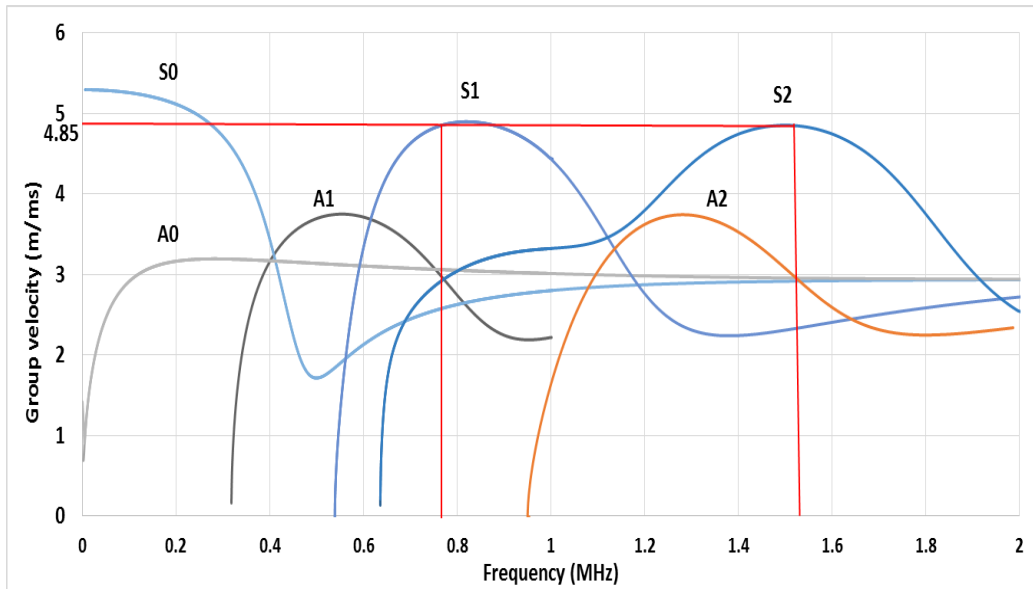
Differences in fatigue crack detection using nonlinear guided waves between plate and pipe structures are investigated in this chapter and the nonlinear index proposed from Chapter 5 is used to provide an effective approach for analysing nonlinearity in pipe structures. Guided wave propagation and the interaction with close crack in a plate and a pipe structure, both of which introduced a contact acoustic nonlinearity (CAN), was analysed through a FE analysis. To validate the simulation results, experimental testing was performed using piezoelectric transducers to generate guided waves in a specimen with a fatigue crack. Both methods revealed that the second harmonic wave generated by the breathing behaviour of the fatigue crack in a pipe had multiple wave modes, different to the plate scenario using nonlinear guided waves.

### **6.1 Fatigue crack detection in plates using second harmonic generation**

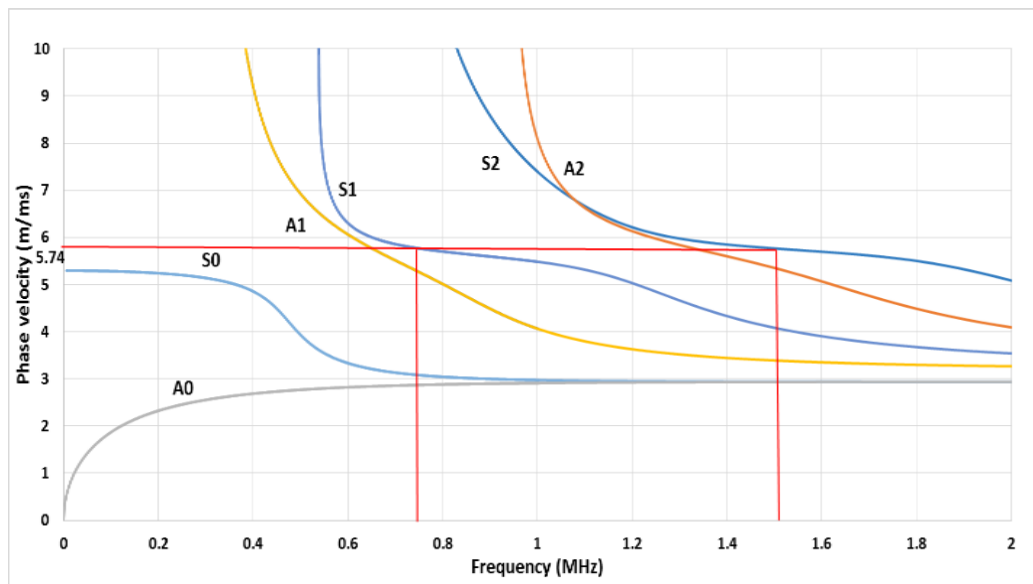
For basic understanding of the second harmonic generation method in fatigue crack detection, a plate specimen was taken as an example in both simulation and experiment. FE simulation model with seam crack modelling the interaction between guided waves and breathing crack was carried out. Simulation results were validated by a previous analytical study with varying seam crack length and also confirmed with experimental test. The results from the plate will be compared with pipe structures in following section.

### 6.1.1 Mode selection

Before the simulation model was set up, proper wave mode and frequency need to be determined to generate second harmonic. Dispersion curves were drawn by DISPERS software for a steel plate with a dimension of 360×80×5 mm as shown in Figure 6.1



(a)



(b)

Figure 6.1 Dispersion curve of 5 mm steel plate for (a) group velocity and (b) phase velocity.

The fundamental wave was selected as S1 at frequency of 763 kHz with a group velocity of 4850 m/s, which would convert to secondary wave S2 at the double frequency 1526 kHz when it encountered close crack with nonlinearities generated.

## **6.1.2 Modelling of steel plate**

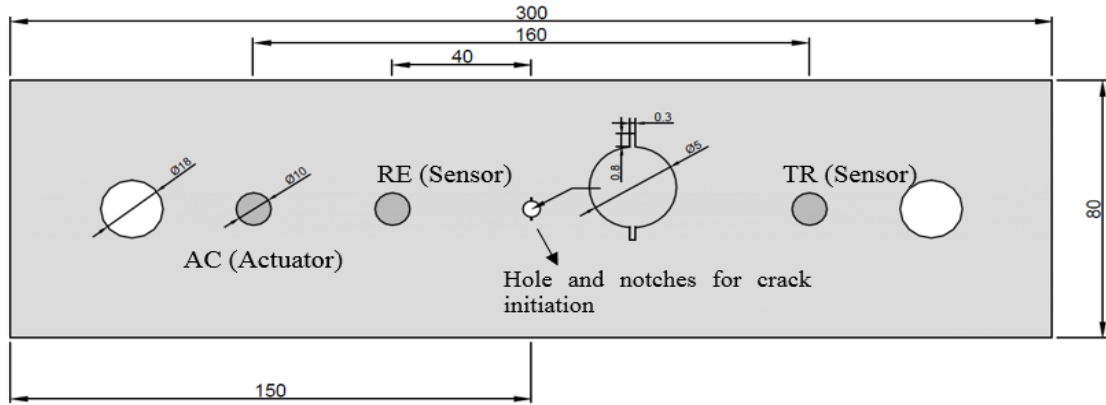
### **6.1.2.1 Numerical analysis**

A 3D model with solid elements (C3D8R) was developed using FEM software Abaqus Dynamic/Explicit® to study the nonlinearity caused by a fatigue crack in the steel plate. To achieve the convergence and accuracy of the computation, the minimum element length and time increment were selected as 0.5 mm and  $1 \times 10^{-8}$  s, respectively. The material properties of the steel plate are listed in Table 6.1.

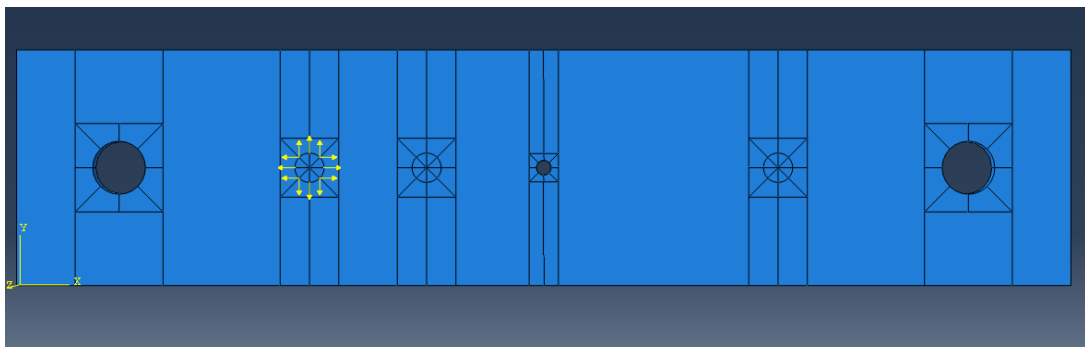
Table 6.1 Material properties for 5 mm steel plate.

<b>Material properties</b>	<b>Density (kg/m<sup>3</sup>)</b>	<b>Young's Modulus (GPa)</b>	<b>Poisson's Ratio</b>
	7850	203	0.28

The actuator was simulated with the same dimension of the real piezoelectric lead zirconate titanate (PZT) used in the experiments. A 15.5 cycle Hanning-windowed tone burst at a central frequency of 763 kHz was applied as uniform in-plane radial concentrated forces on the nodes along the periphery of the actuator model to simulate Lamb wave excitation. Two sensors TR and RE were used to receive the transmitted and reflected signals respectively. In the middle of the plate, a hole with two notches was simulated for the initiation of the fatigue crack, following the same geometry in the experiment test. Figure 6.2 shows the configuration and the snap shot of the model in Abaqus.



(a)



(b)

Figure 6.2 (a) Configuration of steel plate and (b) simulation model in Abaqus.

To model a fatigue crack in the plate, an Abaqus seam crack definition was used on each surface of the crack, as illustrated in Figure 6.3, to enable the breathing behaviour when waves interact with the crack, detail simulation method is in Section 4.1.1.2. The crack was through the thickness and the length was changed at the tip of notch from 1 mm to 7 mm on each side of the hole with an increment of 0.5 mm.

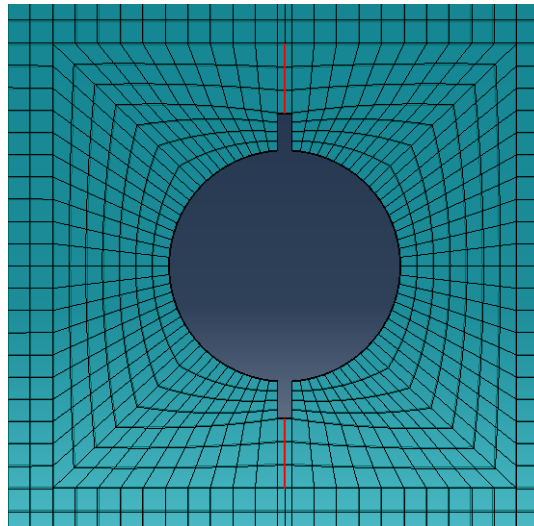
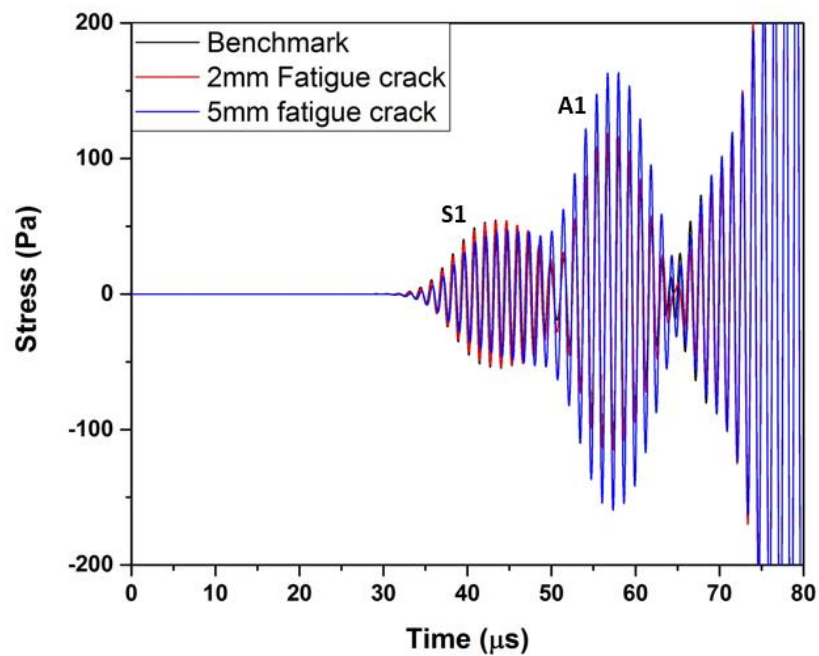


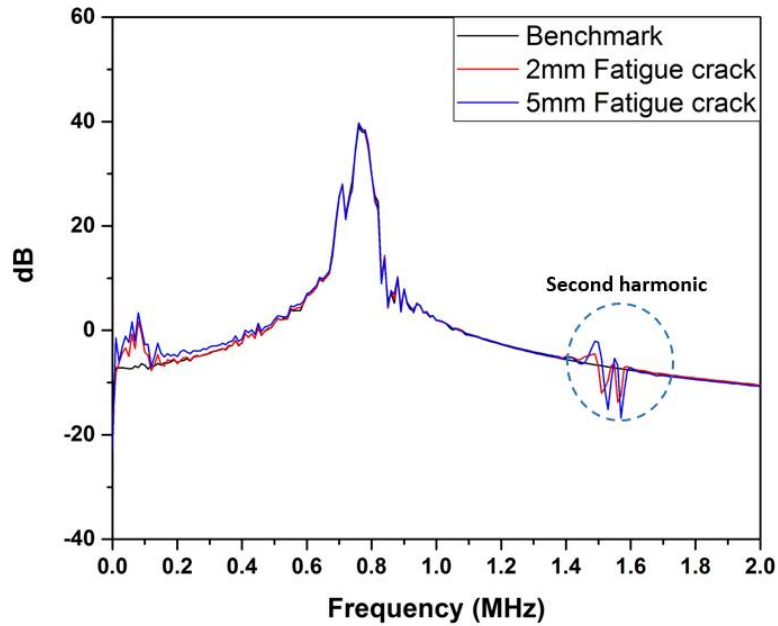
Figure 6.3 Modelling of "seam" crack.

### 6.1.2.2 Simulation Results

Two typical transmitted signals from the cases of 2 mm and 5 mm seam cracks compared with the benchmark in both time domain and frequency domain after FFT are shown in Figure 6.4.



(a)



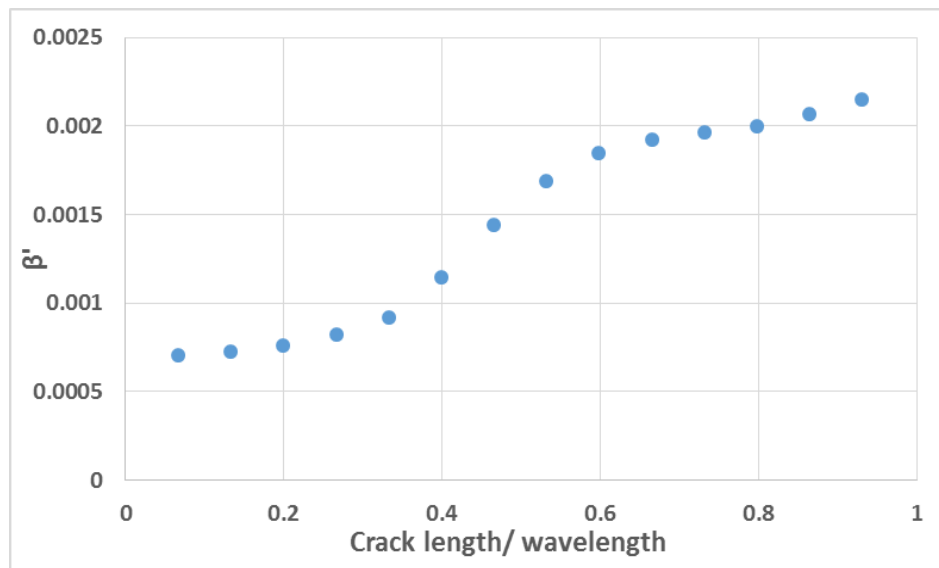
(b)

Figure 6.4 (a) Transmitted signal in the time domain and (b) frequency domain.

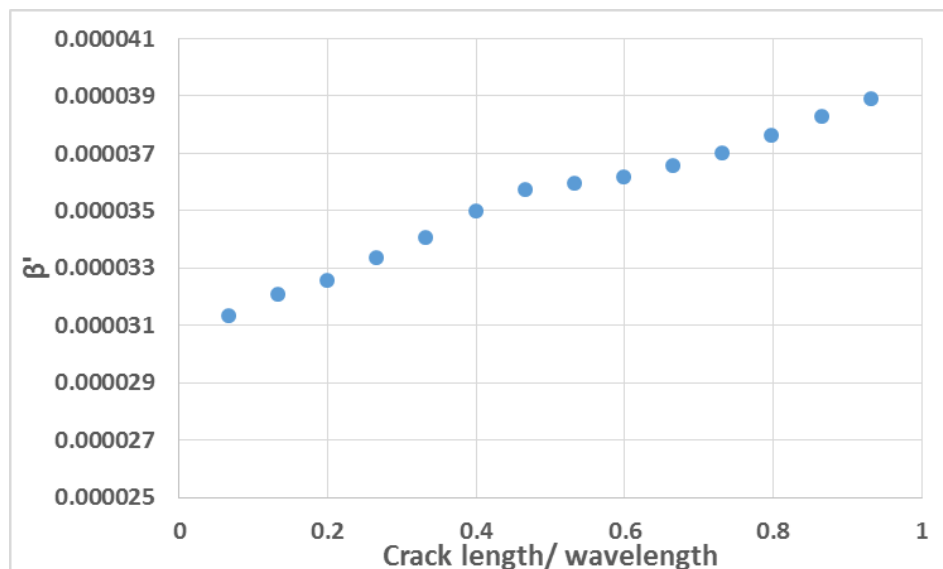
It can be seen that in the time domain, the signal of 2 mm seam crack case has no obvious difference with the benchmark, but for the damage case with 5 mm seam crack, the amplitude of S1 mode is smaller than benchmark though the difference is marginal and the arrival time of first wave packet of all these cases are same since the length of seam crack is short. However, after processed with the FFT, in the frequency domain, an obvious second harmonic around 1526 kHz is generated which indicates the existence of fatigue damage.

Relative nonlinear parameter  $\beta' = \frac{A_2}{A_1^2}$  was then calculated for all cases with different crack lengths, where  $A_1$  is the amplitude of the fundamental frequency and  $A_2$  is the amplitude of second harmonic. After calculation, the relationship between  $\beta'$  and the crack length to wavelength ratio is plotted in Figure 6.5, where the wavelength of the fundamental wave mode is 7.52 mm. The results show that nonlinear parameter increases monotonously with the crack length for both reflection and transmission signals, which

is consistent with the results in [153] as shown in Figure 6.6. The nonlinear relation is mainly because of the influence of diffraction. On the other hand, reference [153] only considered the reflected signal with the crack length to wavelength ratio up to 0.5 while the simulation was extended to the ratio of 1 for both reflected and transmitted signals in this study.



(a)



(b)

Figure 6.5 Relative nonlinear parameter  $\beta'$  in terms of crack length/wavelength (a) transmitted signal; (b) reflected signal.

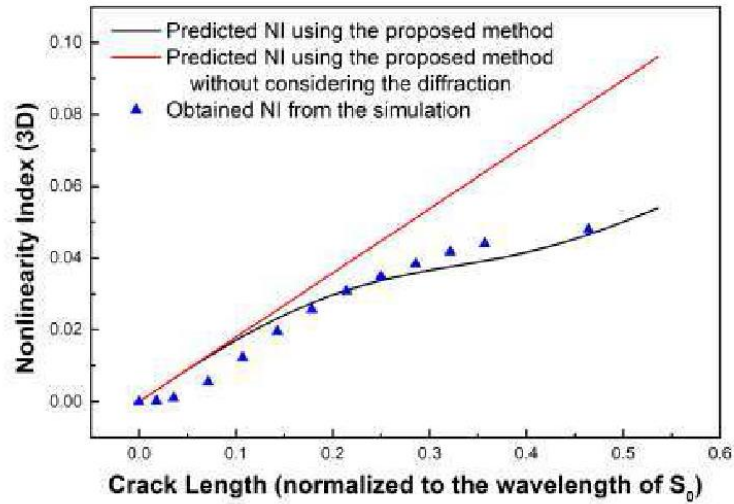


Figure 6.6 Nonlinear index verses the crack length in reference [153].

A Hanning-windowed finite impulse response (FIR) bandpass filter in MATLAB was subsequently designed to extract transmitted wave within the frequency range of interest while excluding the wave components in other frequency bands. The upper and lower thresholds of the frequency range was selected as  $\pm 100$  kHz centred by both fundamental and double frequency. 3000 filter order was selected when using the filter. The amplitudes of wave components at the fundamental and double frequency bands were extracted in terms of time as shown in Figure 6.7.

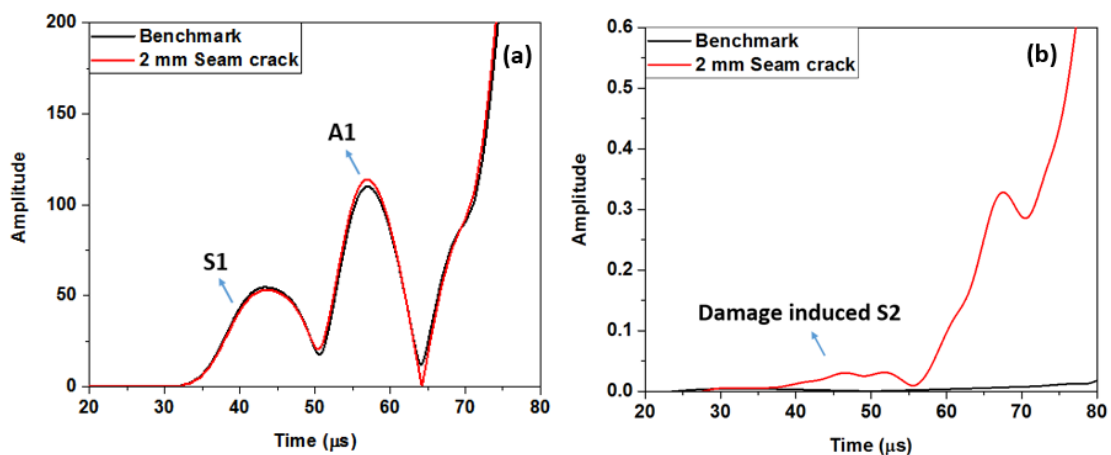


Figure 6.7 (a) Amplitude profiles at the fundamental frequency and (b) amplitude profiles at the double frequency.

As seen in Figure 6.7(a), the first peak denoted the first arrived transmitted S1 mode at time 33  $\mu\text{s}$ , which indicates similar group velocity as in theoretical calculation, followed by the A1 mode. The amplitude profiles of the benchmark and the signal with a crack at the fundamental frequency were almost identical, which further confirmed that there were no apparent waves scattered by the small-size crack, and therefore it is difficult to identify the location or severity of the crack using signals at fundamental frequency. As for the wave components at double frequency, the amplitude profiles were different for the benchmark and the signal with damage, where an additional peak starting at time 36  $\mu\text{s}$  can be observed, which is denoted as S2 mode generated by S1 mode when it encountered the seam crack, followed by A2 mode. It is also noticed that minor second harmonics already existed in the benchmark signal, which may mainly attribute to the geometry nonlinearities in the model.

### **6.1.3 Experimental studies for crack propagation in steel plates**

#### **6.1.3.1 Experiment set up**

The detection of fatigue crack propagation in steel plates using nonlinear ultrasonics was also evaluated through experimental studies. The specimen dimension and material properties were same as those in the simulation model and the surface of the specimen was sandblasted and cleaned with acetone to remove dust. Three PZT transducers were attached on the plate with superglue and wires were soldered on the transducers for signal collection as shown in Figure 6.8. The signal was excited at the actuator and received by the sensors for reflected and transmitted signals with a sampling frequency of 50 MHz after 512 samples were averaged.

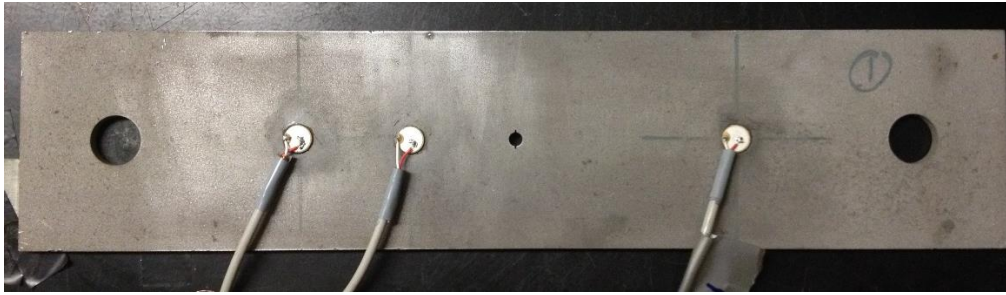


Figure 6.8 5 mm steel plate specimen.

The excitation was a 15.5-cycles tone burst signal at a central frequency of 763 kHz with an excitation voltage of 400 V<sub>p-p</sub>. A signal generating and collection system including a signal generator, an amplifier, a high voltage low pass filter and an oscilloscope is used as shown in Figure 6.9.

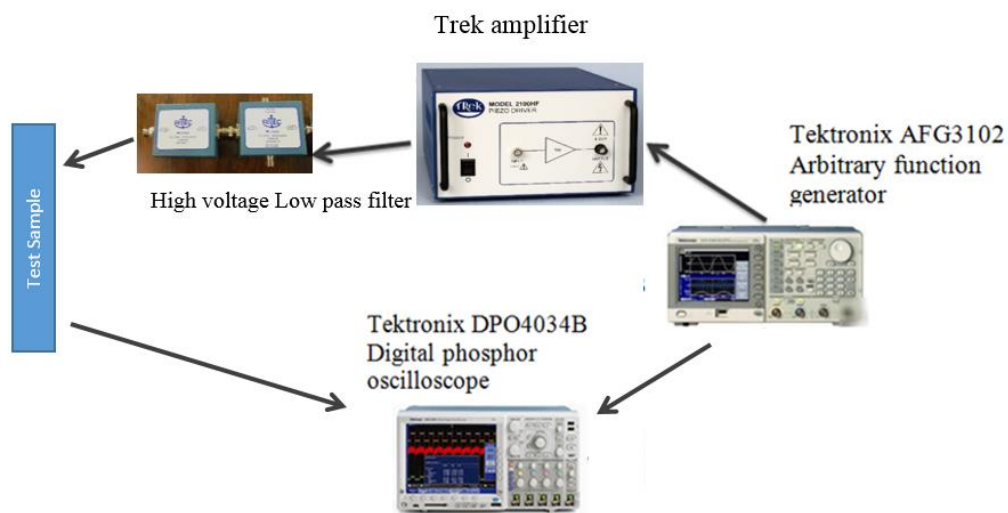


Figure 6.9 Data acquisition procedure in experiment.

The fatigue crack in the steel plate was generated using an Instron 8802 servo hydraulic testing machine. Sinusoidal cyclic tensile loads were applied, with a frequency of 20 Hz and a stress ratio of 0.1. The maximum stress was set to be 150 MPa, which is about 50% of the yield strength, resulting in a maximum load of 60 kN and a minimum load of 6 kN. The signals were kept recording until there was obvious second harmonic in the frequency domain in both reflected and transmitted signals after a fast Fourier transform, indicating

-Quantitative evaluation of fatigue crack using nonlinear guided waves in pipelines-

the nonlinearity caused by damage. The test procedure and set-up are shown in Figure 6.10.

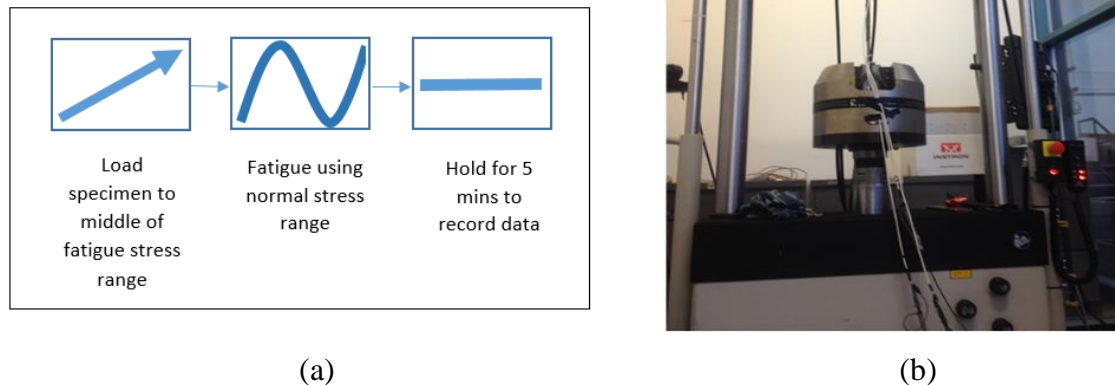


Figure 6.10 Fatigue machine (a) test procedure and (b) set up.

### 6.1.3.2 Experiment results

After collecting signals, transmitted and reflected signals were processed with FFT and obvious second harmonic appears at 50000 fatigue cycles as in Figure 6.11. The transmitted signal was further processed through MATLAB with a band pass filter around fundamental and double frequency with a bandwidth of  $\pm 50$  kHz. Then a Hilbert transform was used to observe the amplitude of wave packet of interest. Obvious second harmonic wave appeared at one of the transmitted signals in the time domain after signal processing is shown in Figure 6.12(b). It is shown that for the received signal at fundamental frequency (as in Figure 6.12(a)), as the crack length increases, there is no apparent difference between benchmark and the signal at 50000 fatigue cycles, which is similar with the simulation results. The arrival time of first wave S1 is at 37  $\mu$ s, slightly later than the simulation results (33  $\mu$ s) but is still acceptable. And at the double frequency in the time domain, the second harmonic wave S2 arrived at 40  $\mu$ s has an amplitude much

-Quantitative evaluation of fatigue crack using nonlinear guided waves in pipelines-

higher than the benchmark, indicating the nonlinearity caused by fatigue crack in the plate. It can be seen in the benchmark signal there is also nonlinearity which is higher than that in the simulation results, which may be caused by material and system nonlinearities in experiments.

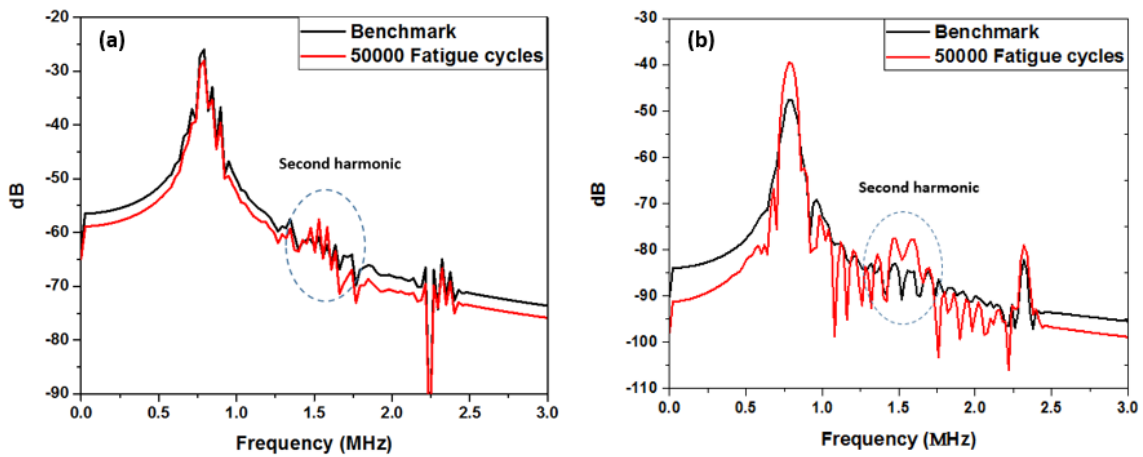


Figure 6.11 Signal after FFT in the frequency domain of (a) reflection and (b) transmission.

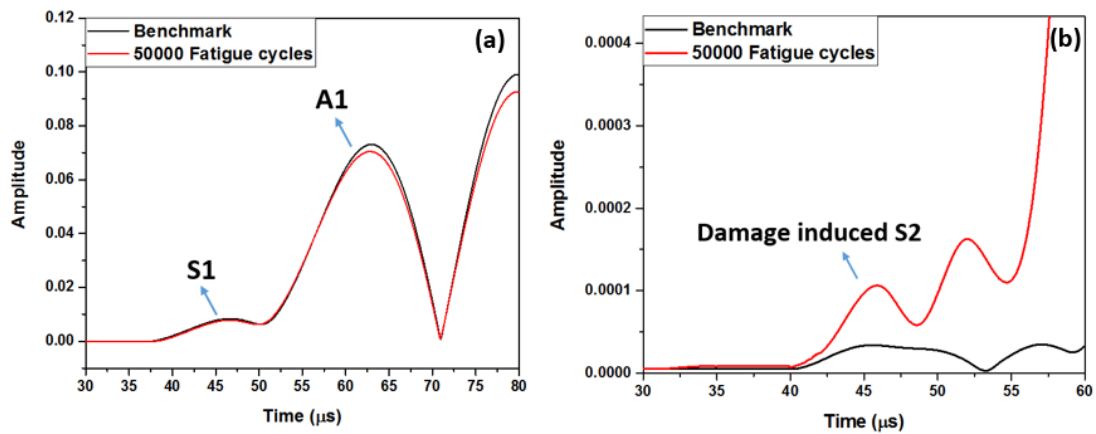


Figure 6.12 Transmitted signal after band pass filter at (a) fundamental frequency and (b) at double frequency.

## 6.2 Material nonlinearity in pipes

Many studies have focused on the analysis of material nonlinearity in plates [159] and pipes [14, 15, 108]. Before the analysing of fatigue crack detection with nonlinear guided

-Quantitative evaluation of fatigue crack using nonlinear guided waves in pipelines-

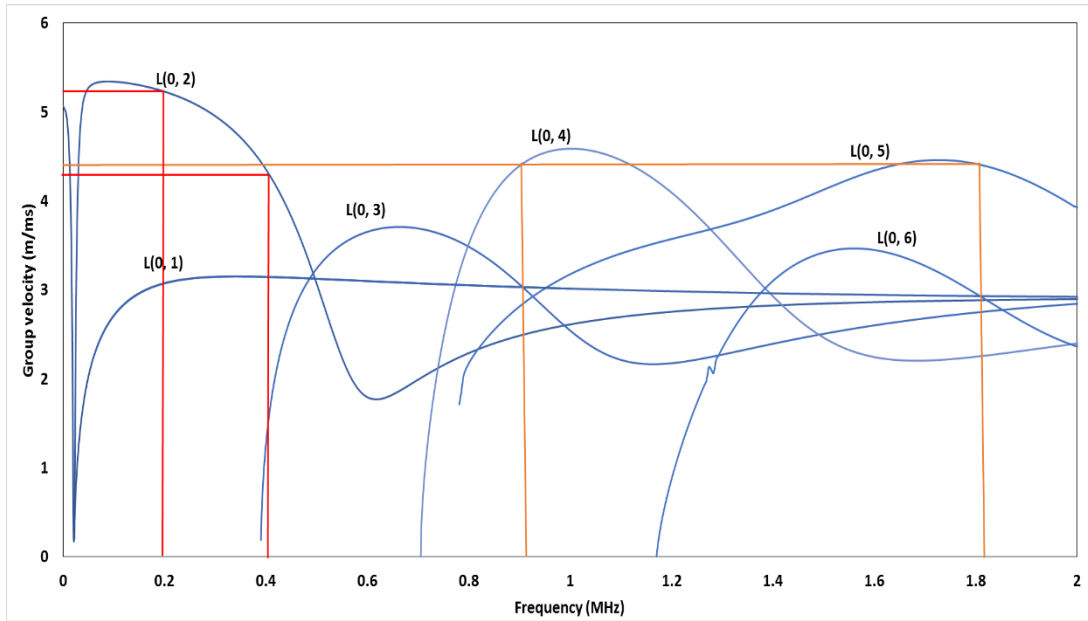
waves in pipe structures, material nonlinearity in pipes are studied. Two criterions for the generation of cumulative second harmonic have been mentioned in previous studies [14, 15, 108]: non-zero power flux and synchronism. In this section, FE simulation models of a pipe with excitation condition with and without following the criteria of accumulative second harmonic generation will be established to compare the results and to figure out the necessity of considering these conditions for the CAN detection in following sections.

### **6.2.1 Simulation models for material nonlinearity**

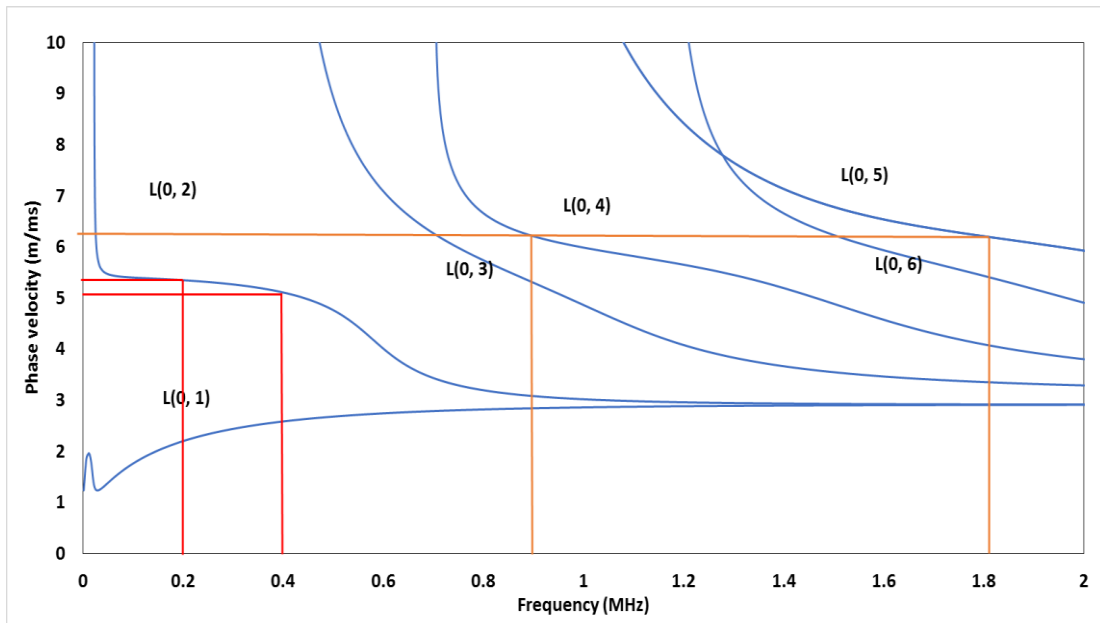
To generate cumulative second harmonic in pipes, two conditions need to be satisfied: synchronism and non-zero power flux, which means that the phase velocity and group velocity of the fundamental and second harmonic waves have to be consistent. In this section, simulation models with FE method will be conducted to confirm these conditions and the reliability of the model. Results from models with and without satisfying these conditions will be compared and discussed.

#### **6.2.1.1 Mode selection**

To select proper excitation wave mode and frequency, the dispersion curve of an 80 mm outer diameter and 4 mm wall thickness was plotted in Figure 6.13. Mode pair for two cases with and without satisfying conditions for cumulative second harmonic need to be selected. From the figure, L(0, 2) mode at 200 kHz and L(0, 4) mode at 907 kHz were selected as fundamental mode for these two cases, where the mode pair L(0, 4) at 907 kHz and L(0, 5) at 1814 kHz have same group and phase velocity, while the mode pair L(0, 2) at 200 kHz and L(0, 2) at 400 kHz did not satisfy the conditions.



(a)



(b)

Figure 6.13 Dispersion curve of a 80 mm outer diameter aluminium pipe for (a) group velocity and (b) phase velocity.

### 6.2.1.2 Numerical analysis for two cases

A 3D model simulated by Abaqus/Explicit was utilised to simulate these two cases. The maximum element size in the model was 1 mm, calculated based on the case with 907 kHz input which has smaller wavelength at double frequency than another case. The time step is  $5e-8$  s.

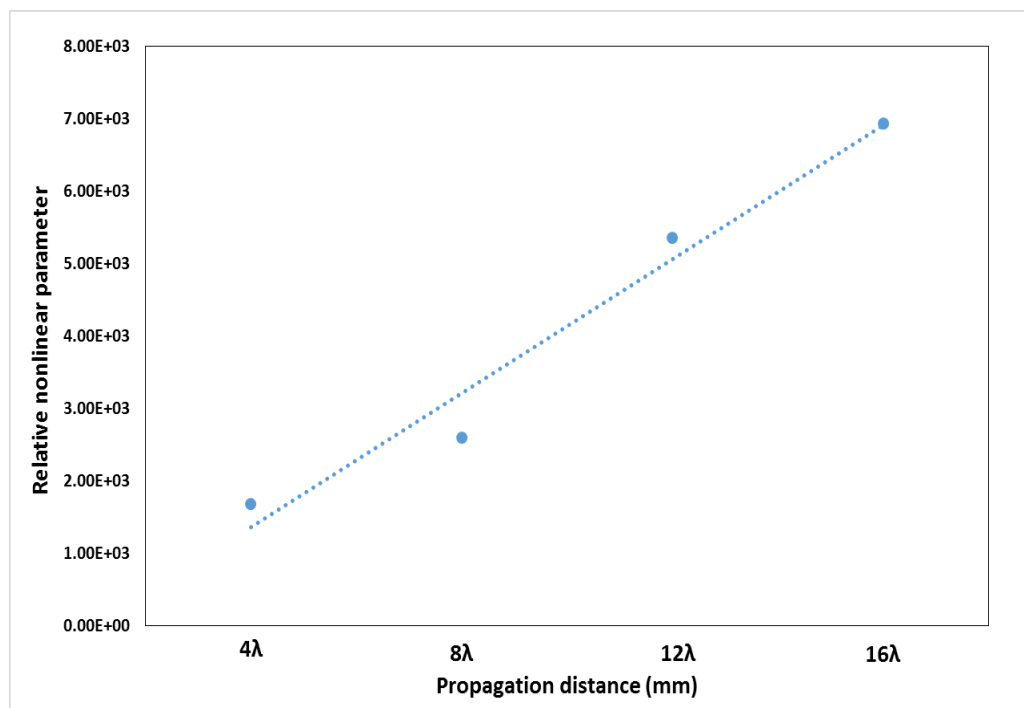
5.5 cycles and 10 cycles Hanning-windowed tone burst signal were excited at 200 kHz and 907 kHz, respectively. To generate pure longitudinal wave and suppress the flexural wave modes in the simulation, a ring of actuators contains 32 elements was simulated with a point load at each element centre in the direction of pipe axis, similar to the case in Section 5.3.1. Four monitoring points were set at  $4\lambda$ ,  $8\lambda$ ,  $12\lambda$ , and  $16\lambda$  in a line along the propagation distance to observe the accumulation of the second harmonic for each case, where  $\lambda$  is the wavelength of excitation at 200 kHz as 26 mm and 907 kHz as 6.8 mm respectively. To introduce the material nonlinearity which exists homogeneously in the simulation model, third order elastic constants [13] were considered for material properties and then imported into the model with a user subroutine VUMAT file [97]. The material properties are listed in Table 6.2.

Table 6.2 Material properties for simulation model.

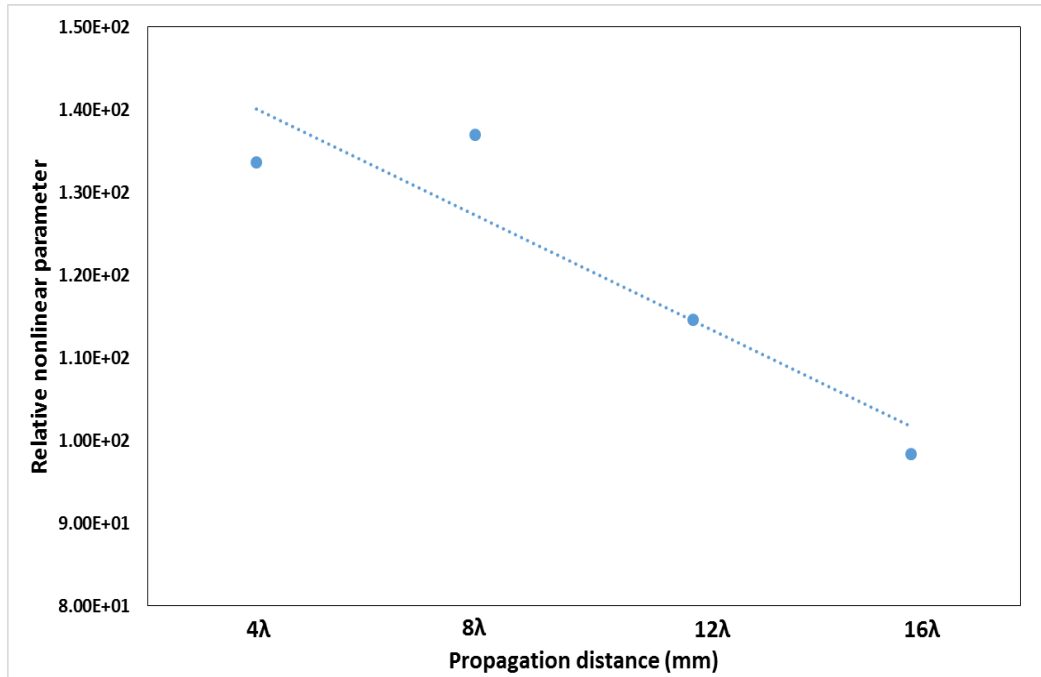
<b>Material properties</b>	
<b>Density (kg/m<sup>3</sup>)</b>	2700
<b>Young's modulus (GPa)</b>	68.9
<b>Poisson's ratio</b>	0.33
<b>Third elastic constants (GPa)</b>	A -320
	B -200
	C -190

### 6.2.2 Results of simulation methods

Band pass filter in MATLAB with central frequency at fundamental and double frequency with  $\pm 50$  kHz and  $\pm 100$  kHz bandwidth were used on revived signals from 907 kHz input and 200 kHz input respectively. Relative nonlinear parameters as in Section 6.1.2.2 were calculated in the time domain for all the received signals and plotted with propagation distance, as in Figure 6.14.



(a)



(b)

Figure 6.14 Relative nonlinear parameter with propagation distance for (a) 907 kHz and (b) 200 kHz.

As seen in the figure, for 907 kHz input case which satisfied the criteria of synchronism and non-zero power flux, the relative nonlinear parameter keeps increase linearly with the propagation distance. However, when these conditions were not satisfied in Figure 6.14(b) for 200 kHz input, the nonlinear parameter cannot accumulate as the wave propagated and the energy of second harmonic dissipated, which resulted in a decrease in the nonlinear parameter with the propagation distance.

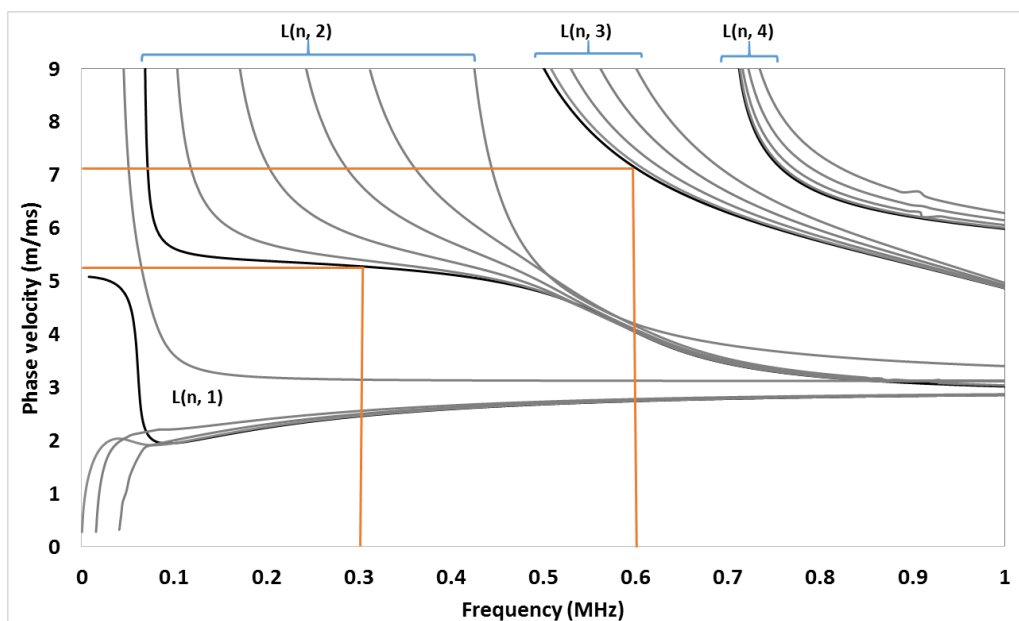
Therefore, appropriate selection of the mode pair for second harmonic generation will significantly affect the measurement of nonlinearity from material itself. In the following studies, when CAN is the focus to investigate, the material nonlinearity should be minimised by choosing mode pair that will not generate cumulative second harmonic.

## 6.3 Fatigue crack detection in pipes with second harmonic generation method

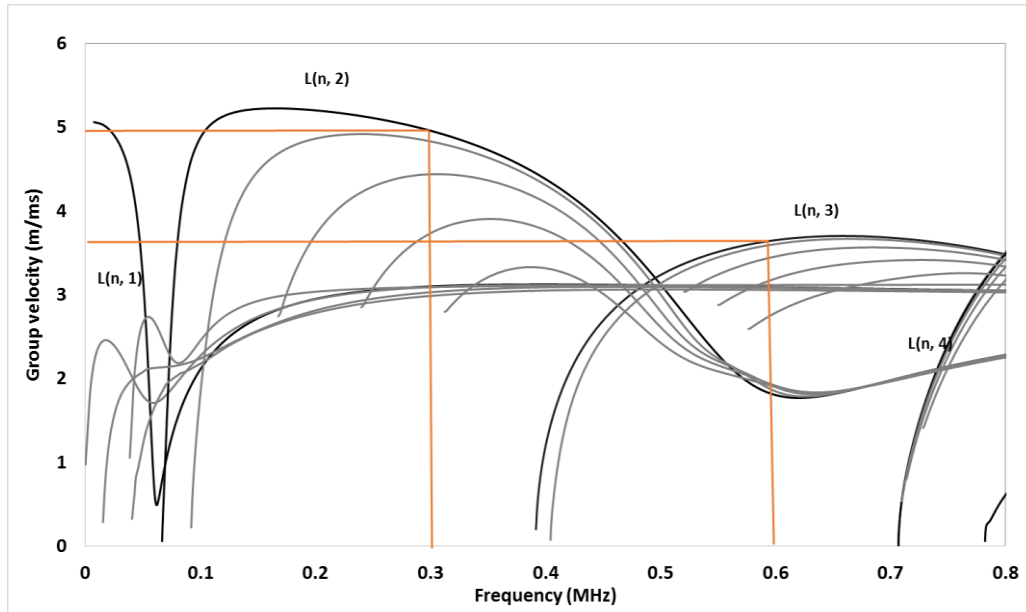
In this section, both numerical and experimental methods are conducted to detect the CAN caused by a fatigue crack through second harmonic generation method in an aluminium pipe. Material nonlinearity is included in simulation model to be consistent with the benchmark in experiment test and the simulation method is similar with Section 6.2.1.

### 6.3.1 Excitation selection

To select an appropriate wave mode for second harmonic generation, the dispersion curve of an aluminium pipe with 30 mm outer diameter and 4 mm wall thickness was plotted, as in Figure 6.15.



(a)



(b)

Figure 6.15 Dispersion curve of 30 mm OD and 4 mm wall thickness aluminium pipe. (a) Phase velocity; (b) Group velocity.

Wave mode  $L(0, 2)$  is selected as fundamental wave since it is non-dispersive over a wide range frequency and has the fastest group velocity within this frequency range. The minimum excitation frequency of the signal generator in experiment is 200 kHz, therefore, different excitation frequency from 200 kHz to 400 kHz were tried in experiment and finally 300 kHz was selected, which can avoid the cumulative effect induced by material nonlinearity and highlight the second harmonic generated by CAN. The fundamental wave mode  $L(0, 2)$  would be converted to  $L(0, 3)$  at 600 kHz but with a different group velocity. Therefore, the cumulative effect of material nonlinearity would be minimised due to the group velocity difference. Meanwhile, from the dispersion curve, it could be observed that the lower order flexural wave modes,  $F(n, 2)$ , had group velocities close to the longitudinal wave  $L(0, 2)$ . In this case, more than one wave mode would be generated from the same group as input, unless a specific arrangement of wave excitation was designed. For convenience, a notation from Rose [25] was adopted in the subsequent

study, in which  $L(n, m)$  was defined as a longitudinal mode group, including axisymmetric modes  $L(0, m)$  and non-axisymmetric modes  $F(n, m)$ . The integer  $n$  is the circumferential order of a mode and the integer  $m$  denotes the group order of a mode. In this study, therefore, the fundamental waves were a group of waves  $L(n, 2)$  consisting of longitudinal mode  $L(0, 2)$  and flexural modes  $F(n, 2)$  ( $n=1,2,3\dots$ ). And as analysed in Chapter 5, more than one wave modes would be generated at the double frequency in this pipe structure.

### **6.3.2 Signal processing method**

For the received signals from the numerical and experimental analyses, a similar signal processing method was applied in MATLAB. After each signal was received, a  $180^\circ$  out-of-phase signal was input to the pipe again at the same location, followed by the same signal collection procedure. These two received signals were then superimposed to reduce the fundamental component contribution and enhance the second harmonic [160]. Subsequently, the short-time Fourier transform (STFT) was performed on each of the combined signals with proper window size, and the component slices at double frequency were extracted and converted back to the time domain using the inverse fast Fourier transform [97]. Meanwhile, the STFT was also applied on the original signals before they were superimposed with the  $180^\circ$  out-of-phase signals and the slices at fundamental frequency were also extracted. Finally, signals of fundamental and double frequencies in the time domain were obtained and interpreted. The processing procedure is flowcharted in Figure 6.16.

-Quantitative evaluation of fatigue crack using nonlinear guided waves in pipelines-

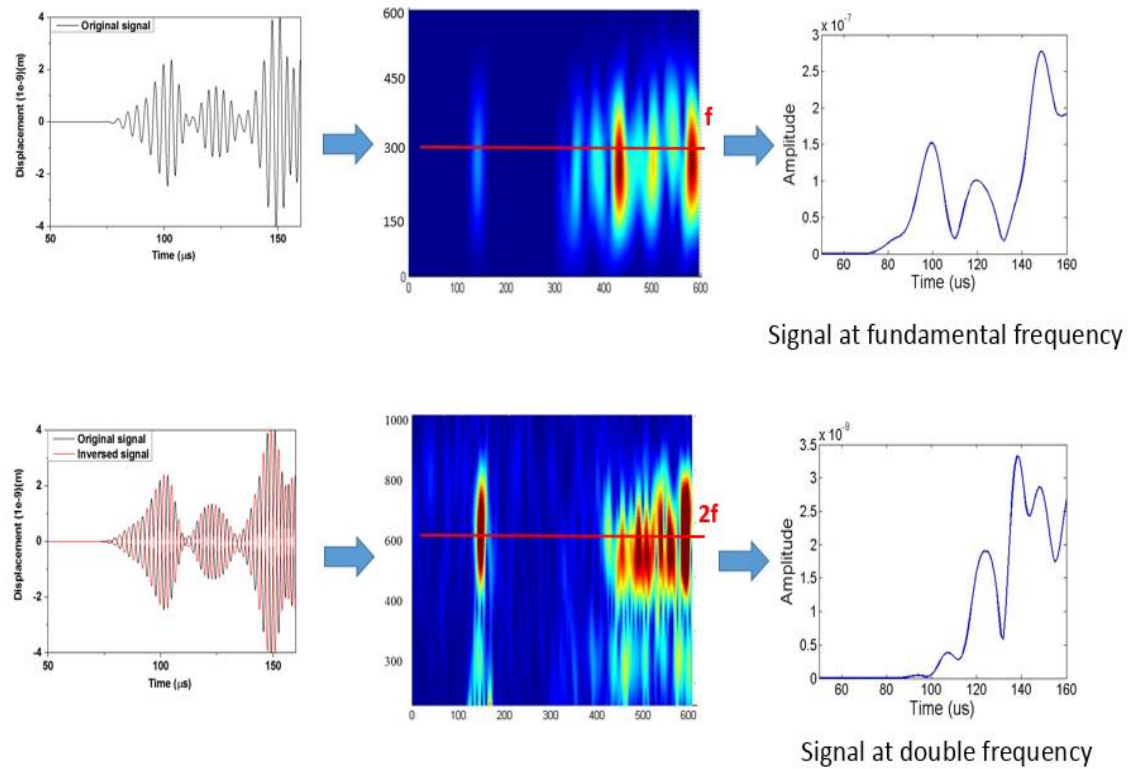


Figure 6.16 Signal processing procedure.

### 6.3.3 Numerical analysis

#### 6.3.3.1 Simulation model

Different numerical techniques are usually used to investigate the interaction between guided waves and damage, such as spectral element method [161] and finite element method [162], also, similar numerical methods used to simulate different microcrack models were discussed in [163]. In this study, a 3D model simulated by Abaqus/Explicit with a seam crack was utilised to analyse the propagation of longitudinal and flexural wave modes and the nonlinearity caused by both the material and the “breathing” crack. An aluminium pipe 4 mm thick, 30 mm outer diameter and 1 m long was modelled. The material properties are listed in Table 6.3.

Table 6.3 Material properties of aluminium pipe.

<b>Material properties</b>	
<b>Density (kg/m<sup>3</sup>)</b>	2700
<b>Young's modulus (GPa)</b>	70
<b>Poisson's ratio</b>	0.33
<b>Yield strength (MPa)</b>	310
<b>Tensile strength (MPa)</b>	276
<b>Third elastic constants (GPa)</b>	A -320
	B -200
	C -190

A through-thickness notch 8 mm long and 2 mm wide was prepared in the middle of the pipe for fatigue crack initiation, similar to the following experimental settings. The central excitation frequency was 300 kHz and a 6-cycle tone burst signal was excited. The excitation signal was applied as a pointed load at four edges of the transducer along the direction of the axis of the pipe, as shown in Figure 6.17.

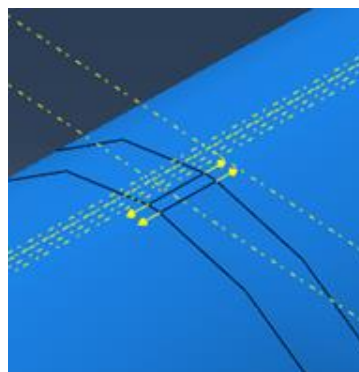


Figure 6.17 Loads applied in simulation model.

As only one actuator was used in the model,  $L(n, 2)$  consisting of both longitudinal mode  $L(0, 2)$  and flexural modes  $F(n, 2)$  at the selected frequency were generated. Two

monitoring points were located in front of and behind the notch for receiving transmitted and reflected signals respectively. The arrangement of the actuator, notch and monitoring points is shown in Figure 6.18.

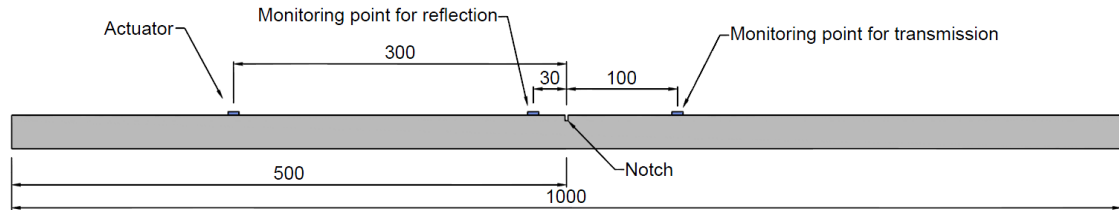


Figure 6.18 Configuration of the specimen.

Three-dimensional eight-node brick elements (C3D8R) were utilised, and the maximum element size and time step were calculated by equations [145]

$$L_{max} \leq \frac{\lambda_{min}}{7} = \frac{11.83}{7} = 1.69mm, \quad (6.1)$$

$$\Delta t \leq \frac{L_{max}}{c_g} = \frac{0.001}{4950} = 2.02 \times 10^{-7}s, \quad (6.2)$$

where  $L_{max}$  is the maximum element size in this model,  $\lambda_{min}$  is the minimum wavelength and  $c_g$  is the fastest group velocity among all wave modes. In the model, the element size was determined as 1 mm, which was roughly 18 elements per wavelength for L(0, 2) mode and 12 elements per wavelength for L(0, 3) mode, and a time step of 5e-8 s was selected for stability of calculation.

To introduce the material nonlinearity which exists homogeneously in the simulation model, the procedure is similar with Section 6.2. Third order elastic constants [13] were considered for material properties and then imported into the model with a user subroutine VUMAT file [97]. The third order elastic constants are listed in Table 6.3. To model the “breathing” crack in the model, the seam crack definition was used on each surface of the

-Quantitative evaluation of fatigue crack using nonlinear guided waves in pipelines-

crack, as illustrated in Figure 6.19, to enable the breathing behaviour when waves interacted with the crack. The crack was through-thickness and 1 mm long in the circumferential direction, located at both tips of the notch.

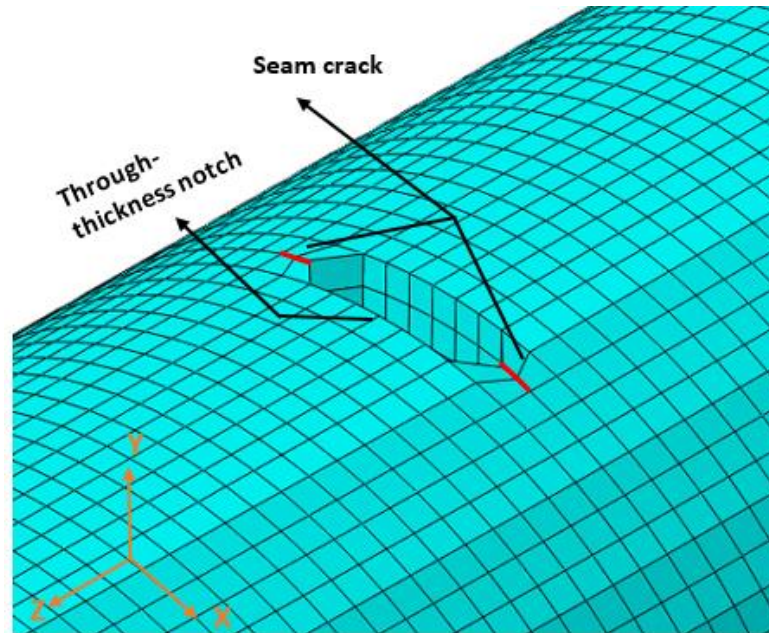


Figure 6.19 Seam crack in pipe model.

### **6.3.3.2 Results from numerical analysis**

For the transmitted signal, the signal received directly from simulation is shown in Figure 6.20. Due to the single transducer excitation, more than one wave packet appears in the received signal. The arrival time of the first wave packet is 83  $\mu\text{s}$ , which is consistent with the theoretical velocity of  $L(0, 2)$  from the dispersion curve, followed by flexural wave modes and  $L(n, 1)$  modes. Signals after processing for the case with material nonlinearity only are shown in Figure 6.21, which are in the time domain at fundamental frequency and at double frequency. It is obvious that the second harmonic wave arrives at the same time as the fundamental wave. The average amplitude level at double frequency is about 0.01% of that at 300 kHz.

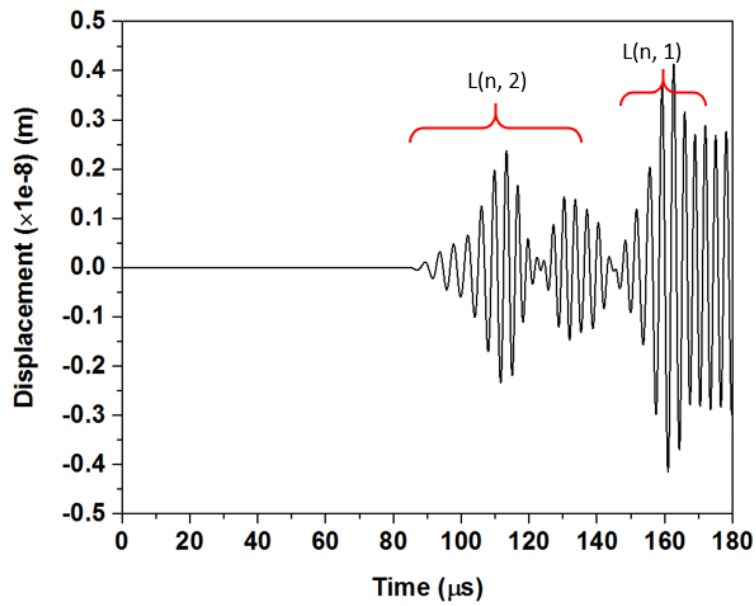


Figure 6.20 Transmitted signal from simulation model.

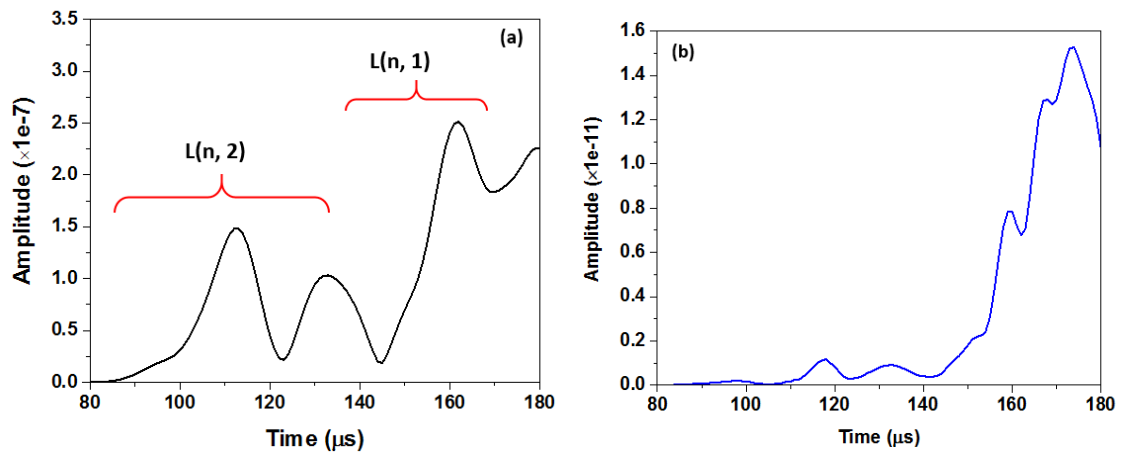


Figure 6.21 Transmitted signal from model with material nonlinearity after STFT (a) at fundamental frequency; (b) at double frequency.

Figure 6.22 shows the case with a seam crack, in which the signal at fundamental frequency displays no great difference from that with material nonlinearity only, while the second harmonic wave arrives at 93  $\mu\text{s}$ , which is later than the fundamental one, since the group velocity of  $L(0, 3)$  at double frequency was slower than that of  $L(0, 2)$  at fundamental frequency, reflecting the fact that the nonlinearity was induced by the close crack. There are also multiple waves generated at double frequency before the arrival

time of  $L(0, 1)$ , which contains longitudinal mode  $L(0, 3)$  and flexural modes from the same group  $F(n, 3)$ . The average amplitude of the second harmonic wave is approximately 1.3% of the fundamental wave, which is higher than the nonlinearity caused by material. The results from the pipe structures differs from the experiment results in Section 6.1 of a plate specimen, where only one wave packet was generated at double frequency.

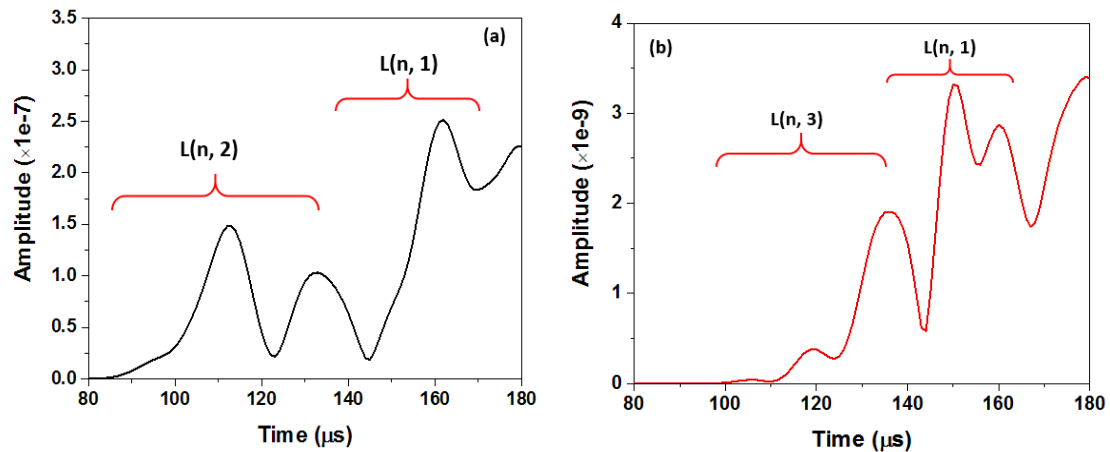


Figure 6.22 Transmitted signal from model with CAN after STFT (a) at fundamental frequency; (b) at double frequency.

For the reflected signal (Figure 6.23), the first arriving wave packet is  $L(n, 2)$  directly from the actuator, followed by reflected  $L(n, 2)$  from the notch and the direct  $L(n, 1)$ . In the case with material nonlinearity at double frequency, the waves arrive at almost the same time (59  $\mu s$ ) as the fundamental wave, and the average amplitude level at double frequency is around 0.04% of that at fundamental frequency. This value is slightly higher than that in transmitted signal since the sensor is closer to the crack for reflected signal. As for the model with the seam crack in Figure 6.24, the first arriving wave at double frequency is at 72  $\mu s$ , which indicates the arrival of  $L(0, 3)$ . There are also multiple wave packets including flexural waves before the arrival of  $L(0, 1)$  at 107  $\mu s$ , with the average amplitude approximately 1.2% of the fundamental wave, which is much higher than the amplitude caused by material nonlinearity.

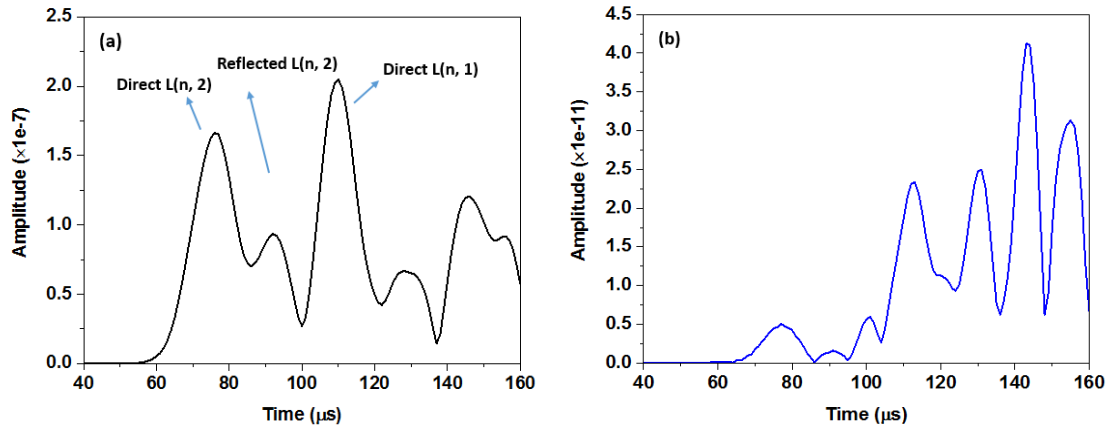


Figure 6.23 Reflected signal from model with material nonlinearity after STFT (a) at fundamental frequency; (b) at double frequency.

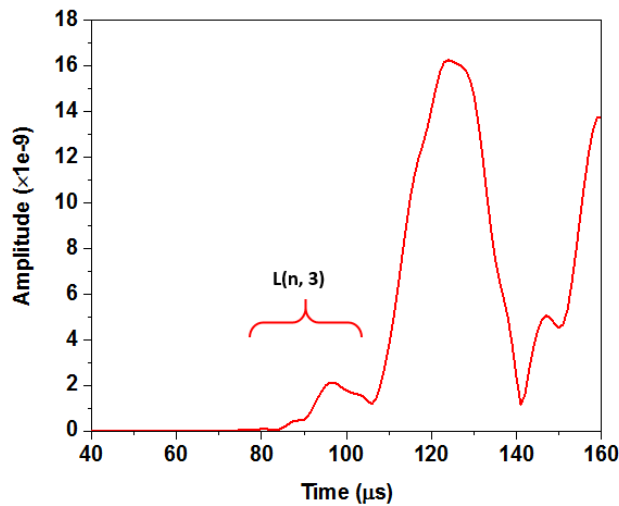


Figure 6.24 Reflected signal from model with CAN after STFT at double frequency.

### 6.3.4 Experimental validation

Experimental testing was performed for validation of the simulation results. Three-point bending fatigue test on an aluminium pipe was carried out to generate the fatigue crack in the middle of the pipe. Signals were collected and processed to obtain the second harmonic waves.

#### **6.3.4.1 Specimen preparation**

Two 6061-T6 aluminium pipes with the same material properties and dimensions as in the simulation model were used for experiment test. A through thickness notch was drilled in the middle of the pipe for fatigue crack initiation. The surface of the pipe was polished with sand papers and cleaned with acetone. Different size of piezoelectric transducers were tried on the pipe to receive reasonable signals as described in Section 4.2.3 and finally rectangular piezoelectric transducers 5 mm×10 mm and 5 mm ×5 mm acting as actuator and receivers respectively were attached on the pipe with superglue in a line with the same locations as in the simulation model (in Figure 6.25). Wires were connected to the transducers with soldering and during the fatigue test all the wires and transducers were protected to prevent breaking.

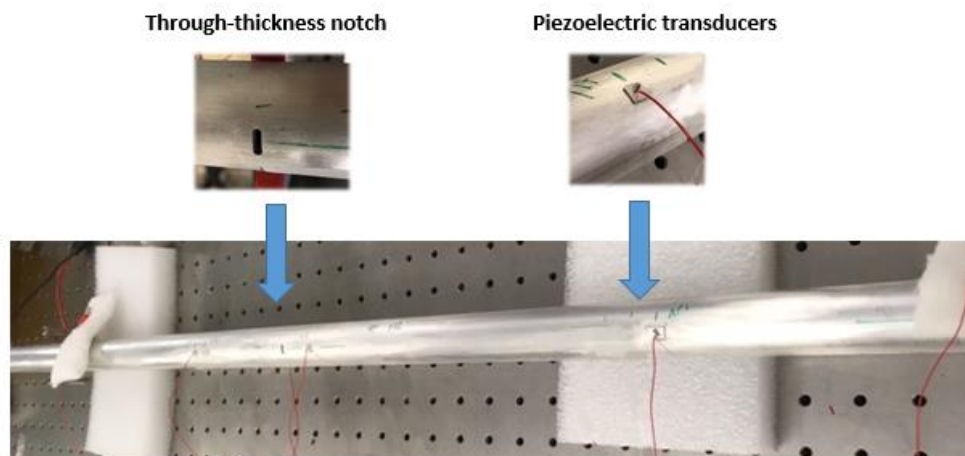


Figure 6.25 Pipe specimen preparation.

#### **6.3.4.2 Experiment set up**

To induce a fatigue crack, a steel frame was designed to hold the pipe and was combined with the fatigue machine. The dimension of the steel frame is in Figure 6.26, where the

-Quantitative evaluation of fatigue crack using nonlinear guided waves in pipelines-

pipe passing through the holder was fixed with bolt. The pipe was therefore under three-point bending with a cyclic load in the middle, as in Figure 6.27.

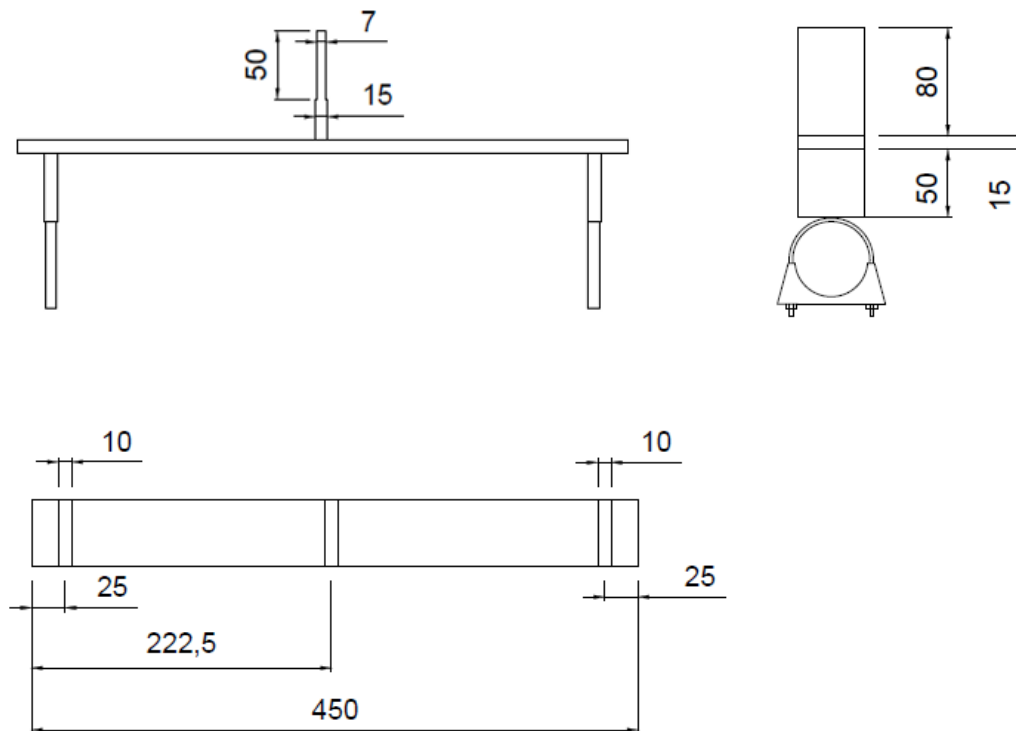


Figure 6.26 Design of steel frame for three-point bending fatigue test.

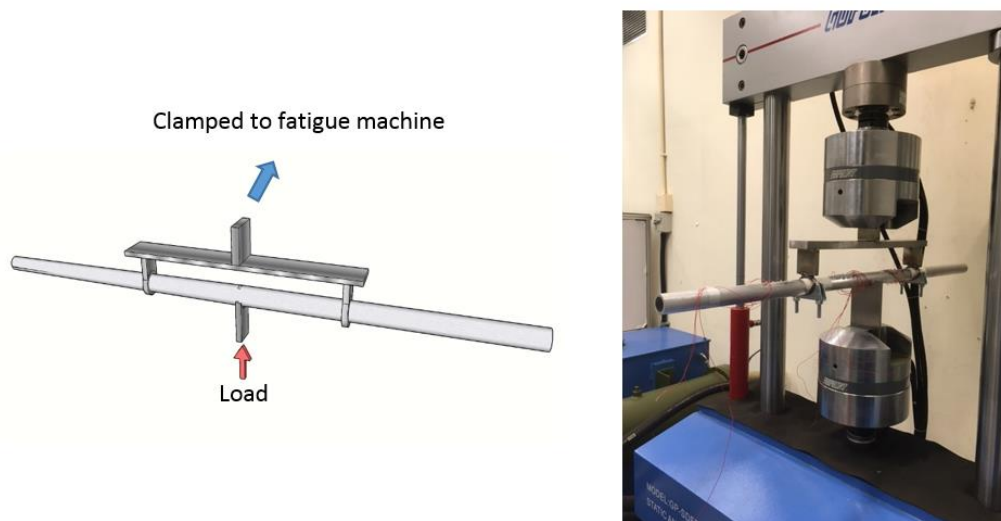


Figure 6.27 Three-point bending fatigue test.

-Quantitative evaluation of fatigue crack using nonlinear guided waves in pipelines-

The cyclic load ranged from 0.2 kN to 2 kN with a 5 Hz load frequency and the maximum load was equivalent to about 50% of the yield stress of the pipe. A signal generating and collecting system (see Figure 6.28) including Ritec RAM-5000 SNAP and an Agilent digital oscilloscope was used to generate and receive the signals. The system also contained a high-power low-pass filter which could suppress harmonics higher than 300 kHz from the source before the signal was input to the transducer.

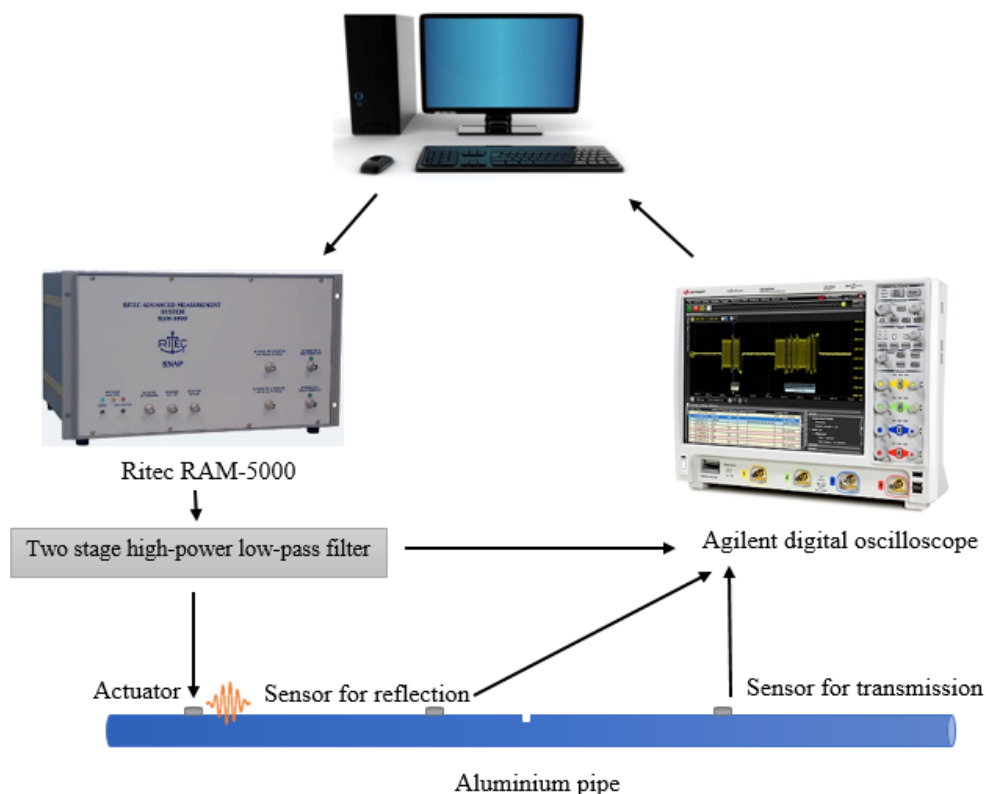


Figure 6.28 Signal generation and collection system.

A 6-cycle tone burst signal at a central frequency of 300 kHz was applied on the actuator and the reflected and transmitted signals were monitored by sensors until the second harmonic wave appeared in received signals when fatigue cycles reached 22000. All the received signals were averaged 1024 times with the sampling frequency of 200 MHz before recording. Also, the load from the fatigue machine was removed during signal collection to prevent any influence of external load on the “breathing” behaviour of the

fatigue crack. To ensure that the nonlinearity monitored was induced by the opening and closing behaviour of the fatigue crack, application of the cyclic load was continued until the nonlinearity in the signal disappeared at about 42000 fatigue cycles, which indicated that the crack had developed to macro size. After that, the pipe side with the fatigue crack was turned 180° to face downwards and then a static load was applied upwards to the middle of the bottom of the pipe to close the crack, so as to observe whether the “breathing” behaviour still existed in the crack.

#### **6.3.4.3 Results from experiment**

The received transmitted signal before fatigue test from experiments is shown in Figure 6.29. The arrival time of the first wave packet is around 86  $\mu\text{s}$ , which is very close to the velocity in simulation. There were also similar multiple wave packets within the period of interest from 86  $\mu\text{s}$  to 126  $\mu\text{s}$ , which contains  $L(0, 2)$  and  $F(n, 2)$  modes as a group of  $L(n, 2)$ . The shape of the received wave was slightly different from that obtained in the simulation results, due to the unavoidable differences between simulation and experiments, e.g. the efficiency of the transducer and certain flexural modes that were not generated appropriately. For the case without the introduction of fatigue crack in the pipe, some material nonlinearities existed and the signals after processing are plotted in Figure 6.30(a). From the figure, it can be seen that the second harmonic wave arrives at approximately the same time as the fundamental wave. However, the average amplitude of the second harmonic wave is about 0.8% of that in fundamental signal, which is much higher than in the corresponding simulation results. This difference is acceptable since ideally in practice the material is not homogeneous and there are also inherent nonlinear sources from the equipment and environment.

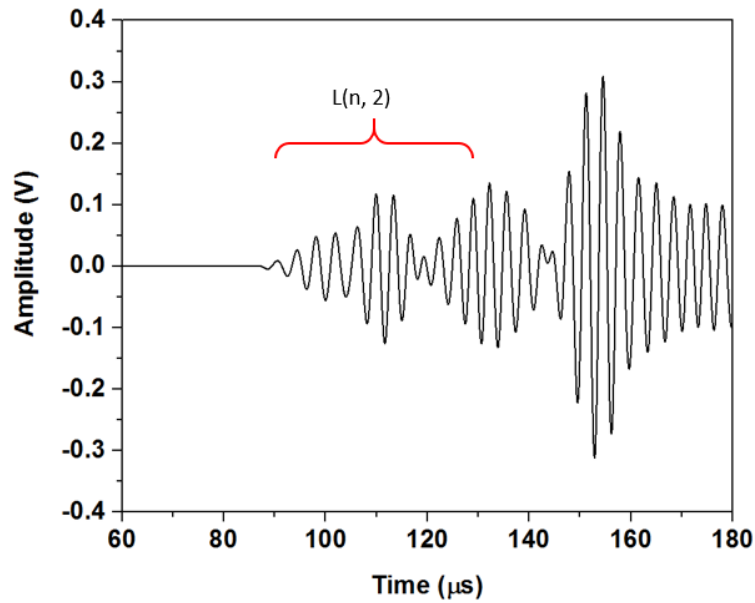


Figure 6.29 Transmitted signal from experiment.

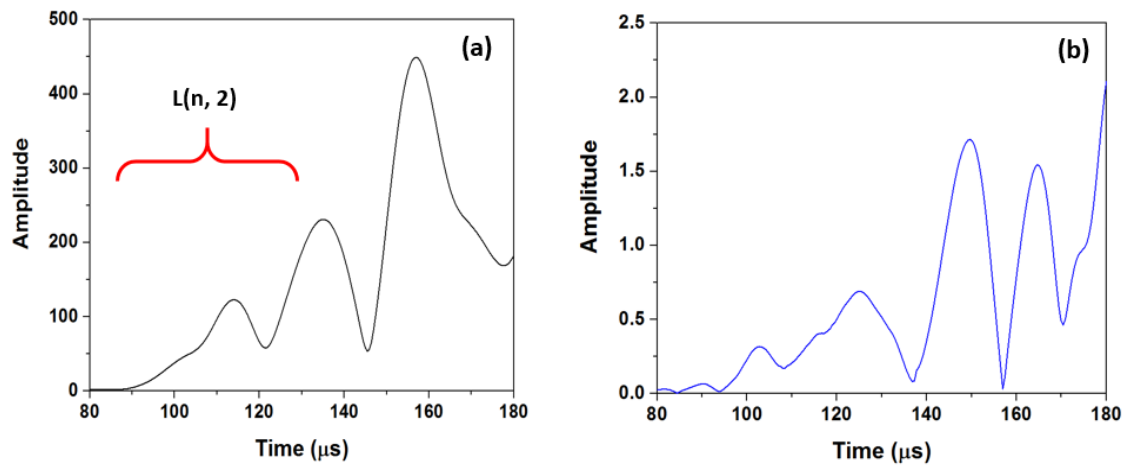


Figure 6.30 Transmitted signal from experiment before fatigue test after STFT (a) at fundamental frequency; (b) at double frequency.

During the fatigue test, signal collection was stopped at 22000 fatigue cycles when an obvious increase in the second harmonic wave was observed in the signals. Comparison of the signals before and after fatigue testing of two specimens are shown in Figure 6.31. As in the simulation results, the second harmonic wave (red line) arrives later than the benchmark signal in experiments and more than one generated wave packet is higher than

the wave packets caused by material nonlinearity. The average amplitude level is above 2% of the signal at the fundamental frequency. To confirm the results from the experiment is repeatable, another specimen with the same configuration was also studied, and the results of the transmitted signals is shown in Figure 6.31(b), where the average amplitude of second harmonic wave in benchmark signal is about 0.9% of that in the fundamental signal and the average amplitude of the second harmonic wave in damage case is about 1.8% of the signal at the fundamental frequency, similar to the results from the first specimen.

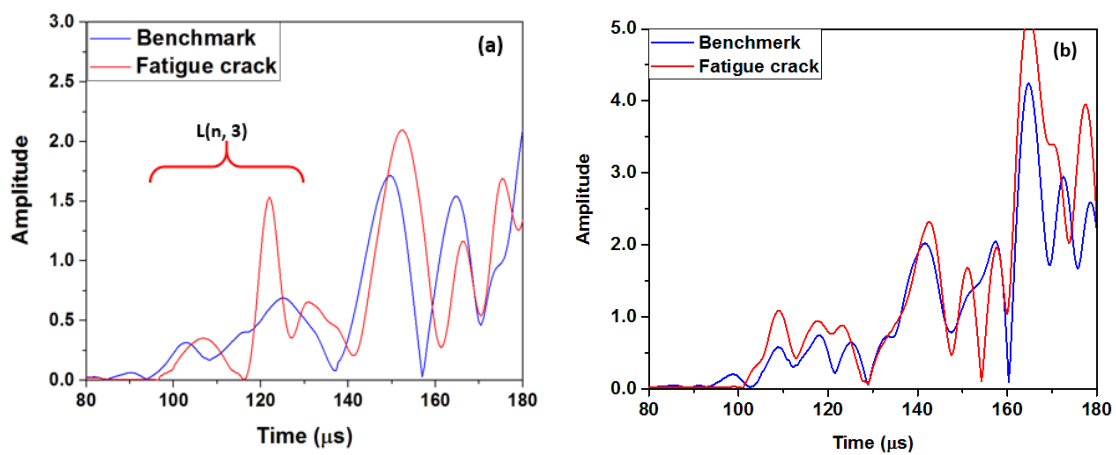


Figure 6.31 Transmitted signal from experiment before fatigue test (blue line) and after 22000 fatigue cycles (red line) at double frequency (a) specimen 1; (b) specimen 2.

For the reflected signals (Figure 6.32), the received signal also contains direct wave  $L(n, 2)$ , reflected  $L(n, 2)$  and direct  $L(n, 1)$ , and the velocities of these wave packets are approximately the same as those in the simulation results. The signal at double frequency shows that the first second harmonic wave arrived at  $58 \mu\text{s}$  when there was only material nonlinearity and at  $78 \mu\text{s}$  for the case of fatigue crack, which is close to the theoretical group velocity of  $L(0, 3)$  mode. Compared with the transmitted signal, the multi-mode second harmonic waves were not that apparent due to the short distance from the sensor to the crack, where the different wave modes have not been separated completely.

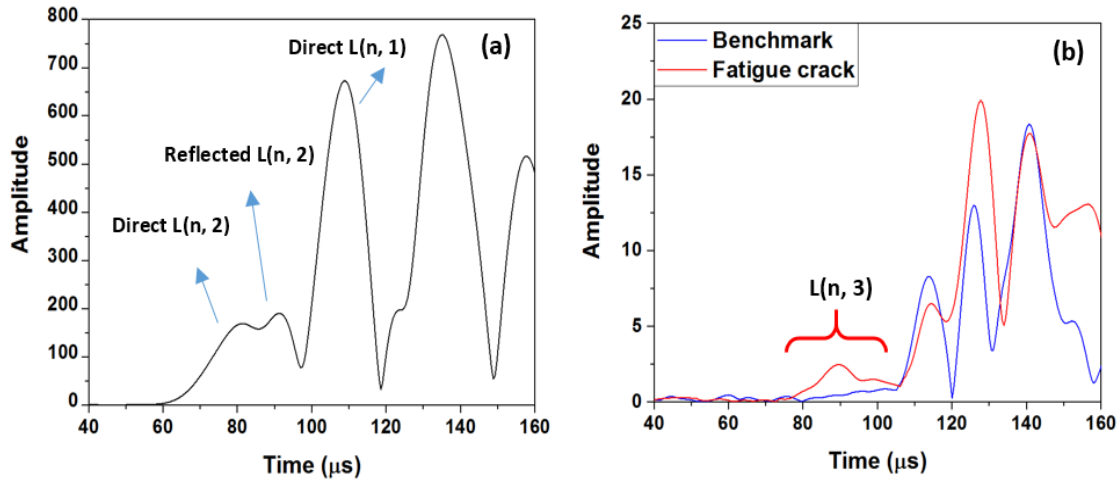


Figure 6.32 Reflected signal from experiment after 22000 fatigue cycles after STFT (a) at fundamental frequency; (b) at double frequency.

To confirm that the nonlinearity in the experiments was caused by the opening and closing behaviour of the fatigue crack under tension and compression phase of guided waves, the pipe side with the crack was faced downwards after the nonlinearity was minimised to noise level in the collected signal. Then a static load at 100 N was applied upwards in an attempt to close the crack. The transmitted signals before and after applying the static load were recorded and processed with the same procedure as abovementioned, as illustrated in Figure 6.33. In the time period of interest, during which the second harmonic wave packet is expected to arrive, there is an obvious difference between the signals before and after applying the static load. The blue line shows that at the end of the fatigue test, the nonlinearity decreases to the noise level and the amplitude of second harmonic wave is much lower than that seen in Figure 6.31(a). In the red line, however, which represents the case where the static load was applied to close the crack, the amplitude of wave packets increases significantly at 97 μs, although it is still lower than that shown in Figure 6.31(a). Thus it was confirmed that the nonlinearity shown in Figure 6.31 and Figure 6.32 was caused by the fatigue crack. By the end of fatigue testing, however, the

-Quantitative evaluation of fatigue crack using nonlinear guided waves in pipelines-

crack was too large to close entirely although its tip still evidenced breathing behaviour, which made a marginal contribution to the nonlinearity when the static load was applied.

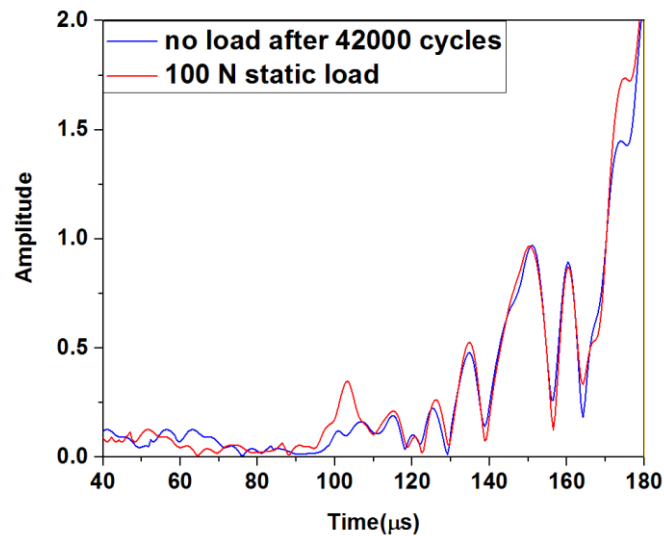


Figure 6.33 Signals after 42000 fatigue cycles and with static load.

## 6.4 Result comparisons between plate and pipe structures

Compared with pipe structures, plate structures feature relatively simple dispersion curves, where fewer wave modes co-exist at a given frequency. Results from a previous study in Section 6.1 of fatigue crack detection using nonlinear guided waves in a steel plate are compared here with results from the pipe. It should be mentioned that the simulation method of the seam crack was the same as in the pipe model, but material nonlinearity was not introduced in the plate model. Since the material nonlinearity is marginal compared to CAN, especially in numerical analysis, the difference of considering material nonlinearity in simulation model is ignored.

From the plate experiment results shown in Figure 6.12, with one actuator excitation, a single wave mode S1 arrives at 37  $\mu\text{s}$  at fundamental frequency in the time domain and there is no great difference compared with the benchmark. At the double frequency, for the benchmark case there are already some nonlinearities from the material itself, similar

to the pipe model case. In the case with fatigue crack, however, there is only one mode S2 at time 40  $\mu$ s, which was induced by the damage. The result in simulation is similar, with only one wave mode generated as second harmonic wave. In contrast, in the case of pipe structures with one actuator excitation as well, more than one wave mode was induced by the fatigue crack at double frequency, with close group velocities. The reason may be attributed to the fact that the group velocities of different wave modes, such as the antisymmetric mode and symmetric mode in plate structures, are distinct from each other and can be separated easily after a certain propagation distance. Therefore, the second harmonic wave from plate structures is generally simple with only one mode induced, whereas there would be multiple wave modes in pipe structures. The observation of multiple wave modes generated at double frequency is also shown in theoretical model in the previous chapter.

When nonlinearity in a plate structure is measured, a relative nonlinear parameter  $\beta'$  is usually used, which is the ratio of the peak value of the amplitude of the second harmonic wave to the square of the peak value of the amplitude of the fundamental wave. However, when more than one wave packet present at both fundamental and double frequency, calculation of this parameter could not be carried out precisely and a new parameter is required to measure the nonlinearity. In this circumstance, a parameter considering all generated wave packets was used, as proposed in Chapter 5, which was the envelope of the second harmonic wave within a time period divided by the envelope of the fundamental wave considering all the wave modes induced by CAN (see Figure 6.34). The time window for the transmitted signal was selected from the arrival time of the first wave packet to the theoretical arrival time of wave mode L(0, 1).

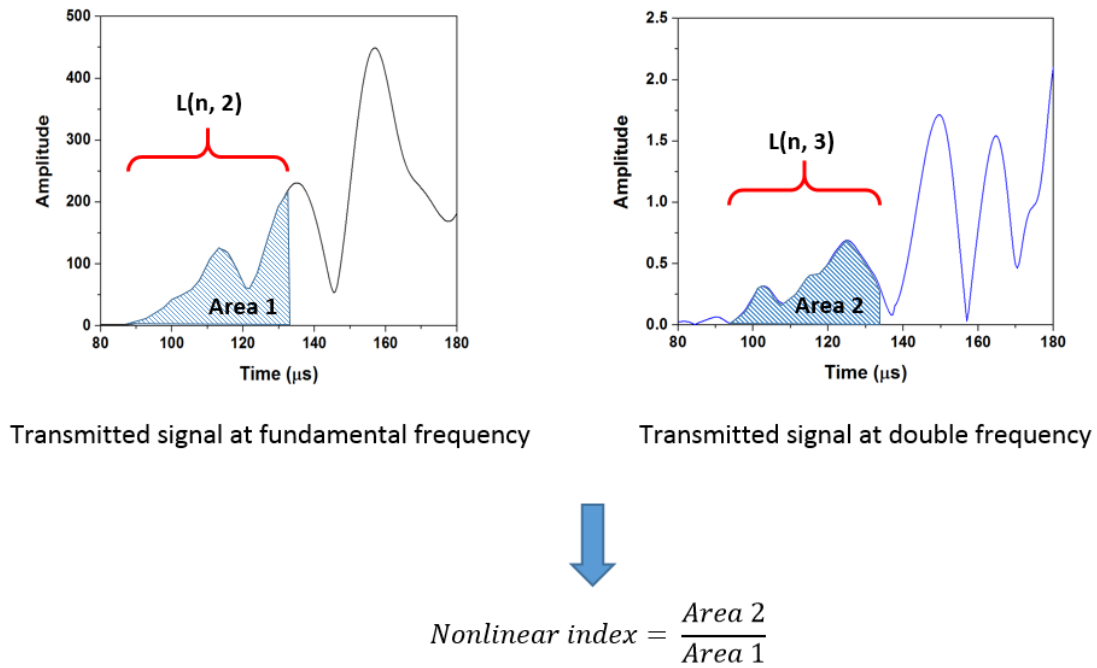


Figure 6.34 Calculation of nonlinear index.

Following equation in Figure 6.34, the nonlinear indices were calculated for the two pipe specimens with same configuration in experiment. The trend line in Figure 6.35 illustrates the nonlinear indices under the different loading conditions from experiments, i.e. (1) before fatigue testing as benchmark, (2) after 22000 cycles, (3) at the end of fatigue testing, and (4) with a static load. From the figure, it can be seen that the nonlinearity for both specimens clearly increases at 22000 cycles compared with the benchmark and then drops to a level similar to that at the beginning after about 42000 cycles. With the application of a static load which closes part of the crack, the nonlinearity increases again but it is still much lower than that at 22000 cycles, indicating that the crack has developed into an open crack and only its tip had breathing behaviour under the static load.

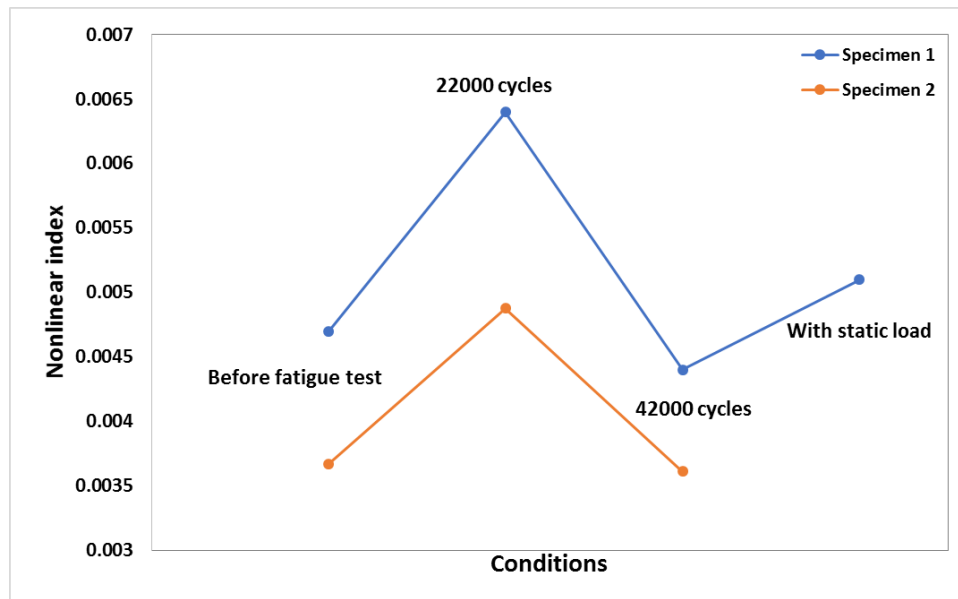


Figure 6.35 Nonlinear indices under different loading conditions.

## 6.5 Summary

This chapter focuses on the detection of fatigue crack in both plate and pipe structures with second harmonic generation method, where numerical studies and experimental test are conducted. Third order elastic constant and a seam crack are considered in the simulation model for material nonlinearity and CAN respectively. Piezoelectric transducers working with an advanced signal collecting system are adopted in the experimental testing for wave nonlinearity acquisition. Both modelling and experimental results show the nonlinearity caused by a “breathing” crack, and observation of multiple second harmonic waves in the pipe is different to the results from the study in a plate structure.

With the understanding of the interaction between nonlinear waves and the fatigue crack in a pipe structure and differences with the plate structure, study considering the quantitative assessment of the fatigue crack in pipes will be elaborated in next chapter.

## **Chapter 7 Quantitative evaluation of fatigue crack in pipe-like structures**

In this chapter, the nonlinear index is used to comprehensively investigate the interaction between fatigue crack propagation and guided waves and to quantify the relation between crack length and wave nonlinearity induced by a “breathing” crack in an aluminium pipe. Numerical simulation and experimental testing are conducted and signals in both transmission and reflection configurations were collected. Finally, the differences between the results from simulation and experiment are discussed.

The wave mode selected for the second harmonic generation is the same as Section 6.3.1. Wave mode  $L(n, 2)$  is selected as the fundamental waves at the excitation frequency 300 kHz, and  $L(n, 3)$  mode at the double frequency 600 kHz is generated by fatigue crack as the second harmonic waves.

### **7.1 Numerical analysis for quantitative evaluation of fatigue crack in pipes**

FE model including material nonlinearity and CAN is accomplished to simulate the interaction between nonlinear guided waves and fatigue crack. The transmission and reflection characteristics from the simulation are analysed for benchmark and different lengths of crack.

#### ***7.1.2 Simulation model***

A 3D model in Abaqus/Explicit was utilised to simulate the nonlinearity caused by both the material and the close crack. The pipe model dimensions were wall thickness 4 mm, outer diameter 30 mm and length 1 m. For fatigue crack initiation, an 8 mm long 2 mm wide through-thickness notch was modelled by removal of elements in the middle of the

pipe. The excitation signal and the location of actuator and sensors were same as in Section 6.3.  $L(n, 2)$ , consisting of both longitudinal mode  $L(0, 2)$  and flexural modes  $F(n, 2)$  at the selected frequency, was excited due to the actuation of one transducer. Details of the locations of the transducers and monitoring points are shown in Figure 6.18.

The element type, mesh and time step were also same as in Section 6.3.3. The simulation of material nonlinearity and fatigue crack followed the same procedure in Section 6.3.3. The basic material properties as well as the third order elastic constants are listed in Table 6.3. To introduce the fatigue crack in the model, a seam crack definition was used to achieve breathing behaviour under propagating waves [97], similar to Section 6.3.3 as illustrated in Figure 7.1(a), where the through-thickness close crack exists at both tips of the notch. In Figure 7.1(b), it can be seen that the compressional part of the wave closes the crack and as a result the stress can pass through, whereas in Figure 7.1(c), the tensional part of the wave opens the crack and the stress is blocked by the crack. There was also a slip between two crack edges observed in Figure 7.1(c) in the crack length direction, which is due to the bending induced by the flexural waves in pipes. The length of the crack was increased from 1 mm to 14 mm at each tip, which extended to about half the circumference of the pipe with an increment of 1 or 2 mm in the circumferential direction, for analysing the relation between the nonlinear parameter and the crack length.

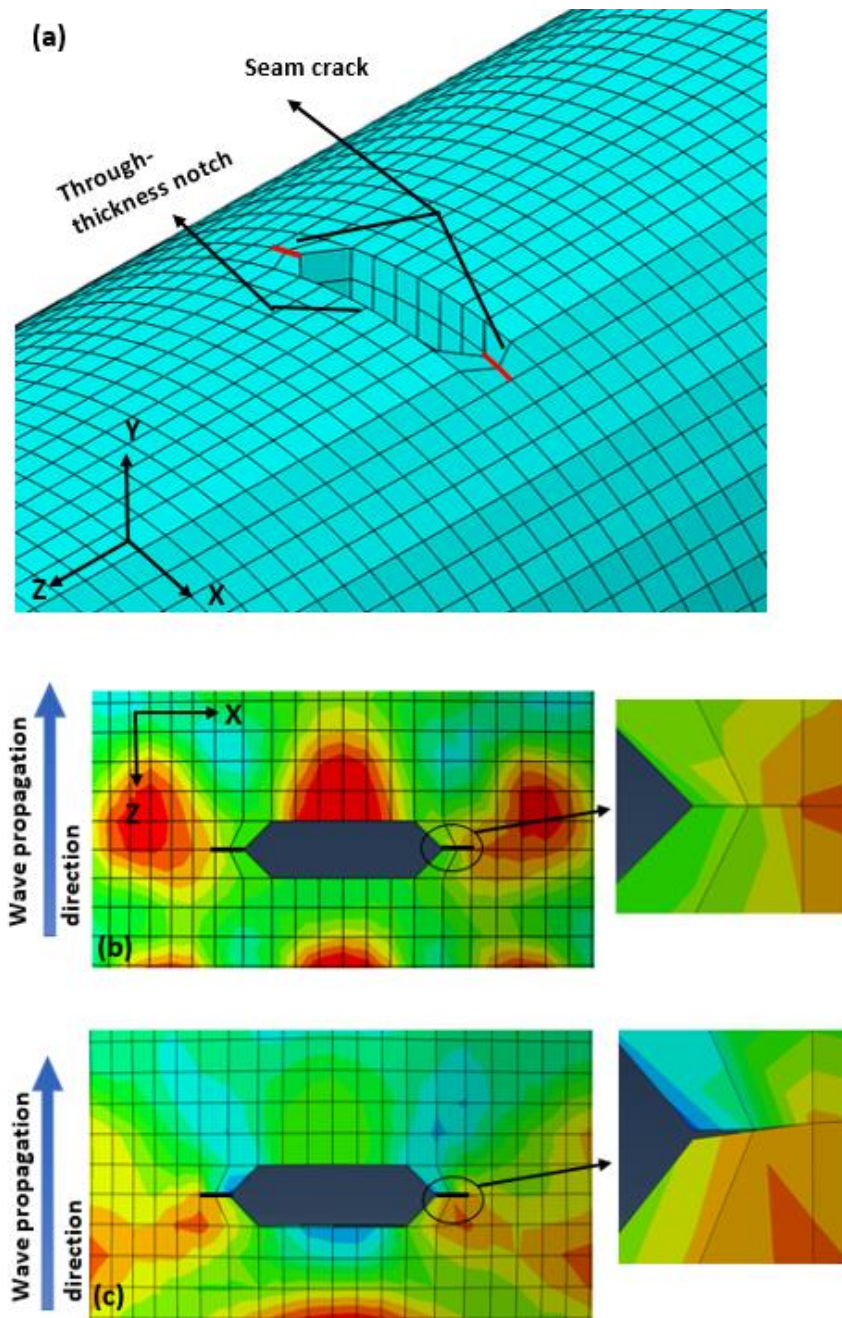


Figure 7.1 (a) Seam crack in simulation model; (b) waves pass through the seam crack when it closes; (c) waves are blocked by the seam crack.

### 7.1.3 Simulation results

To extract the waves at double frequency, after each signal was received, same signal processing procedure was performed as in Section 6.3.2.

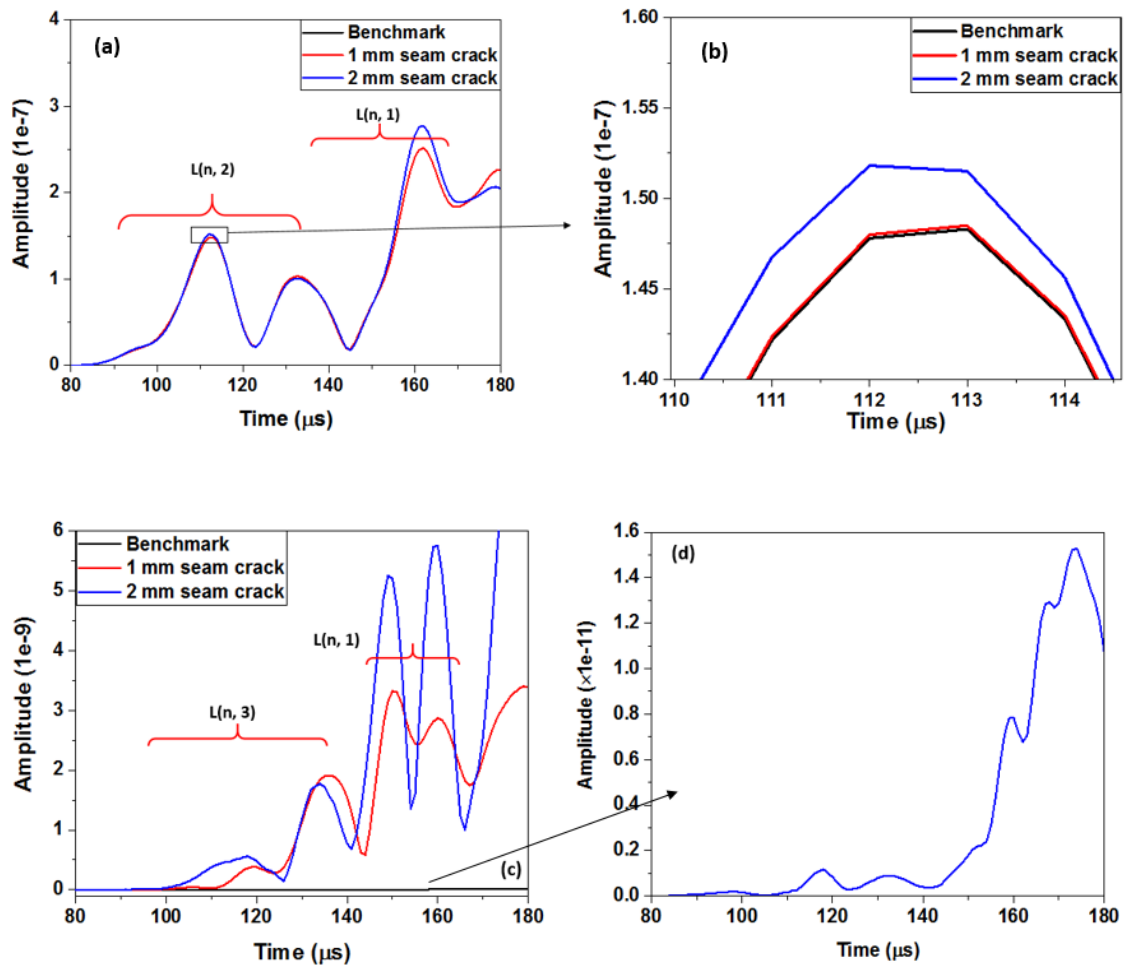
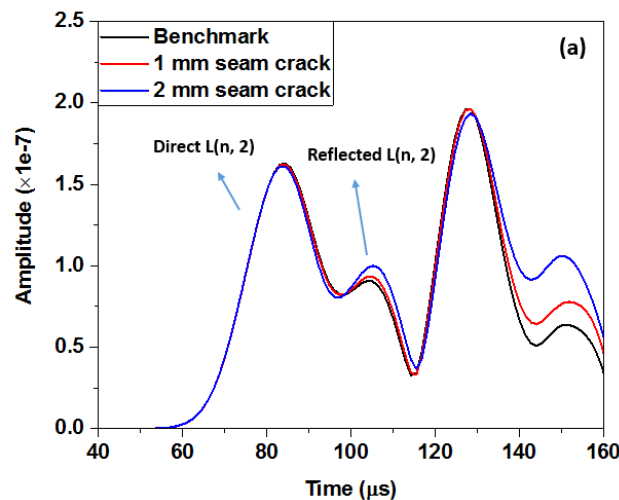


Figure 7.2 Transmitted signal from model with CAN after STFT compared with benchmark signals (a) at fundamental frequency; (b) signals at fundamental frequency after zoomed in; (c) signals at double frequency and (d) benchmark signal at double frequency.

As shown in Figure 7.2 for transmission signals after processing, the cases with 1 mm and 2 mm seam cracks at the fundamental frequency show minor differences compared with the benchmark signal, whereas the second harmonic wave arrives later than the fundamental one, mainly due to the fact that the group velocity of  $L(0, 3)$  induced by the close crack at double frequency is slower than that of  $L(0, 2)$  at fundamental frequency. For both 1 mm and 2 mm seam crack cases, multiple waves are generated at double frequency as shown in Figure 7.2(c) before the arrival time of  $L(0, 1)$ , which is a group of wave modes  $L(n, 3)$ , including the fastest longitudinal mode  $L(0, 3)$  and flexural modes

from the same group  $F(n, 3)$ . It can be figured out that the average amplitude of the second harmonic of the 2 mm crack case is about 1.4% of fundamental wave, slightly greater than that of the 1 mm crack case, which is approximately 1.3% of the fundamental wave. However both are still much greater than that caused by material nonlinearity in benchmark as shown in Figure 7.2(d).

Similarly, nonlinearity induced by seam crack was also observed in the reflected signals at double frequency, as in Figure 7.3. For the signals at fundamental frequency, the direct wave  $L(n, 2)$  shows no difference for different damage cases, but after they reflected from the seam crack, the amplitude is higher than the benchmark signal, especially for a longer seam crack. The arrival time of second harmonic wave is at about  $72 \mu\text{s}$  which is also later than benchmark for 1 mm and 2 mm seam crack cases due to the conversion to  $L(n, 3)$  modes. The average amplitude of the second harmonic wave of the 2 mm crack case is about 2.3% of fundamental wave and is greater than that of the 1 mm crack case, and both of them are much higher than that of the benchmark which is about 0.004% with material nonlinearity only.



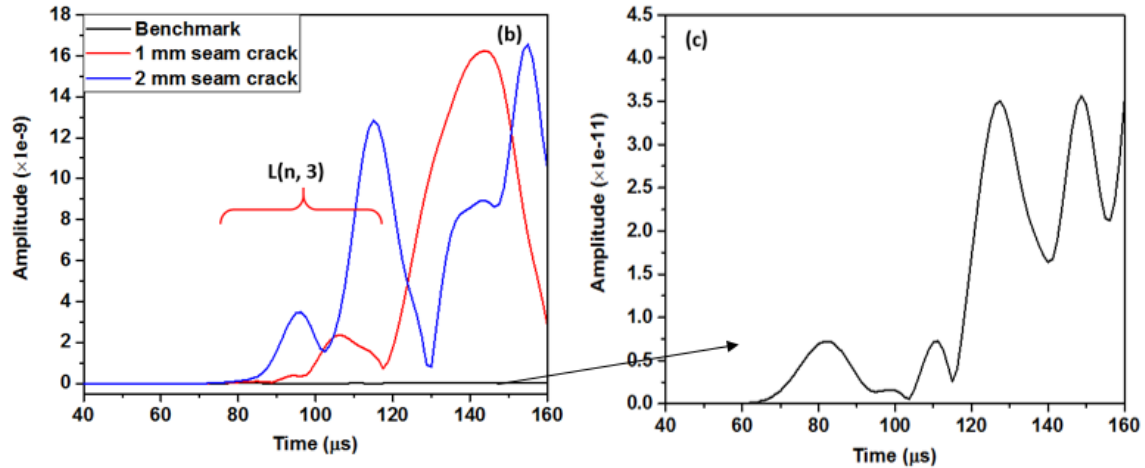


Figure 7.3 Reflected signal from model with CAN after STFT compared with benchmark signals (a) at fundamental frequency; (b) at double frequency and (c) benchmark signal at double frequency.

## 7.2 Experimental test for quantitative evaluation of fatigue crack in pipes

Fatigue test was carried out on the aluminium pipe and an advanced signal processing system is used to obtain the nonlinearity induced by the development of fatigue crack. The transmitted and reflected signals from experiment were investigated to establish the relation between nonlinearity and the severity of fatigue crack.

### 7.2.1 Experiment set up

Experimental testing was performed on an aluminium pipe with the same material properties and dimensions as in the simulation model. Here, 5 mm × 10 mm rectangular and 5 mm × 5 mm square surface-bonded piezoelectric transducers were used as actuator and receivers in the experiment, with the same locations as in the simulation model. A system for generating and collecting signals was adopted in the experimental testing, which included a Ritec RAM-5000 SNAP and an Agilent digital oscilloscope. A high-power low-pass filter was connected to the system, which could suppress harmonics

higher than the fundamental frequency from the source before the signal was input to the transducer.

When a 6-cycle tone-burst signal at a central frequency of 300 kHz was generated, the reflected and transmitted signals were recorded before the fatigue test as benchmark signals. A fatigue machine combined with a steel frame was utilised to introduce the fatigue crack in the pipe. During testing, the pipe was under three-point bending with a cyclic load in the middle. The cyclic load from the fatigue machine ranged from 0.2 kN to 2 kN, with the equivalent highest stress on the cross section at about 50% of the yield stress of the pipe, and the loading frequency was at 2 Hz. During fatigue testing, the transmitted and reflected signals were continuously collected every 2000 cycles until 22000 cycles, after which the collection interval was changed to 4000 cycles. Fatigue testing was stopped at 42000 cycles when the nonlinearity in the received signals dropped to noise level. Signals were averaged 1024 times with a sampling frequency of 200 MHz before recording. It should be noted that during each moment of signal collection the load from the fatigue machine was removed to avoid any adverse effect of the external loads on the “breathing” behaviour of the fatigue crack.

### **7.2.2 Experimental results**

Same signal processing method in simulation was used in experiment receiving.

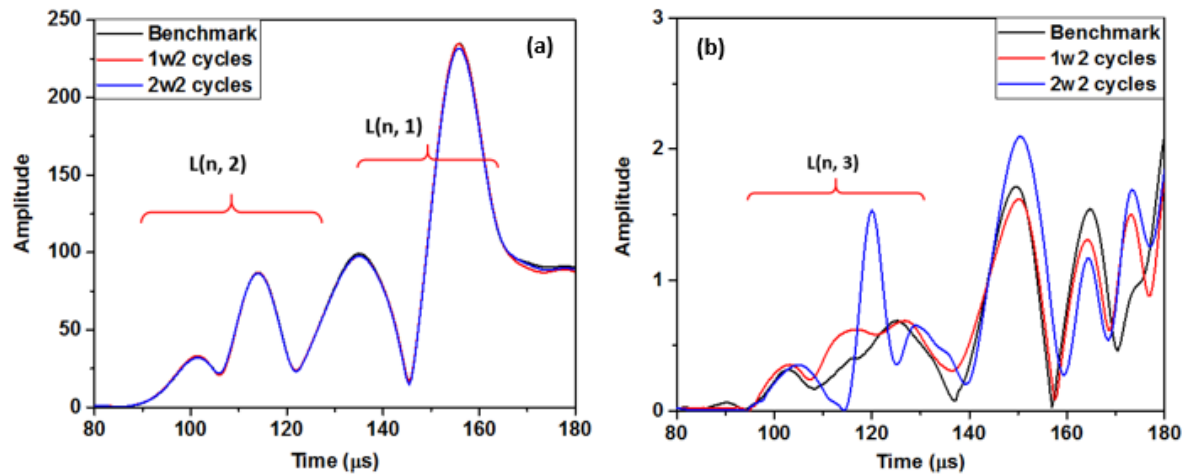


Figure 7.4 Transmitted signal from experiment at different fatigue cycles compared with benchmark signal (a) at fundamental frequency; (b) at double frequency.

As shown in Figure 7.4 for the transmitted signal after signal processing, the arrival time of the first wave packet is very close to that in simulation, and there are also similar multiple wave packets within the time period of interest from 86  $\mu\text{s}$  to 126  $\mu\text{s}$  which are  $L(0, 2)$  and  $F(n, 2)$  modes as a group of  $L(n, 2)$ . The shape of the wave received experimentally was slightly different from the simulation results, due to unavoidable differences between simulation and experiment such as the actual efficiency of the transducer used in the experiment to generate different wave modes.

Comparing with the benchmark signal before the fatigue test, signals for the damage cases after 12000 and 22000 fatigue cycles as show no obvious difference from the benchmark at fundamental frequency, as in Figure 7.4(a). In the comparison between those two damage cases at double frequency in Figure 7.4(b), the average amplitude level of the second harmonic wave after 22000 cycles is more than 2% of the wave at the fundamental frequency, which is higher than the case after 12000 cycles; more importantly, both damage cases show greater nonlinearity than that in the benchmark. On the other hand, the average amplitude of the second harmonic wave of the benchmark, which is about

0.8% of that at fundamental frequency, is much higher than that in simulation. This difference can be attributed to unavoidable nonlinearities from equipment and environment, as well as to the material nonlinearity of the pipe which was not ideally homogeneous. Furthermore, it can be seen in Figure 7.4(b) that the second harmonic wave from both damage cases arrives later than the benchmark signal and more than one wave packet is generated, which was similar with the simulation results.

The reflected signals also have similar results as in Figure 7.5. For the signals at fundamental frequency, there is direct wave  $L(n, 2)$ , reflected wave  $L(n, 2)$  and direct wave  $L(n, 1)$ . The waves reflected from notch have marginal difference in different cases. For the signals at double frequency, the multi-mode second harmonic waves are not as obvious as in the transmitted signals because the different wave modes with close velocities are not completely separated within the shorter distance from the sensor to the fatigue crack. The arrival time of first wave packet for damage cases is later than the benchmark, indicating the  $L(n, 3)$  modes generated by breathing crack. The average amplitude of the second harmonic wave of the benchmark, which is about 0.7% of that at fundamental frequency, is also much higher than that in simulation. In the comparison between those two damage cases at double frequency, the average amplitude level of the second harmonic wave after 12000 cycles is about 1.3% of the wave at the fundamental frequency, which is smaller than the case after 22000 cycles at 2%, while both damage cases show greater nonlinearity than that in the benchmark.

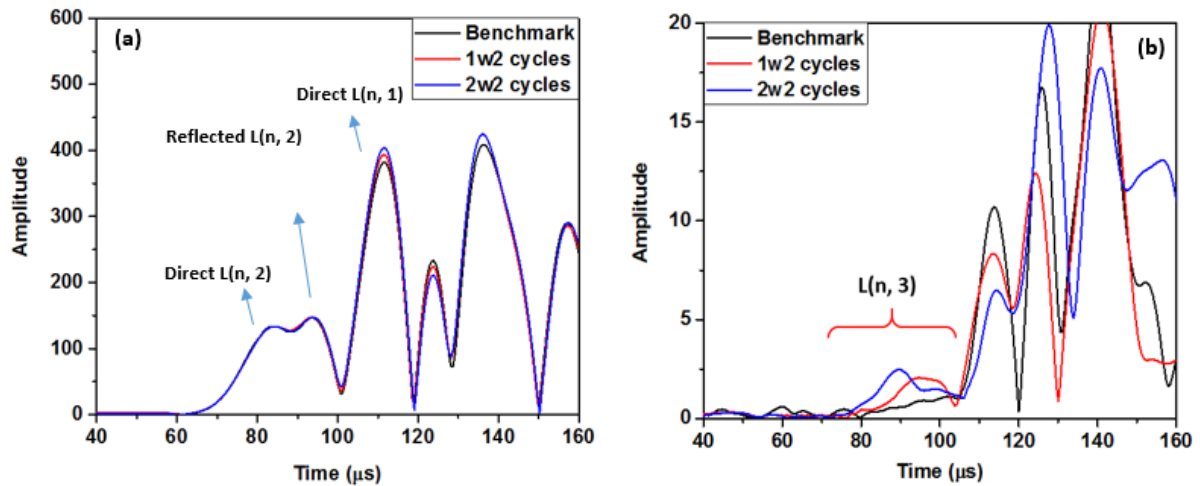


Figure 7.5 Reflected signal from experiment at different fatigue cycles compared with benchmark signal (a) at fundamental frequency; (b) at double frequency.

### 7.3 Nonlinear index with fatigue crack growth

In this section, all the receive signals from simulation and experiment results with variable seam crack length or fatigue cycles are evaluated using a nonlinear parameter to quantify the fatigue crack severity. The relation between nonlinear index and seam crack length or fatigue cycles are established and the trends are analysed.

#### 7.3.1 Nonlinear parameter

From the signals received in simulation and experiment, it could be observed that the nonlinearity changed with the seam crack length and fatigue cycle respectively. Generally, a relative nonlinear parameter  $\beta' = A_2/A_1^2$  is used to measure the nonlinearity in a system, where  $A_1$  and  $A_2$  are the amplitudes of fundamental wave and second harmonic wave in time domain [164, 165] or frequency domain [99, 166]. However, due to the multiple wave mode generation at fundamental and double frequencies and the nonlinearity is mainly from the crack breathing behaviour, the conventional relative nonlinear parameter is not suitable to evaluate the CAN in pipe structures. A proper parameter in the time domain was proposed in Chapter 6 to include all the wave packets induced by damage in

order to quantitatively evaluate the nonlinearity caused by the breathing crack in the pipe. In this study, the nonlinear parameter for both transmitted and reflected signals were defined as the integral of the amplitude profile of  $L(n, 3)$  until the arrival time of  $L(0, 1)$  extracted at double frequency divided by the integral of the amplitude profile of  $L(n, 2)$  before the arrival time of  $L(0, 1)$  at the fundamental frequency. Such a nonlinear index was calculated for all damage cases in experiment and simulation and was used as a measurement of the nonlinearity in the pipe so as to quantify the severity of the fatigue crack. It should be noticed that the window size as well as start and end point of the window were fixed for different damage cases to obtain comparable results.

### **7.3.2 Nonlinear indices from simulation**

As shown in Figure 7.6, for both transmitted and reflected signals the nonlinear index increases monotonously with crack length until it reaches a maximum value at about 6 mm at each notch tip and then it begins to drop to approximately half of that maximum value. Trend lines are plotted in the figure to shown the change more clearly. The nonlinear index close to zero at 0 mm crack length is the benchmark signal which contains material nonlinearity only, indicating that it can be ignored when compared with the damage cases. It is interesting that the total crack length for both tips (12 mm) when nonlinearity reaches the maximum is close to the wavelength of the second harmonic wave at double frequency, which is around 13 mm. It was understood that the increase in nonlinearity until the crack reached 6 mm was mainly caused by the increase in the portion of the crack which could be completely closed and opened by the incident wave. When the crack was too long, however, such as longer than 6 mm in this study, since the closing of the far edge of the crack depends on the wave detour to it, vibration of the far edge of the crack was minimised because the incident wave was incapable of detouring to the middle part of the crack and only the edge of the crack close to the actuator vibrated.

In such cases, the crack gradually evolved into an open crack, where only the tip of the seam crack still showed breathing behaviour which contributed to a lower nonlinearity. It should be noticed that the CAN from this simulation model was not influenced by the input voltage, therefore, the trend of nonlinear index in Figure 7.6 will not change with varying input signals.

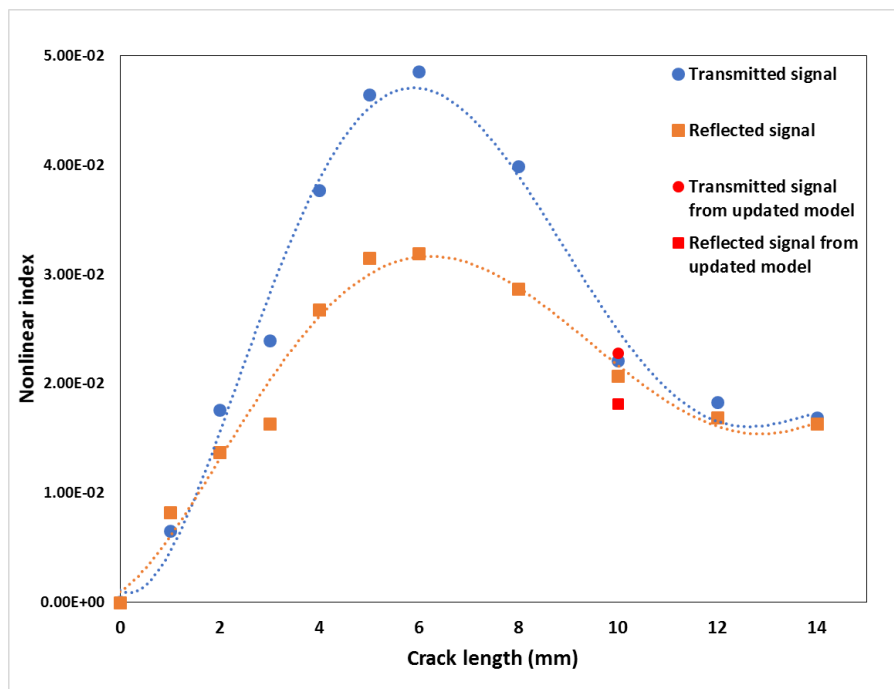


Figure 7.6 Nonlinear index vs crack length at each tip of notch in pipe model.

To confirm this assumption about the cause of the drop of nonlinearity in simulation, a FE model based on the original one was further developed. The curves in Figure 7.6 indicate that the nonlinear indices for 3 mm and 10 mm long cracks (at each tip of the notch) were similar. On the basis of the aforementioned assumption, the middle part (7 mm) of the 10 mm seam crack would become open when the waves passed through. Therefore, the length of the notch was extended in the updated numerical model from the original 8 mm to 22 mm in the middle, where 14 mm represents the middle part of two 10 mm seam cracks (7 mm at each tip) that has become open. Thus only 3 mm seam cracks at the two tips of the new notch were created, as shown in Figure 7.7. In the updated

-Quantitative evaluation of fatigue crack using nonlinear guided waves in pipelines-

model in Figure 7.7(b), the pipe dimension, material properties and mesh setting were all the same as in original model, as was the simulation method of the seam crack and material nonlinearity.

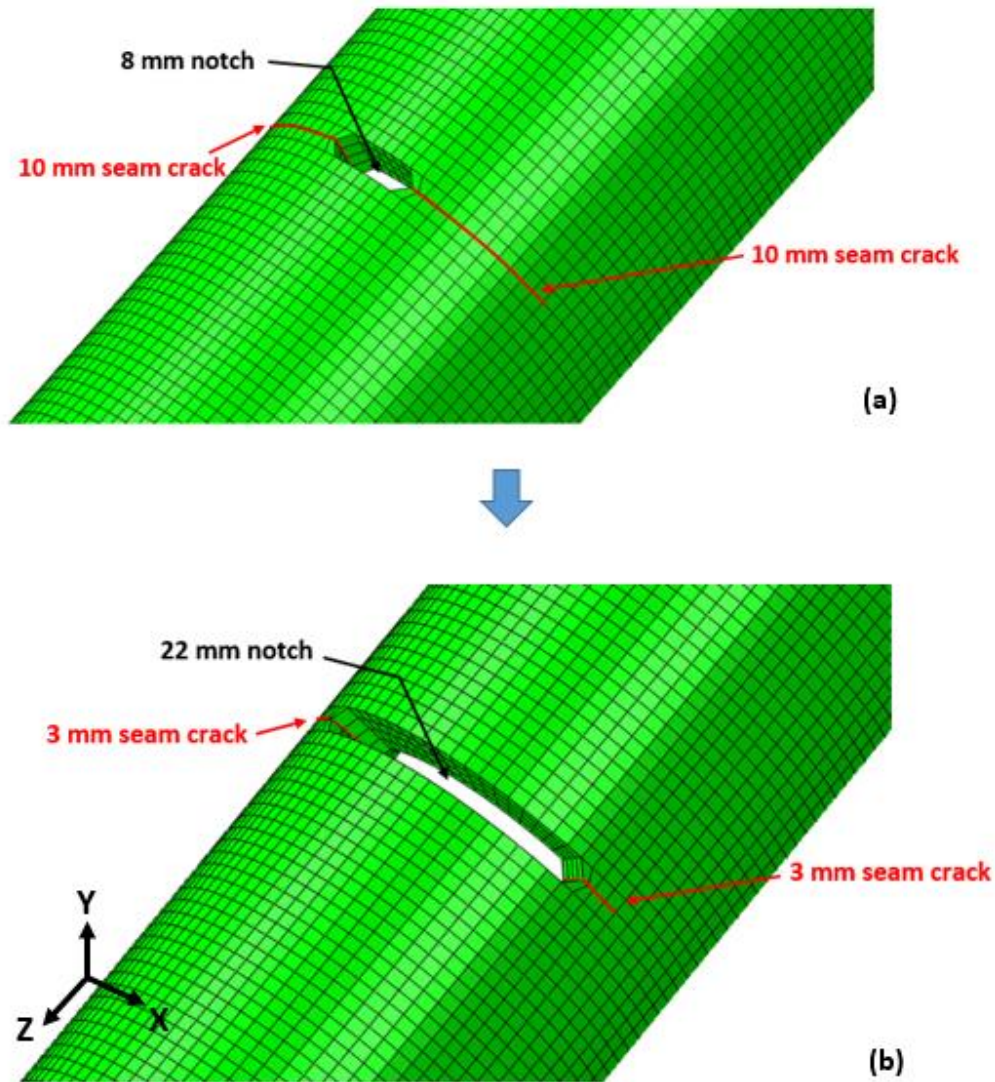


Figure 7.7 (a) Original model; (b) Modified model with notch extended in the middle.

The resultant nonlinear index from this updated model is 0.0228 (shown as a red dot in Figure 7.6), which is close to the nonlinear index from the 3 mm crack length case at 0.0235 and the 10 mm crack length at 0.0224 from the transmitted signals. Similar results are also observed from the reflected signals (shown as a red square in Figure 7.6), where the value from the updated model is 0.0182, between 0.0171 (for 3 mm crack length) and

0.0202 (for 10 mm crack length). These results confirm the assumption that the decrease of nonlinearity in the simulation model was caused by the disappearance of breathing behaviour in the middle part of the crack, which becomes an open crack to the incident guided waves.

### **7.3.3 Experimental result**

The nonlinear indices were also calculated for all received signals in experiment under different fatigue cycles as shown in Figure 7.8, which is curve-fitted using a fifth order polynomial function with the most appropriate fitting trend. It can be seen that the nonlinear index increases gradually with the fatigue cycle until about 26000 cycles and then decreases to the same level as in the benchmark. The peak is similar for both reflected and transmitted signals, confirming that the nonlinearity is from the fatigue crack. The fatigue crack development at early stage including material dislocation and the forming of microcracks that gradually evolve to a fatigue crack. The increase in nonlinearity reveals the accumulative material dislocation around the tips and also the increasing of the part of microcrack contributing to breathing behaviour which is the same as the increasing stage in simulation result. It should be mentioned that at the end of the fatigue test, the crack length observed in the experiment was about 1 mm, which was only at the beginning stage of the simulation model. The drop of nonlinearity in both simulation and experiment is because the crack or part of the crack become open. However, the nonlinear index in the experiment began to drop at such an early stage, indicating that different to numerical simulation, the breathing behaviour in practice existed only at the early stage of a fatigue crack, which would become an open crack immediately upon growing to a macro scale.

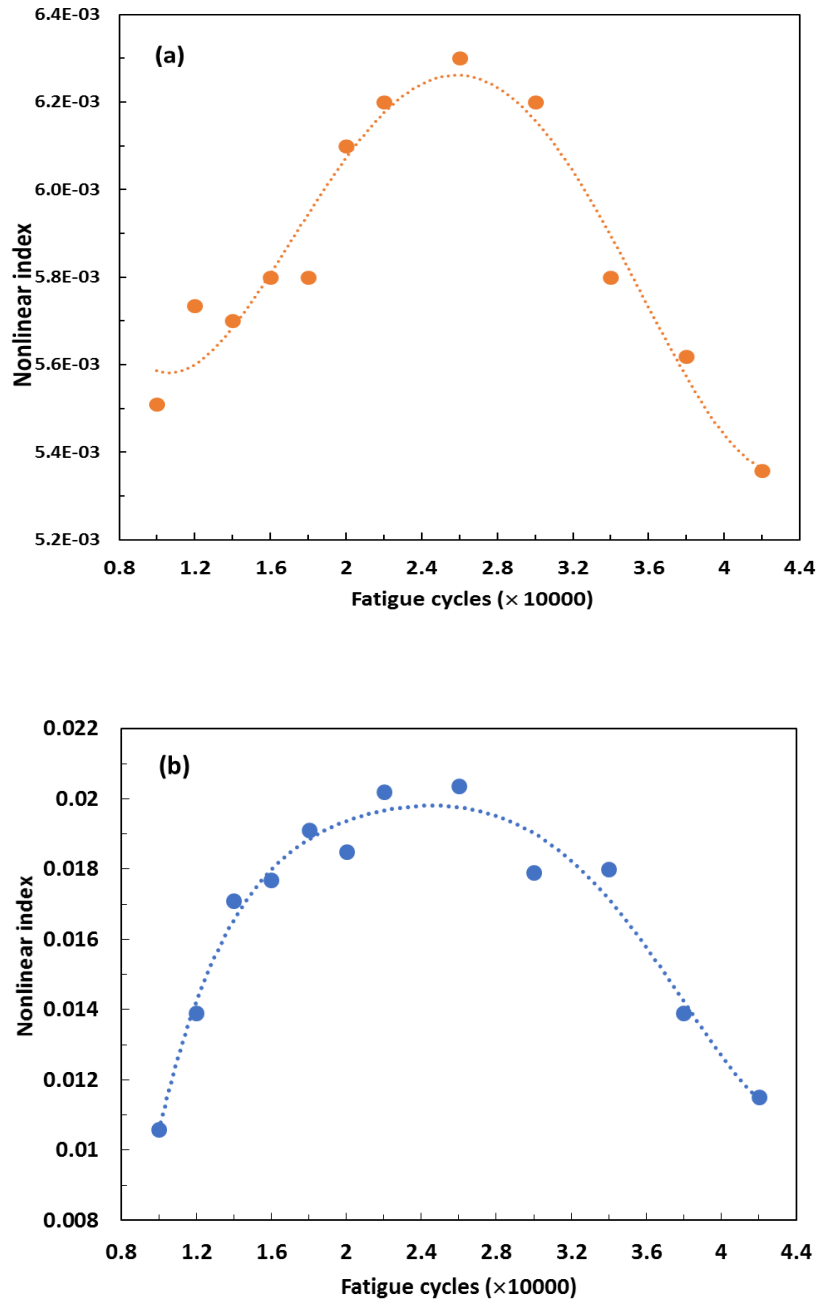


Figure 7.8 Nonlinear index vs fatigue cycle from experimental testing for (a) transmitted signals; (b) reflected signals.

To confirm this assumption, some typical reflected signals at fundamental frequency are plotted in Figure 7.9, including signals at benchmark, 12000, 22000, 34000 and 42000 fatigue cycles. As evident in the Figure, before 22000 fatigue cycles, there is no significant difference in the reflected  $L(0, 2)$  from the notch. However, the reflected

fundamental wave L(0,2) clearly increases at 34000 and 42000 cycles, revealing that the crack evolves from micro to macro one and even the fundamental wave may be able to detect its existence.

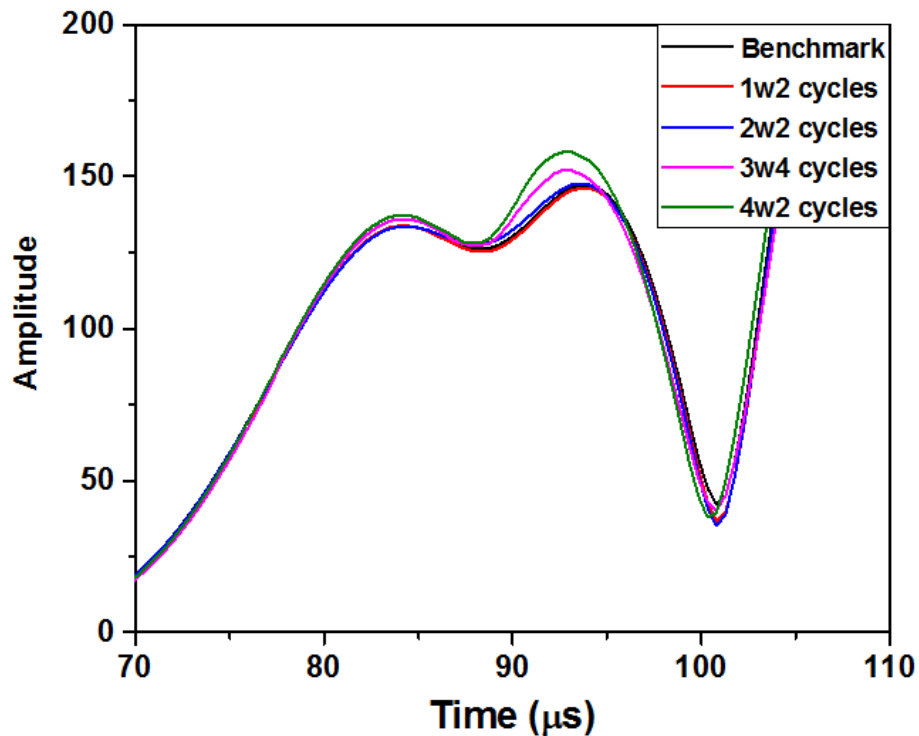


Figure 7.9 Reflected signals under different fatigue cycles at fundamental frequency.

It should be mentioned that the second harmonic wave has attenuation along the direction of wave propagation and over a specific distance from the fatigue crack, the CAN was hard to identify. Several points A, B, C along the pipe axis at 100 mm, 115 mm and 140 mm away from the crack was monitored to qualify the energy dissipation of the second harmonic waves. The nonlinear index and the integral of the amplitude profile of second harmonic wave were calculated for three different points. The results are plotted in Figure 7.10 and Figure 7.11. As shown in the figure, both nonlinear index and the integral of second harmonic wave profile decrease with the propagation distance. In particular, the latter has reduced 72.7% within the distance 40 mm, which is three times of the wavelength of the L(0, 3) at double frequency. It means the energy of second harmonic

waves dissipates quickly and the amplitudes of second harmonic waves highly depend on the distance. The selection of proper distance from the fatigue crack to the monitoring points will influence the quality and accuracy of the CAN measurement. In the experiment, a distance from sensor to the fatigue crack of 300 mm was also recorded and it is noticed that the nonlinearity induced by the crack dropped to noise level at this position, revealing that the energy of nonlinearity dissipated fast and over this distance, nonlinearity caused by damage cannot be measured properly.

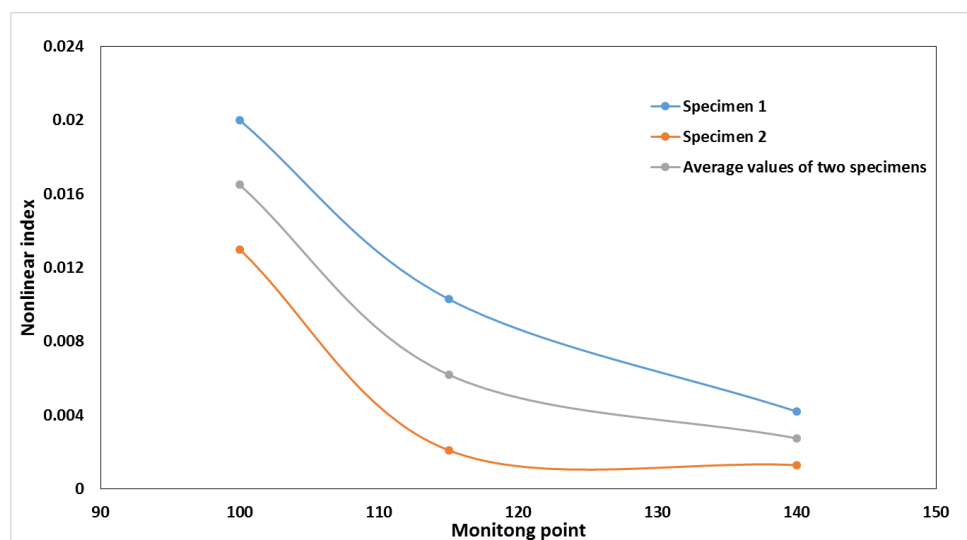


Figure 7.10 Nonlinear index vs the propagation distance.

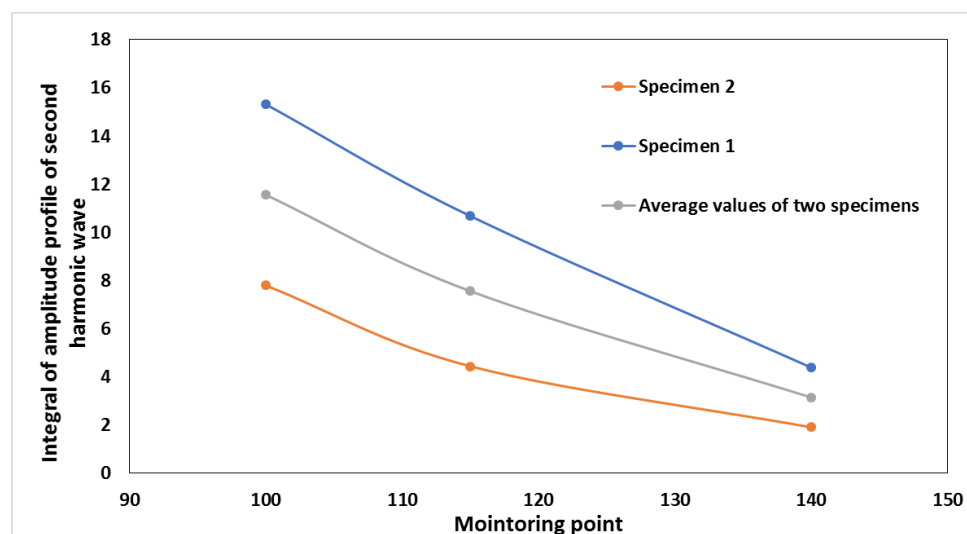


Figure 7.11 Integral of amplitude profile of second harmonic wave vs propagation distance.

## 7.4 Summary

This study applies an appropriate nonlinear index to quantify the relation between nonlinear guided waves and a fatigue crack in an aluminium pipe due to the existence of multiple modes in the pipe structure. Both numerical and experimental studies are carried out considering material nonlinearity and CAN while the differences between experimental and simulation results are discussed. In the simulation model, the seam crack length is continuously increased to simulate growth of a fatigue crack. For the experimental testing, a fatigue machine is used for fatigue crack generation. From the numerical and experimental analyses, it is found that the nonlinear index increased monotonously with crack length at the early stage since the increasing length of the breathing crack but begin to decrease at a specific crack length, mainly because (a) the middle part of the longer crack could not fully generate breathing behaviour in the numerical method; and (b) the crack was changed from micro scale to macro scale in the experimental testing. The results from both studies show that the nonlinear index can quantify the nonlinearity in pipe structures caused by damage and it can detect the initial stage of a fatigue crack within 1 mm in practice, providing higher sensitivity than linear guided waves in terms of microcrack detection.

## **Chapter 8 Conclusions**

### **8.1 Main findings of this thesis**

The aim of the work presented in this thesis was to use proper nonlinearity methodologies to detect the existence of fatigue crack and quantitatively analyse the propagation of fatigue crack in metallic pipes. Guided waves are already widely used for the detection of pipes with gross damage. The strategy proposed here is to detect close crack with breathing behaviour which can induced CAN in pipes, such as the fatigue crack at early stage of its fatigue life.

In order to reach the goal, the following research studies were carried out.

First, in Chapter 2 the basic properties of Lamb waves and guided waves in plate and pipe structures were reviewed including the wave propagation, dispersion and attenuation, providing understanding of different wave modes and knowledge of the selection of proper wave modes for pipe detection.

A comprehensive literature review was conducted in Chapter 3, introducing the scattering by damage with linear and nonlinear characteristics in pipe structures and relevant methods to detect the existence, severity and location of the damage. Special features in pipe detection were also investigated, such as the bends in pipes and the EOCs effect on pipe detection.

Further study on the nonlinear method in pipe structures were presented in Chapter 4. Some preliminary work were carried out, including the optimisation of the mesh in the simulation model to ensure the calculation convergence and accuracy, and the study of wave excitation and acquisition in simulation and experiment. Since the nonlinearity is much smaller compared to the excitation signal and it has high sensitivity, it will be affected by the environment and the testing system obviously. The wave excitation and

-Quantitative evaluation of fatigue crack using nonlinear guided waves in pipelines-

acquisition of nonlinearity in experiment highly depends on the PZT shape, input voltage, specimen preparation, the system used for signal generation and collection, as well as the loading condition during signal collection. To select appropriate nonlinear method for this study, mixed frequency response and higher harmonic generation method, mainly used in pipe detection was analysed and compared with numerical studies. Both two methods can detect the existence of fatigue crack through the observation of sidebands or second harmonics.

For vibro-acoustic modulation method, there was no obvious sidebands generated beside the main frequency but only second harmonic for the damaged pipe. The location of vibration in this method can influence the generated second harmonic and addition of vibration can increase the second harmonic in the frequency domain compared with the case when there is only ultrasonic wave excited. For acoustic and ultrasonic modulation, the longer interaction time between the input signals, the higher the energy of modulation. Therefore, when using mixed frequency response method, the input signal should be long and stable to generate the sidebands, which however is not suitable to extract the time information and to interpret the received signals.

In contrast, the results from higher harmonic generation method showed that second harmonic method is more suitable for locating the position of the crack since it works well with a tone burst signal which indicated the time of arriving at the crack and a short signal is preferred for signal processing and interpretation in a pipe structure with complex multiple wave modes. Therefore, the second harmonic method was used to detect and quantitative evaluate the fatigue crack in the pipe.

After some preliminary work for the simulation and experimental methods, an analytical model was proposed in Chapter 5. Then the theoretical nonlinearity curve in terms of crack length was obtained, which indicates the flexural modes has amplitude comparable

with the longitudinal waves. As a result, when calculating wave nonlinearity, the influence of flexural waves must be considered. The results from theoretical model was also confirmed with a numerical analysis. Due to the close group velocity between longitudinal and flexural waves of the same wave mode group, these multiple second harmonic waves are difficult to be separated. To solve this problem, a nonlinear parameter considering all generated wave packets was proposed to measure the nonlinearity in pipe structures with second harmonic generation method, which is the integral of the amplitude profile of the wave at double frequency within a time period of interest divided by the integral of the amplitude profile of the wave at the fundamental frequency.

With the proposed nonlinear index, fatigue crack detection in plate and pipe structures were conducted through numerical and experimental studies in Chapter 6. Similar to the theoretical results, in the pipe specimen for both simulation and experiment results, more than one wave packet appears in the received signal at double frequency. For the case with material nonlinearity only, the average amplitude of the second harmonic wave from the experiment result is much higher than that in the corresponding simulation. For the case when nonlinearity was induced by the crack, both of the average amplitude of the second harmonic waves in simulation and experiment are much higher than the material nonlinearities. In contrast, for the plate structure, there is only one mode at double frequency induced by the damage, which is different to the results from pipe structures. The reason may be attributed to the fact that the group velocities of different wave modes in a plate, are distinct from each other and can be separated easily after a certain propagation distance. Nevertheless for both structural types, the nonlinearity caused by the crack can be detected through the observation of second harmonic waves.

After confirm the feasibility of the second harmonic generation method for the fatigue crack detection, further study on the quantitatively evaluation of fatigue crack growth were completed in Chapter 7.

Numerical and experimental analyses were performed in an aluminium pipe. From the simulation results, the nonlinear index increases monotonously with crack length until it reaches a maximum value at about 6 mm at each notch tip and then it begins to drop to approximately half of that maximum value. The increase in nonlinearity until the crack reached 6 mm was mainly caused by the increase in the portion of the crack which had breathing behaviour. When the crack was too long, the crack had evolved into an open crack and only the tip of the seam crack contributed to the nonlinearity.

From experiment results, the nonlinear index increases gradually with the fatigue cycle until about 26000 cycles and then decreases to the same level as in the benchmark. The increase in nonlinearity reveals the accumulative material dislocation and the formation of initial fatigue crack and also it began to drop at an early stage, when the crack is smaller than 1 mm, indicating that different to numerical simulation, the breathing behaviour in practice existed only at the early stage of a fatigue crack, which would become an open crack immediately upon growing to a macro scale.

The results from both studies show that the nonlinear index can quantify the nonlinearity in a pipe structure caused by damage and it can detect the initial stage of a fatigue crack within 1 mm in practice, providing higher sensitivity than linear guided waves in terms of microcrack detection.

## **8.2 Future work**

Nonlinear guided wave testing and evaluation is a popular research field, with many outstanding challenges that need to be solved. Upon the completeness of the study in this thesis, suggestions for further works are as follows:

- Optimised theoretical model illustrating the mechanism of CAN in 3D pipe structures is still necessary, considering the flexural wave as the excitation and the possible second harmonic wave modes which induced by the fatigue crack;
- Adding the vibration to enhance the second harmonic can be further studied in a pipe structure to improve the result in the experiment;
- The simulation of fatigue crack in the numerical modelling needs to consider advanced models that are more equivalent to practice scenarios, such as rough crack surface and plastic zone around the crack tips in a pipe structure;
- The practical application of nonlinear guided waves in industry is quite limited since the nonlinearity can arise from environment and devices which distort the nonlinearities from the damage. The removal of these undesired nonlinearities needs further studies and the generation of harmonics or sidebands requires careful design;
- Proper signal processing method is required to separate the multiple wave modes induced by the fatigue crack. Analysis of different modes individually may contain more information for further assessment of the fatigue crack;
- Combined with linear method efficiently, the nonlinear method can be used to analyse the whole fatigue life in a pipe, where further study is required in investigate each stage of the interaction between fatigue crack and the guided waves;
- Other nonlinear methods such as subharmonic generation, third harmonic generation and the generation of circumferential SH waves at the breathing crack tips may be useful to measure the fatigue crack propagation;
- The determination of location and orientation of fatigue crack in a pipe structure still needs further studies;

-Quantitative evaluation of fatigue crack using nonlinear guided waves in pipelines-

- When detecting fatigue crack at certain complex parts in pipes such as bends, welds and flanges, which complicate wave propagation and may cause mode conversion in particular, further investigation with efficient signal interpretation approaches is necessary;
- Operational and environmental variations (temperature, surrounding materials, etc.) are of vital importance since the baseline signal may change accordingly. Therefore, further study of the effect of EOCs with necessary calibration and techniques without baseline data (benchmark-free) is required for pipe inspection under changing EOCs.

## References

- [1] "Varanus Island a decade on: The remote explosion that ignited a WA gas crisis," in *The West Australian*, ed, 2018.
- [2] "8 dead, 35 injured in gas pipeline explosion in SW China," in *Global Times*, ed: Xinhua, 2017.
- [3] "Crack and Explosion Show Risks of Europe's Aging Energy Networks," in *Bloomberg*, ed, 2017.
- [4] A. Demma, P. Cawley, M. Lowe, and A. G. Roosenbrand, "The reflection of the fundamental torsional mode from cracks and notches in pipes," *The Journal of the Acoustical Society of America*, vol. 114, pp. 611-625, 2003.
- [5] A. Demma, P. Cawley, M. Lowe, A. G. Roosenbrand, and B. Pavlakovic, "The reflection of guided waves from notches in pipes: a guide for interpreting corrosion measurements," *NDT & E International*, vol. 37, pp. 167-180, 2004.
- [6] X. Wang, P. W. Tse, C. K. Mechefske, and M. Hua, "Experimental investigation of reflection in guided wave-based inspection for the characterization of pipeline defects," *NDT & E International*, vol. 43, pp. 365-374, 2010.
- [7] A. Løvstad and P. Cawley, "The reflection of the fundamental torsional guided wave from multiple circular holes in pipes," *NDT & E International*, vol. 44, pp. 553-562, 2011.
- [8] A. Løvstad and P. Cawley, "The reflection of the fundamental torsional mode from pit clusters in pipes," *NDT & E International*, vol. 46, pp. 83-93, 2012.
- [9] A. Klepka, W. Staszewski, R. Jenal, M. Szwed, J. Iwaniec, and T. Uhl, "Nonlinear acoustics for fatigue crack detection – experimental investigations of vibro-acoustic wave modulations," *Structural Health Monitoring*, vol. 11, pp. 197-211, 2012.
- [10] H. Sohn, H. J. Lim, M. P. DeSimio, K. Brown, and M. Derriso, "Fatigue crack detection using guided waves nonlinear modulation," 2013.
- [11] F. Aymerich and W. J. Staszewski, "Impact damage detection in composite laminates using nonlinear acoustics," *Composites Part A: Applied Science and Manufacturing*, vol. 41, pp. 1084-1092, 2010.
- [12] Ł. Pieczonka, A. Klepka, W. J. Staszewski, T. Uhl, and F. Aymerich, "Analysis of vibro-acoustic modulations in nonlinear acoustics used for impact damage

- detection - numerical and experimental study," *Key Engineering Materials*, vol. 558, pp. 341-348, 2013.
- [13] W. J. De Lima and M. F. Hamilton, "Finite amplitude waves in isotropic elastic waveguides with arbitrary constant cross-sectional area," *Wave Motion*, vol. 41, pp. 1-11, 2005.
- [14] Y. Liu, E. Khajeh, C. J. Lissenden, and J. L. Rose, "Higher order interaction of elastic waves in weakly nonlinear hollow circular cylinders. II. Physical interpretation and numerical results," *Journal of Applied Physics*, vol. 115, pp. 214902-214902-10, 2014.
- [15] Y. Liu, E. Khajeh, C. J. Lissenden, and J. L. Rose, "Interaction of torsional and longitudinal guided waves in weakly nonlinear circular cylinders," *The Journal of the Acoustical Society of America*, vol. 133, pp. 2541-2553, 2013.
- [16] V. K. Chillara and C. J. Lissenden, "Analysis of second harmonic guided waves in pipes using a large-radius asymptotic approximation for axis-symmetric longitudinal modes," *Ultrasonics*, vol. 53, pp. 862-869, 2013.
- [17] W. Li and Y. Cho, "Thermal fatigue damage assessment in an isotropic pipe using nonlinear ultrasonic guided waves," *Experimental Mechanics*, vol. 54, pp. 1309-1318, 2014.
- [18] M. Deng, G. Gao, and M. Li, "Experimental observation of cumulative second-harmonic generation of circumferential guided wave propagation in a circular tube," *Chinese Physics Letters*, vol. 32, pp. 124305-124305-4, 2015.
- [19] L. Pochhammer, "Ueber die fortpflanzungsgeschwindigkeiten kleiner schwingungen in einem unbegrenzten isotropen kreiscylinder," *Journal für die reine und angewandte Mathematik (Crelle's Journal)*, vol. 1876, p. 324, 1876.
- [20] C. Chree, "The equations on an isotropic elastic solid in polar and cylindrical coordinates, their solutions and applications," *Trans. Cambridge Philos. Soc.*, vol. 14, pp. 250-369, 1889.
- [21] D. C. Gazis, "Three - dimensional investigation of the propagation of waves in hollow circular cylinders. I. Analytical foundation," *The Journal of the Acoustical Society of America*, vol. 31, pp. 568-573, 1959.
- [22] D. C. Gazis, "Three - dimensional investigation of the propagation of waves in hollow circular cylinders. II. Numerical results," *The Journal of the Acoustical Society of America*, vol. 31, pp. 573-578, 1959.

- [23] A. H. Meitzler, "Mode coupling occurring in the propagation of elastic pulses in wires," *The Journal of the Acoustical Society of America*, vol. 33, pp. 435-445, 1961.
- [24] J. Zemanek, "An experimental and theoretical investigation of elastic wave propagation in a cylinder," *The Journal of the Acoustical Society of America*, vol. 51, pp. 265-283, 1972.
- [25] J. L. Rose, *Ultrasonic guided waves in solid media*. New York: Cambridge University Press, 2014.
- [26] M. G. Silk and K. F. Bainton, "The propagation in metal tubing of ultrasonic wave modes equivalent to Lamb waves," *Ultrasonics*, vol. 17, pp. 11-19, 1979.
- [27] J. L. Rose, *Ultrasonic waves in solid media*. UK: The press syndicate of the university of cambridge, 2004.
- [28] P. D. Wilcox, M. J. S. Lowe, and P. Cawley, "Mode and transducer selection for long range Lamb wave inspection," *Journal of Intelligent Material Systems and Structures*, vol. 12, pp. 553-565, 2001.
- [29] D. N. Alleyne and P. Cawley, "The effect of discontinuities on the long-range propagation of Lamb waves in pipes," *Proceedings of the Institution of Mechanical Engineers, Part E: Journal of Process Mechanical Engineering*, vol. 210, pp. 217-226, 1996.
- [30] D. N. Alleyne, M. J. S. Lowe, and P. Cawley, "The reflection of guided waves from circumferential notches in pipes," *Applied Mechanics*, vol. 65, pp. 635-641, 1998.
- [31] P. W. Tse and X. J. Wang, "Semi-quantitative analysis of defect in pipelines through the use of technique of ultrasonic guided waves," *Key Engineering Materials*, vol. 413-414, pp. 109-116, 2009.
- [32] P. T. Xiaojuan Wang, ChrisK.Mechefske , MengHua, "Experimental investigation of reflection guided wave-based inspection for the characterization of pipeline defects," *NDT&E International*, vol. 43, pp. 365-374, 2010.
- [33] D. Sonia and B. Fouad, "Propagation of guided waves in a hollow circular cylinder application to non destructive testing," presented at the EPJ Web of Conferences, 2010.
- [34] B. Verma, T. K. Mishra, K. Balasubramaniam, and P. Rajagopal, "Interaction of low-frequency axisymmetric ultrasonic guided waves with bends in pipes of

- arbitrary bend angle and general bend radius," *Ultrasonics*, vol. 54, pp. 801-808, 2014.
- [35] Y. B. a. Z. L. Jianmin Qu, "dispersion of guided circumferential waves in a circular annulus," *Review of Progress in Quantitative Nondestructive Evaluation*, vol. 15, pp. 169-176, 1996.
- [36] H. Kwun and S. Y. Kim, "Reflection of the fundamental torsional wave from a stepwise thickness change in a pipe," *Journal of the Korean Physical Society*, vol. 46, pp. 1352-1357, 2005.
- [37] R. Carandente, J. Ma, and P. Cawley, "The scattering of the fundamental torsional mode from axi-symmetric defects with varying depth profile in pipes," *The Journal of the Acoustical Society of America*, vol. 127, pp. 3440-3448, 2010.
- [38] R. Carandente, A. Lovstad, and P. Cawley, "The influence of sharp edges in corrosion profiles on the reflection of guided waves," *NDT & E International*, vol. 52, pp. 57-68, 2012.
- [39] Nurmalia, N. Nakamura, H. Ogi, and M. Hirao, "Mode conversion and total reflection of torsional waves for pipe inspection," *Japanese Journal of Applied Physics*, vol. 52, 2013.
- [40] L. Zhang, B. J. Gavigan, and J. L. Rose, "High frequency guided wave natural focusing pipe inspection with frequency and angle tuning," *Journal of Pressure Vessel Technology*, vol. 128, pp. 433-438, 2005.
- [41] E. Leinov, M. J. S. Lowe, and P. Cawley, "Investigation of guided wave propagation and attenuation in pipe buried in sand," *Journal of Sound and Vibration*, vol. 347, pp. 96-114, 2015.
- [42] C.-W. Kuo and C. Steve Suh, "On the Dispersion and Attenuation of Guided Waves in Tubular Section with Multi-Layered Viscoelastic Coating — Part I: Axial Wave Propagation," *International Journal of Applied Mechanics*, vol. 09, p. 1750001, 2017.
- [43] M. J. S. Lowe and P. Cawley "Long range guided wave inspection usage—current commercial capabilities and research directions," ed, 2006.
- [44] D. N. Alleyne, B. Pavlakovic, M. J. S. Lowe, and P. Cawley, "Rapid, long range inspection of chemical plant pipework using guided waves," *AIP Conference Proceedings*, vol. 557, pp. 180-187, 2001.
- [45] J. D. Achenbach *Wave Propagation in Elastic Solids*. New York North-Holland, 1984.

- [46] B. A. Auld, *Acoustic Fields and Waves in Solids*: R.E. Krieger, 1990.
- [47] D. N. Alleyne and P. Cawley, "The excitation of Lamb waves in pipes using dry-coupled piezoelectric transducers," *Journal of Nondestructive Evaluation*, vol. 15, pp. 11-20, 1996.
- [48] Guided Ultrasonics Ltd. Available: <http://www.guided-ultrasonics.com/>
- [49] Y. E. Kwon, H. W. Kim, and Y. Y. Kim, "High-frequency lowest torsional wave mode ultrasonic inspection using a necked pipe waveguide unit," *Ultrasonics*, vol. 62, pp. 237-243, 2015.
- [50] J. Li and J. L. Rose, "Excitation and propagation of non-axisymmetric guided waves in a hollow cylinder," *The Journal of the Acoustical Society of America*, vol. 109, pp. 457-464, 2001.
- [51] L. Tang and B. Wu, "Excitation Mechanism of Flexural-Guided Wave Modes F(1, 2) and F(1, 3) in Pipes," *Journal of Nondestructive Evaluation*, vol. 36, p. 59, August 07 2017.
- [52] D. N. Alleyne and P. Cawley, "Long range propagation of Lamb waves in chemical plant pipework," *Materials Evaluation*, vol. 55, pp. 504-508, 1997.
- [53] M. J. S. Lowe, D. N. Alleyne, and P. Cawley, "The mode conversion of a guided wave by a part-circumferential notch in a pipe," *Journal of Applied Mechanics*, vol. 65, pp. 649-656, 1998.
- [54] T. R. Hay and J. L. Rose, "Flexible PVDF comb transducers for excitation of axisymmetric guided waves in pipe," *Sensors and Actuators A: Physical*, vol. 100, pp. 18-23, 2002.
- [55] M. Vasiljevic, T. Kundu, W. Grill, and E. Twerdowski, "Pipe wall damage detection by electromagnetic acoustic transducer generated guided waves in absence of defect signals," *The Journal of the Acoustical Society of America*, vol. 123, pp. 2591-2597, 2008.
- [56] P. Cawley, M. J. S. Lowe, D. N. Alleyne, B. N. Pavlakovic, and P. Wilcox, "Practical long range guided wave testing: applications to pipes and rails," *Mater Eval*, vol. 61, pp. 66-74, 2003.
- [57] Y. Liu, C. J. Lissenden, and J. L. Rose, "Nonlinear ultrasonic guided waves for microstructure characterization of hollow cylinders," presented at the 13th International Symposium on Nondestructive Characterization of Materials (NDCM-XIII), Le Mans, France, 2013.

- [58] Y. a. S. Kim, HongSeok, "Limitation of detection range in guided wave testing of buried pipeline," presented at the International Gas Union Research Conference 2014, 2014.
- [59] Y. Xin, H. Sun, H. Tian, C. Guo, X. Li, S. Wang, *et al.*, "The use of polyvinylidene fluoride (PVDF) films as sensors for vibration measurement: A brief review," *Ferroelectrics*, vol. 502, pp. 28-42, 2016.
- [60] J. J. Ditri, "Utilization of guided elastic waves for the characterization of circumferential cracks in hollow cylinders," *The Journal of the Acoustical Society of America*, vol. 96, pp. 3769-3775, 1994.
- [61] B. A. Auld, *Acoustic fields and waves in solids* vol. 2: RE Krieger, 1990.
- [62] A. Velichko and P. D. Wilcox, "Excitation and scattering of guided waves: Relationships between solutions for plates and pipes," *The Journal of the Acoustical Society of America*, vol. 125, pp. 3623-3631, 2009.
- [63] G. H. Du, Z. M. Zhu, and X. F. Gong, *Acoustics basics*. Nanjing: Nanjing University Publics, 2001.
- [64] A. H. S. H. Bai, N. Popplewell, S.K. Datta, "Scattering of guided waves by circumferential cracks in composite cylinders," *International Journal of Solids and Structures*, vol. 39, pp. 4583–4603, 2002.
- [65] W. Tse, P. Wang, and X. Wang, "Corrosion identification of gas pipe risers in buildings using advanced ultrasonic guided waves," in *Proceedings of the 7th World Congress on Engineering Asset Management (WCEAM 2012)*, ed: Springer International Publishing, 2015, pp. 583-592.
- [66] P. W. Tse and X. Wang, "Characterization of pipeline defect in guided-waves based inspection through matching pursuit with the optimized dictionary," *NDT & E International*, vol. 54, pp. 171-182, 2013.
- [67] X. Wang, P. W. Tse, and A. Dordjevich, "Evaluation of pipeline defect's characteristic axial length via model-based parameter estimation in ultrasonic guided wave-based inspection," *Measurement Science and Technology*, vol. 22, pp. 025701-025701-13, 2010.
- [68] M. Clough, M. Fleming, and S. Dixon, "Circumferential guided wave EMAT system for pipeline screening using shear horizontal ultrasound," *NDT & E International*, vol. 86, pp. 20-27, 2017.

- [69] R. Howard and F. Cegla, "Detectability of corrosion damage with circumferential guided waves in reflection and transmission," *NDT & E International*, vol. 91, pp. 108-119, 2017.
- [70] S. Heinlein, P. Cawley, and T. K. Vogt, "Reflection of torsional T(0,1) guided waves from defects in pipe bends," *NDT & E International*, vol. 93, pp. 57-63, 2018.
- [71] Y. Wang, L. Zhu, S. Li, and L. Chen, "Non-destructive testing of multi-bends pipe using guided waves " presented at the The 2014 4th International Conference on Mechatronics, Control and Electronic Engineering (MCE 2014), Shenyang, China, 2014.
- [72] E. Rojas, A. Baltazar, and C. Treesatayapun, "Investigation on damage identification in a pipe using torsional guided waves," *AIP Conference Proceedings*, vol. 1806, p. 030018, 2017.
- [73] Nurmalia, N. Nakamura, H. Ogi, and M. Hirao, "EMAT pipe inspection technique using higher mode torsional guided wave T(0,2)," *NDT & E International*, vol. 87, pp. 78-84, 2017.
- [74] R. Piervincenzo, B. Ivan, M. Alessandro, and L. d. S. Francesco, "Defect classification in pipes by neural networks using multiple guided ultrasonic wave features extracted after wavelet processing," *Journal of Pressure Vessel Technology*, vol. 127, pp. 294-303, 2005.
- [75] U. Amjad, C. H. Nguyen, S. Yadav, E. Mahmoudabadi, and T. Kundu, "Change in time-of-flight of longitudinal (axisymmetric) wave modes due to lamination in steel pipes," in *SPIE Smart Structures and Materials+ Nondestructive Evaluation and Health Monitoring*, 2013, pp. 869515-1-9.
- [76] U. Amjad, S. K. Yadav, and T. Kundu, "Detection and quantification of pipe damage from change in time of flight and phase," *Ultrasonics*, vol. 62, pp. 223-236, 2015.
- [77] M. Fink, "Time reversal of ultrasonic fields. I. Basic principles," *IEEE transactions on ultrasonics, ferroelectrics, and frequency control*, vol. 39, pp. 555-566, 1992.
- [78] F. Deng, C. He, and B. Wu, "Time reversal method for pipe inspection with guided wave," *AIP Conference Proceedings*, vol. 975, pp. 131-138, 2008.
- [79] F. Deng, "Defect imaging using time reversal guided waves in pipes," *Applied Mechanics and Materials*, vol. 188, pp. 283-286, 2012.

- [80] Z. Liu, Q. Xu, Y. Gong, C. He, and B. Wu, "A new multichannel time reversal focusing method for circumferential Lamb waves and its applications for defect detection in thick-walled pipe with large-diameter," *Ultrasonics*, vol. 54, pp. 1967-1976, 2014.
- [81] J. Davies, F. Simonetti, M. Lowe, and P. Cawley, "Review of synthetically focused guided wave imaging techniques with application to defect sizing," *AIP Conference Proceedings*, vol. 820, pp. 142-149, 2006.
- [82] J. Davies and P. Cawley, "The application of synthetic focusing for imaging crack-like defects in pipelines using guided waves," *IEEE transactions on ultrasonics, ferroelectrics, and frequency control*, vol. 56, pp. 759-771, 2009.
- [83] J. Zhou, C. He, Y. Zheng, B. Wu, and W. Qi, "Defect imaging in pipe with guided wave using common source method," *Engineering Mechanics*, pp. 65-72, 2012.
- [84] Z. Sun, A. Sun, and B.-F. Ju, "Guided wave imaging of oblique reflecting interfaces in pipes using common-source synthetic focusing," *Journal of Sound and Vibration*, vol. 420, pp. 1-20, 2018.
- [85] R. L. Kevin, V. M. Eugene, and K. H. Mark, "Ultrasonic Lamb wave tomography," *Inverse Problems*, vol. 18, pp. 1795-1808, 2002.
- [86] K. R. Leonard and M. K. Hinders, "Guided wave helical ultrasonic tomography of pipes," *The Journal of the Acoustical Society of America*, vol. 114, pp. 767-774, 2003.
- [87] K. R. Leonard and M. K. Hinders, "Lamb wave tomography of pipe-like structures," *Ultrasonics*, vol. 43, pp. 574-583, 2005.
- [88] P. Huthwaite and M. Seher, "Robust helical path separation for thickness mapping of pipes by guided wave tomography," *IEEE transactions on ultrasonics, ferroelectrics, and frequency control*, vol. 62, pp. 927-938, 2015.
- [89] F. Yan, R. L. Royer, and J. L. Rose, "Ultrasonic guided wave imaging techniques in structural health monitoring," *Journal of Intelligent Material Systems and Structures*, vol. 21, pp. 377-384, 2010.
- [90] R. L. Royer Jr, J. Van Velsor, and J. L. Rose, "An ultrasonic guided wave tomography approach for pipeline health monitoring," *The e-Journal of Nondestructive Testing*, 2009.
- [91] L. J. Breon, J. K. Van Velsor, and J. L. Rose, "Guided wave damage detection tomography for structural health monitoring in critical zones of pipelines," *Materials Evaluation*, vol. 65, pp. 1215-1219, 2007.

- [92] A. J. Brath, F. Simonetti, P. B. Nagy, and G. Instanes, "Guided Wave Tomography of Pipe Bends," *IEEE Transactions on Ultrasonics, Ferroelectrics, and Frequency Control*, vol. 64, pp. 847-858, 2017.
- [93] A. J. Brath, F. Simonetti, P. B. Nagy, and G. Instanes, "Experimental Validation of a Fast Forward Model for Guided Wave Tomography of Pipe Elbows," *IEEE Transactions on Ultrasonics, Ferroelectrics, and Frequency Control*, vol. 64, pp. 859-871, 2017.
- [94] M. Deng and J. Pei, "Assessment of accumulated fatigue damage in solid plates using nonlinear Lamb wave approach," *Applied physics letters*, vol. 90, p. 121902, 2007.
- [95] A. Martowicz, P. Packo, W. Staszewski, and T. Uhl, "Modelling of nonlinear vibro-acoustic wave interaction in cracked aluminium plates using local interaction simulation approach," in *Proceedings of ECCOMAS*, 2012, pp. 10-14.
- [96] Y. Liu, C. J. Lissenden, and J. L. Rose, "Cumulative second harmonics in weakly nonlinear plates and shells," in *SPIE Smart Structures and Materials+ Nondestructive Evaluation and Health Monitoring*, 2013, pp. 86950S-86950S-12.
- [97] M. Hong, Z. Su, Q. Wang, L. Cheng, and X. Qing, "Modeling nonlinearities of ultrasonic waves for fatigue damage characterization: Theory, simulation, and experimental validation," *Ultrasonics*, vol. 54, pp. 770-778, 2014.
- [98] M. Hong, Z. Su, Y. Lu, H. Sohn, and X. Qing, "Locating fatigue damage using temporal signal features of nonlinear Lamb waves," *Mechanical Systems and Signal Processing*, vol. 60-61, pp. 182-197, 2015.
- [99] Y. Yang, C.-T. Ng, A. Kotousov, H. Sohn, and H. J. Lim, "Second harmonic generation at fatigue cracks by low-frequency Lamb waves: Experimental and numerical studies," *Mechanical Systems and Signal Processing*, vol. 99, pp. 760-773, 2018.
- [100] C. Ma, W. Zhu, Y. Xiang, M. Deng, and H. Zhang, "Characterization of micro-crack evolution using Nonlinear Lamb waves," in *Proceedings of Meetings on Acoustics 6ICU*, 2017, p. 030006.
- [101] D. Broda, W. Staszewski, A. Martowicz, T. Uhl, and V. Silberschmidt, "Modelling of nonlinear crack-wave interactions for damage detection based on ultrasound—a review," *Journal of Sound and Vibration*, vol. 333, pp. 1097-1118, 2014.

- [102] V. Gusev, V. Tournat, and B. Castagnède, "Nonlinear acoustic phenomena in micro - inhomogenous media," *Materials and Acoustics Handbook*, pp. 431-471, 2010.
- [103] V. K. Chillara and C. J. Lissenden, "Review of nonlinear ultrasonic guided wave nondestructive evaluation: theory, numerics, and experiments," *Optical Engineering*, vol. 55, pp. 011002-011002, 2016.
- [104] L. D. Landau and E. Lifshitz, "Theory of Elasticity, vol. 7," *Course of Theoretical Physics*, vol. 3, p. 109, 1986.
- [105] W. J. N. De Lima and M. F. Hamilton, "Finite-amplitude waves in isotropic elastic plates," *Journal of Sound and Vibration*, vol. 265, pp. 819-839, 2003.
- [106] B. A. Auld, *Acoustic fields and waves in solids*: Рипол Классик, 1973.
- [107] A. D. Craik, *Wave interactions and fluid flows*: Cambridge University Press, 1988.
- [108] Y. Liu, C. J. Lissenden, and J. L. Rose, "Higher order interaction of elastic waves in weakly nonlinear hollow circular cylinders. I. Analytical foundation," *Journal of Applied Physics*, vol. 115, pp. 214901-214901-11, 2014.
- [109] J. M. Richardson, "Harmonic generation at an unbonded interface—I. Planar interface between semi-infinite elastic media," *International Journal of Engineering Science*, vol. 17, pp. 73-85, 1979.
- [110] O. V. Rudenko and C. A. Vu, "Nonlinear acoustic properties of a rough surface contact and acoustodiagnostics of a roughness height distribution," *Acoustic Physics*, vol. 40, pp. 593-596, 1994.
- [111] I. Y. Solodov, N. Krohn, and G. Busse, "CAN: an example of nonclassical acoustic nonlinearity in solids," *Ultrasonics*, vol. 40, pp. 621-625, 2002.
- [112] I. Solodov, N. Krohn, and G. Busse, "Nonlinear ultrasonic NDT for early defect recognition and imaging," in *European Conference on NDT (ECNDT), Moscow*, 2010.
- [113] K. Wang and Z. Su, "Analytical modeling of contact acoustic nonlinearity of guided waves and its application to evaluating severity of fatigue damage," in *SPIE Smart Structures and Materials+ Nondestructive Evaluation and Health Monitoring*, 2016, pp. 98050L-98050L-13.
- [114] K.-Y. Jhang, "Nonlinear ultrasonic techniques for nondestructive assessment of micro damage in material: A review," *International Journal of Precision Engineering and Manufacturing*, vol. 10, pp. 123-135, 2009.

- [115] F. D. Murnaghan, "Finite deformations of an elastic solid," *American Journal of Mathematics*, vol. 59, pp. 235-260, 1937.
- [116] L. Brillouin, "Tensors in Mechanics and Elasticity," 1964.
- [117] F. Liu, Y. Lu, Y. Bai, F. Li, and Z. Wang, "Numerical simulation of nonlinear ultrasonic guided waves for micro-cracking detection in pipelines," in *SMAR 2015-third conference on Smart Monitoring, assessment and rehabilitation of Civil Structures*, Antalya, Turkey, 7 – 9 September 2015.
- [118] K. E. A. Van Den Abeele, P. A. Johnson, R. A. Guyer, and K. R. McCall, "On the quasi-analytic treatment of hysteretic nonlinear response in elastic wave propagation," *The Journal of the Acoustical Society of America*, vol. 101, pp. 1885-1898, 1997.
- [119] K. R. Mccall and R. A. Guyer, "Equation of state and wave propagation in hysteretic nonlinear elastic materials," *Journal of Geophysical Research: Solid Earth*, vol. 99, pp. 23887-23897, 1994.
- [120] X. Guo, D. Zhang, and J. Zhang, "Detection of fatigue-induced micro-cracks in a pipe by using time-reversed nonlinear guided waves: A three-dimensional model study," *Ultrasonics*, vol. 52, pp. 912-919, 2012.
- [121] K. Yamanaka, Y. Ohara, M. Oguma, and Y. Shintaku, "Two-dimensional analyses of subharmonic generation at closed cracks in nonlinear ultrasonics," *Applied physics express*, vol. 4, p. 076601, 2011.
- [122] Y. Shen and C. E. Cesnik, "Modeling of nonlinear interactions between guided waves and fatigue cracks using local interaction simulation approach," *Ultrasonics*, vol. 74, pp. 106-123, 2017.
- [123] D. Ming-Xi, G. Guang-Jian, and L. Ming-Liang, "Experimental observation of cumulative second-harmonic generation of circumferential guided wave propagation in a circular tube," *Chinese Physics Letters*, vol. 32, p. 124305, 2015.
- [124] A. M. Sutin and P. A. Johnson, "Nonlinear elastic wave NDE II. Nonlinear wave modulation spectroscopy and nonlinear time reversed acoustics," *AIP Conference Proceedings*, vol. 760, pp. 385-392, 2005.
- [125] L. Pieczonka, W. J. Staszewski, and T. Uhl, "Investigation of nonlinear vibro-acoustic wave modulation mechanisms in composite laminates," *Key Engineering Materials*, vol. 569-570, pp. 96-102, 2013.

- [126] L. Pieczonka, A. Klepka, A. Martowicz, and W. J. Staszewski, "Nonlinear vibroacoustic wave modulations for structural damage detection: an overview," *Optical Engineering*, vol. 55, p. 011005, 2016.
- [127] D. Donskoy, A. Ekimova, E. Luzzato, J.-L. Lottiaux, S. Stoupin, and A. Zagrai, "N-SCAN®: New vibro-modulation system for detection and monitoring of cracks and other contact-type defects," presented at the SPIE's 10th Annual International Symposium on Smart Structures and Materials and 8th Annual International Symposium on NDE for Health Monitoring and Diagnostics, San Diego, CA, 2003.
- [128] H. Jin Lim, H. Sohn, and P. Liu, "Binding conditions for nonlinear ultrasonic generation unifying wave propagation and vibration," *Applied Physics Letters*, vol. 104, p. 214103, 2014.
- [129] C. J. Lissenden, Y. Liu, V. K. Chillara, G. Choi, and H. Cho, "Nonlinear guided wave mixing for localized material state characterization," *Physics Procedia*, vol. 70, pp. 668-671, 2015.
- [130] D. M. Donskoy and A. M. Sutin, "Vibro-acoustic modulation nondestructive evaluation technique," *Journal of Intelligent Material Systems and Structures*, vol. 9, pp. 765-771, 1998.
- [131] J. Jiao, L. Zheng, G. Song, C. He, and B. Wu, "Vibro-acoustic modulation technique for micro-crack detection in pipeline," in *Seventh International Symposium on Precision Engineering Measurements and Instrumentation*, 2011, pp. 83213X-83213X-8.
- [132] A. Demma, P. Cawley, M. Lowe, and B. Pavlakovic, "The effect of bends on the propagation of guided waves in pipes," *Journal of Pressure Vessel Technology*, vol. 127, pp. 328-335, 2005.
- [133] R. M. Sanderson, D. A. Hutchins, D. R. Billson, and P. J. Mudge, "The investigation of guided wave propagation around a pipe bend using an analytical modeling approach," *The Journal of the Acoustical Society of America*, vol. 133, pp. 1404-1414, 2013.
- [134] H. Sohn, "Effects of environmental and operational variability on structural health monitoring," *Philosophical Transactions of the Royal Society of London A: Mathematical, Physical and Engineering Sciences*, vol. 365, pp. 539-560, 2007.

- [135] F. Lanza di Scalea and S. Salamone, "Temperature effects in ultrasonic Lamb wave structural health monitoring systems," *The Journal of the Acoustical Society of America*, vol. 124, pp. 161-174, 2008.
- [136] M. Eybpoosh, M. Berges, and H. Noh, "Investigation on the effects of environmental and operational conditions (EOC) on diffuse-field ultrasonic guided-waves in pipes," in *Computing in Civil and Building Engineering (2014)*, Orlando, Florida, United States, 2014, pp. 1198-1205.
- [137] M. Eybpoosh, M. Berges, and H. Y. Noh, "Nonlinear feature extraction methods for removing temperature effects in multi-mode guided-waves in pipes," in *SPIE Smart Structures and Materials+ Nondestructive Evaluation and Health Monitoring*, 2015, pp. 94371W-94371W-16.
- [138] M. Eybpoosh, M. Berges, and H. Y. Noh, "An energy-based sparse representation of ultrasonic guided-waves for online damage detection of pipelines under varying environmental and operational conditions," *Mechanical Systems and Signal Processing*, vol. 82, pp. 260-278, 2017.
- [139] M. J. S. Lowe and P. Cawley, "Long range guided wave inspection usage—current commercial capabilities and research directions," *Department of Mechanical Engineering, Imperial College London, London*, 2006.
- [140] S. Harumichi and O. Hisato, "Guided waves propagating in a water-filled stainless steel pipe," *Japanese Journal of Applied Physics*, vol. 53, pp. 07KC13-1-5, 2014.
- [141] S. Jin, L. Sun, G. Liu, Y. Li, and H. Zhang, "Study on ultrasonic guided waves in fluid-filled pipes surrounded by water," in *2006 International Pipeline Conference*, Calgary, Alberta, Canada, 2006, pp. 755-760.
- [142] S. Djili, F. Benmeddour, E. Moulin, J. Assaad, and F. boubenider, "Notch detection in copper tubes immersed in water by leaky compressional guided waves," *NDT & E International*, vol. 54, pp. 183-188, 2013.
- [143] E. Leinov, P. Cawley, and M. J. S. Lowe, "Investigation of guided waves propagation in pipe buried in sand," *AIP Conference Proceedings*, vol. 1581, pp. 271-278, 2014.
- [144] F. Bertoncini, G. D. Lorenzo, G. Giunta, M. Raugi, and F. Turcu, "Effect of attenuation on inspection range and sensitivity in long-range guided wave NDT of coated and buried pipes," *The e-Journal of the nondestructive testing*, vol. 11, 2010.

- [145] O. Diligent, T. Grahn, A. Boström, P. Cawley, and M. J. S. Lowe, "The low-frequency reflection and scattering of the S<sub>0</sub> Lamb mode from a circular through-thickness hole in a plate: Finite Element, analytical and experimental studies," *The Journal of the Acoustical Society of America*, vol. 112, pp. 2589-2601, 2002.
- [146] M. I. Friswell and J. E. T. Penny, "Crack Modeling for Structural Health Monitoring," *Structural Health Monitoring*, vol. 1, pp. 139-148, 2002/06/01 2002.
- [147] F. Semperlotti, K. W. Wang, and E. C. Smith, "Localization of a Breathing Crack Using Super-Harmonic Signals due to System Nonlinearity," *AIAA Journal*, vol. 47, pp. 2076-2086, 2009.
- [148] "Nonlinear elastic constants of solids with cracks," *The Journal of the Acoustical Society of America*, vol. 102, pp. 3349-3354, 1997.
- [149] T. W. Wang and C. H. Yang, "Effective Models of PZT Actuators for Numerical Simulation of Elastic Wave Propagation," *Applied Mechanics and Materials*, vol. 553, pp. 705-710, 2014.
- [150] R. d. Medeiros, M. L. Ribeiro, M. Sartorato, G. Marinucci, and V. Tita, "Computational simulation using PZT as sensor elements for damage detection on impacted composite cylinders," in *Proceedings of the 1st International Symposium on Solid Mechanics MecSol2013. Porto Alegre, Rio Grande do Sul, Brazil*, <http://www.ufrgs.br/mecsol2013/articles/MecSol2013-007.pdf>, 2013.
- [151] H. Sungwon and C. Fu-Kuo, "Adhesive interface layer effects in PZT-induced Lamb wave propagation," *Smart Materials and Structures*, vol. 19, p. 025006, 2010.
- [152] W. Ostachowicz, P. Kudela, P. Malinowski, and T. Wandowski, "Damage localisation in plate-like structures based on PZT sensors," *Mechanical Systems and Signal Processing*, vol. 23, pp. 1805-1829, 2009.
- [153] K. WANG and Z. SU, "A structural health monitoring approach based on contact acoustic nonlinearity and its application to quantitative evaluation of fatigue cracks," presented at the 8th European Workshop on Structural Health Monitoring (EWSHM 2016), Bilbao, Spain, 2016.
- [154] O. Diligent, T. Grahn, A. Boström, P. Cawley, and M. J. Lowe, "The low-frequency reflection and scattering of the S<sub>0</sub> Lamb mode from a circular through-thickness hole in a plate: Finite Element, analytical and experimental studies," *The Journal of the Acoustical Society of America*, vol. 112, pp. 2589-2601, 2002.

- [155] J. D. Achenbach and Y. Xu, "Wave motion in an isotropic elastic layer generated by a time-harmonic point load of arbitrary direction," *The Journal of the Acoustical Society of America*, vol. 106, pp. 83-90, 1999.
- [156] J. J. L. Sanders, "Circumferential Through-Cracks in Cylindrical Shells Under Tension," *Journal of Applied Mechanics*, vol. 49, pp. 103-107, 1982.
- [157] S. H. Yoo and J. Pan, "Approximate Crack Opening Displacement Solutions for Long Circumferential Cracks in Pipes Subjected to Bending and Tension," *Journal of Pressure Vessel Technology*, vol. 114, pp. 178-180, 1992.
- [158] L. Weibin, C. Younho, and D. A. Jan, "Detection of thermal fatigue in composites by second harmonic Lamb waves," *Smart Materials and Structures*, vol. 21, p. 085019, 2012.
- [159] C. Bermes, J.-Y. Kim, J. Qu, and L. J. Jacobs, "Experimental characterization of material nonlinearity using Lamb waves," *Applied Physics Letters*, vol. 90, pp. 021901-021901-3, 2007.
- [160] J.-Y. Kim, L. J. Jacobs, J. Qu, and J. W. Littles, "Experimental characterization of fatigue damage in a nickel-base superalloy using nonlinear ultrasonic waves," *The Journal of the Acoustical Society of America*, vol. 120, pp. 1266-1273, 2006.
- [161] Y. Wang and H. Hao, "Modelling of guided wave propagation with spectral element: application in structural engineering," *Applied Mechanics and Materials*, vol. 553, pp. 687-692, 2014.
- [162] L. Moreau, A. Velichko, and P. D. Wilcox, "Accurate finite element modelling of guided wave scattering from irregular defects," *NDT & E International*, vol. 45, pp. 46-54, 2012.
- [163] D. Broda, W. J. Staszewski, A. Martowicz, T. Uhl, and V. Silberschmidt, "Modelling of nonlinear crack-wave interactions for damage detection based on ultrasound—a review," *Journal of Sound and Vibration*, vol. 333, pp. 1097-1118, 2014.
- [164] P. Christoph, K. Jin-Yeon, Q. Jianmin, and J. J. Laurence, "Evaluation of fatigue damage using nonlinear guided waves," *Smart Materials and Structures*, vol. 18, p. 035003, 2009.
- [165] P. Zuo, Y. Zhou, and F. Zheng, "Numerical studies of nonlinear ultrasonic guided waves in uniform waveguides with arbitrary cross sections," *AIP Advances*, vol. 6, p. 075207, 2016.

-Quantitative evaluation of fatigue crack using nonlinear guided waves in pipelines-

- [166] W. Li and Y. Cho, "Combination of nonlinear ultrasonics and guided wave tomography for imaging the micro-defects," *Ultrasonics*, vol. 65, pp. 87-95, 2016.

## List of Publications

### Journal papers:

J. Li, Y. Lu, R. Guan, and W. Qu, "Guided waves for debonding identification in CFRP-reinforced concrete beams," *Construction and Building Materials*, vol. 131, pp. 388-399, 2017.

Y. Wang, R. Guan, and Y. Lu, "Nonlinear Lamb waves for fatigue damage identification in FRP-reinforced steel plates," *Ultrasonics*, vol. 80, pp. 87-95, 2017.

R. Guan, Y. Lu, W. Duan, and X. Wang, "Guided waves for damage identification in pipeline structures: A review," *Structural Control and Health Monitoring*, vol. 24, e2007, 2017.

R. Guan, Y. Lu, K. Wang, Z. Su, "Fatigue crack detection in pipes with multiple mode nonlinear guided waves," *Structural Health Monitoring*, vol. 0, p. 1475921718791134, 2018.

R. Guan, Y. Lu, K. Wang, Z. Su, " Quantitative fatigue crack evaluation in pipeline structures using nonlinear cylindrical waves" (ready to submission).

R. Guan, Y. Lu, K. Wang, Z. Su, "A theoretical model of contact acoustic nonlinearity in pipe structures with longitudinal mode excitation" (ready to submission).

### Conference papers:

R. Guan, Y. Lu, W. Duan and X. Wang, "Numerical simulation of fatigue cracking identification in pipes with nonlinear guided waves" in SMAR 2017-the fourth Conference on Smart Monitoring, Assessment and Rehabilitation of Civil Structures, Zurich, Switzerland, 2017.

-Quantitative evaluation of fatigue crack using nonlinear guided waves in pipelines-

Y. Wang, R. Guan and Y. Lu, "Fatigue cracking identification using nonlinear Lamb waves for FRP-reinforced steel plates" in SHMII-8 Structural Health Monitoring of Intelligent Infrastructure Conference 2017, Brisbane, Australia, 2017.

R. Guan, Y. Lu, K. Wang, Z. Su, " Detection of fatigue crack in an aluminium pipe with nonlinear guided waves" in 7th Asia-Pacific Workshop on Structural Health Monitoring (APWSHM-2018), Hong Kong, 2018.

**Industry newsletter:**

R. Guan, Y. Lu, K. Wang, Z. Su, "Fatigue crack detection in pipelines using nonlinear guided waves" Australian Network of Structural Health Monitoring (ANSHM) Newsletter, Issue 16, pp 8-11, 2018.